A REFINED POTENTIAL THEORY FOR THE INCOMPRESSIBLE UNSTEADY SUBCRITICAL-REYNOLDS NUMBER FLOWS ON CANONICAL BLUFF BODIES

A Thesis
Presented to
The Academic Faculty

by

Taofiq Omoniyi Amoloye

In Partial Fulfillment
of the Requirements for the Degree
Doctor of Philosophy in the
School of Aerospace Engineering

Georgia Institute of Technology
December 2020

A REFINED POTENTIAL THEORY FOR THE INCOMPRESSIBLE UNSTEADY SUBCRITICAL-REYNOLDS NUMBER FLOWS ON CANONICAL BLUFF BODIES

Approved by:

Professor Marilyn J. Smith, Advisor
School of Aerospace Engineering
Georgia Institute of Technology

Professor Brian German
School of Aerospace Engineering
Georgia Institute of Technology

Professor Jechiel Jagoda
School of Aerospace Engineering
Georgia Institute of Technology

Professor John McCuan
School of Mathematics
Georgia Institute of Technology

Professor Stephen M. Ruffin
School of Aerospace Engineering
Georgia Institute of Technology

Date Approved: November 16, 2020

This work is dedicated wholeheartedly to God, The Almighty Who says:

"Read! In the Name of your Lord Who created.

He created man from a clot.

Read! And your Lord is the Most Generous.

He Who taught by the pen.

He taught man what he did not know."[Translation from the Arabic text]

Al-Quran, The Clot (Chapter 96):1-5

ACKNOWLEDGEMENTS

The comments, pieces of advice, patience and understanding of my advisor, Professor Marilyn J. Smith, are very acknowledged and highly appreciated. I would also like to express my gratitude to her for soliciting supplemental teaching assistantship funding for me from the school of aerospace engineering. I extend this gratitude to the school in general.

It was always good to see Professor Jechiel Jagoda right from my first meeting with him ever. Over time, he became to me a dependable mentor and a friend especially in the numerous times of distress in the course of my studies. He also helped to solicit for my teaching assistant positions. I am very thankful for this. The rest of my thesis committee also offered comments and guidance which were invaluable and very appreciated.

Dr. Nicholson Konrad Koukpaizan, a then fellow Ph.D. candidate, always encouraged the avenue in which I was able to discuss and assess the viability of some rudimentary ideas which eventually culminated in this work. This is very appreciated.

I express my profound gratitude to the present and past administrations of Kwara State University (KWASU), Malete, Nigeria for the financial support of my post graduate studies. I remember the time of my one-on-one job interview meeting with the then Vice-Chancellor, Professor Abdul-Rasheed Na'Allah, when he laid down the vision of where our dear university hopes to be with the three-pronged ideal of teaching, research and community development. I also remember when, at one of his regular visits to the college of engineering, he displayed a public vote of confidence in my suitability as an ambassador for our great university. For these times among many others and the continued long-standing and time-tested commitment of the university

to this ideal as it particularly relates to my graduate studies, I am not only grateful to the university and ultimately to God, but I am also humbled by the opportunity I was given to serve. My funding guarantors, Professor Sulaiman Jamiu and Professor Shaykh-Luqman Jimoh did me a great service for which I am very grateful. I cannot thank Dr. Sherifat Hussein-Abubakar enough for the motherly role she always played for me and for being my spokesperson at KWASU. Many thanks are also in order to Professor Leo Daniel and Professor Chris Odetunde for all the roles they played in the successful completion of my studies.

I shall not forget to acknowledge all my students at KWASU and in particular, HabeebuLlah Olaitan AbdulKadir, whose enthusiastic question in class on February 19, 2014 aroused my curiosity for this study.

I would be lacking hindsight if I did not acknowledge the contributions of my teachers and lecturers, both formal and informal, who have contributed immensely to my general knowledge and in particular, to my knowledge of aerodynamics. Of notable mention are Dr. K. Bofah of Kwame Nkrumah University of Science and Technology in Kumasi, Ghana and John D. Anderson, Jr. of the Smithsonian Institution, Washington DC, United States of America. The former introduced me thoroughly, in the pursuit of my Bachelor's degree, to the *Fundamentals of Aerodynamics* using one of the numerous well-known texts written by the latter.

I would be too ungrateful not to acknowledge my friends who may have been on the lookout for this paragraph. I have your names ingrained in my heart, and I thank you for the friendship we share which I hold dearly.

I am much more indebted to my siblings, uncles, aunts, cousins and entire family (biological and adopted), too numerous to mention here, for their unconditional and unending love and prayers. It would amount to another thesis write-up to effectively express my thanks to everyone. However, naturally, Dr. Mrs. Azizah Omotoyosi Amoloye-Adebayo, Mrs. Taofiqah Omotayo Abu, Dr. Hikmah Omodesola Ibrahim

(Mrs.) and Engr. Mubarak Omobolaji Amoloye deserve unconditional mention as much as my love and appreciation. Also, it behoves me to mention my fraternal love and admiration for all the members of the Alfarooq Masjid community who made Atlanta a home-away-from-home for me especially in the months of Ramadan. Of very notable mention are Mr. Mustapha Khalifah and Mr. Khaldoun Malas through whose selfless generosities I found divine mercy.

Words cannot begin to express my gratitude, appreciation, love and adoration for my mother, Dr. Mrs. Bilqis Ajoke Amoloye, and my late father, Dr. Abdul-Jelil Adebayo Amoloye. I had a dream when I was very young, and I am living it now thanks to your belief and support. In a similar vein, I remain forever indebted to my adopted parents in their numbers (the *committee of friends* and others) who, indeed, have chosen to remain friends of the family as much in my father's demise as in his lifetime many years ago. I also need to mention and thank my uncle, Mr. Yunus Amoloye from whose discussion of the globe and outer space, my young mind of around 6 years began to wonder about aerospace engineering.

I have found that I am able to look into engineering problems critically and suggest solutions even when they are not immediately relevant to my field. I recognise this as a favour and blessing of God, Who, I believe, was not only my general Supervisor for this work but also, the Only Supervisor I have known for all my affairs. I appreciate and submit to Him for the inspiration for and the completion of this study. I declare that to Him belongs the ultimate acknowledgment and glory.

AlhamduliLlah Rabbil A'lameen (Praise be to God, the Lord of the worlds)!

TABLE OF CONTENTS

LIST OF TABLES

LIST OF FIGURES

NOMENCLATURE

Abbreviations

CFD	Computational Fluid Dynamics
CMI	The Clay Mathematics Institute of Cambridge Massachussets
CPT	Classical Potential Theory
DNS	Direct Numerical Simulation
KWASU	Kwara State University, Malete, Nigeria
LES	Large Eddy Simulation
NLF	Non-lifting flow
NSE	Navier-Stokes Equations
RPT	Refined Potential Theory
tHRLES	transitional Hybrid Reynolds-averaged Navier-Stokes-LES

Subscripts

0	zero,initial,total or stagnation condition
$2D$	Two-dimensional
$3D$	Three-dimensional
∞	Free stream
B	Body
e	Edge of boundary layer

kvs	Kármán vortex street
s	Separation point
t	Thickness
Tr	Transition point
W	Rotated
w	Wall condition

Greek

α	Pitch angle about the z-axis $[rad]$
β	Yaw angle about the y-axis $[rad]$
χ	A constant
δ	Boundary layer thickness $[m]$
ϵ	A constant
η	A constant
Γ	Vortex strength, Circulation $[m^2/s]$
γ	Ratio of specific heats
κ	*Kwasu* function $[kg/ms]$
Λ	Source/sink strength $[m^2/s]$
λ	Second coefficient of viscosity $[m^2/s]$
ω	Vorticity vector $[s^{-1}]$
μ	Dynamic viscosity $[Ns/m^2]$

μ_g	Gravitational parameter $[m^3/s^2]$; Wake-analogy factor $[m^3/s^2]$
ν	Kinematic viscosity $[m^2/s]$
Ω	Right ascension $[deg]$
Φ	Gravitational potential $[m^2/s^2]$
ϕ	Classical velocity potential $[m^2/s]$
Ψ	Perifocal stream function $[m^2/s]$
ψ	Classical stream function $[m^2/s]$
ρ	Density $[kg/m^3]$
σ	A constant
τ	Shear stress $[N/m^2]$
Θ	True anomaly/Perifocal circumferential coordinate $[rad]$
θ	Circumferential coordinate $[rad]$
θ_s	Separation angle $[rad]$
Υ	Argument of perigee $[deg]$
ε	Orbit or path eccentricity
φ, φ_i	Azimuthal spherical coordinate $[rad]$; Orbit inclination $[deg]$
ϖ	Angular velocity $[rad/s]$
ϱ	Perifocal radial coordinate $[m]$
ς	Roll angle about the x-axis $[rad]$
ζ	A constant

Operators

$\frac{D}{Dt}$	Substantial derivative
∇	Gradient operator
$\nabla\cdot$	Divergence operator
$\nabla\times$	Curl operator
∇^2	Laplacian operator

Roman

$\mathbf{a}$	Acceleration vector $[m^2/s]$
$\mathbf{F}$	Force vector $[N]$
$\mathbf{g}$	Body force vector $[N]$
$\mathbf{h}$	Specific angular momentum vector $[m^2/s]$
$\mathbf{Q}$	Euler angle transformation matrix
$\mathcal{M}$	Mass $[kg]$
$\mathcal{R}$	Real part of a complex valued function
$\mathcal{T}$	Period of an orbit $[s]$
$\mathcal{V}$	Volume $[m^3]$
$\tilde{x}, \tilde{y}, \tilde{z}$	Wind axis cartesian coordinate triad $[m]$
A	Axial force $[N]$
a	Speed of sound $[m/s]$
b	A constant

D	Diameter of cylinder $[m]$; Drag force $[N]$
G	Universal gravitational constant $[m^3/kgs^2]$
h	Specific angular momentum $[m^2/s]$; Hour
j	A constant
k	Doublet strength $[m^2/s]$
L	Lift force $[N]$
l	A constant
M	Mach number
N	Normal force $[N]$; A constant
$O()$	Order of
p	Pressure $[N/m^2]$
R	Radius $[m]$
$r, \mathbf{r}$	Radial Coordinate $[m]$; Position vector $[m]$
r_c	Vortex core radius $[m]$
Re	Reynolds number based on cylinder diameter,$Re = \frac{V_\infty D}{\nu}$
S	Side force $[N]$; Reference Area $[m^2]$
t	Time $[s]$
u	Pathline displacement along x-axis $[m]$
v	Pathline displacement along y-axis $[m]$
$V, \mathbf{V}$	Speed $[m/s]$; Velocity vector $[m/s]$

w	Pathline displacement along z-axis $[m]$
x, y, z	Longitudinal, Transverse, Vertical body-fixed coordinate axes (geometric) $[m]$

SUMMARY

The three main approaches to exploring fluid dynamics are actual experiments, numerical simulations, and theoretical solutions. In classical potential theory, the steady inviscid incompressible flow over a body can be obtained by the superposition of elementary flows with known analytical solutions. Analytical solutions can offer huge advantages over numerical and experimental solutions in the understanding of fluid flows and design. These advantages are in terms of cost and time consumption. However, the classical potential theory falls short of reconciling the actions of viscosity in an experimentally observed flow with the theoretical analysis of such a flow. As such, it is unable to resolve the boundary layer and predict the especially important flow separation phenomenon that results in the pressure drag experienced by a body in the flow. This has relegated potential theory to idealized flows of little practical importance.

Therefore, an attempt is made in this thesis to refine the classical potential theory of the flow over a circular cylinder to bridge the gap between the theory and experimentally observed flows. This is to enhance the ability to predict and/or control the flows' aerodynamic quantities and the evolution of the wake for design purposes. The refinement is achieved by introducing a viscous sink-source-vortex sheet on the surface of the cylinder to model the boundary layer. These vortices, sources and sinks introduced at the cylinder surface are modeled as concentric at every location. The vortices are modeled as Burgers' vortices, and analytic expressions for their strengths and those of the sinks/sources are obtained from the classical theory. These are employed to obtain a viscous and time-dependent stream function that captures critical

qualitative features of the flow including flow separation, reattachment, wake formation, and vortex shedding.

After that, a viscous potential function, the *Kwasu* function, with which the pressure field is obtained from the Navier-Stokes equation, is derived from the stream function. It is obtained by defining the viscous stream function on a principal axis of the flow about which the vorticity vector is identically zero. Strategies have also been developed to account for the finite extent of the cylinder and dynamic unsteadiness of the flow, and to predict the points of separation/reattachment/transition and the boundary layer thickness. Additionally, the strategies are used to obtain forces and apply the solution to arbitrary geometries focusing on spheres and spheroids. These strategies include the gravity analogy that considers a fluid element-cylinder scenario to be like a two-body problem in orbital mechanics. This analogy introduces the perifocal frame of fluid motion and exploits it to resolve the d'Alembert's Paradox. The perifocal frame is also used to predict flow separation/reattachment/transition and explain the observation of sign changes in the shear stress distribution at the rear of a circular cylinder in a crossflow.

The refined potential theory is verified against experimental and numerical data on the cylinder in an incompressible crossflow at $Re_\infty = 3,900$. Its drag prediction is within the error bound of measured data and tHRLES (transitional Hybrid Reynolds-averaged Navier-Stokes Large Eddy Simulation) prediction. The predictions of the pressure distribution, separation point and Strouhal number are also within acceptable ranges. Its prediction of the force coefficients over the range $25 \leq Re_\infty < 300,000$ is validated against experimental and theoretical data on the cylinder in crossflow. There is a good agreement in the magnitude and trend for $Re_\infty > 100$. For $Re_\infty < 100$, there is a disparity in magnitude that is unsafe for design purposes. Similarly, it under-predicts the coefficient of drag in some of the explored axial flow configurations. However, at $Re_\infty = 96,000$ and an aspect ratio

of 2, the RPT drag prediction falls within 1.2% of validated computational result. The energy spectra of the wake velocity display the Kolmogorov's Five-Thirds law of homogeneous isotropic turbulence. This verifies and validates the unsteadiness in refined potential theory as turbulent in nature.

The drag coefficient of a sphere for $25 \leq Re_\infty < 300,000$ is explored to demonstrate the application of refined potential theory. Additionally, the flow over a sphere at $Re_\infty = 100,000$ is explored in detail. A generally good agreement is observed in the prediction of the experimental trend for $Re_\infty \geq 2,000$. The transitional incompressible flows over a $6:1$ prolate spheroid at an angle of attack $\beta = 45^\circ$ for $Re_\infty = 3,000$ and $Re_\infty = 4,000$ are also explored. The present theoretical pressure distribution has a close agreement with the DNS (direct numerical simulation) result in the starboard rear of the spheroid. However, the magnitude of the predicted force coefficients are generally less than five times the corresponding DNS results. The asymmetry of the DNS pressure distribution in the meridian plane is not captured. Therefore, further analyses of the spheroid flow including the separation locations are recommended for further studies.

It is concluded that the refined potential theory can be used to resolve, explore and/or control the aerodynamic quantities of the flows around canonical bluff bodies as well as the evolution of their wakes.

CHAPTER I

INTRODUCTION AND BACKGROUND

1.1 Introduction and Motivation

Traditionally, the steady inviscid incompressible flow over a body can be obtained by solving the steady Euler equations with the appropriate boundary conditions or by the superposition of elementary flows with known solutions using potential theory [19]. This is in recognition of the fact that the velocity field of such a flow obeys the Laplace equation which is linear and lends itself to analytical solutions by the method of separation of variables. The applicability of the Laplace equation on incompressible flows has experimental evidence, and its solution for some bodies and configurations share some qualitative characteristics with experimentally observed flows as exemplified by the streamlines of the unseparated flow over a circular cylinder at $Re_\infty = 1.54$ presented in Fig. 1. In this figure, the flows are from left to right. This was, hitherto, the state of the art in the closed-form mathematical solution of the cylinder flow. To make a distinction between this and the theory presented herein, it will be referred to with the adjective 'classical'. At first, the qualitative comparison between Figs. 1a and 1b seems accurate. However, a quantitative comparison reveals some differences. Due to the assumption of an ideal fluid in the classical theory, it would be expected that its prediction should only approach reality in the inviscid limit as the Reynolds number becomes so high that the effects of the viscous terms vanish from the equations of motion of an experimentally observed flow contrary to the figures. In addition to this mismatch in Reynolds number limits, the classical theory always realizes a slip velocity at the wall and assumes the flow to be irrotational in the entire domain, in contrast to the mechanism which gives rise to the observed

presence of the boundary layer and vorticity in actual viscous flows. Finally, the gap between the prediction of zero drag for a steady flow in the classical theory and actual experiments is dubbed the d'Alembert's Paradox [20]. Classical inviscid theory falls short of reconciling the actions of viscosity and frictional forces in an experimentally observed flow with the theoretical analysis of such a flow. As such, it is unable to resolve the boundary layer and predict the especially important flow separation phenomenon that results in the pressure drag experienced by a body in the flow.

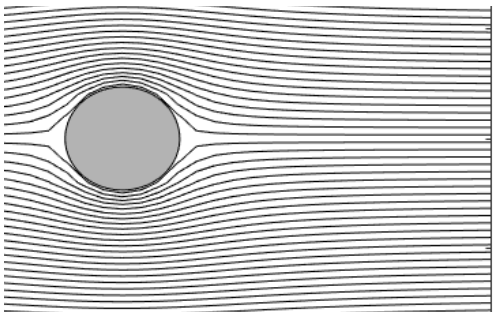

(a) The streamlines from the classical potential theory at the inviscid limit, $Re_\infty \to \infty$ (plotted by the current author).

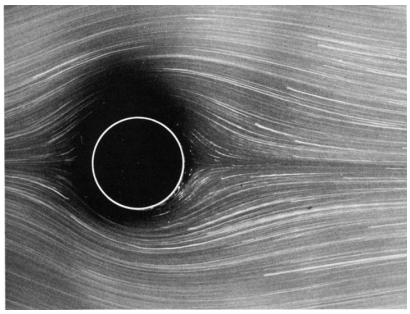

(b) The streamlines for the experimentally observed creeping flow over the cylinder [5] ($Re_\infty = 1.54$)

Figure 1: A comparison of streamlines from theory and experiment

Actual flows are viscous flows whose physics are governed by the Navier-Stokes equations (NSE)[5, 21, 22]. An attempt to refine the classical potential theory of the flow over the finite circular cylinder to capture important features of a bluff body flow including flow separation and reattachment, wake formation, and vortex shedding as well as compressibilty effects is synonymous with obtaining an analytical solution to the NSE. Adequate solutions of the NSE should appropriately predict flow separation and result in a finite drag on a body within the flow. However, the NSE are highly complex and non-linear. Up to this date, there is no known physically acceptable analytical solution of the full NSE for some specified freestream

and boundary conditions for arbitrary bodies. At the turn of the 21st century, the Clay Mathematics Institute of Cambridge Massachussets (CMI) included finding a solution, the proof of a solution, the proof of no solutions to these equations as one of its seven millennium prize problems [22]. CMI has been at the forefront of the coordination of the worldwide search for the general solution(s) (or proof of no solution(s)) to these relations. A check on the status of the problem on its website (accessed on November 16, 2020) still reveals it to be unsolved despite some recent attempts by various researchers [23–32]. However, with limiting but suitable assumptions and approximations, exact and approximate analytical solutions of these relations have been obtained for some special flows. Additionally, direct numerical solution (DNS) of these flow fields within a discretized domain can be obtained with the use of high-speed computers. Depending on the complexity of the flow and the computational speed, such simulations can take weeks of wall time.

Efforts at solving the NSE eventually led to the formulation in the early 1900s of Boundary Layer Theory (BLT) which simplifies the NSE into the boundary layer equations (BLE) [5, 10, 15, 33]. In his proposition of BLT, Prandtl recognised that the viscous effects in a wall-bounded flow are largely confined to the thin boundary layer just adjacent to the wall. Prandtl's premise on BLT is the experimentally backed assumption of the no-slip condition at the wall. He surmised that the no-slip condition, imposed on the flow by friction and viscosity, ensures that the fluid adheres to, and also assumes the velocity of the wall. Since the velocity field of the flow is continuous, the fluid rapidly accelerates to the local freestream velocity at the edge of the boundary layer where inviscid theory reasonably holds [10]. The boundary layer hypothesis has proven crucial in understanding and predicting viscous phenomena including flow separation and skin friction drag, as well as aerodynamic heating. With Prandtl's submission, the solutions of the flow field around bodies have been obtained with inviscid theory applied outside the boundary layer coupled

with the solution of the boundary layer equations. This has proven successful in over a century of applications, and it has been generally considered as the resolution of the d'Alembert's Paradox. Nonetheless, there are conflicting discussions on the validity of the no-slip boundary condition in the literature [34, 35] as exemplified by the recent work of Hoffman et al. [27, 36] who were able to compute drag with a slip boundary condition from the computational solution of the unsteady Euler equations with values comparable to those obtained in actual experiments.

Following the introduction of the proper orthogonal decomposition (POD) reduced order modeling in fluid dynamics, various attempts have been made at its application to the case of the circular cylinder. Particular interests have been taken in understanding and characterizing the wake dynamics as well as 'training' the resulting model in a Galerkin projection to capture the dynamics of the flow at different Reynolds numbers other than the one used for the POD modes extraction [37]. This seems promising; however, Deane et al. [37] observed that the 'trained' model is highly sensitive to the Reynolds number used to extract the POD modes for the cylinder wake flow. This is because the mean flow used for the Galerkin projection is itself Reynolds-number-dependent. Therefore, the Reynolds-number-dependence of the mean flow must be extracted from a series of experimental and/or numerical data which will serve as inputs to the POD process. This further amplifies the volume of data, cost and time needed to obtain a sufficiently accurate reduced order model.

The current gap in resolving these cylinder flows is necessary to improve the advances in the theoretical prediction of fluid dynamic phenomena. Many approaches have been tried, but they have been limited in the dimensions of the flow and the regime of the Reynolds number. Therefore, this thesis proceeds with a review of literature and the presentation of the aim and objectives of this work in the following subsections of the current chapter, the details of the theoretical formulation in chapter 2, the verification and validation of the theory on the finite cylinder in chapter 3, the

application of the theory on the sphere and spheroid in chapter 4, the conclusive remarks in chapter 5, and a discussion on the recommendations for future work in chapter 6.

1.2 Literature Review on Extant Solutions and Models

The set of the NSE for the compressible flow of a Newtonian fluid in an arbitrary control volume are expressed in single vector equations, using the indicial notation as

$$\oint_{\mathcal{V}} \left[\frac{\partial \rho}{\partial t} + \nabla \cdot (\rho \mathbf{V}) \right] d\mathcal{V} = 0 \tag{1}$$

$$\oint_{\mathcal{V}} \left[\frac{D(\rho \mathbf{V})}{Dt} + \nabla p - \rho \mathbf{g} - \frac{\partial}{\partial x_j} \left[\mu \left(\frac{\partial v_i}{\partial x_j} + \frac{\partial v_j}{\partial x_i} \right) + \delta_{ij} \lambda \nabla \cdot \mathbf{V} \right] \right] d\mathcal{V} = 0 \,. \tag{2}$$

A Newtonian fluid is one for which there exists a linear relationship between stress and strain [15]. Equation 1 is a statement of the conservation of mass, and Eqn. 2 embodies the conservation of momentum for fluid flows [5, 15, 22].

The indicial notation in Eqn. 2 is necessary to express the stress tensor [15]. The general form of this tensor including a normal stress component, thermodynamic pressure (p), and the tangential stress (shear stress) is given as

$$\tau_{ij} = -p\delta_{ij} + \mu \left(\frac{\partial v_i}{\partial x_j} + \frac{\partial v_j}{\partial x_i} \right) + \delta_{ij} \lambda \nabla \cdot \mathbf{V} \,. \tag{3}$$

for a Newtonian viscous fluid [15]. When an analogy between Eqn. 3 and the strain relation in elasticity is drawn, the summation of Eqn. 3 is employed to define the mechanical pressure, $\tilde{p}$, as

$$\tilde{p} = -\frac{1}{3} (\tau_{xx} + \tau_{yy} + \tau_{zz}) = p - \left(\lambda + \frac{2}{3} \mu \right) \nabla \cdot \mathbf{V} \tag{4}$$

identifying the pressure as a tensor invariant [15, p. 67]. Thus, the term $\left(\lambda + \frac{2}{3}\mu\right) \nabla \cdot \mathbf{V}$ in Eqn. 4 accounts for the difference between the thermodynamic pressure in an undisturbed freestream and the mechanical pressure due to a flow in question [15, 33, 38, 39]. It is important for compressible flows and flows in which the viscous normal

stresses are not negligible. However, when the flow is incompressible ($\nabla \cdot \mathbf{V} = 0$), there is no distintion between $\tilde{p}$ and p, and the second coefficient of viscosity, λ, vanishes from the governing equation [15].

It is usually taken that the integrands in Eqns. 1 and 2 are identically equal to zero at every point in the flow since the choice of the control volume must be arbitrary [5]. Then, the issue with the NSE, formulated by CMI [22], is to obtain a realistic closed-form solution to

$$\frac{\partial (\rho \mathbf{V})}{\partial t} + \nabla \cdot (\mathbf{V}(\rho \mathbf{V})) = \nabla (2\mu \nabla \cdot \mathbf{V}) + \nabla \times (\mu \omega) - \nabla p - \rho \mathbf{g} \quad (t \geq 0) \tag{5}$$

satisfying, simultaneously, the continuity equation

$$\frac{\partial \rho}{\partial t} + \nabla \cdot (\rho \mathbf{V}) = 0 \quad (t \geq 0), \tag{6}$$

subject to the appropriate boundary conditions with an initial divergence-free velocity field and an assumption of incompressibility. A solution is accepted as physically reasonable if it defines the velocity, $\mathbf{V}$, and the pressure, p, as smooth functions of the spatio-temporal dimensions and has bounded energy for $t \geq 0$ [22].

Equation 5 is rewritten as

$$\begin{aligned}
&\frac{\partial (\rho \mathbf{V})}{\partial t} + \nabla \cdot (\mathbf{V}(\rho \mathbf{V})) = \nabla (2\mu \nabla \cdot \mathbf{V}) + \nabla \times (\mu \omega) - \nabla p - \rho \mathbf{g} \\
&\rho \frac{\partial \mathbf{V}}{\partial t} + \mathbf{V} \frac{\partial \rho}{\partial t} + \mathbf{V} \nabla \cdot (\rho \mathbf{V}) + (\rho \mathbf{V}) \cdot \nabla \mathbf{V} = \nabla (2\mu \nabla \cdot \mathbf{V}) + \nabla \times (\mu \omega) - \nabla p - \rho \mathbf{g} \\
&\rho \frac{\partial \mathbf{V}}{\partial t} + \mathbf{V} \underbrace{\left[\frac{\partial \rho}{\partial t} + \nabla \cdot (\rho \mathbf{V}) \right]}_{=0} + (\rho \mathbf{V}) \cdot \nabla \mathbf{V} = \nabla (2\mu \nabla \cdot \mathbf{V}) + \nabla \times (\mu \omega) - \nabla p - \rho \mathbf{g} \\
&\rho \frac{\partial \mathbf{V}}{\partial t} + \rho \underbrace{((\mathbf{V} \cdot \nabla) \mathbf{V})}_{= \nabla \frac{V^2}{2} - \mathbf{V} \times \omega} = \nabla (2\mu \nabla \cdot \mathbf{V}) + \nabla \times (\mu \omega) - \nabla p - \rho \underbrace{\mathbf{g}}_{= \nabla g} \\
&\rho \frac{\partial \mathbf{V}}{\partial t} + \nabla \left(p + \rho \frac{V^2}{2} + \rho g - 2\mu \nabla \cdot \mathbf{V} \right) = \rho \mathbf{V} \times \omega + \nabla \times (\mu \omega)
\end{aligned} \tag{7}$$

to highlight the role of the vorticity vector, ω, in the convective acceleration term through the application of some vector identity [15]. The body force vector, $\mathbf{g}$, is also assumed to be the gradient of a scalar force potential, g.

Fefferman reports that some of the already proposed solutions to these relations in two-dimensions are unstable in the time domain and offer no clear path to solutions in three-dimensions. He makes no mention of whether an accepted solution would be that of a free flow or a wall-bounded flow, and if wall-bounded, no indications as to the acceptable boundary condition at the wall. This provides some leeway to researchers to work with the most appropriate formulations. He concludes that the problem persists when using known standard mathematical methods for solving partial differential equations and calls for new ideas [22].

In the classical theory, the velocity field can be expressed as the gradient of a scalar function, the classical velocity potential, ϕ, as

$$\mathbf{V} = \nabla\phi \, . \tag{8}$$

Equivalently, the velocity field can also be expressed as the curl of the vector of classical scalar stream functions, ψ, as

$$\mathbf{V} = \nabla \times \overrightarrow{\psi} = \begin{vmatrix} \mathbf{e}_r & \mathbf{e}_\theta & \mathbf{e}_\mathrm{z} \\ \dfrac{\partial}{\partial r} & \dfrac{1}{r}\dfrac{\partial}{\partial \theta} & \dfrac{\partial}{\partial z} \\ \psi_r & \psi_\theta & \psi_z \end{vmatrix} \, . \tag{9}$$

For an "incompressible fluid," the classical velocity potential is a smooth exact solution to the full NSE by identity [15, 29, 33, 40, 41] as

$$\nabla\left(\rho\frac{\partial\phi}{\partial t} + p + \frac{1}{2}\rho V^2 + \rho g - (2\mu\nabla\cdot(\nabla\phi))\right) = \rho(\nabla\phi)\times\omega + \nabla\times(\mu\omega) = 0 \, . \tag{10}$$

This is because it satisfies the continuity equation ($\nabla\cdot\mathbf{V} = \nabla\cdot(\nabla\phi) = 0$) and the irrotationality condition ($\omega = 0$). However, it is unrealistic due to its definitive inability to accommodate the omnipresence of vorticity in actual wall-bounded flows [15, 42].

For two-dimensional "incompressible" flows, ψ, on the one hand, satisfies the continuity equation identically. Its physical realization has been the basis for its well-documented usage in the literature in the vorticity-stream function formulation to

the solution of flow fields around objects (Eqn. 12) [15,43–46]. On the other hand, ψ cannot satisfy the NSE by identity in

$$\rho\left(\nabla\times\frac{\partial\overrightarrow{\psi}}{\partial t}\right)+\nabla\left(p+\frac{1}{2}\rho V^2+\rho g-2\mu\nabla\cdot(\nabla\times\overrightarrow{\psi})\right)=\rho(\nabla\times\overrightarrow{\psi})\times\omega+\nabla\times(\mu\omega) \tag{11}$$

due to the cross-derivatives and its rotationality condition ($\omega\neq 0$).

A number of different computational approaches to solving this problem exists based on the variables used. Either the solution is sought in terms of the primitive variables of velocity and pressure; or in terms of the stream function and vorticity; or in terms of the stream function alone [47].

In terms of the stream function, ψ, and planar vorticity, ω_z, the governing NSE for two-dimensional constant property flow is presented as

$$\begin{aligned}\omega_z &= -\left(\frac{1}{r}\frac{\partial}{\partial r}\left(r\frac{\partial\psi}{\partial r}\right)+\frac{1}{r^2}\frac{\partial^2\psi}{\partial\theta^2}\right)\\ \frac{\partial\omega_z}{\partial t}+\frac{1}{r}\frac{\partial\psi}{\partial\theta}\frac{\partial\omega_z}{\partial r}-\frac{1}{r}\frac{\partial\psi}{\partial r}\frac{\partial\omega_z}{\partial\theta} &= \nu\left(\frac{1}{r}\frac{\partial}{\partial r}\left(r\frac{\partial\omega_z}{\partial r}\right)+\frac{1}{r^2}\frac{\partial^2\omega_z}{\partial\theta^2}\right)\end{aligned}\quad , \tag{12}$$

which is known as the vorticity equation. The cylindrical polar coordinate provides a convenient coordinate system to examine the flow over the circular cylinder [15,43–46].

Researchers have obtained numerical solutions of the two-dimensional vorticity equation using available finite-differencing computational fluid dynamics (CFD) methods. Some have also expanded the stream function and vorticity as truncated Fourier series, inserted them in Eqn. 12, and sought numerical solutions as a semi-analytical method [44]. An accepted general analytical solution of the vorticity equation does not exist even though it is one dimension less complicated than the full NSE. However, an exact analytical solution of this equation exist for a viscous line vortex. The steady inviscid theory also provides an analytical solution for the trivial case in which $\omega_z = 0$. Additionally, Talaei and Garrett [31] propose a general analytical solution to this equation for an axially symmetric two-dimensional flow around a sphere assuming that the stream function is subject to a separation of variables.

The failure of steady inviscid theory in its agreement with actual experiments is generally attributed to the loss of the no-slip condition at the wall [21]. When the fluid is idealized as having no viscosity, it is generally the case that the only condition imposed on Eqn. 12 at the surface is the impermeability of the normal velocity [21]. However, Hoffman et al. in 2016 employed the slip-boundary condition at the surface in the computational solution of the approximate incompressible NSE in order to circumvent the limitation of computations at high Reynolds numbers to resolve boundary layers. They report values for the lift and drag on an aircraft comparable to those obtained in actual experiments. They suggest that the integrated properties of the flow are pressure-based, rather than viscous driven [27].

With a very high velocity gradient between the wall and the local freestream, vorticity is introduced into the flow, and convected downstream [5, 15, 36, 42]. The vorticity effect of the boundary layer has been numerously idealized in theoretical solutions by an inviscid vortex sheet [5, 42] as exemplified by thin airfoil theory [5]. This is also the approach proposed by Helmholtz, and later, Levi-Civita, in his contributions to the theoretical prediction of finite drag on a non-accelerating moving body in an inviscid fluid - the wake hypothesis [48]. Whilst being successful in the prediction of lift on the airfoil, it is less so with drag [5]. Traditionally, the non-lifting flow over bodies have been simulated with source/sink sheets, and the lifting flow with vortex or doublet sheets through panel methods. In order to overcome some problems encountered in the panel methods, some investigators have used the combination of sources, sinks and vortices in their panels [5]. In the present work, such ideas are employed idealizing the boundary layer flow as one consisting of contributions from local vortices and sources/sinks that are mutually concentric at every location on the wall.

Hoffmann et al. weigh in on Fefferman's analyses as they conclude against the existence of a "well-posed smooth solution to the [NSE] with smooth data." [27, 36]

Buckmaster and Vicol [28] are in agreement with this conclusion. They buttress this point of view with their findings and proofs that weak solutions to the NSE are non-unique [28].

However, while resting on the use of approximate solutions constructed on an effective difference scheme, Chen and Kratka "establish the existence of global solutions to the initial boundary value problem for the [multidimensional] NSE for compressible heat-conducting flow with large spherically symmetric initial data between the solid core and the free boundary connected to the surrounding vacuum state."[49] They also show that, in this flow problem, no cavities develop between the solid core and the free boundary which expands with some finite speed [49].

Muriel [24,25] used the calculation of the time evolution of a one-particle distribution function initialized with spatially uniform data along with a choice of a Gaussian pair potential between particles to arrive at a divergence-free velocity field, but he encountered problems in the integration of the NSE to obtain a scalar pressure field. He concludes with a suggestion that the pressure field is a higher-order tensor field.

Realizing this difficulty in deriving a viscous potential for the velocity with self-consistency with the pressure field, Scholle et al. [26] reformulate the two-dimensional NSE in terms of complex variables to obtain a first integral in the form of a new real-valued scalar potential and a complex-valued velocity field from which the pressure can be obtained. Furthermore, they obtain a real-valued tensorial representation of the complex-valued first integral of the reformulated NSE. A scalar pressure field can then be computed after solving a set of second-order partial differential equations, in a semi-analytic manner, subject to the flow-specific boundary condition(s) [26]. In their most recent advancement of the work in 2018 [29], they offer an extension of the two-dimensional derivation to the general case of an unsteady three-dimensional viscous flow using tensor calculus. Their approach results in a tensor-valued field equation and a vector-valued field equation that are constrained by a vector potential introduced

for the velocity and involves five unknown fields. These were solved analytically (for a translating disc in a viscous fluid and a non-axisymmetric stagnation flow) and numerically (for a viscous flow in a cubic domain) in a successful verification of their methodology. To achieve these results, some of the equations involving the unknown potentials were eliminated using the guage invariance or symmetry of the NSE [29].

However, a viscous-potential function, $\tilde{\kappa}$, that satisfies the physical relationship between the scalar pressure field and the velocity field as

$$\nabla\left(\rho\frac{\partial\tilde{\kappa}}{\partial t}+p+\frac{1}{2}\rho V^2+\rho g-2\mu\nabla^2\tilde{\kappa}\right)=0 \tag{13}$$

has been proposed to obtain realistic closed-form solutions of the NSE [31, 40, 41, 50]. This fact is well-known, and it has been researched by many [26, 29, 31, 50, 51]. Although, widely considered an oxymoron, the idea of a viscous potential flow or function is not new [41]. Joseph advocates this in his historical review of the potential flow of viscous fluids. The idea can be traced back to both George Stokes [41] and Horace Lamb [41], and later to Joseph and Wang [41]. In addition, a potential-based Lagrangian solution to the NSE has been obtained for some compressible flows for which the dynamic viscosity is neglected in favor of the bulk viscosity [29]. However, generalizing these formulations to obtain the full solutions of unsteady viscous three-dimensional compressible flows cannot always be guaranteed to be analytically tractable [29].

Stokes' earlier attempt at the theoretical study of the cylinder flow had resulted in the paradox named after him which was resolved by Oseen [15]. Neglecting the inertia terms in the NSE, Stokes sought and derived a stream function that solved the steady motion of a sphere in a flow, but not that of a cylinder. Oseen partially incorporated the inertia terms in a proposed set of linearized equations. Lamb solved these linearized equations and found his solutions valid only for small Reynolds numbers [40]. The scope of the asymptotic theoretical analyses on the NSE, building on the works of Oseen and Lamb, have been generally limited to the low-Reynolds-number

flows [9, 31, 52]. However, Talaei's and Garrett's [31] proposed analytical solution to the two-dimensional vorticity equation for a moving sphere in a quiescent and viscous fluid extends these analyses to high Reynolds numbers.

White [15] writes that an assumption of an ideal zero viscosity fluid is not always necessary to define a potential flow, but when the vorticity vector is identically zero regardless of the viscosity, the velocity vector must be the gradient of a potential function. This is the case everywhere in the high Reynolds number flow past a solid body except in the boundary layer [15]. Therefore, he concludes that the classical potential theory describes exact solutions of the full NSE [15, p. 85]. Schlichting [33, pp. 72-73] and Anderson [5, p. 209] agree with White's analyses. Anderson also employs the continuity equation for an incompressible potential flow to establish the applicability of the Laplace equation to such a flow [5, p. 236]. The summation of particular solutions of the Laplace equation is also one of its solutions because the Laplace equation is linear [5]. Thus, complex flows of practical importance are derived from the analytical superposition of individual elementary flows that are solutions of the Laplace equation with appropriate boundary conditions [5, pp. 238-239]. Lamb [40] also discusses the Clebsch transformation that extends the definition of a velocity potential to inviscid flows with non-zero vorticity. In that formulation, the vorticity is identified as an invariant for a barotropic flow [26, 29, 51].

Closed-form analytical solutions have the advantages that their development illuminates the physics behind a problem; they give information on the relationships between the pertinent variables; and they are very useful for rapid and less expensive preliminary design purposes [5]. In the absence of comprehensive theoretical solutions, the need to obtain accurate qualitative and quantitative characterizations of the dynamics of fluid flows precipitated the development of reduced order models of high fidelity numerical solutions and/or experiments [53]. Some of the methodologies in use to obtain these models include the Proper Orthogonal Decomposition (POD) and

the Dynamic Mode Decomposition (DMD). The POD is introduced to fluid dynamics with the idea that spatial velocity correlations can be orthogonally decomposed for the identification of the dominant eigen modes that characterize the coherent structures in the flow [54, 55]. Developing a dynamic model from these spatial modes, i.e., computing the temporal coefficients, requires projecting these modes onto the NSE. Alternatively, these coefficients are obtained directly from the input data set by computing the ratio of a single snapshot matrix with the generated modes. In a two-pronged approach, the DMD decomposes the flow field into its spatial modes and the corresponding eigenvalues which signifies the dynamic evolution of these modes with time without the need to project the spatial modes onto the governing equation of the system [56]. Attempts are usually made to train the reduced order models derived from these data analysis methodologies using the NSE. These are geared towards making them useful for other geometries and Reynolds numbers than the ones from which they were obtained. However, their success is not always guaranteed [37, 57]. This process is also reminiscent of the search for an analytical solution(s) to the complete NSE. Raissi et al. present the hidden fluid mechanics algorithm which they claim can encode the NSE from an input data set and provide a trained model that is agnostic to geometry, initial and boundary conditions [58]. However, the success of this and other input-data-dependent methods depend highly on the fidelity of the input data that in some cases are very expensive to collect.

Therefore, the need to obtain a viscous scalar potential function which captures known and observable features of experimentally observed wall bounded flows including flow separation, wake formation, vortex shedding, compressibility effects as well as Reynolds-number-dependence still exists. Such a function must be defined appropriately to combine the properties of a three-dimensional potential function to satisfy the inertia terms of the NSE and the features of a stream function to satisfy the continuity equation, the viscous vorticity equation and the viscous terms of the

NSE.

1.3 Aim and Objectives

Following the findings in the review of the literature, the aim of the research is to develop a refined potential theory (RPT) within which the entire flow field around a canonical bluff body (cylinder) can be investigated to bridge the gap between the classical potential theory (CPT) and experimentally observed flows in order to enhance the ability to predict and/or control the aerodynamic quantities of the flow as well as the evolution of the wake for design purposes in the sub-critical and critical Reynolds number regime.

The following are the objectives of the research.

1. To develop a theoretical solution of the viscous flow over the infinite cylinder that does not rely on experimental or computational data inputs and explore its extrapolation to incorporate three-dimensional effects of a finite cylinder.
2. To explore and develop approaches to map the theoretical finite cylinder flow field onto geometries inclusive of spheres and spheroids.
3. To carry out a quantitative verification and validation process of the proposed theoretical solution against the available analytic, numerical and experimental data for incompressible flow over the cylinder across the sub-critical and critical Reynolds number ranges.
4. To demonstrate the extension of the proposed theoretical solution against available incompressible, analytic, numerical and experimental data for spheres and spheroids.

CHAPTER II

PRESENT INVESTIGATION AND THEORETICAL FORMULATION

Figure 2 presents an overview of the three fundamental approaches to exploring the governing equations of fluid dynamics. In conjunction with Table 1, this figure also highlights the existing gap between CPT and experimentally observed flows. The items in the lower block of Table 1 are the specific features of CPT that RPT addresses. The double arrows in Fig. 2 indicate that in the current practice of fluid dynamics, there are mutual interactions between the three approaches [5]. Although the objective one of the present thesis is to develop a standalone theoretical solution for the cylinder flow, observations of experimental flow physics and numerical solutions are employed in its development.

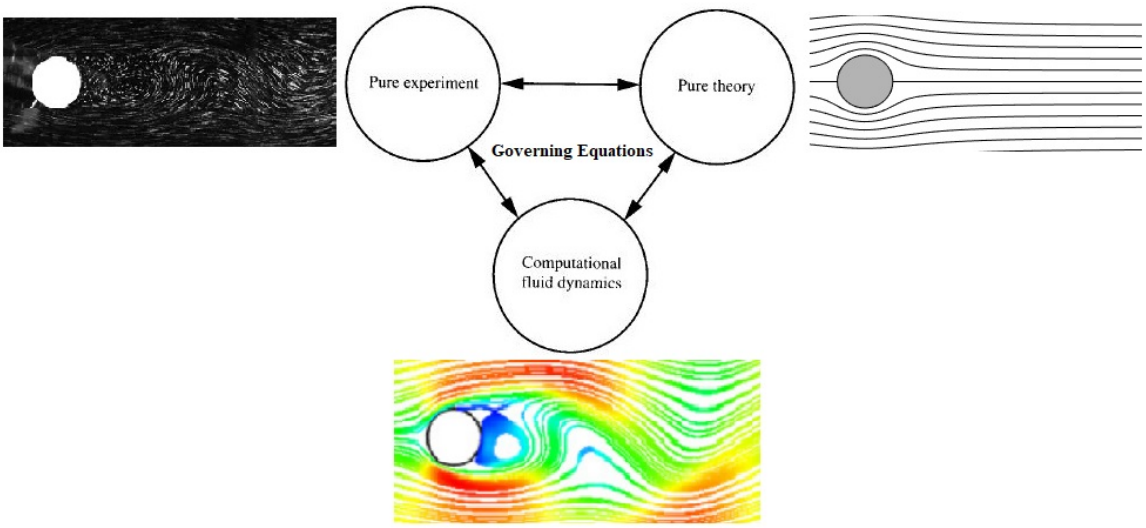

Figure 2: A cylinder flow at $Re_\infty = 100$ illustrating the three main approaches to fluid dynamics (adapted from Refs. [4–6]).

Table 1: An overview of the existing gap between CPT and experimentally observed flows.

	CPT	Experimentally observed flows	RPT
Satisfies Continuity Eqn., $\nabla \cdot \mathbf{V} = 0$	✓	✓	?
Bounded at infinity	✓	✓	?
Smooth and Continuous	✓	✓	?
Satisfies NSE	✓	✓	?
$d\mathbf{s} \times \mathbf{V} = 0$	✓	✓	?
Three-dimensions	mostly ×	✓	?
No-slip condition	×	×, ✓	?
Vorticity, $\omega \neq 0$	×	✓	?
Boundary layer	×	✓	?
Re_∞ dependence	×	✓	?
Wake	×	✓	?
Vortex shedding	×	✓	?
Unsteadiness, Turbulence	×	✓	?
Compressible	✓	✓	?
Drag	×	✓	?

The items in the upper block of Table 1 for which there is a match between CPT and experimentally observed flows are leveraged in the development of RPT. Therefore, the goals of the present methodology are to construct a viscous and time-dependent stream function, $\psi_{viscous}$ from the classical theory. This stream function conserves mass and energy. It is obtained as

$$\psi_{viscous} = \psi_{inviscid} + \psi_{vortex} + \psi_{sink/source} + \psi_{perifocal} + \psi_{vortexshedding} \tag{14}$$

using superposition. Usually, the superposition principle does not pertain to non-linear systems like a cylinder flow. However, the use of a superposed stream function offers an avenue to resolve the mathematical non-linearity through experimental observations of the flow physics. This is because the stream function has both mathematical description and physical representation as the mass flow rate between streamlines. A streamline is a line drawn in a flow such that the local velocity is always tangential to it [59]. The streamlines of an experimentally observed flow are identifiable with flow visualization techniques [5, 7, 9, 15, 46, 59, 60]. Some other researchers including

Talaei and Garrett [31] have also used summations of stream functions in their viscous flow analyses. Additionally, the stream function satisfies the linear Laplace equation when the non-linear vorticity is identically zero. Thus, after its construction, $\psi_{viscous}$ is integrated to obtain the viscous scalar potential function, $\tilde{\kappa}$ that is discussed in chapter one. This is to satisfy the NSE and obtain the pressure field. $\tilde{\kappa}$ is referred to as the *Kwasu* function in Ref. 50 (current author's own publication). Finally, $\tilde{\kappa}$ is extended to three-dimensions and arbitrary geometries.

2.1 The Eulerian Kwasu Function: A Viscous Velocity Potential

2.1.1 Conservation of Mass

For an "incompressible" flow in which the density, ρ is assumed to be constant, the continuity equation

$$\frac{\partial \rho}{\partial t} + \nabla \cdot (\rho \mathbf{V}) = 0 \quad (t \geq 0) \tag{15}$$

reduces to

$$\nabla \cdot \mathbf{V} = 0 \quad (t \geq 0).$$

This means the velocity field is perpetually divergence-free. The flow is governed by the Laplace equation because the classical velocity potential, ϕ, can be defined such that

$$\nabla \cdot \mathbf{V} = \nabla \cdot (\nabla \phi) = \nabla^2 \phi = 0 \quad (t \geq 0).$$

The classical stream function, ψ also identically satisfies the divergence-free condition since

$$\mathbf{V} = \frac{1}{r}\frac{\partial \psi}{\partial \theta} \mathrm{e_r} - \frac{\partial \psi}{\partial r} \mathrm{e}_\theta + 0 \mathrm{e_z}$$

and

$$\begin{aligned}\nabla \cdot \mathbf{V} &= \frac{1}{r}\frac{\partial(rV_r)}{\partial r} + \frac{1}{r}\frac{\partial V_\theta}{\partial \theta} \\ &= \frac{V_r}{r} + \frac{\partial V_r}{\partial r} + \frac{1}{r}\frac{\partial V_\theta}{\partial \theta} \\ &= \frac{1}{r^2}\frac{\partial \psi}{\partial \theta} - \frac{1}{r^2}\frac{\partial \psi}{\partial \theta} + \frac{1}{r}\frac{\partial^2 \psi}{\partial r \partial \theta} - \frac{1}{r}\frac{\partial^2 \psi}{\partial \theta \partial r} \\ &= 0 \quad (t \geq 0).\end{aligned} \tag{16}$$

However, it only satisfies the Laplace equation when the flow is considered irrotational. An irrotational flow is one in which the vorticity vector, ω is a null vector [5, 20]. For a two-dimensional flow, the condition for irrotation is

$$\omega_z = \frac{1}{r}\left(\frac{\partial(rV_\theta)}{\partial r} - \frac{\partial(V_r)}{\partial \theta}\right) = 0\,. \tag{17}$$

For ψ, this means

$$\begin{aligned}\omega_z &= \frac{1}{r}\left(\frac{\partial(rV_\theta)}{\partial r} - \frac{\partial(V_r)}{\partial \theta}\right) \\ &= -\frac{1}{r}\left(\frac{\partial \psi}{\partial r} + r\frac{\partial^2 \psi}{\partial^2 r} + \frac{1}{r}\frac{\partial^2 \psi}{\partial^2 \theta}\right) \\ &= -\left(\frac{1}{r}\frac{\partial \psi}{\partial r} + \frac{\partial^2 \psi}{\partial^2 r} + \frac{1}{r^2}\frac{\partial^2 \psi}{\partial^2 \theta}\right) \\ &= 0\,.\end{aligned} \tag{18}$$

That is the Laplacian of the stream function

$$\nabla^2 \psi = 0\,,$$

and it satisfies the Laplace equation. ϕ identically satisfies the irrotational condition [5, 20] since

$$\begin{aligned}\omega_z &= \frac{1}{r}\left(\frac{\partial(rV_\theta)}{\partial r} - \frac{\partial(V_r)}{\partial \theta}\right) \\ &= \frac{1}{r^2}\frac{\partial \phi}{\partial \theta} - \frac{1}{r^2}\frac{\partial \phi}{\partial \theta} + \frac{1}{r}\left(\frac{\partial^2 \phi}{\partial r \partial \theta} - \frac{\partial^2 \phi}{\partial \theta \partial r}\right) \\ &= 0\,.\end{aligned} \tag{19}$$

Experimentally observed flows are rotational although some of their regions can be assumed irrotational [5, 15, 20, 61]. It can be seen from Eqns. 16-19 that when the flow is rotational, ϕ is not defined. However, ψ is defined. It is observable with

flow visualization techniques that reveal streamlines [60]. Streamlines are level sets of ψ. ψ identically satisfies the continuity equation. For an experimentally observed rotational flow, it satisfies the Poisson's equation ($\nabla^2\psi = -\omega_z$) but not the Laplace equation [20]. Both of these differential equations are linear and obey the superposition principle [62]. Therefore, the use of a superposed streamfunction to study experimentally observed flows is justified.

Separated-variables solutions to the Laplace equation abound in mathematics literature [62]. In a cylindrical polar coordinate system, the general solution is obtained as an infinite Fourier series for ψ and ϕ as

$$\psi(r,\theta) = A_0 + B_0 \ln r + \sum_{m>0} \left(A_m r^m + B_m r^{-m}\right) \sin\left[m\left(\theta - \theta_m\right)\right] \tag{20}$$

$$\phi(r,\theta) = A_0 - B_0\theta + \sum_{m>0} \left(A_m r^m - B_m r^{-m}\right) \cos\left[m\left(\theta - \theta_m\right)\right], \tag{21}$$

where m is a positive integer and θ_m is an arbitrary constant angle. ψ and ϕ are harmonic functions because they satisfy the Laplace equation [62]. Depending on the values for m and the arbitrary constants (A_0, A_m, B_0 and B_m) in these equations, these solutions correspond to the inviscid irrotational incompressible lifting flow of a uniform freestream over a number of two-dimensional geometries ranging from the circular cylinder ($m = 1$) [5] to semi-infinite wedges ($m > 1$) [63]. These general solutions are identifiable as superposition of elementary flows [5, 63]. This has remained the state of the art in the closed-form mathematical solution of the steady incompressible flow field around infinitely spanned geometries - potential flow theory [20]. Any arbitrary definition of the constants in these solutions do not preclude the functional relationship they describe between the dependent and independent variables that makes them viable solutions of the fluid dynamics equations (refer to Eqns. 10-11). Schlichting writes that "frictionless flows [potential flows] may also be regarded as exact solutions of the Navier-Stokes equations, because in such cases the frictional terms vanish identically." [33, p. 72] However, the gap between the prediction of zero

drag therefrom for a steady flow and results from experimentally observed flows is dubbed the d'Alembert's Paradox [5, 20].

Other elementary flows such as sinks, sources and vortices are also present in complex flows like the experimentally observed cylinder flow. These flows are illustrated in Fig.3. The potential solution for a vortex can be obtained as

$$\psi = \frac{\Gamma}{2\pi} \ln r \tag{22}$$

$$V_\theta = -\frac{\Gamma}{2\pi r} \, . \tag{23}$$

where Γ is the circulation or strength of the vortex [5]. However, experimentally observed flows are viscous [15]. For a line viscous vortex, the incompressible NSE reduce to the heat equation for which various analytic solutions exist in the literature [46, 62]. Amongst such solutions is the Lamb-Oseen vortex model [46, p. 262]. The circulation for this model is given as

$$\Gamma = \int_0^r 2\pi r \omega_z dr = -\Gamma_0 \left[\mathrm{e}^{\left(-\frac{r^2}{r_c^2}\right)} \right]_0^r \, , \tag{24}$$

where $r_c^2 = 4\nu t$, ω_z is the planar vorticity, Γ_0 is the initial circulation, ν is the kinematic viscosity of the fluid and r_c is the vortex core radius. This is a time-dependent model of the viscous decay of the vortex [15, p. 207]. When the time component in the equation is fixed, this vortex solution becomes the Burgers' vortex model [46]. Burgers' vortices have been used to model eddies in turbulent flows successfully [46, p. 265]. Therefore, a viscous stream function can be defined for a vortex as

$$\begin{aligned} \psi &= \frac{\Gamma}{2\pi} \ln r \\ &= \frac{\Gamma_0 \left(1 - \mathrm{e}^{\left(-\frac{r^2}{r_c^2}\right)} \right)}{2\pi} \ln r \end{aligned} \tag{25}$$

using Eqn.24.

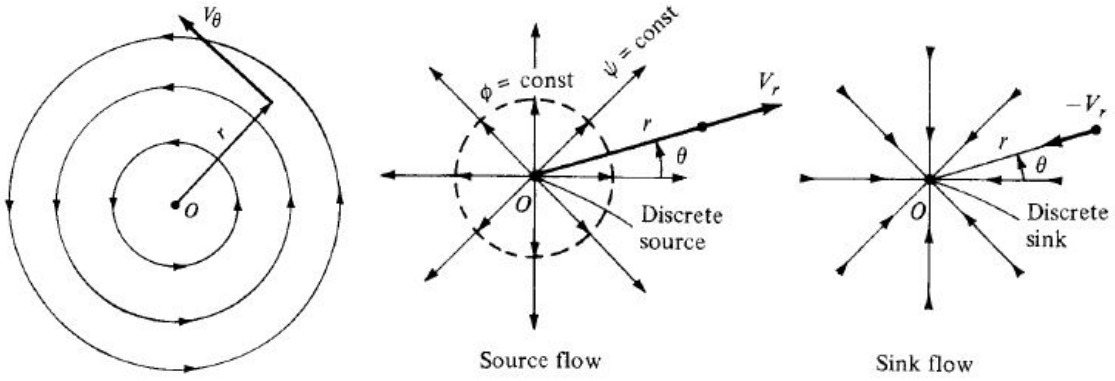

(a) Vortex (b) Source/Sink

Figure 3: The streamlines of a Vortex and Source/Sink [5].

Similarly, the stream function for a potential sink/source and the radial velocity can be expressed as

$$\psi = \frac{\Lambda}{2\pi}\theta \tag{26}$$

$$V_r = \frac{\Lambda}{2\pi r} \tag{27}$$

where Λ is the strength of the sink/source [5].

To highlight the contributions from the elementary uniform, doublet and vortex flows, Eqn. 20 is rewritten as

$$\begin{aligned}
&\psi(r,\theta) = A_0 + B_0 \ln r + \textstyle\sum_{m>0} \left(A_m r^m + B_m r^{-m}\right) \sin\left[m\left(\theta - \theta_m\right)\right] \\
&= -B_0 \ln R + B_0 \ln r + \textstyle\sum_{m>0} A_m r^m \left(1 + \dfrac{B_m}{A_m r^m r^m}\right) \sin\left[m\left(\theta - \theta_m\right)\right] \\
&= B_0 \ln\left(\frac{r}{R}\right) + \textstyle\sum_{m>0} A_m r^m \sin\left[m\left(\theta - \theta_m\right)\right] \left(1 - \left(\frac{R^2}{r^2}\right)^m\right) ,
\end{aligned} \tag{28}$$

in which $A_0 = -B_0 \ln R$ and $R^{2m} = -B_m/A_m$. It can be seen that B_0 is associated with the strength of the vortex flow. If it is a constant value and $m = 1$, Eqn. 28 corresponds to an inviscid flow over a rotating cylinder that produces lift depicted in Fig. 4 [5, pp. 266-280]. Because ψ is a harmonic function, Eqn. 28 is smooth and continuous except as $r \to 0^+$ where it blows up. This is not problematic because it

is smooth and continuous in the domain $r > R$ that corresponds to the external flow on the cylinder.

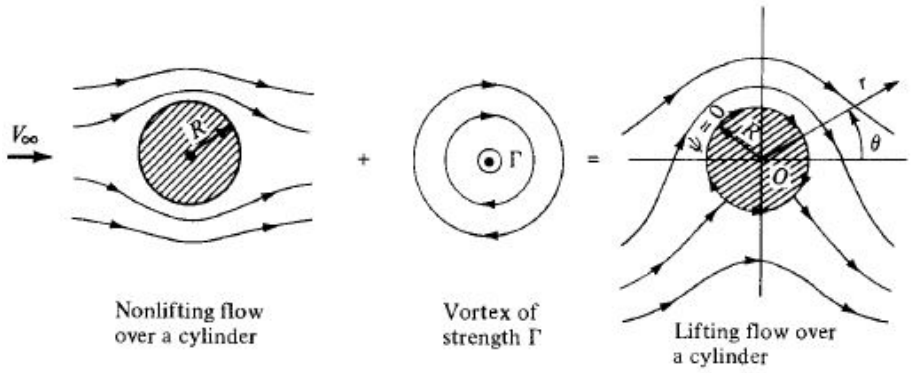

Figure 4: A lifting flow over a circular cylinder [5].

To obtain the components of velocity, the stream function is differentiated in the relevant directions to give

$$V_r = \frac{1}{r}\frac{\partial B_0}{\partial \theta}\ln\left(\frac{r}{R}\right) + \sum_{m>0} mA_m r^{m-1}\cos\left[m\left(\theta-\theta_m\right)\right]\left(1-\left(\frac{R^2}{r^2}\right)^m\right) ,$$

$$V_\theta = -\frac{B_0}{r} - \frac{\partial B_0}{\partial r}\ln\left(\frac{r}{R}\right) - \sum_{m>0} mA_m r^{m-1}\sin\left[m\left(\theta-\theta_m\right)\right]\left(1+\left(\frac{R^2}{r^2}\right)^m\right)$$

and

$$V = \left\{\left(\frac{1}{r}\frac{\partial B_0}{\partial \theta}\ln\left(\frac{r}{R}\right) + \sum_{m>0} mA_m r^{m-1}\cos\left[m\left(\theta-\theta_m\right)\right]\left(1-\left(\frac{R^2}{r^2}\right)^m\right)\right)^2 + \right.$$
$$\left.\left(-\frac{B_0}{r} - \frac{\partial B_0}{\partial r}\ln\left(\frac{r}{R}\right) - \sum_{m>0} mA_m r^{m-1}\sin\left[m\left(\theta-\theta_m\right)\right]\left(1+\left(\frac{R^2}{r^2}\right)^m\right)\right)^2\right\}^{1/2} . \tag{29}$$

For the non-lifting flow (NLF) over a circular cylinder in which the uniform flow is parallel to the body x-axis as illustrated in Fig. 5, $B_0 = \theta_m = 0, m = 1, A_1 = V_\infty$, $B_1 = k/2\pi$ and $R^2 \equiv k/2\pi V_\infty$ in Eqn. 28 and the corresponding expressions for its velocity field [5]. That is, the stream function is

$$\psi_{NLF} = V_\infty r\sin\theta\left(1-\frac{R^2}{r^2}\right) , \tag{30}$$

the velocity components are

$$\begin{aligned} V_{r_{NLF}} &= V_\infty \cos\theta \left(1 - \frac{R^2}{r^2}\right) \\ V_{\theta_{NLF}} &= -V_\infty \sin\theta \left(1 + \frac{R^2}{r^2}\right) \end{aligned} \quad , \tag{31}$$

and the speed is

$$\begin{aligned} V_{NLF} &= V_\infty \sqrt{\left(\cos\theta \left(1 - \frac{R^2}{r^2}\right)\right)^2 + \left(-\sin\theta \left(1 + \frac{R^2}{r^2}\right)\right)^2} \\ &= V_\infty \sqrt{\left(1 - \frac{R^2}{r^2}\right)^2 + 4\,\frac{R^2 \sin^2\theta}{r^2}} \,. \end{aligned} \tag{32}$$

In Fig. 5, κ stands for the doublet strength [5]. This is different from the predominant use of κ for the *Kwasu* function in this thesis.

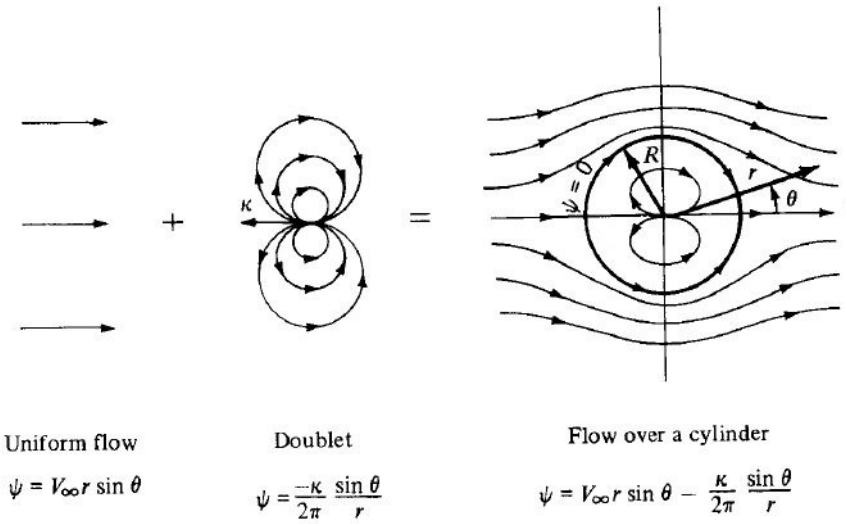

Figure 5: The superposition of a uniform flow and a doublet into the NLF over a circular cylinder [5].

The freestream is assumed to be steady, uniform and unperturbed by the cylinder. That is, at $r = \infty$,

$$\begin{aligned} \psi_{NLF} &= V_\infty r \sin\theta \\ V_{NLF} &= V_\infty \end{aligned} \,. \tag{33}$$

This is consistent with experimentally observed flows [5]. At the cylinder surface where $r = R$, Eqns. 30 and 31 yield

$$\begin{aligned} \psi_{NLF} &= 0 \\ V_{r_{NLF}} &= 0 \\ V_{\theta_{NLF}} &= -2V_\infty \sin\theta \end{aligned} \quad . \tag{34}$$

$\psi_{NLF} = 0$ identifies the cylinder surface as a streamline of the flow. $V_{r_{NLF}} = 0$ predicts that there is no flow through the surface since it is impermeable [5,20]. Both of these are in agreement with an experimentally observed flow [5]. However, the prediction of a slip tangential velocity, $V_{\theta_{NLF}} \neq 0$, on this non-rotating wall violates the no-slip condition that has been observed in experiments [5,60].

The no-slip condition gives rise to the boundary layer. A boundary layer is that region of an experimentally observed flow adjacent to the surface where viscous effects including rotation are dominant [5,15,61]. ψ_{NLF} is inviscid or non-viscous and features no boundary layer [5]. Due to wall friction, an experimentally observed local freestream velocity is retarded to the surface velocity. This results in a vertical velocity profile illustrated in Fig. 6 and a crossflow velocity gradient [5,15,61]. Boundary layers are usually small in comparison to the body, and the crossflow velocity gradient occurs over a relatively short distance [10,33,40]. There is also a streamwise gradient of velocity.

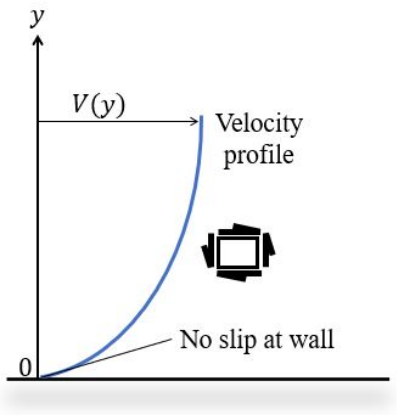

Figure 6: The no-slip condition and the boundary layer.

A fluid element idealized by the square in Fig. 6 begins to rotate under these gradients as it translates downstream. Thus, vorticity is introduced into an experimentally observed flow field. Although vorticity does not preclude the use of a superposed stream function, it is the main source of non-linearity in the momentum equation [15].

Experimentally observed flows conserve mass and momentum simultaneously. Therefore, the viscous stream function of the cylinder flow should satisfy the NSE.

2.1.2 Conservation of Momentum

The integral compressible NSE are expressed in an equivalent differential form in

$$\rho\frac{\partial\left(\mathbf{V}\right)}{\partial t}+\rho\nabla\left(\frac{V^2}{2}+g\right)+\nabla\left(p-2\mu\nabla\cdot\mathbf{V}\right)=\rho\mathbf{V}\times\omega+\nabla\times\left(\mu\omega\right)\quad(t\geq 0).$$

A solution to the incompressible NSE for the pressure field is sought in terms of a known stream function/velocity components in

$$\rho\left(\nabla\times\frac{\partial\overrightarrow{\psi}}{\partial t}\right)+\rho\nabla\left(\frac{V^2}{2}+g\right)+\nabla\left(p-2\mu\nabla\cdot(\nabla\times\overrightarrow{\psi})\right)$$
$$=\rho(\nabla\times\overrightarrow{\psi})\times\omega+\nabla\times\left(\mu\omega\right)$$

However, a number of issues immediately arise. One is that the stream function $\psi_{viscous}$ is two-dimensional whereas experimentally observed cylinder flows are three-dimensional [9, p. 246]. Stream functions are usually difficult to define for general three-dimensional space [5, 46]. Additionally, integrating the pressure out of this equation by vector identity manipulations is impossible due to the terms involving the vorticity and the local temporal derivative [26,29]. Although, $\psi_{viscous}$ may be continuously differentiable in space and time, present mathematical methods with the use of a symbolic mathematical software like $Maple^{TM}$ may not offer anti-derivatives for such an involved equation. Numerical integration would not be consistent with solving the problem analytically. However, when that is done, different results may be obtained from integrating in either of the two spatial directions. Muriel [24] encountered this problem, and he suggests that the pressure is a higher-order tensor which converges to a scalar value in a long-time limit. However, the current literature on pressure appears to suggest otherwise [5, 15]. Sheng proposes a review of the fundamental physical bases of the NSE with which he envisions easier solutions of NSE [30]. However, his proposition paves no path towards resolving the vorticity vector [30]. A possible option is to carry out the foregoing theoretical development in terms of the classical velocity potential which is well defined for three-dimensional flows and would satisfy the unsteady Bernoulli equation (Eqn. 10). It cannot be overemphasized, however, that the classical velocity potential is mathematically undefined in its present form for a rotational flow.

For viscous fluid flows, the condition of irrotationality must be dropped [42]. This essentially negates the physical existence of the classical velocity potential. However, the presence of pressure as a scalar quantity in the NSE suggests a potential function for a rotational velocity field exists [29, 40]. That function is a stream function and a velocity potential simultaneously. This is the central idea to the *Kwasu* function [50].

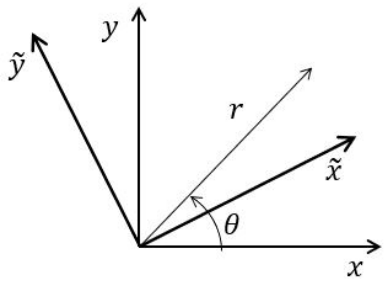

Figure 7: The relationship between cylindrical polar and Cartesian coordinate systems.

Obtaining the incompressible *Kwasu* function, $\tilde{\kappa}$ from

$$\begin{aligned} \tilde{\kappa} &= \int V_r \partial r + f(\theta) = \int \frac{1}{r} \frac{\partial \psi_{viscous}}{\partial \theta} \partial r + f(\theta) \\ \tilde{\kappa} &= \int V_\theta r \partial \theta + f(r) = -\int \frac{\partial \psi_{viscous}}{\partial r} r \partial \theta + f(r) \end{aligned} \tag{35}$$

may require a direct integration process that is not supported by available modern mathematical methods. However, this can be accomplished by resolving $\psi_{viscous}$ in the Cartesian coordinate system as follow. The cylindrical polar coordinate variables are related to the Cartesian x-y axis as

$$r = \sqrt{x^2 + y^2} \qquad \theta = \arctan(y, x) \, .$$

This is illustrated in Fig. 7. There are at least 360 other $\tilde{x}$-$\tilde{y}$ axes that can be defined in relation to the same cylindrical polar coordinates in Fig. 7. These correspond to successive units of θ. So, the angle in $\psi_{viscous}$ is redefined as

$$\theta = \arctan(y, x) \Rightarrow \arctan(x, y) \tag{36}$$

in which the negative wind $\tilde{x}$-axis is coincident with the positive body y-axis. Thus, the function $\tilde{\kappa}$ that satisfies the continuity equation and the incompressible NSE is summarized in Table 2.

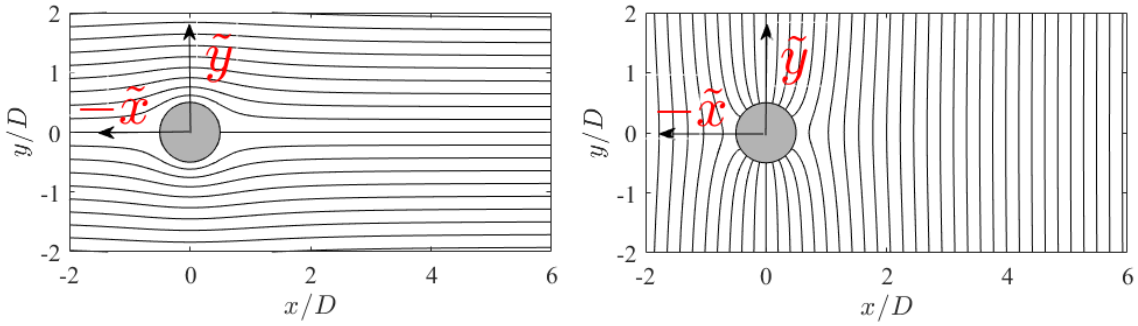

(a) $\psi = r\sin\theta\left(1 - \dfrac{R^2}{r^2}\right)$ (b) $\phi = r\cos\theta\left(1 + \dfrac{R^2}{r^2}\right)$

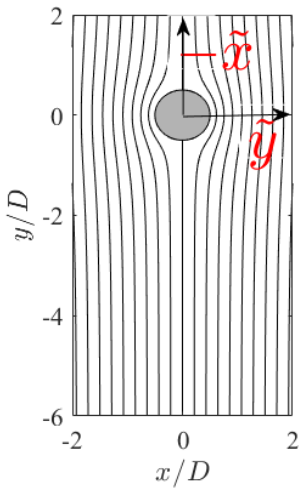

(c) $\tilde{\kappa} = r\sin\left(\arctan\left(r\cos\theta, r\sin\theta\right)\right)\left(1 - \dfrac{R^2}{r^2}\right)$

Figure 8: A visual comparison of the stream function, ψ, *Kwasu* function, $\tilde{\kappa}$ and the classical velocity potential, ϕ.

Table 2 also compares $\tilde{\kappa}$ with the classical stream function and the classical velocity potential. This is illustrated in Figs. 8 - 11 that present plots of the level sets of the three functions and their velocity fields for the inviscid non-lifting flow. The freestream flow parallel to the negative wind $\tilde{x}$-axis that is coincident with the negative body x-axis in Figs. 8a and 8b now approaches from the positive body y-axis in Fig. 8c. The streamlines and the potential lines in Figs. 8a and 8b respectively are

Table 2: Properties of the *Kwasu* function in comparison to the classical velocity potential and the stream function.

	ϕ	$\tilde{\kappa}$	ψ
V_r	$\frac{\partial \phi}{\partial r}$	$\frac{1}{r}\frac{\partial \tilde{\kappa}}{\partial \theta}$	$\frac{1}{r}\frac{\partial \psi}{\partial \theta}$
V_θ	$\frac{1}{r}\frac{\partial \phi}{\partial \theta}$	$-\frac{\partial \tilde{\kappa}}{\partial r}$	$-\frac{\partial \psi}{\partial r}$
V_z	$\frac{\partial \phi}{\partial z}$	$\frac{\partial \tilde{\kappa}}{\partial \tilde{z}}$	$-$
V_x	$\frac{\partial \phi}{\partial x}$	$\frac{\partial \tilde{\kappa}}{\partial \tilde{x}}$	$\frac{\partial \psi}{\partial y}$
V_y	$\frac{\partial \phi}{\partial y}$	$\frac{\partial \tilde{\kappa}}{\partial \tilde{y}}$	$-\frac{\partial \psi}{\partial x}$
V_r	$V_x \cos\theta + V_y \sin\theta$	$-V_x \sin\theta + V_y \cos\theta$	$V_x \cos\theta + V_y \sin\theta$
V_θ	$-V_x \sin\theta + V_y \cos\theta$	$-\left(V_x \cos\theta + V_y \sin\theta\right)$	$-V_x \sin\theta + V_y \cos\theta$
V_z	$-(V_x \sin\theta - V_y \cos\theta)\cos\varphi$	$-\left(V_x \cos\theta + V_y \sin\theta\right)\cos\varphi$	$-$

orthogonal. However, they describe the same velocity field [5]. Whereas the stream function is differentiated in a perpendicular direction to a flow to obtain the velocity components in Fig. 9, the classical velocity potential is differentiated in the flow direction to obtain the same velocity components in Fig. 10. This is the reason the classical velocity potential solution results in an irrotational flow, and the stream function solution does not [5].

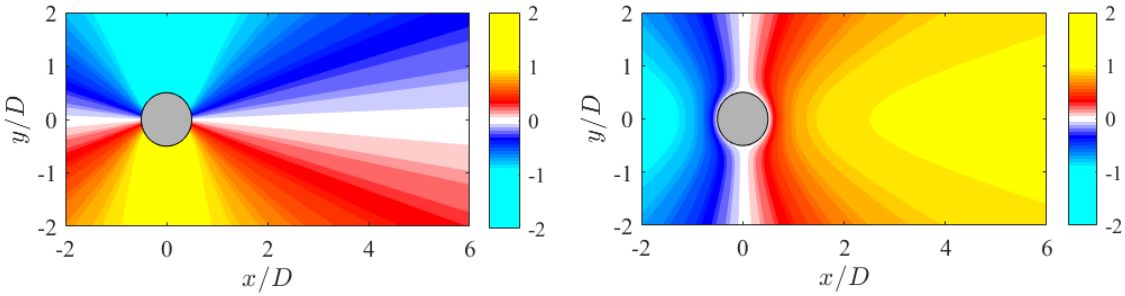

(a) $V_\theta = -\dfrac{\partial \psi}{\partial r}$

(b) $V_r = \dfrac{1}{r}\dfrac{\partial \psi}{\partial \theta}$

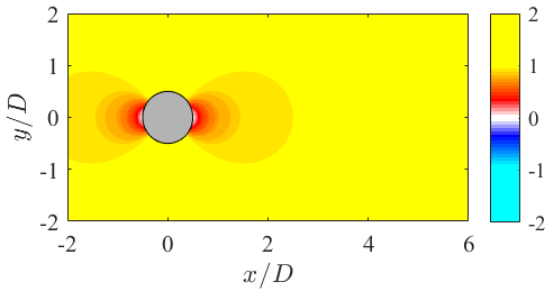

(c) $V_x = \dfrac{\partial \psi}{\partial y}$

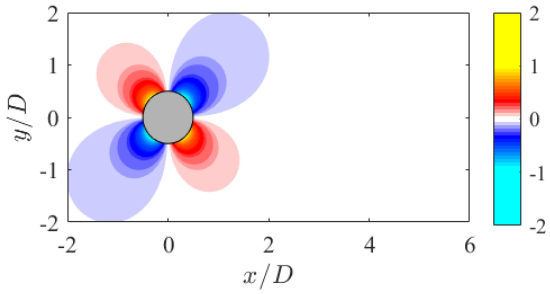

(d) $V_y = -\dfrac{\partial \psi}{\partial x}$

Figure 9: An illustration of the non-dimensional planar velocity field of the stream function in the inviscid non-lifting cylinder flow.

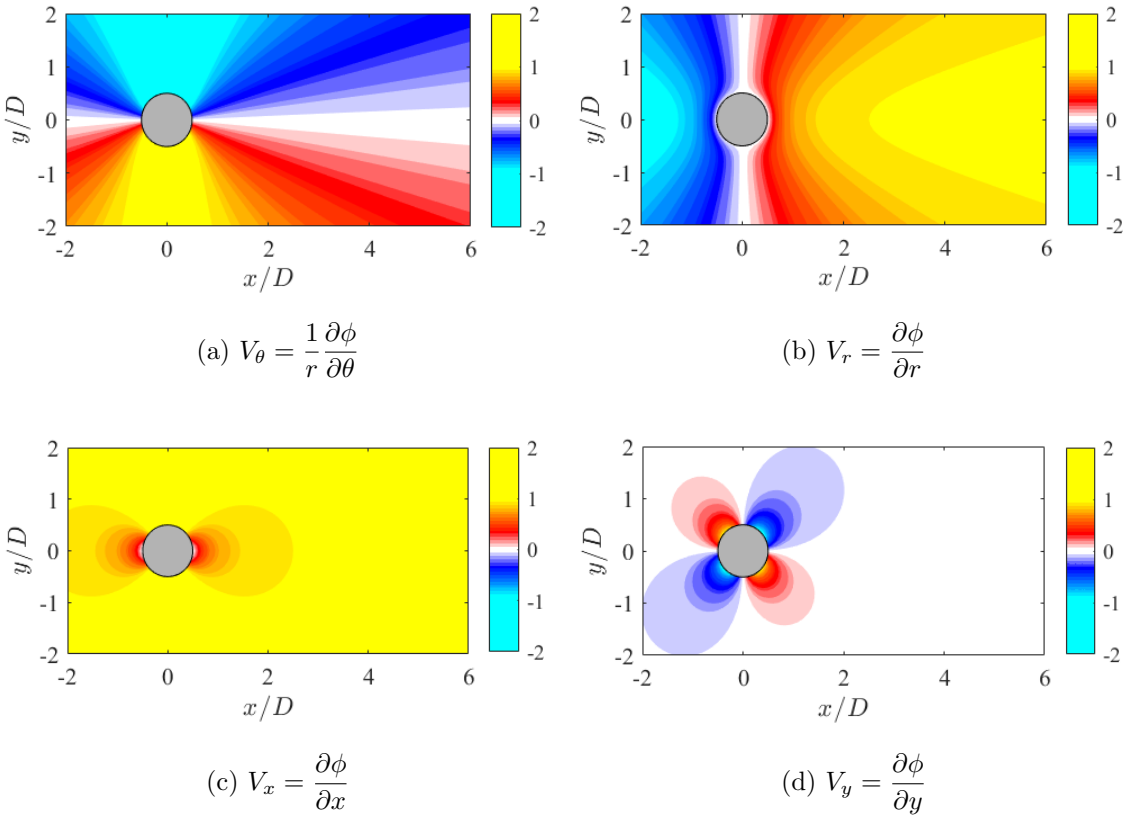

(a) $V_\theta = \frac{1}{r}\frac{\partial \phi}{\partial \theta}$

(b) $V_r = \frac{\partial \phi}{\partial r}$

(c) $V_x = \frac{\partial \phi}{\partial x}$

(d) $V_y = \frac{\partial \phi}{\partial y}$

Figure 10: An illustration of the non-dimensional planar velocity field of the classical velocity potential in the inviscid non-lifting cylinder flow.

In the polar coordinate system, the velocity components are obtained from $\tilde{\kappa}$ in a similar way to the classical stream function as depicted in Figs.11a and 11b. However in the Cartesian coordinate system, $\tilde{\kappa}$ is defined on a principal axis for a viscous rotational flow about which the vorticity vector is identically zero [33, pp. 57-58]. This axis is almost aligned with the wind axis with its negative x-axis pointing into the incident flow. $\tilde{\kappa}$ is a potential function in this axis, and its velocity components

are obtained as

$$
\begin{aligned}
& x = r\cos\theta \quad y = r\sin\theta \quad z = r\cos\varphi \\
& V_{\tilde{x}} = \frac{\partial\tilde{\kappa}}{\partial r}\frac{\partial r}{\partial x} + \frac{\partial\tilde{\kappa}}{r\partial\theta}\frac{r\partial\theta}{\partial x} = -V_\theta\cos\theta - V_r\sin\theta \\
& V_{\tilde{y}} = \frac{\partial\tilde{\kappa}}{\partial r}\frac{\partial r}{\partial y} + \frac{\partial\tilde{\kappa}}{r\partial\theta}\frac{r\partial\theta}{\partial y} = -V_\theta\sin\theta + V_r\cos\theta \\
& V_z = \frac{\partial\tilde{\kappa}}{\partial r}\frac{\partial r}{\partial z} = -V_\theta\cos\varphi
\end{aligned}
\tag{37}
$$

These are illustrated in Figs.11c and 11d for the $z = 0$ plane. Positive z-axis extends out of the page. Figure 12 shows that the radial velocity vanishes at the surface because the surface is impermeable.

The vorticity components in the principal axis are computed as

$$
\begin{aligned}
& \frac{\partial V_{\tilde{x}}}{\partial y} = \frac{\partial^2\tilde{\kappa}}{\partial y\partial x} \\
& = \frac{\partial}{\partial y}\left(\frac{\partial\tilde{\kappa}}{\partial r}\frac{\partial r}{\partial x} + \frac{\partial\tilde{\kappa}}{r\partial\theta}\frac{r\partial\theta}{\partial x}\right) \\
& = \left(\frac{\partial^2\tilde{\kappa}}{\partial r^2}\frac{\partial r}{\partial y} + \frac{\partial^2\tilde{\kappa}}{r\partial r\partial\theta}\frac{r\partial\theta}{\partial y}\right)\frac{\partial r}{\partial x} + \frac{\partial\tilde{\kappa}}{\partial r}\frac{\partial^2 r}{\partial y\partial x} + \left(\frac{\partial^2\tilde{\kappa}}{r\partial r\partial\theta}\frac{\partial r}{\partial y} + \frac{\partial^2\tilde{\kappa}}{r^2\partial\theta^2}\frac{r\partial\theta}{\partial y}\right)\frac{r\partial\theta}{\partial x} \\
& + \frac{\partial\tilde{\kappa}}{r^2\partial\theta}\frac{r^2\partial^2\theta}{\partial y\partial x} \\
& = \left(-\frac{\partial V_\theta}{\partial r}\sin\theta\cos\theta + \frac{\partial V_r}{\partial r}\cos^2\theta + \frac{V_\theta}{r}\sin\theta\cos\theta\right) - \frac{\partial V_r}{\partial r}\sin^2\theta - \frac{V_r}{r}(1 - 2\cos^2\theta) \\
& - \frac{\partial V_r}{r\partial\theta}\sin\theta\cos\theta\ ,
\end{aligned}
\tag{38}
$$

$$
\begin{aligned}
& \frac{\partial V_{\tilde{x}}}{\partial z} = \frac{\partial^2\tilde{\kappa}}{\partial z\partial x} \\
& = \frac{\partial}{\partial z}\left(\frac{\partial\tilde{\kappa}}{\partial r}\frac{\partial r}{\partial x} + \frac{\partial\tilde{\kappa}}{r\partial\theta}\frac{r\partial\theta}{\partial x}\right) \\
& = \left(\frac{\partial^2\tilde{\kappa}}{\partial r^2}\frac{\partial r}{\partial x} + \frac{\partial^2\tilde{\kappa}}{r\partial r\partial\theta}\frac{r\partial\theta}{\partial x}\right)\frac{\partial r}{\partial z} \\
& = -\left(\frac{\partial V_\theta}{\partial r}\cos\theta + \frac{\partial V_r}{\partial r}\sin\theta\right)\cos\varphi\ ,
\end{aligned}
\tag{39}
$$

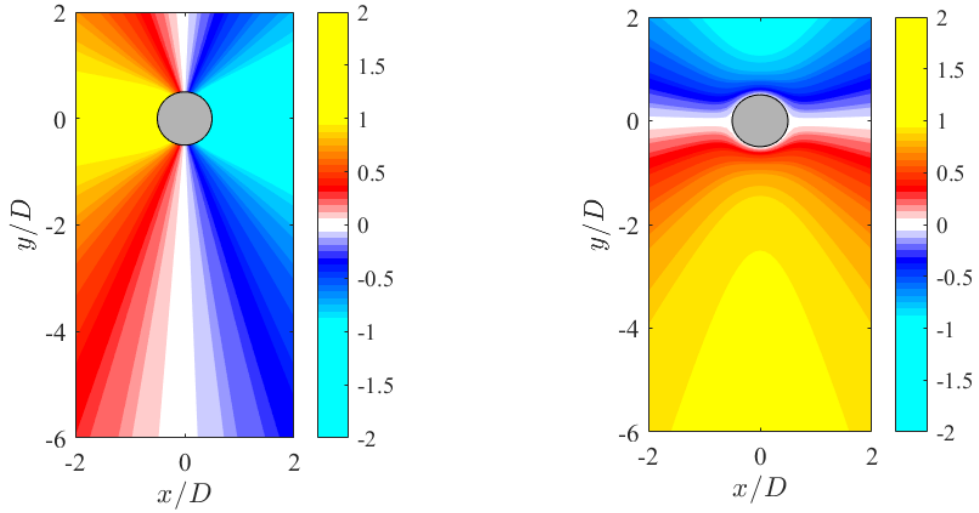

(a) $V_\theta = -\dfrac{\partial \tilde{\kappa}}{\partial r}$

(b) $V_r = \dfrac{1}{r}\dfrac{\partial \tilde{\kappa}}{\partial \theta}$

(c) $V_x = \dfrac{\partial \tilde{\kappa}}{\partial x}$

(d) $V_y = \dfrac{\partial \tilde{\kappa}}{\partial y}$

Figure 11: An illustration of the non-dimensional planar velocity field of the *Kwasu* function in the inviscid non-lifting cylinder flow.

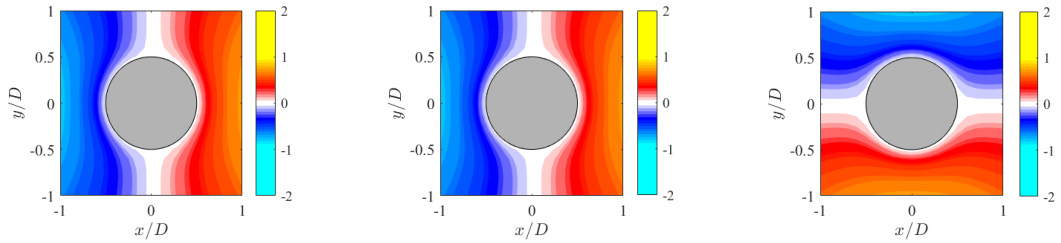

(a) $V_r = \frac{1}{r}\frac{\partial \psi}{\partial \theta}$ (b) $V_r = \frac{\partial \phi}{\partial r}$ (c) $V_r = \frac{1}{r}\frac{\partial \tilde{\kappa}}{\partial \theta}$

Figure 12: A zoomed-in view of the radial velocity field.

$$
\begin{aligned}
&\frac{\partial V_{\tilde{y}}}{\partial x} = \frac{\partial^2 \tilde{\kappa}}{\partial x \partial y} \\
&= \frac{\partial}{\partial x}\left(\frac{\partial \tilde{\kappa}}{\partial r}\frac{\partial r}{\partial y} + \frac{\partial \tilde{\kappa}}{r\partial \theta}\frac{r\partial \theta}{\partial y}\right) \\
&= \left(\frac{\partial^2 \tilde{\kappa}}{\partial r^2}\frac{\partial r}{\partial x} + \frac{\partial^2 \tilde{\kappa}}{r\partial r \partial \theta}\frac{r\partial \theta}{\partial x}\right)\frac{\partial r}{\partial y} + \frac{\partial \tilde{\kappa}}{\partial r}\frac{\partial^2 r}{\partial x \partial y} + \left(\frac{\partial^2 \tilde{\kappa}}{r\partial r \partial \theta}\frac{\partial r}{\partial x} + \frac{\partial^2 \tilde{\kappa}}{r^2 \partial \theta^2}\frac{r\partial \theta}{\partial x}\right)\frac{r\partial \theta}{\partial y} \\
&+ \frac{\partial \tilde{\kappa}}{r^2 \partial \theta}\frac{r^2 \partial^2 \theta}{\partial x \partial y} \\
&= \left(-\frac{\partial V_\theta}{\partial r}\sin\theta\cos\theta - \frac{\partial V_r}{\partial r}\sin^2\theta + \frac{V_\theta}{r}\sin\theta\cos\theta\right) + \frac{\partial V_r}{\partial r}\cos^2\theta - \frac{V_r}{r}(1 - 2\cos^2\theta) \\
&- \frac{\partial V_r}{r\partial \theta}\sin\theta\cos\theta \,,
\end{aligned}
\tag{40}
$$

$$
\begin{aligned}
&\frac{\partial V_{\tilde{y}}}{\partial z} = \frac{\partial^2 \tilde{\kappa}}{\partial z \partial y} \\
&= \frac{\partial}{\partial z}\left(\frac{\partial \tilde{\kappa}}{\partial r}\frac{\partial r}{\partial y} + \frac{\partial \tilde{\kappa}}{r\partial \theta}\frac{r\partial \theta}{\partial y}\right) \\
&= \left(\frac{\partial^2 \tilde{\kappa}}{\partial r^2}\frac{\partial r}{\partial y} + \frac{\partial^2 \tilde{\kappa}}{r\partial r \partial \theta}\frac{r\partial \theta}{\partial y}\right)\frac{\partial r}{\partial z} \\
&= -\left(\frac{\partial V_\theta}{\partial r}\sin\theta - \frac{\partial V_r}{\partial r}\cos\theta\right)\cos\varphi \,,
\end{aligned}
\tag{41}
$$

$$
\begin{aligned}
\frac{\partial V_z}{\partial x} &= \frac{\partial^2 \tilde{\kappa}}{\partial x \partial z} \\
&= \frac{\partial}{\partial x}\left(\frac{\partial \tilde{\kappa}}{\partial r}\frac{\partial r}{\partial z}\right) \\
&= \frac{\partial^2 \tilde{\kappa}}{\partial r^2}\frac{\partial r}{\partial x}\frac{\partial r}{\partial z} + \frac{\partial^2 \tilde{\kappa}}{r\partial\theta\partial r}\frac{r\partial\theta}{\partial x}\frac{\partial r}{\partial z} \\
&= -\left(\frac{\partial V_\theta}{\partial r}\cos\theta + \frac{\partial V_r}{\partial r}\sin\theta\right)\cos\varphi \,,
\end{aligned}
\tag{42}
$$

$$
\begin{aligned}
\frac{\partial V_z}{\partial y} &= \frac{\partial^2 \tilde{\kappa}}{\partial y \partial z} \\
&= \frac{\partial}{\partial y}\left(\frac{\partial \tilde{\kappa}}{\partial r}\frac{\partial r}{\partial z}\right) \\
&= \frac{\partial^2 \tilde{\kappa}}{\partial r^2}\frac{\partial r}{\partial y}\frac{\partial r}{\partial z} + \frac{\partial^2 \tilde{\kappa}}{r\partial\theta\partial r}\frac{r\partial\theta}{\partial y}\frac{\partial r}{\partial z} \\
&= -\left(\frac{\partial V_\theta}{\partial r}\sin\theta - \frac{\partial V_r}{\partial r}\cos\theta\right)\cos\varphi \,,
\end{aligned}
\tag{43}
$$

$$
\begin{aligned}
\omega_x &= \frac{\partial V_z}{\partial y} - \frac{\partial V_{\tilde{y}}}{\partial z} \\
&= -\left(\frac{\partial V_\theta}{\partial r}\sin\theta - \frac{\partial V_r}{\partial r}\cos\theta\right)\cos\varphi - \left(-\left(\frac{\partial V_\theta}{\partial r}\sin\theta - \frac{\partial V_r}{\partial r}\cos\theta\right)\cos\varphi\right) \\
&= 0 \,,
\end{aligned}
\tag{44}
$$

$$
\begin{aligned}
\omega_y &= \frac{\partial V_{\tilde{x}}}{\partial z} - \frac{\partial V_z}{\partial x} \\
&= -\left(\frac{\partial V_\theta}{\partial r}\cos\theta + \frac{\partial V_r}{\partial r}\sin\theta\right)\cos\varphi - \left(-\left(\frac{\partial V_\theta}{\partial r}\cos\theta + \frac{\partial V_r}{\partial r}\sin\theta\right)\cos\varphi\right) \\
&= 0
\end{aligned}
\tag{45}
$$

and

$$
\begin{aligned}
\omega_z &= \frac{\partial V_{\tilde{y}}}{\partial x} - \frac{\partial V_{\tilde{x}}}{\partial y} \\
&= \left(-\frac{\partial V_\theta}{\partial r} \sin\theta\cos\theta - \frac{\partial V_r}{\partial r} \sin^2\theta + \frac{V_\theta}{r} \sin\theta\cos\theta \right) + \frac{\partial V_r}{\partial r} \cos^2\theta - \frac{V_r}{r}(1 - 2\cos^2\theta) \\
&- \frac{\partial V_r}{r\partial\theta} \sin\theta\cos\theta - \left[\left(-\frac{\partial V_\theta}{\partial r} \sin\theta\cos\theta + \frac{\partial V_r}{\partial r} \cos^2\theta + \frac{V_\theta}{r} \sin\theta\cos\theta \right) - \frac{\partial V_r}{\partial r} \sin^2\theta \right. \\
&\left. - \frac{V_r}{r}(1 - 2\cos^2\theta) - \frac{\partial V_r}{r\partial\theta} \sin\theta\cos\theta \right] \\
&= \left(-\frac{\partial V_\theta}{\partial r} \sin\theta\cos\theta - \frac{\partial V_r}{\partial r} \sin^2\theta + \frac{V_\theta}{r} \sin\theta\cos\theta \right) + \frac{\partial V_r}{\partial r} \cos^2\theta - \frac{V_r}{r}(1 - 2\cos^2\theta) \\
&- \frac{\partial V_r}{r\partial\theta} \sin\theta\cos\theta + \left(\frac{\partial V_\theta}{\partial r} \sin\theta\cos\theta - \frac{\partial V_r}{\partial r} \cos^2\theta - \frac{V_\theta}{r} \sin\theta\cos\theta \right) + \frac{\partial V_r}{\partial r} \sin^2\theta \\
&+ \frac{V_r}{r}(1 - 2\cos^2\theta) + \frac{\partial V_r}{r\partial\theta} \sin\theta\cos\theta \\
&= 0 \, .
\end{aligned}
\tag{46}
$$

$\omega_z = 0$ is a solution to the two-dimensional vorticity equation

$$
\frac{\partial \omega_z}{\partial t} + V_{\tilde{x}} \frac{\partial \omega_z}{\partial x} + V_{\tilde{y}} \frac{\partial \omega_z}{\partial y} = \nu \left(\frac{\partial^2 \omega_z}{\partial x} + \frac{\partial^2 \omega_z}{\partial y^2} \right) \quad .
$$

However, the flow remains rotational especially towards the surface and in the wake [33].

In the polar coordinate system, $\tilde{\kappa}$ identically satisfies the two-dimensional instantaneous continuity equation, and it yields the component of the vorticity vector for the flow as

$$
\begin{aligned}
\omega_r &= \frac{1}{r} \left(\frac{\partial V_z}{\partial \theta} - \frac{\partial V_\theta}{\partial z} \right) \\
&= -\frac{1}{r} \left(\frac{\partial V_\theta \cos\varphi}{\partial \theta} + \frac{\partial V_\theta}{\partial r} \frac{\partial r}{\partial z} \right) \\
&= -\frac{1}{r} \left(\frac{\partial V_\theta}{\partial \theta} + \frac{\partial V_\theta}{\partial r} \right) \cos\varphi \, ,
\end{aligned}
\tag{47}
$$

$$
\begin{aligned}
\omega_\theta &= \left(\frac{\partial V_r}{\partial z} - \frac{\partial V_z}{\partial r}\right) \\
&= \left(\frac{\partial V_r}{\partial r}\frac{\partial r}{\partial z} + \frac{\partial\left(V_\theta \frac{z}{r}\right)}{\partial r}\right) \\
&= \left(\frac{\partial V_r}{\partial r}\frac{\partial r}{\partial z} + \frac{\partial\left(V_\theta \frac{z}{r}\right)}{\partial r}\right) \\
&= \left(\frac{\partial V_r}{\partial r} + \frac{\partial V_\theta}{\partial r} - \frac{V_\theta}{r}\right)\cos\varphi \,,
\end{aligned}
\tag{48}
$$

and

$$
\begin{aligned}
\omega_z &= \frac{1}{r}\left(\frac{\partial(rV_\theta)}{\partial r} - \frac{\partial(V_r)}{\partial\theta}\right) \\
&= \frac{\partial V_\theta}{\partial r} + \frac{V_\theta}{r} - \frac{\partial V_r}{r\partial\theta} \,.
\end{aligned}
\tag{49}
$$

The pressure, p, which is a scalar quantity (zeroth-order tensor) is invariant to the foregoing rotation of the Cartesian axes [33]. The Laplacian of the *Kwasu* function required to obtain the viscous term of the pressure field is computed as

$$
\begin{aligned}
&\frac{\partial V_{\tilde{x}}}{\partial x} = \frac{\partial^2\tilde{\kappa}}{\partial x^2} \\
&= \frac{\partial}{\partial x}\left(\frac{\partial\tilde{\kappa}}{\partial r}\frac{\partial r}{\partial x} + \frac{\partial\tilde{\kappa}}{r\partial\theta}\frac{r\partial\theta}{\partial x}\right) \\
&= \left(\frac{\partial^2\tilde{\kappa}}{\partial r^2}\frac{\partial r}{\partial x} + \frac{\partial^2\tilde{\kappa}}{r\partial r\partial\theta}\frac{r\partial\theta}{\partial x}\right)\frac{\partial r}{\partial x} + \frac{\partial\tilde{\kappa}}{\partial r}\frac{\partial^2 r}{\partial x^2} + \left(\frac{\partial^2\tilde{\kappa}}{r\partial r\partial\theta}\frac{\partial r}{\partial x} + \frac{\partial^2\tilde{\kappa}}{r^2\partial\theta^2}\frac{r\partial\theta}{\partial x}\right)\frac{r\partial\theta}{\partial x} \\
&+ \frac{\partial\tilde{\kappa}}{r^2\partial\theta}\frac{r^2\partial^2\theta}{\partial x^2} \\
&= -\left(\frac{\partial V_\theta}{\partial r}\cos^2\theta + \frac{\partial V_r}{\partial r}\sin\theta\cos\theta + \frac{V_\theta}{r}(1-\cos^2\theta)\right) - \left(\frac{\partial V_r}{\partial r} - \frac{V_r}{r}\right)\sin\theta\cos\theta \\
&+ \frac{\partial V_r}{r\partial\theta}\sin^2\theta \,,
\end{aligned}
\tag{50}
$$

$$
\begin{aligned}
&\frac{\partial V_{\tilde{y}}}{\partial y} = \frac{\partial^2 \tilde{\kappa}}{\partial y^2} \\
&= \frac{\partial}{\partial y}\left(\frac{\partial \tilde{\kappa}}{\partial r}\frac{\partial r}{\partial y} + \frac{\partial \tilde{\kappa}}{r\partial\theta}\frac{r\partial\theta}{\partial y}\right) \\
&= \left(\frac{\partial^2 \tilde{\kappa}}{\partial r^2}\frac{\partial r}{\partial y} + \frac{\partial^2 \tilde{\kappa}}{r\partial r\partial\theta}\frac{r\partial\theta}{\partial y}\right)\frac{\partial r}{\partial y} + \frac{\partial \tilde{\kappa}}{\partial r}\frac{\partial^2 r}{\partial y^2} + \left(\frac{\partial^2 \tilde{\kappa}}{r\partial r\partial\theta}\frac{\partial r}{\partial y} + \frac{\partial^2 \tilde{\kappa}}{r^2\partial\theta^2}\frac{r\partial\theta}{\partial y}\right)\frac{r\partial\theta}{\partial y} \\
&+ \frac{\partial \tilde{\kappa}}{r^2\partial\theta}\frac{r^2\partial^2\theta}{\partial y^2} \\
&= -\left(\frac{\partial V_\theta}{\partial r}\sin^2\theta - \frac{\partial V_r}{\partial r}\sin\theta\cos\theta + \frac{V_\theta}{r}(1-\sin^2\theta)\right) + \left(\frac{\partial V_r}{\partial r} - \frac{V_r}{r}\right)\sin\theta\cos\theta \\
&+ \frac{\partial V_r}{r\partial\theta}\cos^2\theta\,,
\end{aligned}
\tag{51}
$$

$$
\begin{aligned}
\frac{\partial V_z}{\partial z} &= \frac{\partial^2 \tilde{\kappa}}{\partial z^2} \\
&= \frac{\partial}{\partial z}\left(\frac{\partial \tilde{\kappa}}{\partial r}\frac{\partial r}{\partial z}\right) \\
&= \frac{\partial^2 \tilde{\kappa}}{\partial r^2}\frac{\partial r}{\partial z}\frac{\partial r}{\partial z} + \frac{\partial \tilde{\kappa}}{\partial r}\frac{\partial r^2}{\partial^2 z} \\
&= -\left(\frac{\partial V_\theta}{\partial r}\cos^2\varphi + \frac{V_\theta}{r}\sin^2\varphi\right)\,,
\end{aligned}
\tag{52}
$$

and

$$
\begin{aligned}
&\nabla^2\tilde{\kappa} = \frac{\partial V_{\tilde{x}}}{\partial x} + \frac{\partial V_{\tilde{y}}}{\partial y} + \frac{\partial V_z}{\partial z} \\
&= \frac{\partial^2 \tilde{\kappa}}{\partial x^2} + \frac{\partial^2 \tilde{\kappa}}{\partial y^2} + \frac{\partial^2 \tilde{\kappa}}{\partial z^2} \\
&= -\left(\frac{\partial V_\theta}{\partial r}\cos^2\theta + \frac{\partial V_r}{\partial r}\sin\theta\cos\theta + \frac{V_\theta}{r}(1-\cos^2\theta)\right) - \left(\frac{\partial V_r}{\partial r} - \frac{V_r}{r}\right)\sin\theta\cos\theta \\
&+ \frac{\partial V_r}{r\partial\theta}\sin^2\theta - \left(\frac{\partial V_\theta}{\partial r}\sin^2\theta - \frac{\partial V_r}{\partial r}\sin\theta\cos\theta + \frac{V_\theta}{r}(1-\sin^2\theta)\right) \\
&+ \left(\frac{\partial V_r}{\partial r} - \frac{V_r}{r}\right)\sin\theta\cos\theta + \frac{\partial V_r}{r\partial\theta}\cos^2\theta - \left(\frac{\partial V_\theta}{\partial r}\cos^2\varphi + \frac{V_\theta}{r}\sin^2\varphi\right) \\
&= -\frac{\partial V_\theta}{\partial r} - \frac{V_\theta}{r} + \frac{\partial V_r}{r\partial\theta} - \frac{\partial V_\theta}{\partial r}\cos^2\varphi - \frac{V_\theta}{r}\sin^2\varphi\,.
\end{aligned}
\tag{53}
$$

The foregoing *Kwasu* function is a two-dimensional potential stream function for a crossflow in the center plane of a finite cylinder. To incorporate the cylinder span, the *Kwasu* function axis is transformed to ensure the flow's rotational symmetry in

the wind axis. This is accomplished in Eqn. 36 with the substitution

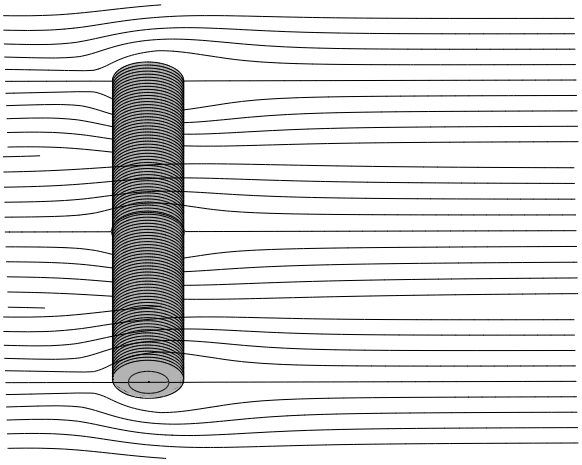

Figure 13: Present theoretical streamlines of an unseparated crossflow over a finite cylinder.

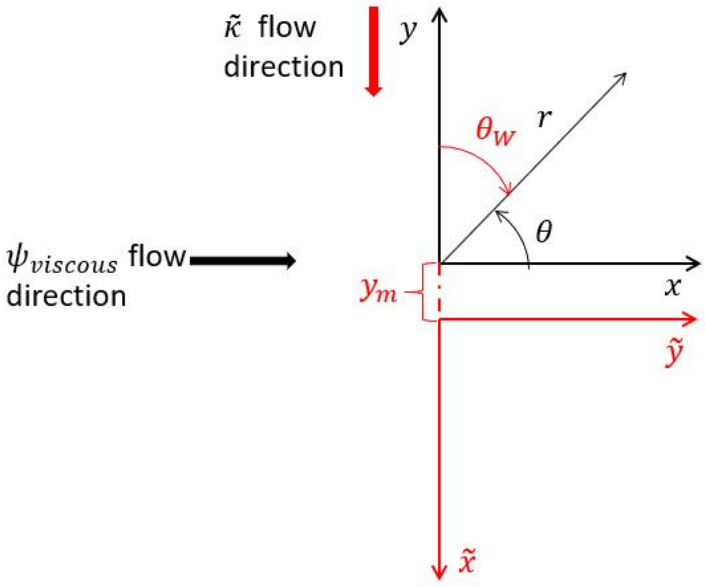

Figure 14: Pictorial representation of y_m and θ_W in the $z = 0$ plane.

$$\begin{aligned} \theta_W &= \arctan\left[x_{3D}, y_{3D}\right] \\ &= \arctan\left[\cos\theta_{3D}\sqrt{x_{3D}^2 + y_{3D}^2}, \sin\theta_{3D}\sqrt{x_{3D}^2 + y_{3D}^2}\right] \end{aligned} \quad , \tag{54}$$

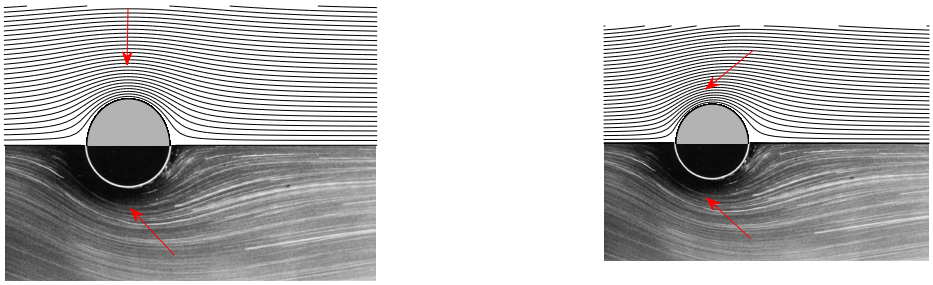

(a) $y_m = 0$ (b) $y_m = 7R_{3D}/20$

Figure 15: Comparison between contour of $\tilde{\kappa}$ (upper images) and an experimentally observed flow (lower images [5, 7]) at $Re = 1.54$.

where

$$\theta_{3D} = \arctan\left(y_{3D} + y_m, x_{3D}\right)$$
$$R_{3D} = \sqrt{R_{2D}^2 + B^2 \cos^2\left(\frac{z_{3D}}{\sqrt{x_{3D}^2 + y_{3D}^2 + z_{3D}^2}}\right)} \quad . \tag{55}$$

In Eqn. 55, y_m is a geometric constant (Fig. 14), and B is the cylinder span. The positive directions of the geometric variables are indicated with the arrowheads in Fig. 14. All the angular coordinates are in radians. R_{2D} and R_{3D} are the body radial coordinate, R, in two- and three-dimensions respectively. Equation 55 defines the two-dimensional $\tilde{\kappa}$ in all $\varphi = constant$ planes of a three-dimensional domain

$$x_{3D} = r\cos\theta\sin\varphi \quad y_{3D} = r\sin\theta\sin\varphi \quad z_{3D} = r\cos\varphi\ . \tag{56}$$

For all of these planes, $\tilde{\kappa}$ is simultaneously a viscous potential function and a stream function following the properties highlighted in Table 2 and Eqn. 61. This is also illustrated in Fig. 13 in which the flow is from left to right.

y_m controls the flow axis about the cylinder as illustrated by the red arrowheads in Fig. 15. In these figures, the flow is also from left to right. When y_m is zero in Fig.15a, the direction of the maximum gradient of the streamlines highlighted by the arrowhead is vertically inwards and directly above the cylinder crest. This is contrary to an experimentally observed flow depicted in the lower image that has this direction

inclined to the cylinder crest. When $y_m = 7R_{3D}/20$ in Fig.15b, there is a consistence with the experimentally observed flow pattern.

In summary, and by inspection of θ_W in Eqn. 54, the wind axis is defined as

$$\begin{aligned} &\tilde{\varphi} = \frac{\pi}{2} \quad \tilde{x} = r\cos\tilde{\theta}\sin\tilde{\varphi} \quad \tilde{y} = r\sin\tilde{\theta}\sin\tilde{\varphi} \quad \tilde{z} = r\cos\tilde{\varphi} = 0 \\ &V_{\tilde{z}} = 0 \quad V_{\tilde{\varphi}} = 0\,. \end{aligned} \tag{57}$$

Fefferman allows an assumption of no body forces ($\mathbf{g} = 0$) or body forces defined by potential functions ($\mathbf{g} = \nabla g$) [22]. With this assumption, the pressure field that identically satisfies the incompressible NSE can be obtained from

$$\nabla\left(\rho\frac{\partial\tilde{\kappa}}{\partial t} + p + \frac{1}{2}\rho V^2 + \rho g - 2\mu\nabla^2\tilde{\kappa}\right) = 0\,.$$

The relationship between ψ, ϕ and $\tilde{\kappa}$ is established as follows. For a two-dimensional flow, lines of constant ψ are streamlines. Along a streamline,

$$\begin{aligned} d\psi &= \frac{\partial\psi}{\partial r}dr + \frac{\partial\psi}{r\partial\theta}rd\theta \\ &= -V_\theta dr + V_r r d\theta \\ &= 0\,, \end{aligned}$$

and

$$\left(\frac{1}{r}\frac{dr}{d\theta}\right)_{\psi=constant} = \frac{V_r}{V_\theta} \quad . \tag{58}$$

Similarly, for a three-dimensional flow, equipotential surfaces are surfaces of constant ϕ. Thus, along an equipotential surface,

$$\begin{aligned} d\phi &= \frac{\partial\phi}{\partial r}dr + \frac{1}{r\sin\varphi}\frac{\partial\phi}{\partial\theta}r\sin\varphi d\theta + \frac{\partial\phi}{r\partial\varphi}rd\varphi \\ &= \frac{\partial\phi}{\partial r}dr + \frac{1}{r\sin\varphi}\frac{\partial\phi}{\partial\theta}r\sin\varphi d\theta + \frac{\partial\phi}{\partial r}\frac{\partial r}{r\partial\varphi}rd\varphi \\ &= V_r dr + V_\theta\sin\varphi r d\theta + V_r dr \\ &= 0 \quad , \end{aligned}$$

and

$$\left(\frac{1}{r}\frac{dr}{d\theta}\right)_{\phi=constant} = -\frac{V_\theta}{2V_r}\sin\varphi \quad . \tag{59}$$

Equivalently, lines of constant $\tilde{\kappa}$ are equipotential streamlines, and surfaces of constant $\tilde{\kappa}$ are equipotential streamsurfaces (or equipotential streamtubes). On such a surface,

$$\begin{aligned} d\tilde{\kappa} &= \frac{\partial\tilde{\kappa}}{\partial r}dr + \frac{\partial\tilde{\kappa}}{r\sin\varphi\partial\theta}r\sin\varphi d\theta + \frac{\partial\tilde{\kappa}}{\partial r}\frac{\partial r}{r\partial\varphi}rd\varphi \\ &= -V_\theta dr + V_r r\sin\varphi d\theta - V_\theta dr \\ &= -V_\theta dr + V_r r\sin\varphi d\theta - V_\theta dr \\ &= 0 \quad , \end{aligned}$$

and

$$\left(\frac{1}{r}\frac{dr}{d\theta}\right)_{\tilde{\kappa}=constant} = \frac{V_r}{2V_\theta}\sin\varphi \quad . \tag{60}$$

Then, Eqns. 58-60 give

$$\left(\frac{1}{r}\frac{dr}{d\theta}\right)_{\psi=constant} = \frac{2}{\sin\varphi}\left(\frac{1}{r}\frac{dr}{d\theta}\right)_{\tilde{\kappa}=constant} = -\frac{\sin\varphi}{2}\frac{1}{\left(\frac{1}{r}\frac{dr}{d\theta}\right)_{\phi=constant}} \quad . \tag{61}$$

To ensure that the equipotential streamsurfaces remain physical, no flow must be allowed to cross them. This means that the cross-product of the surface vector and the velocity vector must be equal to zero as

$$\begin{aligned} \mathbf{ds}\times\mathbf{V} &= \frac{1}{r^2\sin\tilde{\varphi}}\begin{vmatrix} \mathbf{e}_r & (r\sin\tilde{\varphi})\mathbf{e}_\theta & r\mathbf{e}_{\tilde{\varphi}} \\ \partial r & (r\sin\tilde{\varphi})\partial\theta & r\partial\tilde{\varphi} \\ V_r & V_\theta & V_{\tilde{\varphi}} \end{vmatrix} \\ &= \frac{1}{r\sin\tilde{\varphi}}\left(V_{\tilde{\varphi}}\sin\tilde{\varphi}\partial\theta - V_\theta\partial\tilde{\varphi}\right)\mathbf{e}_r - \frac{1}{r}\left(V_{\tilde{\varphi}}\partial r - V_r r\partial\tilde{\varphi}\right)\mathbf{e}_\theta \\ &+\frac{1}{r\sin\tilde{\varphi}}\left(V_\theta\partial r - V_r\left(r\sin\tilde{\varphi}\right)\partial\theta\right)\mathbf{e}_{\tilde{\varphi}} \\ &= 0\mathbf{e}_r - 0\mathbf{e}_\theta - \mathrm{d}\tilde{\kappa}\mathbf{e}_{\tilde{\varphi}} \\ &= 0\,. \end{aligned} \tag{62}$$

Additionally, the continuity equation must be satisfied at all times as

$$\begin{aligned}\nabla \cdot \mathbf{V} &= \frac{1}{r}\frac{\partial (rV_r)}{\partial r} + \frac{1}{r}\frac{\partial V_\theta}{\partial \theta} + \underbrace{\frac{\partial V_{\tilde{z}}}{\partial z}}_{=0} \\ &= \frac{V_r}{r} + \frac{\partial V_r}{\partial r} + \frac{1}{r}\frac{\partial V_\theta}{\partial \theta} \\ &= \frac{1}{r^2}\frac{\partial \tilde{\kappa}}{\partial \theta} - \frac{1}{r^2}\frac{\partial \tilde{\kappa}}{\partial \theta} + \frac{1}{r}\frac{\partial^2 \tilde{\kappa}}{\partial r \partial \theta} - \frac{1}{r}\frac{\partial^2 \tilde{\kappa}}{\partial \theta \partial r} \\ &= 0 \quad (t \geq 0).\end{aligned} \tag{63}$$

The *Kwasu* function is not an axisymmetric solution in the body axis since

$$V_\varphi = \frac{\partial \tilde{\kappa}}{\partial r}\frac{\partial r}{\partial z}\frac{\partial z}{r \partial \varphi} = -V_\theta \sin\varphi \cos\varphi \quad . \tag{64}$$

The derivation of its functional form from classical potential theory is the subject of the following subsections.

2.1.3 Satisfying The Boundary Conditions

The formulation is started by assuming that the cylinder is a sole body of gravity subjected to a flow in an infinite domain and referenced to an inertial spatio-temporal frame. With a further assumption that an experimentally observed flow over a non-rotating cylinder is a subset of the general solution of the Laplace equation (Eqn. 28), the viscous stream function should have the form

$$\psi_{viscous}\left(r, \theta, V_\infty, \nu, t, Re\right) = V_\infty r \sin\theta \left(1 - \frac{R^2}{r^2}\right) + B_0\left(r, \theta, V_\infty, \nu, t, Re\right) \ln\left(\frac{r}{R}\right) , \tag{65}$$

and its velocity should be

$$\begin{aligned}V_{r_{viscous}} &= V_\infty \cos\theta \left(1 - \frac{R^2}{r^2}\right) + \frac{1}{r}\frac{\partial B_0}{\partial \theta} \ln\left(\frac{r}{R}\right) \\ V_{\theta_{viscous}} &= -V_\infty \sin\theta \left(1 + \frac{R^2}{r^2}\right) - \frac{B_0}{r} - \frac{\partial B_0}{\partial r} \ln\left(\frac{r}{R}\right)\end{aligned} \tag{66}$$

where Re is the Reynolds number based on the cylinder diameter. It should also satisfy the freestream boundary condition and the wall no-slip condition.

$B_0 \ln(R)$ enforces the no-slip condition at the wall where $r = R$ as

$$\psi_{viscous} = V_\infty R \sin\theta \left(1 - \frac{R^2}{R^2}\right) + B_0 \ln\left(\frac{R}{R}\right) = 0 \,, \tag{67}$$

$$V_{r_{viscous}} = V_\infty \cos\theta \left(1 - \frac{R^2}{R^2}\right) + \frac{1}{R}\frac{\partial B_0}{\partial \theta} \ln\left(\frac{R}{R}\right) = 0 \,, \tag{68}$$

and

$$V_{\theta_{viscous}} = -V_\infty \sin\theta \left(1 + \frac{R^2}{R^2}\right) - \frac{B_0}{R} - \frac{\partial B_0}{\partial r} \ln\left(\frac{R}{R}\right) = -2V_\infty \sin\theta - \frac{B_0}{R} \,. \tag{69}$$

Equation 69 shows that B_0 is at least $f(r, \theta, V_\infty)$, and its form should be based on the tangential velocity of the NLF to satisfy the no-slip condition. $B_0 \ln(R)$ can be understood as the reaction (based on Newton's third law) at the wall to the introduction of a vortex into the flow.

The limit of Eqn. 65 as $r \to \infty$ is

$$\psi_{viscous} = V_\infty r \sin\theta + B_0 \ln\left(\frac{r}{R}\right) . \tag{70}$$

The freestream uniform flow should be recovered for Eqn. 70 to be bounded. However, the natural logarithm term precludes this except if $B_0 \to 0$ at a faster rate in the limit as $\ln(r/R) \to \infty$. This suggests that B_0 should consist of an exponent of the negative of r that tends to zero as $r \to \infty$ in a viscous and time-dependent way. When this is the case, the vorticity,

$$\begin{aligned}
\omega_z &= \frac{1}{r}\left(\frac{\partial(rV_\theta)}{\partial r} - \frac{\partial(V_r)}{\partial \theta}\right) \\
&= \frac{\partial V_\theta}{\partial r} + \frac{V_\theta}{r} - \frac{\partial V_r}{r \partial \theta} \\
&= 2V_\infty \sin\theta \frac{R^2}{r^3} + \frac{B_0}{r^2} - \frac{2}{r}\frac{\partial B_0}{\partial r} - \frac{\partial^2 B_0}{\partial^2 r} \ln\left(\frac{r}{R}\right) \\
&- V_\infty \sin\theta \left(\frac{1}{r} + \frac{R^2}{r^3}\right) - \frac{B_0}{r^2} - \frac{1}{r}\frac{\partial B_0}{\partial r} \ln\left(\frac{r}{R}\right) \\
&+ V_\infty \sin\theta \left(\frac{1}{r} - \frac{R^2}{r^3}\right) - \frac{1}{r}\frac{\partial^2 B_0}{\partial^2 \theta} \ln\left(\frac{r}{R}\right) \\
&= -\frac{2}{r}\frac{\partial B_0}{\partial r} - \frac{1}{r}\frac{\partial B_0}{\partial r} \ln\left(\frac{r}{R}\right) - \frac{\partial^2 B_0}{\partial^2 r} \ln\left(\frac{r}{R}\right) - \frac{1}{r}\frac{\partial^2 B_0}{\partial^2 \theta} \ln\left(\frac{r}{R}\right) \\
&= -\nabla^2 \left(B_0 \ln\left(\frac{r}{R}\right)\right) \,,
\end{aligned} \tag{71}$$

is also bounded and confined to the boundary layer/wake. It is observable in Eqn. 71 that the inviscid term in $\psi_{viscous}$ does not contribute to the vorticity because it is irrotational.

Thus, based on the preceding discussion and the viscous stream function for a vortex described with the Lamb-Oseen model in Eqn.25, a basic functional form for B_0 is assumed to be

$$\begin{aligned} B_0 &= \frac{\Gamma}{2\pi} \\ &= \frac{\Gamma_0}{2\pi} \mathrm{e}^{\left(-\frac{r^2}{4\nu t}\right)} . \end{aligned} \tag{72}$$

However, when an experimentally observed flow impinges a surface, the local change in momentum of the fluid elements is propagated radially outward from the surface [5, p. 604]. This is assumed to be similar to local source/sink flows situated at the surface. Therefore, to simulate the boundary layer effect theoretically in the NLF, the cylinder surface is replaced with a viscous sink-source-vortex sheet as depicted in Fig. 16a. The sheet has the sinks/sources and the vortices positioned at the same locations. The resulting flow pattern of this superposition at a specific location is illustrated in Fig. 16b. The strengths of the sinks/sources and vortices are dictated by the velocity field of the NLF. Additionally, their locations are defined by the dividing streamline equation for the NLF. These locations are continuous and not discrete. The dividing streamline, $\psi = 0$ in Fig. 5 delineates the external flow from the internal flow and ensures the impermeability of the surface. The strengths of a sink /source and vortex at a specific location on the viscous sheet are not the same but vary in a manner that reflects the physics of the experimentally observed flow. These considerations are employed to modify B_0 further from Eqn.72 in the following subsections.

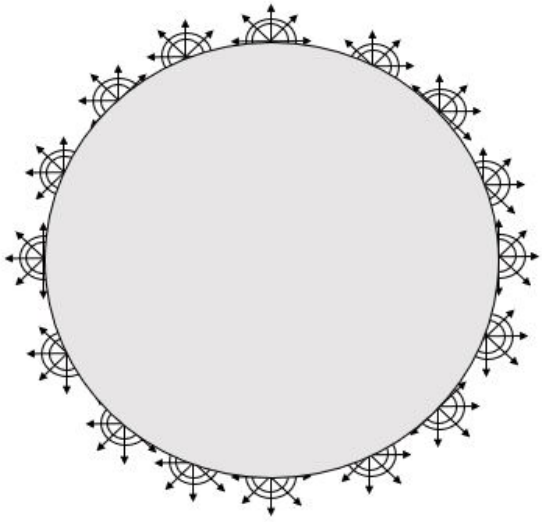

(a) A sink-source-vortex sheet on the cylinder surface

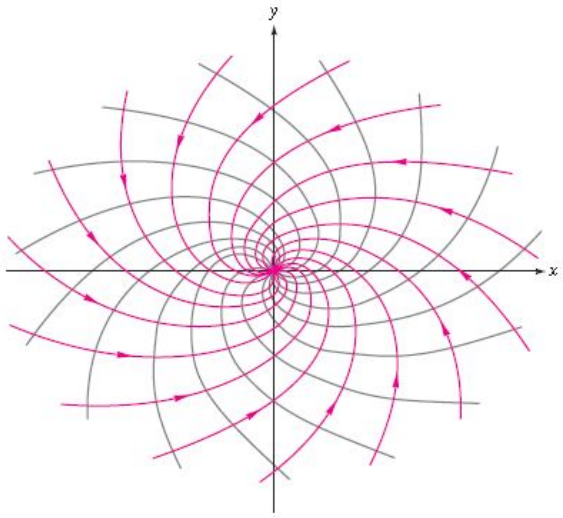

(b) The streamlines of the superposition of a vortex and a sink [61].

Figure 16: Theoretical simulation of the boundary layer effect.

2.1.4 Viscous Incompressible Two-Dimensional Stream Function Without Vortex Shedding

2.1.4.1 Surface Sink-Source-Vortex Sheet

To introduce Re into the expression for B_0, the vortices it describes are assumed to be Burgers' vortices that have their characteristic time, t, fixed in Eqn. 24 [46, p. 265]. The circulation introduced by these vortices is then represented as

$$\Gamma = \Gamma_0 \mathrm{e}^{\left(-\frac{(r-R)^2}{r_c^2}\right)} \tag{73}$$

where the radial distance, r, in Eqn. 72 has been replaced with $r - R$. $r - R$ is the distance measured radially from the cylinder surface that is depicted in Fig. 17. Figure 17 also presents a contour of the NLF speed normalized by the freestream velocity.

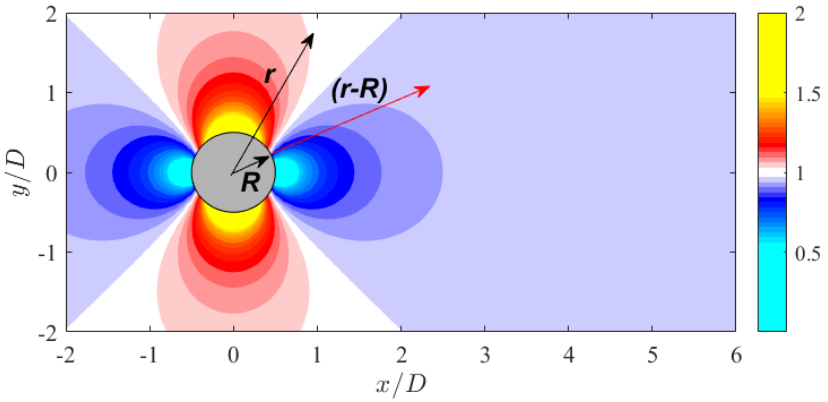

Figure 17: Contour of normalized speed, $V/V_\infty = \sqrt{\left(1-\frac{R^2}{r^2}\right)^2 + 4\,\frac{R^2\sin^2\theta}{r^2}}$, for NLF showing the distance $(r-R)$.

The determination of the vortex core radius, r_c, follows an iterative trial and error process. Using the radial distance from the wall and the expression for the NLF speed, a basic expression is derived as

$$\begin{aligned}
r_c^2 &= 4\nu t \\
&= 4\nu \times \frac{distance}{speed} \\
&= \frac{4\nu(r-R)}{V_\infty\sqrt{\left(1-\frac{R^2}{r^2}\right)^2+4\,\frac{R^2\sin^2\theta}{r^2}}} \\
&= \frac{4\nu R\left(\frac{r}{R}-1\right)}{V_\infty\sqrt{\left(1-\frac{R^2}{r^2}\right)^2+4\,\frac{R^2\sin^2\theta}{r^2}}} \\
&= \frac{4\nu R(2R)\left(\frac{r}{R}-1\right)}{V_\infty(2R)\sqrt{\left(1-\frac{R^2}{r^2}\right)^2+4\,\frac{R^2\sin^2\theta}{r^2}}} \\
&= \frac{\nu}{V_\infty(2R)}\frac{8R^2\left(\frac{r}{R}-1\right)}{\sqrt{\left(1-\frac{R^2}{r^2}\right)^2+4\,\frac{R^2\sin^2\theta}{r^2}}} \\
&= \frac{1}{Re}\frac{8R^2\left(\frac{r}{R}-1\right)}{\sqrt{\left(1-\frac{R^2}{r^2}\right)^2+4\,\frac{R^2\sin^2\theta}{r^2}}}\,.
\end{aligned} \tag{74}$$

This is used to define the strength of the surface vortices as

$$\begin{aligned}
\Gamma &= \Gamma_0 e^{\left(-\frac{R^2\left(\frac{r}{R}-1\right)^2}{r_c^2}\right)} \\
&= \Gamma_0 e^{\left(-\frac{Re\sqrt{\left(1-\frac{R^2}{r^2}\right)^2+4\,\frac{R^2\sin^2\theta}{r^2}}\left(\frac{r}{R}-1\right)}{8}\right)}\,.
\end{aligned} \tag{75}$$

An analytic expression for the initial circulation is obtained from the NLF as

$$V_\theta = -V_\infty \sin\theta \left(1 + \frac{R^2}{r^2}\right) = \frac{\Gamma_0}{2\pi r} \ ,$$

so that the initial circulation of the surface vortices is

$$\Gamma_0 = -2\pi V_\infty \sin\theta r \left(1 + \frac{R^2}{r^2}\right), \ \pi \geq \theta \geq \ -\pi \ . \tag{76}$$

This is in consistence with the initialization Fefferman [22] discusses. The full expression for the strength of the vortices is

$$\Gamma = -2\pi V_\infty \sin\theta r \left(1 + \tfrac{R^2}{r^2}\right) \mathrm{e}^{\left(-\frac{Re\sqrt{\left(1-\frac{R^2}{r^2}\right)^2 + 4\,\frac{R^2 \sin^2\theta}{r^2}}\left(\frac{r}{R}-1\right)}{8}\right)} \ . \tag{77}$$

Then, the surface vortex stream function is expressed as

$$\psi_{vortex} = -V_\infty r \sin\theta \left(1 + \frac{R^2}{r^2}\right) \mathrm{e}^{-\left(\frac{Re\sqrt{\left(1-\frac{R^2}{r^2}\right)^2 + 4\,\frac{R^2 \sin^2\theta}{r^2}}\left(\frac{r}{R}-1\right)}{8}\right)} \ln\left(\frac{r}{R}\right) . \tag{78}$$

The contour of this expression normalized by $V_\infty R$ is illustrated in Fig. 18 for $Re = 26$. The overall flow is from left to right. Figure 18a reveals two vortices located on each half of the cylinder. The vortices' radial and circumferential extents are bounded. The close-up views of the vortices overlaid with the quiver of the velocity vector in Figs. 18b and 18c reveal that they are counter-rotating. The quiver arrowheads are longest towards the cylinder surface because Γ_0 is maximum at the surface. The exponential term dissipates Γ_0 and shortens the arrowheads away from the surface. The natural logarithmic term produces the curvilinear path of the vortices' streamlines.

If the singularities (vortices and sources/sinks) generated at the surface in an experimentally observed flow are actually concentric as hypothesized, then the radial velocity obtained from the vortex sheet will be equal to that expected from the source/sink sheet. Therefore, to set the strength of the source/sink on the cylinder

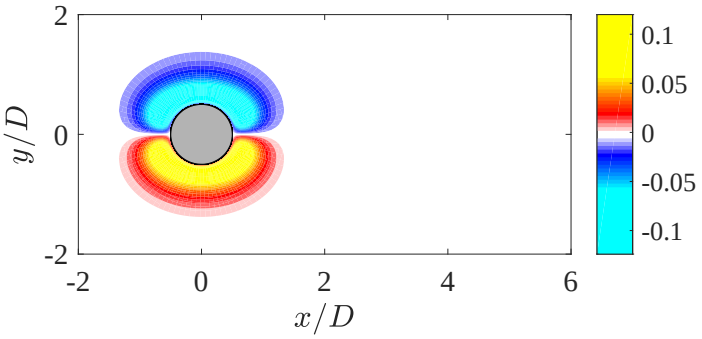

(a) Eqn. 78

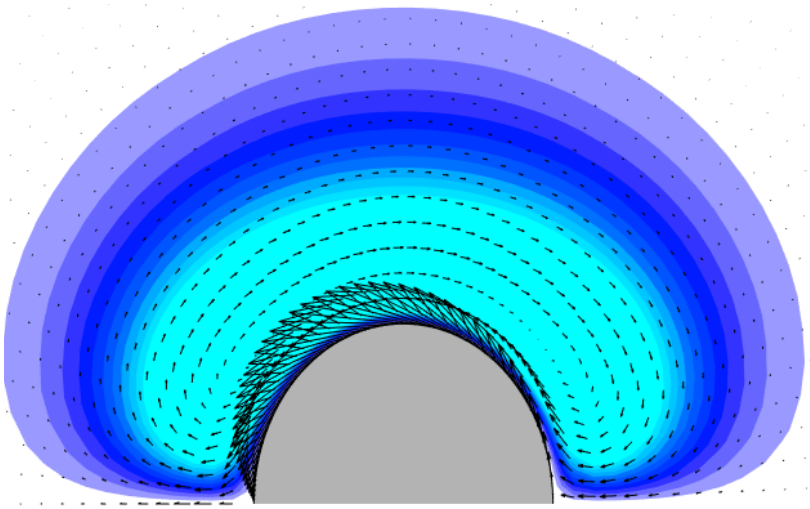

(b) Upper vortex with quiver of velocity field

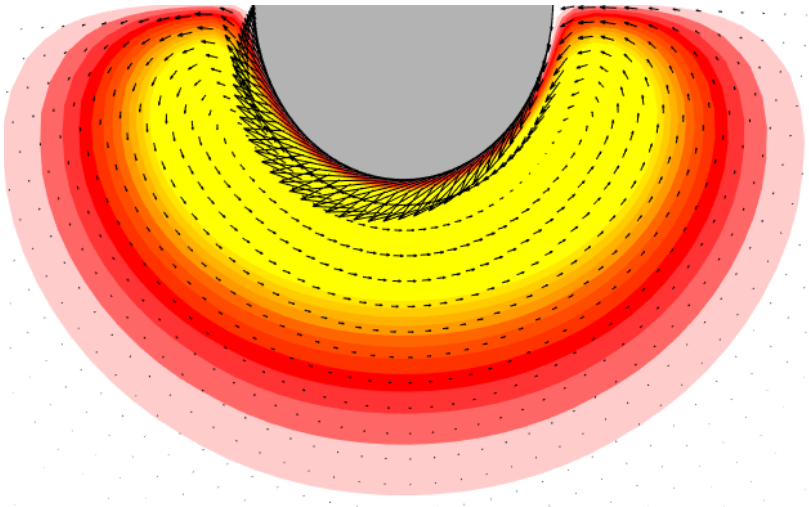

(c) Lower vortex with quiver of velocity field

Figure 18: Contour of $\psi_{vortex}/V_\infty R$ at $Re = 26$.

surface, Eqn. 27 (i.e. $V_r = \Lambda/2\pi r$) is employed noting that the radial velocity is obtained from Eqn. 78 as

$$V_r = -V_\infty \left(1 + \frac{R^2}{r^2}\right) \times \left(\cos\theta - \frac{Re}{2} \frac{\sin^2\theta\cos\theta\left(\frac{r}{R} - 1\right)\frac{R^2}{r^2}}{\sqrt{\left(1 - \frac{R^2}{r^2}\right)^2 + 4\,\frac{R^2\sin^2\theta}{r^2}}}\right) \mathrm{e}^{-\left(\frac{Re\sqrt{\left(1-\frac{R^2}{r^2}\right)^2+4\,\frac{R^2\sin^2\theta}{r^2}}}{8}\left(\frac{r}{R}-1\right)\right)} \ln\left(\frac{r}{R}\right).$$

Then, the strength of the surface sink/source is

$$\begin{aligned} \Lambda &= 2\pi r V_r \\ &= -2\pi V_\infty r \left(1 + \frac{R^2}{r^2}\right) \\ &\times \left(\cos\theta - \tfrac{Re}{2} \frac{\sin^2\theta\cos\theta\left(\frac{r}{R}-1\right)\frac{R^2}{r^2}}{\sqrt{\left(1-\frac{R^2}{r^2}\right)^2+4\,\frac{R^2\sin^2\theta}{r^2}}}\right) \mathrm{e}^{-\left(\frac{Re\sqrt{\left(1-\frac{R^2}{r^2}\right)^2+4\,\frac{R^2\sin^2\theta}{r^2}}\left(\frac{r}{R}-1\right)}{8}\right)} \ln\left(\frac{r}{R}\right). \end{aligned} \tag{79}$$

The strength varies largely with the cosine of the angle, and the remnant of the initial NLF has been carried over in the $(1 + R^2/r^2)$ term. The source/sink sheet strength can be viewed as having a contribution from the uniform flow and another from the doublet. However, these two components should have alternate directions. Examination of the experimentally observed flow over the cylinder dictates the direction of the sinks/sources. At the front stagnation point for instance, where $\cos(\theta)$ is negative, the reflection of sound waves into the upstream flow indicates that these waves should be treated as if coming from a local source on the base doublet at that point. Thus, it is more appropriate to employ the equation

$$\begin{aligned} \Lambda &= 2\pi V_\infty r \left(1 - \tfrac{R^2}{r^2}\right) \\ &\times \left(\cos\theta - \tfrac{Re}{2} \frac{\sin^2\theta\cos\theta\left(\frac{r}{R}-1\right)\frac{R^2}{r^2}}{\sqrt{\left(1-\frac{R^2}{r^2}\right)^2+4\,\frac{R^2\sin^2\theta}{r^2}}}\right) \mathrm{e}^{-\left(\frac{Re\sqrt{\left(1-\frac{R^2}{r^2}\right)^2+4\,\frac{R^2\sin^2\theta}{r^2}}\left(\frac{r}{R}-1\right)}{8}\right)} \ln\left(\frac{r}{R}\right), \end{aligned} \tag{80}$$

in which $(1 + R^2/r^2)$ has been replaced by $(1 - R^2/r^2)$, and the leading negative sign, dropped. Hence, the Re-dependent stream function of the source/sink sheet is given

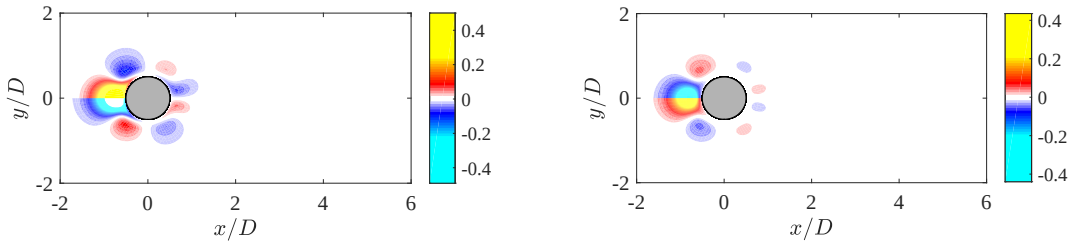

(a) Non-physical (with Eqn. 79)

(b) Physical (with Eqn. 80)

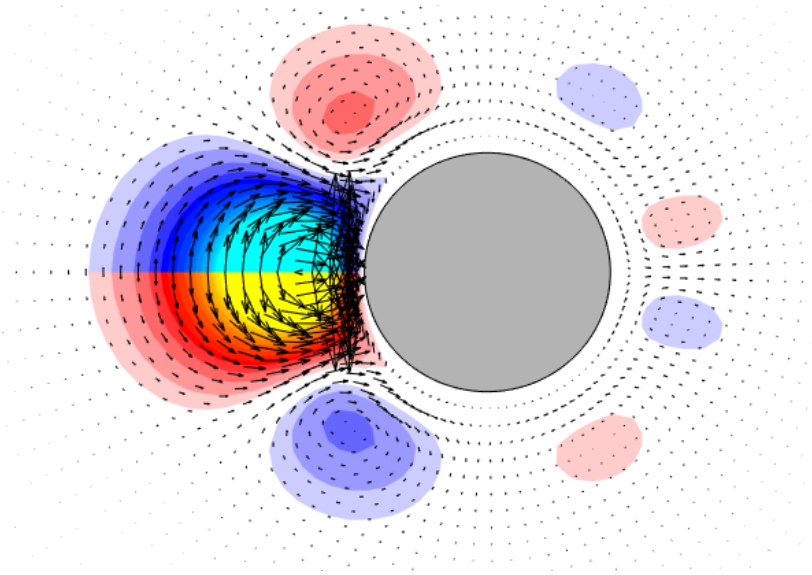

(c) Close-up view of (*b*) with quiver plot of velocity field

Figure 19: Contour of $\psi_{sink/source}/V_\infty R$ at $Re = 26$.

by

$$\psi_{sink/source} = V_\infty r\left(1-\frac{R^2}{r^2}\right) \times\left(\cos\theta - \frac{Re}{2}\,\frac{\sin^2\theta\cos\theta\left(\frac{r}{R}-1\right)\frac{R^2}{r^2}}{\sqrt{\left(1-\frac{R^2}{r^2}\right)^2+4\,\frac{R^2\sin^2\theta}{r^2}}}\right) \mathrm{e}^{-\left(\frac{Re\sqrt{\left(1-\frac{R^2}{r^2}\right)^2+4\,\frac{R^2\sin^2\theta}{r^2}}\left(\frac{r}{R}-1\right)}{8}\right)\theta\ln\left(\frac{r}{R}\right)}. \tag{81}$$

The normalized sink/source sheet stream function is illustrated in Fig. 19. Figures 19a and 19b employ Eqns. 79 and 80 respectively for the strength of the sheet. Figure 19c presents a close-up view of Fig. 19b overlaid with a quiver of the velocity field. The overall flow is still from left to right. Two dominant counter-rotating vortices are observable at the front of the cylinder.

Then, using superposition as depicted in Fig. 20, a viscous stream function is obtained as

$$\begin{aligned}\psi &= \psi_{NLF} + \psi_{vortex} + \psi_{sink/source}\\ &= V_\infty r\sin\theta\left(1-\frac{R^2}{r^2}\right)\\ &\quad -V_\infty r\sin\theta\left(1+\frac{R^2}{r^2}\right)\mathrm{e}^{-\left(\frac{Re\sqrt{\left(1-\frac{R^2}{r^2}\right)^2+4\,\frac{R^2\sin^2\theta}{r^2}}\left(\frac{r}{R}-1\right)}{8}\right)\ln\left(\frac{r}{R}\right)}\\ &\quad +V_\infty r\left(1-\frac{R^2}{r^2}\right)\\ &\quad \times\left(\cos\theta - \frac{Re}{2}\,\frac{\sin^2\theta\cos\theta\left(\frac{r}{R}-1\right)\frac{R^2}{r^2}}{\sqrt{\left(1-\frac{R^2}{r^2}\right)^2+4\,\frac{R^2\sin^2\theta}{r^2}}}\right)\mathrm{e}^{-\left(\frac{Re\sqrt{\left(1-\frac{R^2}{r^2}\right)^2+4\,\frac{R^2\sin^2\theta}{r^2}}\left(\frac{r}{R}-1\right)}{8}\right)(\theta+\sigma)\ln\left(\frac{r}{R}\right)}\end{aligned} \tag{82}$$

for the cylinder flow. Figure 20 illustrates the superposition of the normalized viscous stream function at $Re = 26$. The flow is from left to right in each of the constituent figures. Examining the third term of Eqn. 82, it is evident that there is a bias with θ if the conventional way in which θ varies from 0 to 2π is assumed. This bias is illustrated in Fig. 20d. Therefore, θ is taken to vary from 0 at the rear stagnation point to $+\pi$ at the front stagnation point on the upper half of the cylinder and from 0 at the rear stagnation point to $-\pi$ at the front stagnation point for the lower half. Thus, the

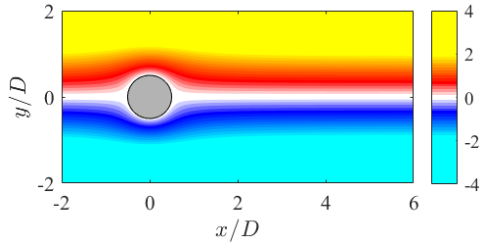

(a) $\psi_{NLF}/V_\infty R$

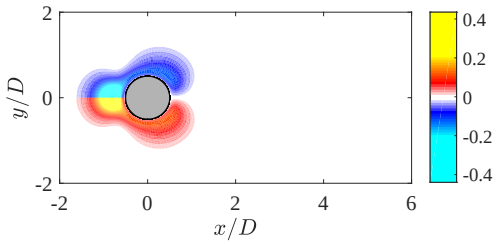

(b) $(\psi_{vortex} + \psi_{sink/source})/V_\infty R$

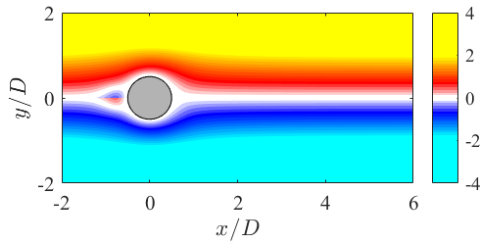

(c) $(\psi_{NLF} + \psi_{vortex} + \psi_{sink/source})/V_\infty R$
$(-\pi \leq \theta \leq \pi)$

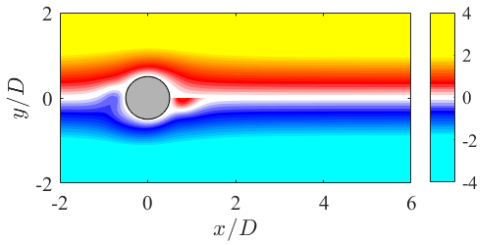

(d) $(\psi_{NLF} + \psi_{vortex} + \psi_{sink/source})/V_\infty R$
$(0 \leq \theta \leq 2\pi)$

Figure 20: Contour plots showing the superposition of $\psi_{viscous}/V_\infty R$ at $Re = 26$.

bias with θ is avoided in Figs. 20a to 20c. σ is $\pm\pi$ depending on the semicircle of the cylinder. The introduction of σ places the stagnation point appropriately at the front of the cylinder and the region of recirculating eddies at the rear as Fig. 21 illustrates.

All the variables and constants in Eqn. 82 are directly from CPT and the Lamb-Oseen vortex model. It is viscous but not time-dependent. It identically satisfies the Laplace equation. It also satisfies the no-slip condition. However, the region of the recirculating eddies and the regions of vorticity around the cylinder predicted with Eqn. 82 diminishes with increasing Re as depicted in Fig. 22. Particularly at $Re = 1$, the recirculating eddies are overblown and non-physical. However, the streamlines of an experimentally observed flow at $Re \approx 1$ are symmetrical about the cylinder. They are un-separated from the cylinder. The current literature further records that for $0 < Re < 4$, the creeping flow, the flow is almost steadily symmetrical about the

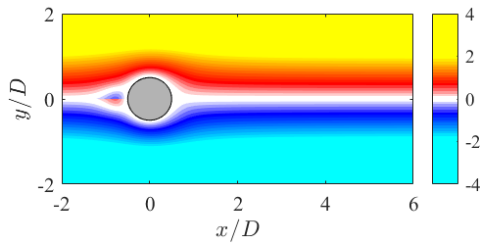

(a) Non-physical ($\sigma = 0$)

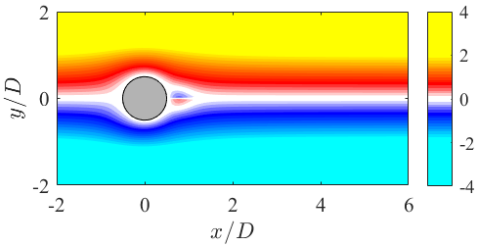

(b) Physically consistent ($\sigma \neq 0$)

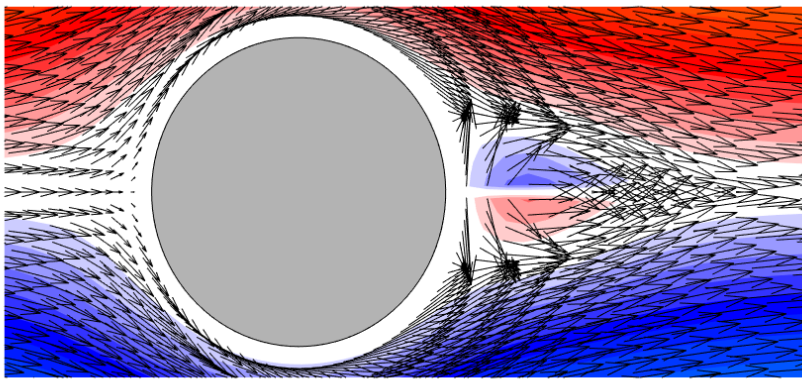

(c) Close-up view of (b) with quiver plot of velocity field

Figure 21: Contour of $\psi_{viscous}/V_\infty R$ at $Re = 26$ showing the effect of σ.

longitudinal and lateral axes of the cylinder [5, 7, 9, 64]. A wake-like structure first becomes noticeable for Re $O(1)$ [7, 9, 64], and a stable pair of recirculating eddies forms in the wake after the flow separates aft of the cylinder for $Re > 6$ [7, 9, 64]. Generally, this recirculation region grows in length and width as a monotonic function of Re [15, 43, 65], however it is reported to diminish with increasing blockage ratio [65]. Additionally, some reported numerical results display a trend towards reduction of the streamwise extent of the bubble for Re between 10 and 100 [65]. For $Re > 40$, the recirculation region destabilizes, the flow becomes unsteady and asymmetric, and the vortices are shed periodically and alternately from the top and bottom sides of the cylinder to form the von Kármán vortex street [5, 9, 15, 64]. These observations are contrary to Fig. 22. Equation 82 also features a singularity when $r = R$ and $\theta = 0$ in the square root in the denominator of the Re-dependent term. These all suggest careful modifications of Eqn. 82 are necessary. These modifications are incorporated by introducing some constants q and c as

$$\begin{aligned}
\psi = {} & V_\infty r \sin\theta \left(1 - \tfrac{R^2}{r^2}\right) \\
& - V_\infty r \sin\theta \left(1 + \tfrac{R^2}{r^2}\right) \mathrm{e}^{-\left(\frac{qRe\sqrt{\left(1-\frac{R^2}{r^2}\right)^2 + 4\,\frac{R^2\sin^2\theta}{r^2}} + c\left(\frac{r}{R}-1\right)}{8}\right)} \ln\left(\tfrac{r}{R}\right) \\
& + V_\infty r \left(1 - \tfrac{R^2}{r^2}\right) \\
& \times \left(\cos\theta - \frac{qRe}{2} \frac{\sin^2\theta\cos\theta\left(\frac{r}{R}-1\right)\frac{R^2}{r^2}}{\sqrt{\left(1-\frac{R^2}{r^2}\right)^2 + 4\,\frac{R^2\sin^2\theta}{r^2}} + c}\right) \mathrm{e}^{-\left(\frac{qRe\sqrt{\left(1-\frac{R^2}{r^2}\right)^2 + 4\,\frac{R^2\sin^2\theta}{r^2}} + c\left(\frac{r}{R}-1\right)}{8}\right)} (\theta + \sigma) \ln\left(\tfrac{r}{R}\right) .
\end{aligned} \tag{83}$$

c can be any small number and is likely not Re- or time-dependent because the experimentally observed flow does not have singularities at all. To preserve the features already captured with Eqn. 82 illustrated in Fig. 23, c should be between zero and the maximum value of the square rooted expression at the surface that is four (4). Therefore, the number two (2) is chosen arbitrarily.

However, q is likely Re-dependent because the experimentally observed flow ranges

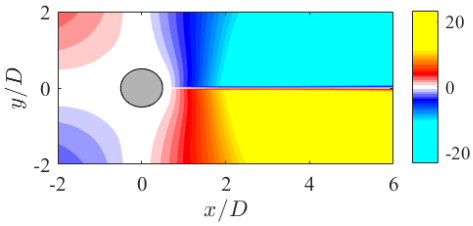

(a) $Re = 1$

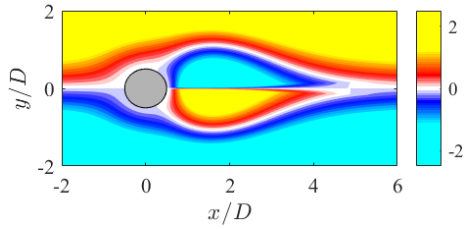

(b) $Re = 5$

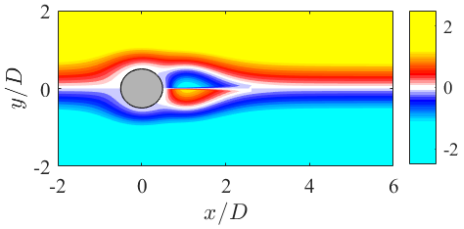

(c) $Re = 10$

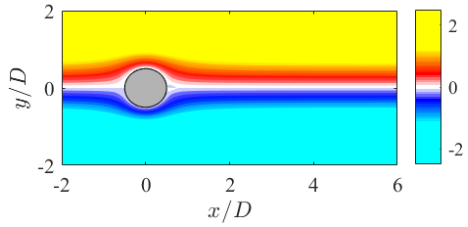

(d) $Re = 130$

Figure 22: Contour of Eqn. 82 normalized with $V_\infty R$ for different Reynolds numbers $c = 0$.

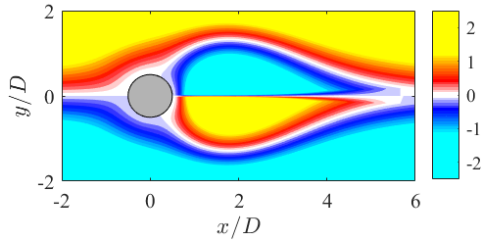

(a) $c = 0$

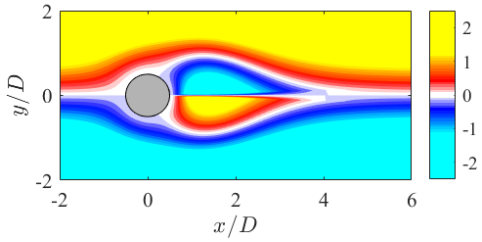

(b) $c = 1$

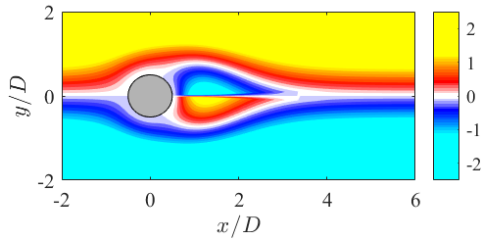

(c) $c = 2$

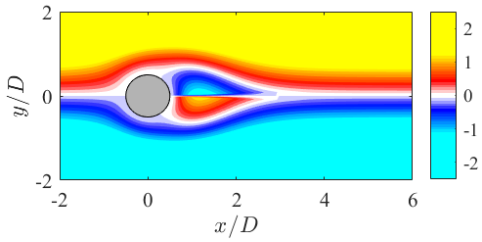

(d) $c = 3$

Figure 23: Contour of Eqn. 83 normalized with $V_\infty R$ for different values of parameter c at $Re = 26$.

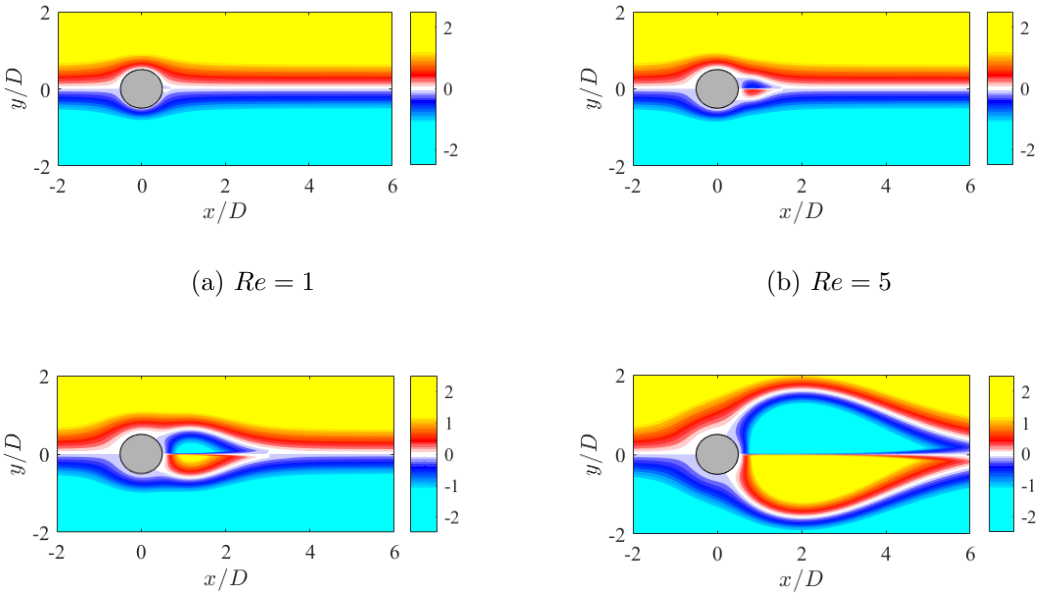

(a) $Re = 1$ (b) $Re = 5$

(c) $Re = 10$ (d) $Re = 130$

Figure 24: Contour of Eqn. 83 normalized with $V_\infty R$ for different Reynolds numbers.

from a symmetrical un-separated flow at $Re = 1$ to a separated flow with a distinct wake at $Re >>> 1$ [5, 15]. It was observed that Eqn. 82 features an overblown re-circulation region at $Re = 1$ that gradually closes up into a symmetrically un-separated flow at $Re \geq 130$. Thus, to reverse this non-physical trend, q should have the form

$$q \approx \frac{130}{Re^2} \tag{84}$$

such that at $Re \leq 1$, an un-separated and symmetric flow is predicted as depicted in Fig. 24. As Re progresses from Fig. 24a to 24c, the re-circulation region also grows progressively in a trend that is consistent with experimentally observed flows. When $Re >>> 1$ in Fig. 24d, the region does not form an unsteady wake but becomes non-physically overblown. However, the width of the separated region in an experimentally observed flow ceases to grow at $Re \approx 50$ when the wake sheds into a vortex street

[5, 15, 64]. Therefore, q is modified with constants b and l into

$$q \approx \frac{130}{Re^2}\left(\frac{bRe}{130}\right)^{\mathrm{e}^{-\frac{l}{Re}}} \tag{85}$$

in which $\mathrm{e}^{-l/Re}$ varies the parenthetical term between one (1) and $bRe/130$ as itself varies between zero for $Re = 1$ and one (1) for $Re >> 1$ respectively. l and b are likely independent of flow conditions. For $l \geq 10$, this behavior is obtainable. For $b \approx 4$, the predicted width of the re-circulation region at $Re \approx 50$ is observed to be qualitatively consistent with experimentally observed flows. Thus, after trials and errors, l and b were chosen to be 10 and 3.9792 respectively. q then becomes

$$\begin{aligned} q &= \frac{130}{Re^2}\left(\frac{3.9792Re}{130}\right)^{\mathrm{e}^{-\frac{10}{Re}}} \\ &= \frac{130}{Re^2}\left(0.03061Re\right)^{\mathrm{e}^{-\frac{10}{Re}}} \quad . \end{aligned} \tag{86}$$

Figure 25 presents a consistence of Eqn.83 with experimentally observed streamlines at $Re = 26$. Table 3 also presents a consistence in the theoretical prediction of the separation points, θ_s (measured from the rear stagnation point), with experimental and numerical trends for varying Re. However, the core of the vortex is smeared and much closer to the centerline in the theoretical result than it is in the experimentally observed flow. Figure 26 also shows a disparity between the surface vorticity distribution predicted from Eqn. 83 and some computational result by Dennis and Shimshoni [8] for a cylinder at $Re = 20$. The theoretical result from Eqn. 83 does not approach zero at the rear of the cylinder where $\theta = 0$ as the numerical result reveals it should. This is non-physical. Therefore, $\psi_{sink/source}$ which produces the recirculating eddies in Eqn. 83 is modified into

Table 3: Comparison of separation point predictions between Eqn.89, CFD results (N-K,K-T,D-C and D-D) and experimental results (Thom, Homann and Grove et al) . N-K: Nieuwstadt and Keller, K-T: Keller and Takami, D-C: Dennis and Chang, D-D: D'Alessio and Dennis

					θ_s (deg)			
Re	Eqn.83	N-K[44]	K-T[44]	D-C[44]	D-D[45]	Patel[66]	Thom[6]	Homann[6]
10	30.41	27.96	29.22	29.79	–	–	≈ 35	–
20	41.76	43.37	43.54	43.54	43.1	43.78	≈ 45	–
30	49.24	49.39	49.85	–	–	–	–	≈ 50
40	54.70	53.34	53.29	53.86	53.0	53.6	≈ 51	–

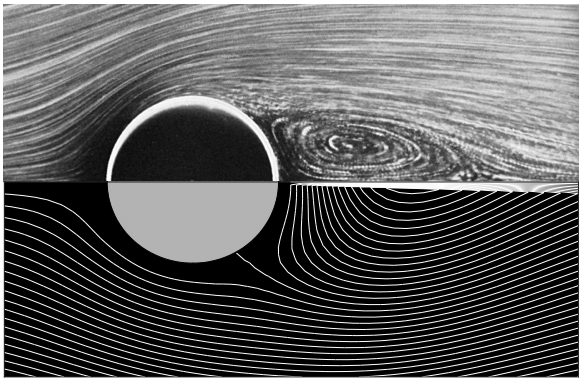

Figure 25: Comparison between an experimentally observed flow (upper image [5, 7]) and contour of Eqn. 83 (lower image) at $Re = 26$.

$$\psi_{sink/source} = V_\infty r\left(1-\frac{R^2}{r^2}\right)\left(\cos\theta - \frac{qRe}{2}\frac{\sin^2\theta\cos\theta\left(\frac{r}{R}-1\right)\frac{R^2}{r^2}}{\sqrt{\left(1-\frac{R^2}{r^2}\right)^2+4\frac{R^2\sin^2\theta}{r^2}+c}}\right) \times \mathrm{e}^{-\left(\frac{qRe\sqrt{\left(1-\frac{R^2}{r^2}\right)^2+4\frac{R^2\sin^2\theta}{r^2}+c}\left(\frac{r}{R}-1\right)}{8}\right)}(\theta+\sigma)\underbrace{(\chi\sin\theta)^{\mathrm{e}^{-\frac{V_\infty t}{r}\left(1-\frac{R}{r}\right)}}}_{new}\ln\left(\frac{r}{R}\right), \tag{87}$$

where

$$\sigma = \begin{cases} -\pi, & \theta \geq 0 \\ \pi, & \theta < 0 \end{cases}$$

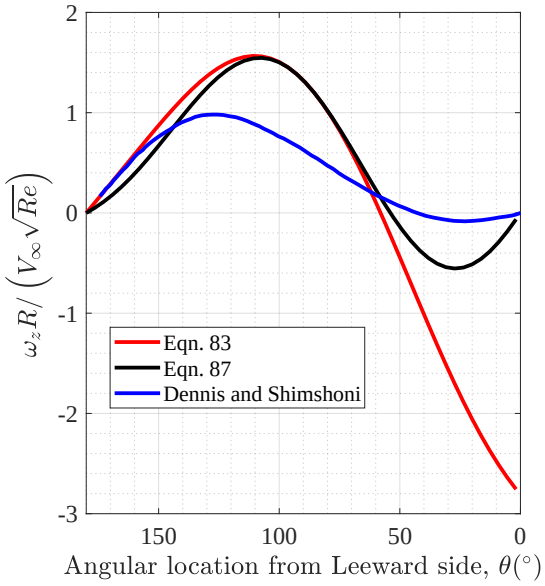

Figure 26: Present $\omega_z R/\left(V_\infty\sqrt{Re}\right)$ distribution from Eqn. 83 compared with computations of Dennis and Shimshoni [8] at $Re = 20$.

and

$$\chi = \begin{cases} 1\ , & \theta \geq 0 \\ -1\ , & \theta < 0\ . \end{cases}$$

In this equation, a product of the new term $(\chi \sin\theta)^{e^{-\frac{V_\infty t}{r}\left(1-\frac{R}{r}\right)}}$ with Eqn. 81 enforces the vanishing of the vorticity at the wall with the sine function when $\theta = 0$. The vorticity distribution obtained from a superposed stream function using Eqn. 87 at a non-dimensional time, $V_\infty t/R \approx 0$ is observed to have achieved this in Fig. 26. Figures 27 to 29 illustrate the effects of the constituent functions in the present modification. In Fig. 27a, the sinusoidal term is further observed to affect the displacement of the wake vortex core from the centreline. However, it disrupts the flow symmetry. The introduction of χ restores the flow symmetry as Figs. 27b, 27c and 28 display. Figure 28 illustrates the velocity field showing the no-slip condition. In Fig. 29a, the sinusoidal term also shortens and rounds the tail of the wake. The flow pattern is

qualitatively consistent with Fig. 29b that presents a transient stage in an experimentally observed cylinder flow development from an impulsive start [10, Fig. 6, p. 279],[33, Fig. 15.5d, p. 426],[7, Fig. 59, p. 36],[15, Fig. 4-50, p. 319].

At the cylinder surface where $r = R$, the modification is

$$\begin{aligned}
&(\chi \sin\theta)^{\mathrm{e}^{-\frac{V_\infty t}{R}\left(1-\frac{R}{R}\right)}} \\
&= (\chi \sin\theta)^{\mathrm{e}^{-0}} \\
&= (\chi \sin\theta)^{1} \\
&= (\chi \sin\theta) \ ,
\end{aligned}$$

and as $r \to \infty$, it is

$$\begin{aligned}
&(\chi \sin\theta)^{\mathrm{e}^{-\frac{V_\infty t}{\infty}}} \\
&= (\chi \sin\theta)^{\mathrm{e}^{-0}} \\
&= (\chi \sin\theta)^{1} \\
&= (\chi \sin\theta) \ .
\end{aligned}$$

Thus, the effect of the sine function is maintained for a constant time. Similarly, for a specific r when $t = 0$, the modification is

$$\begin{aligned}
&(\chi \sin\theta)^{\mathrm{e}^{-\frac{V_\infty \times 0}{r}\left(1-\frac{R}{r}\right)}} \\
&= (\chi \sin\theta)^{\mathrm{e}^{-0}} \\
&= (\chi \sin\theta)^{1} \\
&= (\chi \sin\theta) \ ,
\end{aligned}$$

and the effect of the sine function is maintained. However, as $t \to \infty$, it is

$$\begin{aligned}
&(\chi \sin\theta)^{\mathrm{e}^{-\frac{V_\infty \times \infty}{r}\left(1-\frac{R}{r}\right)}} \\
&= (\chi \sin\theta)^{\mathrm{e}^{-\infty}} \\
&= (\chi \sin\theta)^{0} \\
&= 1 \ ,
\end{aligned}$$

and the effect of the sine function vanishes. Then, the tail of the wake elongates as illustrated in Fig. 29c. Hence, $(\chi \sin\theta)^{\mathrm{e}^{-\frac{V_\infty t}{r}\left(1-\frac{R}{r}\right)}}$ incorporates a temporal and spatial variation of the wake dimension depending on the freestream velocity.

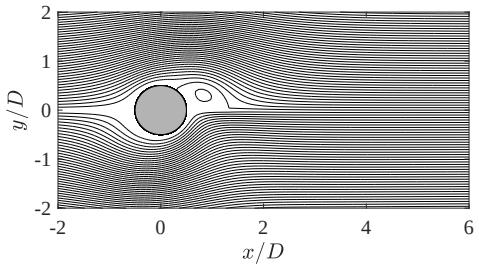

(a) Streamlines showing the effect of $(\theta + \sigma)\sin\theta$.

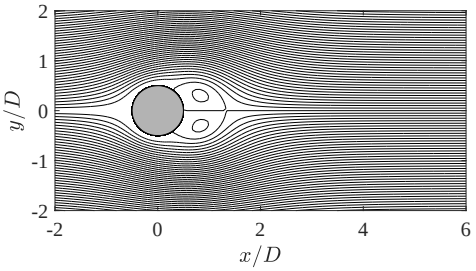

(b) Streamlines showing the effect of $(\theta + \sigma)\,\chi\sin\theta$.

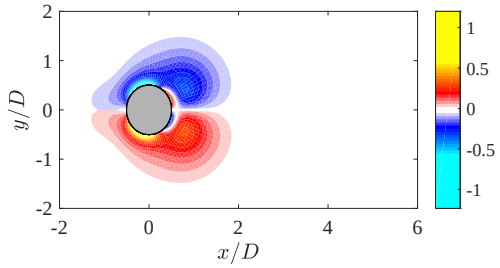

(c) A distribution of $\omega_z R/\left(V_\infty\sqrt{Re}\right)$ showing the effect of $(\theta + \sigma)\,\chi\sin\theta$.

Figure 27: Contour of the superposed stream function with Eqn. 87 showing the effect of the $(\theta + \sigma)\,\chi\sin\theta$ term (Figs. (a) and (b)) and contour of $\omega_z R/\left(V_\infty\sqrt{Re}\right)$ from the same superposition (Fig. (c)) at $Re = 26$ and $V_\infty t/R \approx 0$.

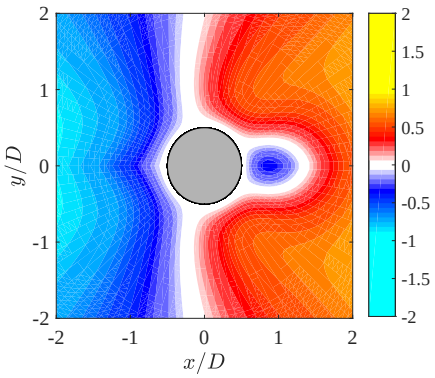

(a) V_r/V_∞

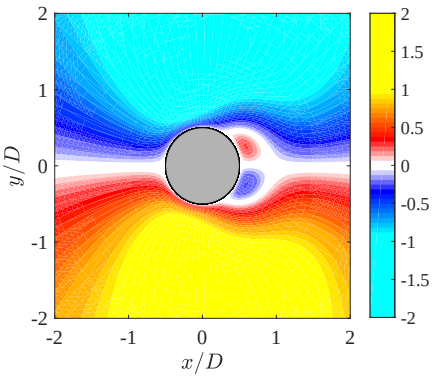

(b) V_θ/V_∞

Figure 28: Contour of the velocity field of Eqn. 87 at $Re = 26$ and $V_\infty t/R \approx 0$ showing the no-slip condition.

The impulsive start of an experimentally observed cylinder flow begins with a nearly inviscid flow that is similar in pattern to the classical potential flow [10, 15, 20, 33]. Then, the boundary layer starts to develop. At $V_\infty t/R \approx 0.35$, separation begins from the rear stagnation point [15]. The resulting region of reverse flow at the rear travels upstream and thickens the boundary layer. This process gives rise to the wake vortices that continue to grow [15,33]. By $V_\infty t/R \approx 1.5$, a large pair of counter-rotating vortices will have emerged [15]. The present theoretical flow pattern in Fig. 29a is not consistent with these experimental observations illustrated in Fig. 29b, but the one in Fig. 29c is consistent with the observations.

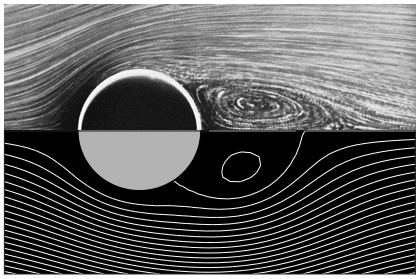

(a) $Re = 26$ ($V_\infty t/R \approx 0$ for present theory (lower image) but unknown for the experimentally observed flow (upper image [5, 7]))

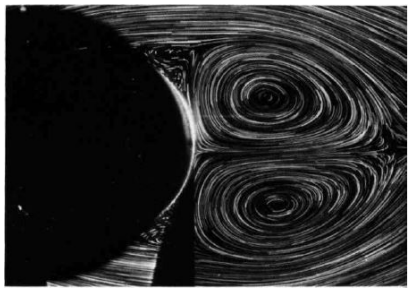

(b) An experimentally observed flow at $Re = 500$ and $V_\infty t/R = 6$ [7].

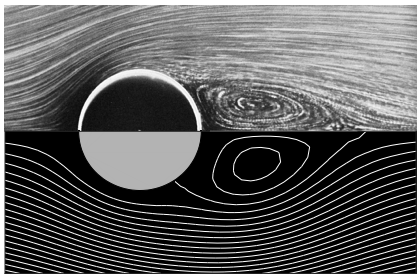

(c) $Re = 26$ ($V_\infty t/R \approx 1.3$ for present theory (lower image) but unknown for the experimentally observed flow (upper image [5, 7]))

Figure 29: The effect of the $(\theta + \sigma)\,(\chi \sin\theta)^{\mathrm{e}^{-\frac{V_\infty t}{r}\left(1-\frac{R}{r}\right)}}$ term in the superposed stream function with Eqn. 87.

Therefore, the basic functional form of B_0 (Eqn. 72) is modified as

$$\begin{aligned} B_0 &= \frac{\Gamma_0}{2\pi}\underbrace{\mathrm{e}^{\left(-\frac{r^2}{4\left(V_\infty^2 t\right)t}\right)}}_{new}\mathrm{e}^{\left(-\frac{r^2}{4\nu t}\right)} \\ &= \frac{\Gamma_0}{2\pi}\mathrm{e}^{-\left(\frac{r^2}{4V_\infty^2 t^2}+\frac{(r-R)^2}{r_c^2}\right)} \\ &= \frac{\Gamma_0}{2\pi}\mathrm{e}^{-\left(\frac{r^2}{4V_\infty^2 t^2}+\frac{qRe\sqrt{\left(1-\frac{R^2}{r^2}\right)^2+4\,\frac{R^2\sin^2\theta}{r^2}}+c\left(\frac{r}{R}-1\right)}{8}\right)}. \end{aligned} \tag{88}$$

The new exponential term in Eqn. 88 is modeled on the previous exponential term in the same equation. The kinematic viscosity, ν that has a dimension of $[\frac{Length \times Length}{Time}]$ is replaced with $V_\infty^2 t$ that has the same dimension. This is because the impulsive start of the flow is a relatively rapid process that is observed to be dependent on the latter (from $V_\infty t/R$) [15, p. 319]. For a specific r, when $t \cong 0$, B_0 is

$$\begin{aligned} B_0 &= \frac{\Gamma_0}{2\pi} \mathrm{e}^{-\left(\frac{r^2}{4V_\infty^2 \times 0} + \frac{qRe\sqrt{\left(1-\frac{R^2}{r^2}\right)^2 + 4\,\frac{R^2 \sin^2\theta}{r^2}} + c\left(\frac{r}{R}-1\right)}{8} \right)} \\ &= \frac{\Gamma_0}{2\pi} \mathrm{e}^{-\infty} \\ &= 0 \,, \end{aligned}$$

and the stream function is

$$\begin{aligned} \psi_{viscous} &= V_\infty r \sin\theta \left(1 - \tfrac{R^2}{r^2}\right) + B_0 \ln\left(\tfrac{r}{R}\right) \\ &= V_\infty r \sin\theta \left(1 - \tfrac{R^2}{r^2}\right) \,. \end{aligned}$$

As $t \to \infty$, B_0 tends to

$$\begin{aligned} B_0 &\to \frac{\Gamma_0}{2\pi} \mathrm{e}^{-\left(\frac{r^2}{4V_\infty^2 \times \infty} + \frac{qRe\sqrt{\left(1-\frac{R^2}{r^2}\right)^2 + 4\,\frac{R^2 \sin^2\theta}{r^2}} + c\left(\frac{r}{R}-1\right)}{8} \right)} \\ &= \frac{\Gamma_0}{2\pi} \mathrm{e}^{-\left(0 + \frac{qRe\sqrt{\left(1-\frac{R^2}{r^2}\right)^2 + 4\,\frac{R^2 \sin^2\theta}{r^2}} + c\left(\frac{r}{R}-1\right)}{8} \right)} \,, \end{aligned}$$

and Eqn. 83 is recovered. However, a singularity occurs at the spatio-temporal origin where $r = t = 0$, and B_0 tends to

$$B_0 \to \frac{\Gamma_0}{2\pi} \mathrm{e}^{-\left(\frac{0}{0}\right)} \,.$$

Then, the superposed stream function is undefined. $r^2/(4V_\infty^2 t^2)$ is not replaced with $(r-R)^2/(4V_\infty^2 t^2)$ in the second row of Eqn. 88 so that the singularity does not occur at the cylinder surface. Therefore, the modified viscous stream function is

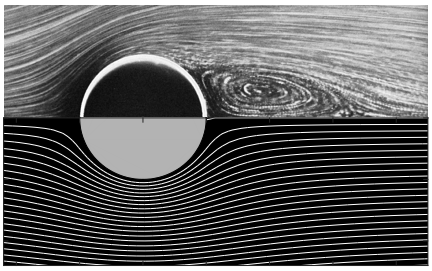

(a) $V_\infty t/R \approx 0$

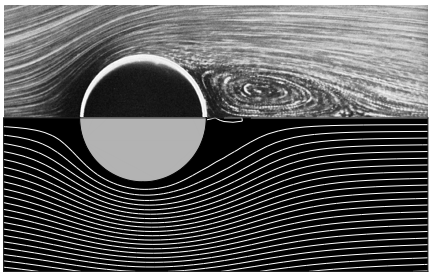

(b) $V_\infty t/R \approx 0.86$

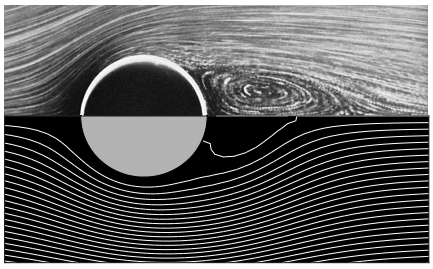

(c) $V_\infty t/R \approx 1.29$

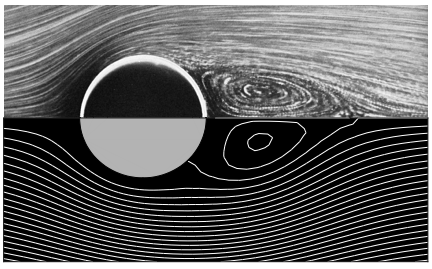

(d) $V_\infty t/R \approx 2.15$

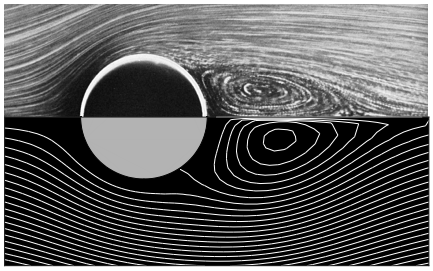

(e) $V_\infty t/R \approx 4.30$

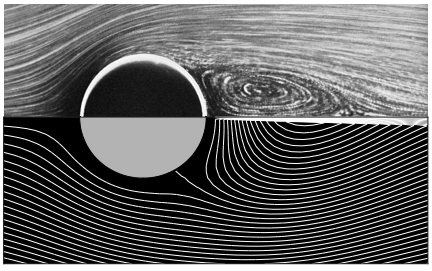

(f) $V_\infty t/R \approx 43$

Figure 30: Contour of Eqn. 89 normalized with $V_\infty R$ for different values of $V_\infty t/R$ at $Re = 26$.

$$
\begin{aligned}
\psi = {} & V_\infty r \sin\theta \left(1 - \tfrac{R^2}{r^2}\right) \\
& - V_\infty r \sin\theta \left(1 + \tfrac{R^2}{r^2}\right) \mathrm{e}^{-\left(\frac{r^2}{4V_\infty^2 t^2} + \frac{qRe\sqrt{\left(1-\frac{R^2}{r^2}\right)^2 + 4\,\frac{R^2\sin^2\theta}{r^2}} + c\left(\frac{r}{R}-1\right)}{8} \right)} \ln\left(\tfrac{r}{R}\right) \\
& + V_\infty r \left(1 - \tfrac{R^2}{r^2}\right) (\theta + \sigma) (\chi \sin\theta)^{\mathrm{e}^{-\frac{V_\infty t}{r}\left(1-\frac{R}{r}\right)}} \\
& \times \left(\cos\theta - \frac{qRe}{2} \frac{\sin^2\theta\cos\theta\left(\frac{r}{R}-1\right)\frac{R^2}{r^2}}{\sqrt{\left(1-\frac{R^2}{r^2}\right)^2 + 4\,\frac{R^2\sin^2\theta}{r^2}} + c} \right) \mathrm{e}^{-\left(\frac{r^2}{4V_\infty^2 t^2} + \frac{qRe\sqrt{\left(1-\frac{R^2}{r^2}\right)^2 + 4\,\frac{R^2\sin^2\theta}{r^2}} + c\left(\frac{r}{R}-1\right)}{8} \right)} \ln\left(\tfrac{r}{R}\right)
\end{aligned}
\tag{89}
$$

where

$$
\sigma = \begin{cases} -\pi, & \theta \geq 0 \\ \pi, & \theta < 0 \end{cases}
$$

and

$$
\chi = \begin{cases} 1\ , & \theta \geq 0 \\ -1\ , & \theta < 0\ . \end{cases}
$$

This is illustrated in Fig. 30 for different values of $V_\infty t/R$ and compared to an experimentally observed flow at $Re = 26$. The experimentally observed flow in these figures are the same, and the time is not reported from the source [7, p. 28]. In Fig. 30a, the theoretical flow is starting up with an unseparated symmetrical flow pattern. At $V_\infty t/R \approx 0.86$ in Fig. 30b, the flow has separated. The vortices form and continue to grow. The present theoretical flow patterns in Figs. 30d and 30e are the most consistent with the photograph of the experimentally observed flow. At a much later time in Fig. 30f, a steady state has been attained. Thus, this figure is similar to Fig. 25 that is obtained with a time-independent Eqn. 83.

2.1.4.2 The Perifocal Stream Function

In the subsequent sections, a gravity analogy is used to describe the affinity between a fluid element and the cylinder wall. This is to derive equations for the predictions of the points of separation, transition, and reattachment, as well as the thickness of

the boundary layer. The analogy introduces the perifocal frame of fluid motion and stream function that are discussed here.

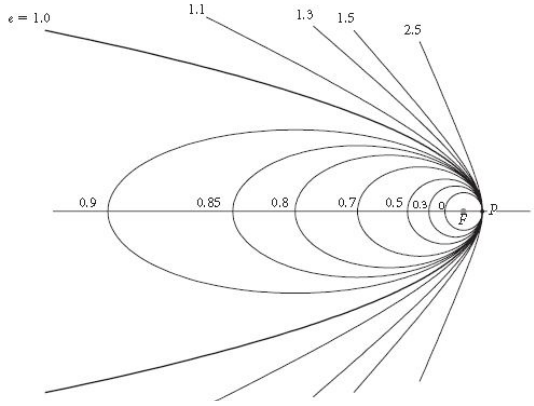

(a) Orbits of various eccentricities having a common focus, F, and a periapsis, P [67].

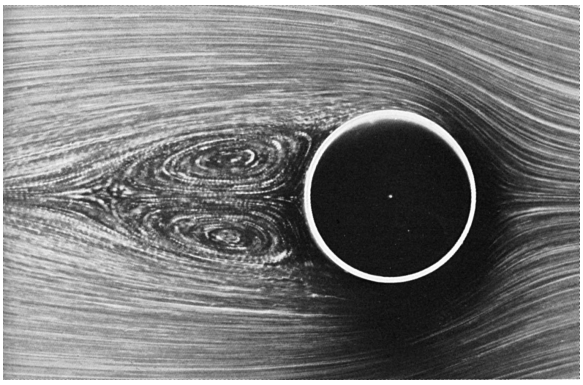

(b) The streamlines of an experimentally observed flow at $Re = 26$ [7].

Figure 31: The reasoning behind the gravity analogy.

Figure 31a presents different orbits, with corresponding eccentricity values ε (e in Fig. 31a), an orbiting body can occupy as it moves under mutual gravitation with a bigger dominant body at the focus, F. The eccentricity is a measure of the circularity of an orbit [67]. The orbits are solutions to the two-body problem in astrodynamics [67]. Depending on the sum of its kinetic energy and potential energy with respect to the focus, an orbiting body launched from the periapsis, P, may occupy a circular or an elliptic orbit ($0 < \varepsilon < 1$) and remain bound under the mutual gravitational interaction with the dominant body at F. It may also occupy either a parabolic ($\varepsilon = 1$) or a hyperbolic ($\varepsilon > 1$) orbit and coast to infinity away from the dominant body. These orbits are pathlines of the orbiting body [67]. Similarly, Fig. 31b presents the fluid element pathlines in an experimentally observed flow at $Re = 26$. A fluid element arriving at the stagnation point remains bound to the influence of the cylinder as it flows around it ($0 < \varepsilon < 1$) before it eventually separates and advects to infinity ($\varepsilon \geq 1$). This behavior is assumed to be dependent on the sum of the kinetic energy

of the fluid element and its potential energy with respect to the cylinder.

The gravitational field of a body (the cylinder in the present case) is given as

$$\Phi(r,\theta,\varphi) = \frac{\mu_g}{r}\left[1 + \sum_{n=1}^{\infty}\left(\frac{R_B}{r}\right)^n \sum_{m=1}^{n}\frac{1}{2^n n!}\frac{d^{n+m}}{d(\sin\varphi)^{n+m}}\left(\sin^2\varphi - 1\right)^n \right. \\ \left. \left(C_{n,m}\left(\cos(m\theta)\cos(m\varphi)\right) + S_{n,m}\left(\sin(m\theta)\cos(m\varphi)\right)\right)\right], \tag{90}$$

where the gravitational parameter, $\mu_g \approx G\mathcal{M}_B$ [68]. In the foregoing context, this is referred to as the wake-analogy factor. Equation 90 is a separated variables solution of the Laplace equation in the spherical polar coordinate system [68, 69]. $C_{n,m}$ and $S_{n,m}$ are unique mass coefficients that are determined empirically [69]. However, for a spherically symmetric mass distribution, the gravitational potential is simply

$$\Phi(r) = -\frac{\mu_g}{r}\,. \tag{91}$$

This is employed as a suitable potential for the center plane of the cylinder. The recommended value of the gravitational constant, G, is $6.67408(31) \times 10^{-11} m^3 kg^{-1} s^{-2}$ [70]. This means that the wake-analogy factor is a very small number for all practical purposes of the cylinder flow. Thus, an arbitrary value of the cylinder mass, $\mathcal{M}_B$, and its actual distribution will not affect the theoretical flow. This is consistent with dimensional analyses that are in agreement with experimental and numerical observations [5, 15]. Therefore, the use of Eqn. 91 for the analogy is justified. Since the differentials of the gravitational potential give the components of gravitational acceleration, the gravitational velocity potential is derived by integrating the gravitational potential in time (t_ϱ) in the perifocal frame. The perifocal frame is a planar frame that is centered at the focus, F, of an orbit as illustrated in Fig. 32 (refer to Curtis [67, p. 108] for a discussion on perifocal frames). The orbit is depicted with the thick curvilinear red arrowhead in this figure. For a steady and uniform mass distribution in the cylinder, the gravitational velocity potential is thus obtained as

$$\phi_{perifocal}(r, t_\varrho) = \int_0^{\mathcal{T}} \Phi(r)\, dt_\varrho = -\frac{\mu_g \mathcal{T}}{r} \tag{92}$$

where $\mathcal{T}$ is the orbital period.

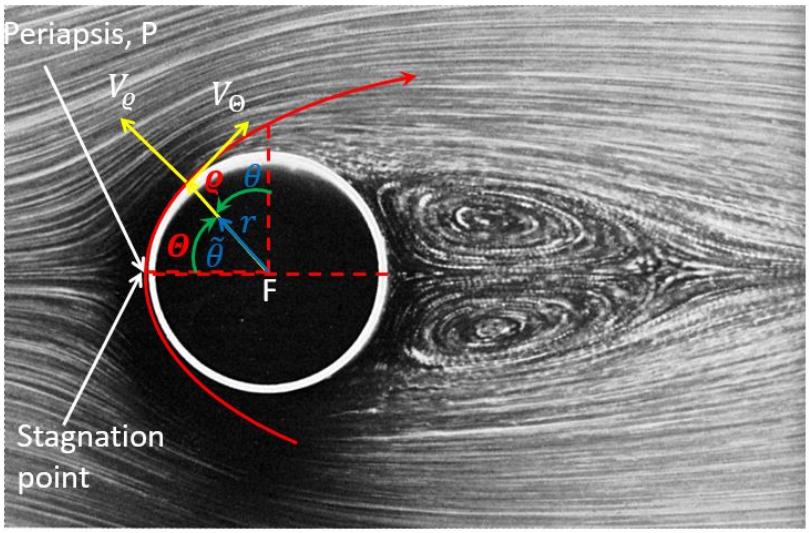

Figure 32: The perifocal frame of fluid motion overlaid on an experimentally observed flow at $Re = 26$ [7].

The path of two bodies moving solely under the influence of mutual gravity is a Keplarian orbit (conic section) defined by

$$\varrho = \frac{h^2}{\mu_g} \frac{1}{1 + \varepsilon \cos \Theta} \, . \tag{93}$$

The origin coincides with the center of mass of the two-body system that is located at one of the foci of the orbit [67, 68]. Equation 93 is also a solution of Newton's second law of motion. It has an inherent assumption that there are no influences from other bodies on the two-body system [67, 68]. Therefore, the foregoing analogy is most consistent with the conservation of the momentum of a perfect gas flowing about a cylinder. A perfect gas is one for which negligible or no mutual interactions are assumed between the molecules [71]. For a fluid particle and the cylinder, the origin of the two-body system is essentially the cylinder's center of mass. This is assumed to be coincident with the geometric center of the cylinder in Fig. 32. The stagnation point and the periapsis are also coincident. In Eqn. 93, ϱ is the radial coordinate or orbital path, h is the specific angular momentum of the orbiting body,

ε is the eccentricity of the orbit, Θ is the circumferential coordinate or true anomaly of the orbit. In the perifocal frame, the particle's velocity components are defined as [67]

$$\begin{aligned} V_\Theta &= \frac{\mu_g}{h}\left(1+\varepsilon\cos\Theta\right) = -\frac{\partial\Psi}{\partial\varrho} \\ V_\varrho &= \frac{\mu_g}{h}\varepsilon\sin\Theta = \frac{1}{\varrho}\frac{\partial\Psi}{\partial\Theta}\,. \end{aligned} \tag{94}$$

The positive directions of these velocity components are illustrated in Fig. 32. Equation 94 gives an indication of a stream function that identically satisfies the steady continuity equation in the perifocal frame of reference as

$$\begin{aligned} \nabla\cdot\mathbf{V} &= \frac{1}{\varrho}\frac{\partial(\varrho V_\varrho)}{\partial\varrho} + \frac{1}{\varrho}\frac{\partial V_\Theta}{\partial\Theta} \\ &= \frac{V_\varrho}{\varrho} + \frac{\partial V_\varrho}{\partial\varrho} + \frac{1}{\varrho}\frac{\partial V_\Theta}{\partial\Theta} \\ &= \frac{1}{\varrho^2}\frac{\partial\Psi}{\partial\Theta} - \frac{1}{\varrho^2}\frac{\partial\Psi}{\partial\Theta} + \frac{1}{\varrho}\frac{\partial^2\Psi}{\partial\varrho\partial\Theta} - \frac{1}{\varrho}\frac{\partial^2\Psi}{\partial\Theta\partial\varrho} \\ &= 0 \quad (t\geq 0). \end{aligned} \tag{95}$$

This perifocal stream function, Ψ, is integrated to be

$$\Psi = -\frac{\mu_g\varrho}{h}(1+\varepsilon\cos\Theta)\,. \tag{96}$$

Applying the Keplerian orbit eccentricity [67],

$$\varepsilon = \sqrt{1+\frac{h^2}{\mu_g^2}(V^2-\frac{2\mu_g}{\varrho})}\,, \tag{97}$$

and the orbital circumferential coordinate variable or true anomaly [67],

$$\Theta = \cos^{-1}\left[\frac{1}{\varepsilon}\left(\frac{h^2}{\mu_g\varrho}-1\right)\right], \tag{98}$$

the expression for the perifocal stream function simplifies to

$$\Psi = -h\,. \tag{99}$$

The orbital period expression is given as [67]

$$\mathcal{T} = \frac{2\pi}{\mu_g^2}\left(\frac{h}{\sqrt{1-\varepsilon^2}}\right)^3\,.$$

This simplifies to

$$\mathcal{T} = 2\pi\mu_g \left(\frac{2\mu_g}{\varrho} - V^2 \right)^{-\frac{3}{2}} \tag{100}$$

using Eqn. 97. The velocity in this expression is obtained as follows

$$V = \sqrt{\begin{array}{l} \left(\frac{1}{r} \left[\frac{\partial \psi_{NLF}}{\partial \theta} + \frac{\partial \psi_{vortex}}{\partial \theta} + \frac{\partial \psi_{sink/source}}{\partial \theta} \right] \right)^2 \\ + \left(- \left[\frac{\partial \psi_{NLF}}{\partial r} + \frac{\partial \psi_{vortex}}{\partial r} + \frac{\partial \psi_{sink/source}}{\partial r} \right] \right)^2 \end{array}} \ . \tag{101}$$

The origins of the body axis and the perifocal frame are coincident as illustrated in Fig. 32, and the radial distance around the cylinder, r, is equivalent to the orbital radial coordinate, ϱ. Thus, the specific angular momentum of the fluid particle in the body axis is

$$\mathbf{h} = \mathbf{r} \times \mathbf{V} \ ,$$

and the magnitude is

$$h = rV_\theta \ . \tag{102}$$

Differentiating Eqn. 92 gives the gravitational circumferential velocity component around the cylinder as

$$V_\theta = \frac{1}{r} \frac{\partial}{\partial \theta} \left(\phi_{perifocal} \right) \ . \tag{103}$$

Hence, the following expression

$$\psi_{perifocal} = \Psi = -h = -\frac{\partial}{\partial \theta} \left(\phi_{perifocal} \right) \tag{104}$$

is derived for the perifocal stream function.

2.1.4.3 Viscous Two-Dimensional Stream Function

The summary of the forgoing superposition is the viscous and time-dependent stream function of the uniform flow on a circular cylinder that is

$$\begin{aligned}
&\psi = \psi_{NLF} + \psi_{vortex} + \psi_{sink/source} + \psi_{perifocal} \\
&= V_\infty r \sin\theta \left(1 - \tfrac{R^2}{r^2}\right) \\
&-V_\infty r \sin\theta \left(1 + \tfrac{R^2}{r^2}\right) \mathrm{e}^{-\left(\frac{r^2}{4V_\infty^2 t^2} + \frac{qRe\sqrt{\left(1-\frac{R^2}{r^2}\right)^2 + 4\,\frac{R^2\sin^2\theta}{r^2}} + c\left(\frac{r}{R}-1\right)}{8}\right)} \ln\left(\tfrac{r}{R}\right) \\
&+V_\infty r \left(1 - \tfrac{R^2}{r^2}\right) (\theta + \sigma) (\chi \sin\theta)^{\mathrm{e}^{-\frac{V_\infty t}{r}\left(1-\frac{R}{r}\right)}} \\
&\times \left(\cos\theta - \tfrac{qRe}{2} \frac{\sin^2\theta\cos\theta\left(\frac{r}{R}-1\right)\frac{R^2}{r^2}}{\sqrt{\left(1-\frac{R^2}{r^2}\right)^2 + 4\,\frac{R^2\sin^2\theta}{r^2}} + c}\right) \mathrm{e}^{-\left(\frac{r^2}{4V_\infty^2 t^2} + \frac{qRe\sqrt{\left(1-\frac{R^2}{r^2}\right)^2 + 4\,\frac{R^2\sin^2\theta}{r^2}} + c\left(\frac{r}{R}-1\right)}{8}\right)} \ln\left(\tfrac{r}{R}\right) \\
&-\frac{\partial}{\partial\theta}\left(\phi_{perifocal}\right),
\end{aligned} \tag{105}$$

where

$$\sigma = \begin{cases} -\pi, & \theta \geq 0 \\ \pi, & \theta < 0 \end{cases}$$

and

$$\chi = \begin{cases} 1\ , & \theta \geq 0 \\ -1\ , & \theta < 0\ . \end{cases}$$

This function resolves the boundary layer and produces a stationary pair of counter-rotating vortices depending on time and/or *Re*.

2.1.5 Viscous Incompressible Two-Dimensional Stream Function With Vortex Shedding

As *Re* increases to about 50, the experimentally observed flow around the circular cylinder undergoes a Hopf bifurcation, and the stationary counter-rotating vortices begin to alternately shed into the von Kármán vortex street [5, 7, 9, 15, 46]. This is

shown in Fig. 33 that presents an experimentally observed flow of water past a cylinder at $Re = 140$. The integrated streaklines of the flow were revealed by electrolytic precipitation of a white colloidal smoke that was illuminated by a sheet of light [7]. The growth of the street width downstream of the cylinder is highlighted with the red arrowheads. Streaklines are traces of all fluid particles that have flowed continuously through a specific spatial location. They are only coincident with streamlines in a steady flow or region of a flow as illustrated in Fig. 34a [5, 15, 46, 59]. The photograph was taken with a simultaneous usage of the aluminum flake and electrolytic precipitation methods that show streamlines and streaklines respectively [59]. The brighter streakline patterns are observed to match the darker background streamlines in Fig. 34a. This is not the case in the unsteady vortex shedding phenomenon whose streamlines and streaklines in Fig. 34b were revealed with the same methods in Fig. 34a [46, 59]. It can be seen that some of the vortex features illuminated by the streamlines are not found on the streaklines [59]. However, both the streamline and the streakline patterns in Fig. 34c are correlated and provide a good visualization of the alternately shed vortices and their staggered location in the street. The streamlines in Fig. 34c were also revealed with aluminum flakes, but the streaklines were revealed with condensed milk [59].

Theoretical simulations of the shedding process are difficult when the street is from a bluff body. Föppl attempted to theorize the stable separated flow before the bifurcation by placing two vortices behind the cylinder [9, 46] as illustrated in Fig. 35a. However, the ensuing surface pressure distribution in Fig. 35b is nonphysical [9]. Talaei's and Garrett's [31] analytical solution of the asymmetric flow around a fast moving sphere exhibits some eddies in the wake region, but these eddies do not alternately shed. Others have also treated the vortex street as staggered double row point vortices or vortex patch arrays [46].

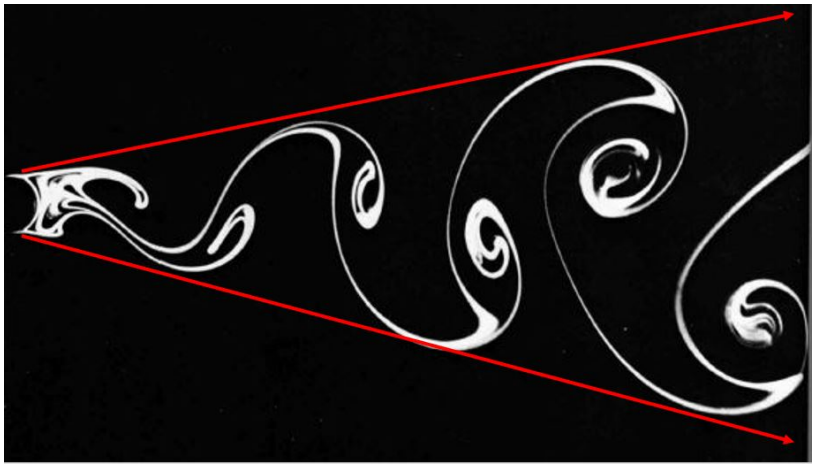

Figure 33: A Kármán vortex street behind a circular cylinder at $Re = 140$ [7].

In the present study, Eqn. 105 is modified to model the vortex street. The exponential term of $\psi_{sink/source}$ (Eqn. 87) which produces the stationary bubble in the flow is exploited to introduce spatial and temporal periodicity in the wake. This is achieved by introducing constants ζ and ι in $\psi_{sink/source}$ as

$$\begin{aligned}
&\psi_{vortexshedding} \\
&= V_\infty r\left(1-\frac{R^2}{r^2}\right)\left(\cos\theta - \frac{\overset{\text{new}}{\downarrow}\ \zeta\ Re}{2}\,\frac{\sin^2\theta\cos\theta\left(\frac{r}{R}-1\right)\frac{R^2}{r^2}}{\sqrt{\left(1-\frac{R^2}{r^2}\right)^2+4\,\frac{R^2\sin^2\theta}{r^2}}+c}\right)(\theta+\sigma)\,(\chi\sin\theta)^{\mathrm{e}^{-\frac{V_\infty t}{r}\left(1-\frac{R}{r}\right)}} \\
&\quad\times \mathrm{e}^{-\left(\begin{smallmatrix}\iota\\ \uparrow\\ \text{new}\end{smallmatrix}+\frac{r^2}{4V_\infty^2 t^2}\right)-\left(\frac{\overset{\text{new}}{\downarrow}\ \zeta\ Re\sqrt{\left(1-\frac{R^2}{r^2}\right)^2+4\,\frac{R^2\sin^2\theta}{r^2}}+c\left(\frac{r}{R}-1\right)}{8}\right)\ln\left(\frac{r}{R}\right)}.
\end{aligned} \tag{106}$$

ι triggers the vortex shedding at $Re \sim 50$. It is likely only dependent on Re. Its function as a bifurcator in the exponential term suggests that it has an inverse relationship with Re as

$$\iota \propto \frac{1}{Re}\,.$$

The constant of proportionality is chosen such that at a specific t and r in Eqn. 106, ι becomes a big number that dominates the exponential argument and makes $\psi_{vortexshedding}$ vanish as Re approaches one. However, the influence of ι should diminish at about $Re = 50$ when the shedding begins. This mode of operation in the exponential term

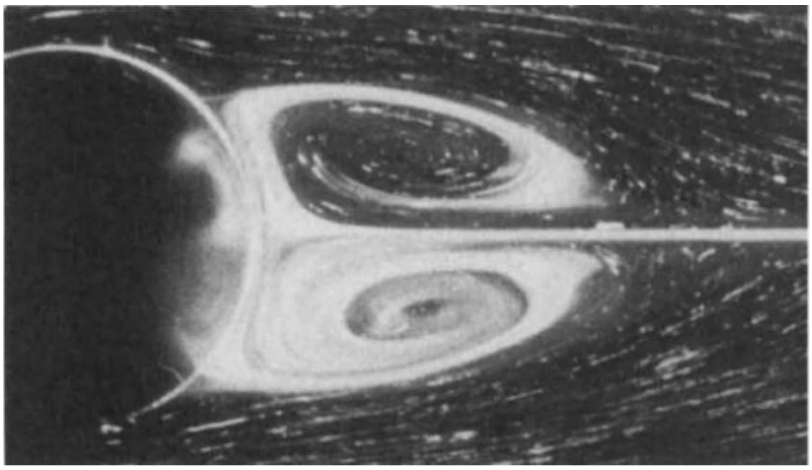

(a) A stable pair of counter-rotating vortices behind a circular cylinder at $Re = 22$ [59].

(b) A Kármán vortex street behind a circular cylinder at $Re = 100$ [46, 59].

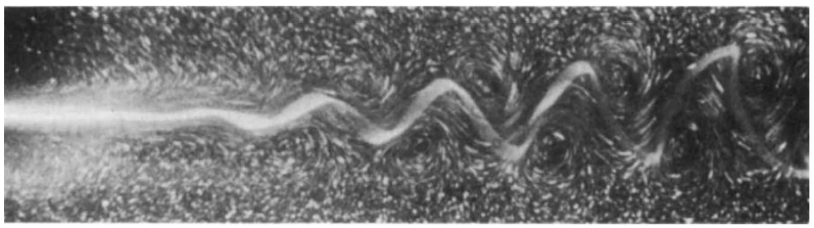

(c) A Kármán vortex street behind a flat plate at zero inclination to the freestream [59].

Figure 34: The differences between streamlines and streaklines.

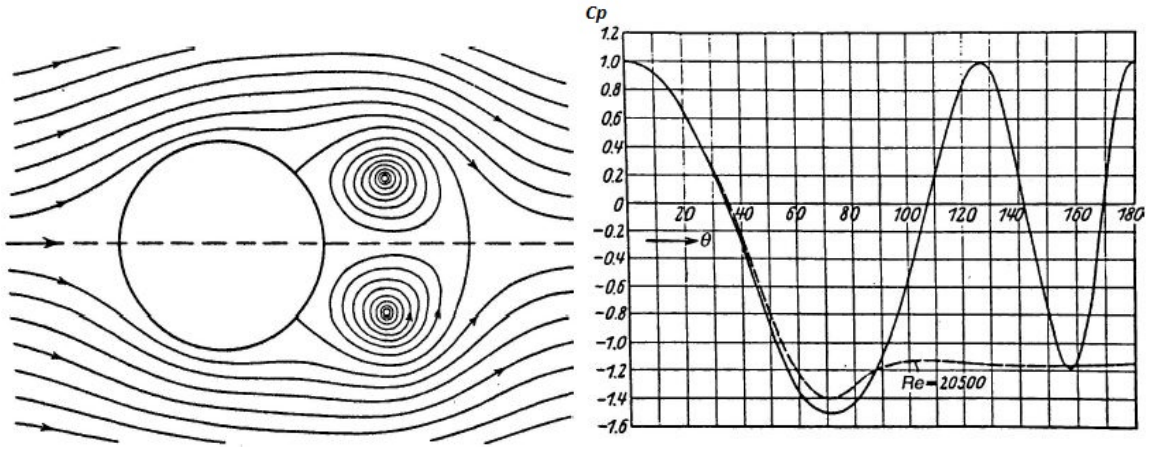

(a) The Föppl streamline pattern.

(b) The Föppl C_p distribution compared with experiment.

Figure 35: The Föppl stationary vortex pair behind a circular cylinder [9].

is also dependent on the relative value of ζ that controls the divergence of the vortex street width downstream of the cylinder. ζ is similar to q in Eqn. 83. When $q = 130/Re^2$ in Eqn. 83, it is observed that it grows the width of the stationary vortices with progressing Re. This is shown in Fig. 24. Therefore, ζ is set to be

$$\zeta = \frac{130}{Re^2} \, .$$

Thus, ι is $O(130/Re)$. It was observed that setting ι as

$$\iota = \frac{125}{Re}$$

ensures that the bifurcation begins at about $Re = 50$.

Once the bifurcation starts, r^2 in the exponent dissipates $\psi_{vortexshedding}$ as $r \to \infty$, and $4V_\infty^2 t^2$ advances its extent away from the cylinder at the freestream velocity. Figure 36 presents the contour of Eqn. 106 for two functional relationships between ζ and Re.

The absolute flow domain in Fig. 36 is

$$x = r\cos\theta \quad y = r\sin\theta$$

which originates at the center of the cylinder. The radial coordinate of a time-dependent relative domain, $r(t)$, that advances from left to right with velocity components

$$\begin{aligned}
V_x &= \frac{\partial \psi}{\partial y}_{NLF} \\
&= \frac{\partial \psi}{\partial r}\frac{\partial r}{\partial y} + \frac{\partial \psi}{r\partial \theta}\frac{r\partial \theta}{\partial y} \\
&= -V_\theta \sin\theta + V_r \cos\theta \\
&= -\left(-V_\infty \sin\theta \left(1 + \tfrac{R^2}{r^2}\right)\right)\sin\theta + \left(V_\infty \cos\theta \left(1 - \tfrac{R^2}{r^2}\right)\right)\cos\theta \\
&= V_\infty \left(1 + \tfrac{R^2}{r^2}\left(\sin^2\theta - \cos^2\theta\right)\right) \ ,
\end{aligned}$$

and

$$\begin{aligned}
V_y &= -\frac{\partial \psi}{\partial x}_{NLF} \\
&= -\left(\frac{\partial \psi}{\partial r}\frac{\partial r}{\partial x} + \frac{\partial \psi}{r\partial \theta}\frac{r\partial \theta}{\partial x}\right) \\
&= V_\theta \cos\theta + V_r \sin\theta \\
&= \left(-V_\infty \sin\theta \left(1 + \tfrac{R^2}{r^2}\right)\right)\cos\theta + \left(V_\infty \cos\theta \left(1 - \tfrac{R^2}{r^2}\right)\right)\sin\theta \\
&= V_\infty \left(\tfrac{R^2}{r^2}\sin\theta\cos\theta\right) \ ,
\end{aligned}$$

is constructed as

$$\begin{aligned}
r(t) &= \sqrt{\left(x - V_x t\right)^2 + \left(y - V_y t\right)^2} \\
&= r\sqrt{\left(\sin\theta - \tfrac{V_\infty t}{r}\left(\tfrac{R^2}{r^2}\sin\theta\cos\theta\right)\right)^2 + \left(\cos\theta - \tfrac{V_\infty t}{r}\left(1 + \tfrac{R^2}{r^2}\left(\sin^2\theta - \cos^2\theta\right)\right)\right)^2} \ .
\end{aligned} \tag{107}$$

This is used to advect the vortices downstream. So Eqn. 106 is modified with $r(t)$ into

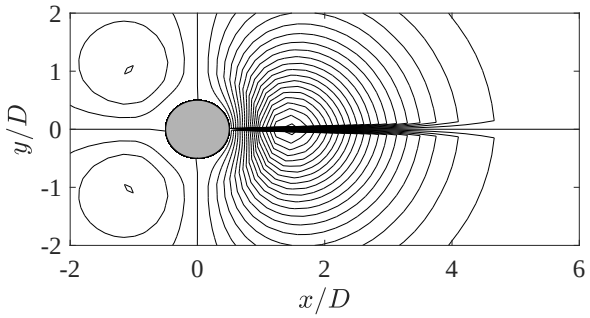

(a) $\zeta = \dfrac{130}{Re^2}\left(0.03061Re\right)^{\mathrm{e}^{-10/Re}}$

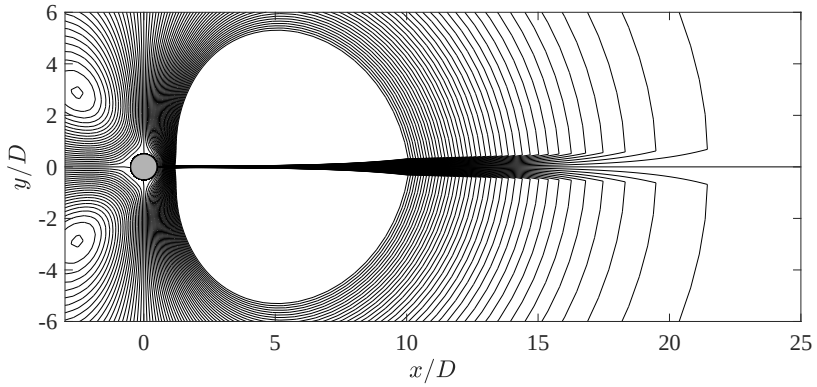

(b) $\zeta = \dfrac{130}{Re^2}$

Figure 36: Contour of Eqn. 106 normalized by $V_\infty R$ at $Re = 140$ and $V_\infty t/R \approx 165.3$ for different values of ζ.

$$
\begin{aligned}
&\psi_{vortexshedding} \\
&= V_\infty r\left(1-\tfrac{R^2}{r^2}\right)\left(\cos\theta-\tfrac{\zeta Re}{2}\,\frac{\sin^2\theta\cos\theta\left(\frac{r}{R}-1\right)\frac{R^2}{r^2}}{\sqrt{\left(1-\frac{R^2}{r^2}\right)^2+4\,\frac{R^2\sin^2\theta}{r^2}}+c}\right)(\theta+\sigma)\left(\chi\sin\theta\right)^{\mathrm{e}^{-\frac{V_\infty t}{r}\left(1-\frac{R}{r}\right)}} \\
&\quad -\left(\iota+\tfrac{r^2}{4V_\infty^2t^2}\right)-\underbrace{\left(\frac{\zeta Re\sqrt{\left(1-\frac{R^2}{r^2}\right)^2+4\,\frac{R^2\sin^2\theta}{r^2}}+c\left(\frac{\overset{\text{new}}{\downarrow}}{\frac{r\,(t)}{R}}-1\right)}{8}\right)}\ln\left(\tfrac{r}{R}\right). \\
&\quad \times\mathrm{e}
\end{aligned}
\tag{108}
$$

Then, the under-braced argument of the exponential term in Eqn. 108 is multiplied with $\eta^{\frac{\mathrm{e}^{-\frac{r^2}{4V_\infty^2t^2}}}{2}}$ to give

$$
\begin{aligned}
&\psi_{vortexshedding} \\
&= V_\infty r\left(1-\tfrac{R^2}{r^2}\right)\left(\cos\theta-\tfrac{\zeta Re}{2}\,\frac{\sin^2\theta\cos\theta\left(\frac{r}{R}-1\right)\frac{R^2}{r^2}}{\sqrt{\left(1-\frac{R^2}{r^2}\right)^2+4\,\frac{R^2\sin^2\theta}{r^2}}+c}\right)(\theta+\sigma)\left(\chi\sin\theta\right)^{\mathrm{e}^{-\frac{V_\infty t}{r}\left(1-\frac{R}{r}\right)}} \\
&\quad -\left(\iota+\tfrac{r^2}{4V_\infty^2t^2}\right)-\underbrace{\left(\frac{\zeta Re\sqrt{\left(1-\frac{R^2}{r^2}\right)^2+4\,\frac{R^2\sin^2\theta}{r^2}}+c\left(\frac{r(t)}{R}-1\right)}{8}\right)\left(\eta^{\frac{\mathrm{e}^{-\frac{r^2}{4V_\infty^2t^2}}}{2}}\right)}\ln\left(\tfrac{r}{R}\right), \\
&\quad \times\mathrm{e}
\end{aligned}
\tag{109}
$$

where

$$
\eta=\begin{cases}1\ , & \theta>\frac{\pi}{2}\ ||\ \ \theta<-\frac{\pi}{2}\\ -1\ , & \frac{\pi}{2}\ \geq\ \ \theta\geq\ -\frac{\pi}{2}\ .\end{cases}
$$

This is to introduce spatio-temporal periodicity into $\psi_{vortexshedding}$ when $\eta^{\frac{\mathrm{e}^{-\frac{r^2}{4V_\infty^2t^2}}}{2}}$ becomes a complex number. It takes advantage of the fact that for a generic time-varying function, $F(t)$, with a complex signal frequency, f_1+if_2, Euler's formula [62, p. 119] gives

$$
\mathrm{e}^{-(f_1+if_2)F(t)}=\mathrm{e}^{-f_1F(t)}\left(\cos\left(f_2F(t)\right)-i\sin\left(f_2F(t)\right)\right)\ . \tag{110}
$$

In the windward half of the flow domain $\eta = 1$, and

$$\eta^{\frac{e^{-\frac{r^2}{4V_\infty^2 t^2}}}{2}} = (1)^{\frac{e^{-\frac{r^2}{4V_\infty^2 t^2}}}{2}} = 1$$

always. This agrees with the actual physics of the flow since no vortices are shed in this flow region. However, the value of $\eta^{\frac{e^{-\frac{r^2}{4V_\infty^2 t^2}}}{2}}$ is conditional in the leeward half of the domain where $\eta = -1$. When $t \cong 0$ and $R \leq r \leq \infty$,

$$\eta^{\frac{e^{-\frac{r^2}{4V_\infty^2 t^2}}}{2}} = (-1)^{\frac{e^{-\frac{r^2}{4V_\infty^2 (0)^2}} \to 0}{2}} = 1 \, .$$

This corresponds to the start-up of the flow prior to the vortex-shedding. After the vortex-shedding begins, the vortices advect into a uniform freestream flow far downstream of the cylinder. Thus, when $0 < t < \infty$ as $r \to \infty$

$$\eta^{\frac{e^{-\frac{r^2}{4V_\infty^2 t^2}}}{2}} \to (-1)^{\frac{e^{-\frac{\infty^2}{4V_\infty^2 t^2}} \to 0}{2}} = 1 \, ,$$

and the freestream flow is recovered. As t progressively grows to infinity, the ratio $r^2/(4V_\infty^2 t^2)$ at any specific location, r, continues to approach zero, and

$$\eta^{\frac{e^{-\frac{r^2}{4V_\infty^2 t^2}}}{2}} = (-1)^{\frac{e^{-\frac{r^2}{4V_\infty^2 (\infty)^2}} \to 1}{2}} = \sqrt{-1} = i \, .$$

Then, the under-braced exponential argument in Eqn. 109 becomes a complex function that is periodic in both space and time because of $r(t)$. By comparing the under-braced exponential argument of Eqn. 109 to the left hand side of Eqn. 110, it is seen that

$$\begin{aligned} F(t) &\equiv \left(\frac{\zeta Re \sqrt{\left(1 - \frac{R^2}{r^2}\right)^2 + 4 \frac{R^2 \sin^2 \theta}{r^2}} + c\left(\frac{r(t)}{R} - 1\right)}{8} \right) \\ i &\equiv \eta^{\frac{e^{-\frac{r^2}{4V_\infty^2 t^2}}}{2}} \\ f_2 &\equiv 1 \, . \end{aligned} \tag{111}$$

f_1 is a damping function that is to be determined. These functions are dimensionless. Figure 37a, in which the flow is still from left to right, illustrates some of the effects

of η in the flow domain. However, the experimentally observed flow in Fig. 33 is attached on the windward face of the cylinder until it separates and starts to shed around the crests of the cylinder. The shedding and periodicity of the flow start from the crests and get pronounced (less damped) towards the rear stagnation point. These suggest that the flow periodicity in the immediate vicinity of the cylinder surface is controlled by a damping function that is dependent on the circumferential coordinate, θ. It is assumed that the value of the function ranges from 0 (no damping) at the rear stagnation point (where $\theta = 0$) to 1 (full damping) at either of the crests (where $\theta = \pm\pi/2$). The $\sin^2\theta$ is a function with this behavior. Thus, f_1 is assumed to be equivalent to $\sin^2\theta$, and Eqn. 109 is modified into

$$\begin{aligned}
&\psi_{vortexshedding} \\
&= V_\infty r\left(1-\tfrac{R^2}{r^2}\right)\left(\cos\theta - \frac{\zeta Re}{2}\,\frac{\sin^2\theta\cos\theta\left(\frac{r}{R}-1\right)\frac{R^2}{r^2}}{\sqrt{\left(1-\frac{R^2}{r^2}\right)^2+4\,\frac{R^2\sin^2\theta}{r^2}}+c}\right)(\theta+\sigma)\,(\chi\sin\theta)^{\mathrm{e}^{-\frac{V_\infty t}{r}\left(1-\frac{R}{r}\right)}} \\
&\quad\times \mathrm{e}^{-\left(\iota+\frac{r^2}{4V_\infty^2 t^2}\right)-\left(\frac{\zeta Re\sqrt{\left(1-\frac{R^2}{r^2}\right)^2+4\,\frac{R^2\sin^2\theta}{r^2}}+c\left(\frac{r(t)}{R}-1\right)}{8}\right)\left(\underset{\text{new}}{\overset{\uparrow}{\sin^2\theta}}+\eta\,\mathrm{e}^{-\frac{r^2}{4V_\infty^2 t^2}}\right)}\ln\left(\tfrac{r}{R}\right).
\end{aligned} \tag{112}$$

Therefore, the $\sin^2\theta$ term damps the extent of the shedding away from the crests towards the cylinder center line as illustrated in Fig. 37b. The contour of individual vortices are observable in this figure as they are advected away from an absolute reference frame that originates at the cylinder center. With $r(t)$ defined as in Eqn. 107, the vortical axes have only relative translation motion, and the vortices are *free*. If the experimentally observed vortices are assumed to be *forced*, their axes can also spin relative to the cylinder axis. Therefore, a relative circumferential coordinate variable, $\theta(t)$, that varies in a clockwise direction in Fig. 36 is defined as

$$\begin{aligned}
\theta(t) &= \theta + \chi\int_0^t \overset{\text{angular velocity}}{\overset{\uparrow}{\frac{V_{\theta_{NLF}}}{r}}}\,dt \\
&= \theta - \frac{\chi V_\infty t\sin\theta}{r}\left(1+\frac{R^2}{r^2}\right),
\end{aligned} \tag{113}$$

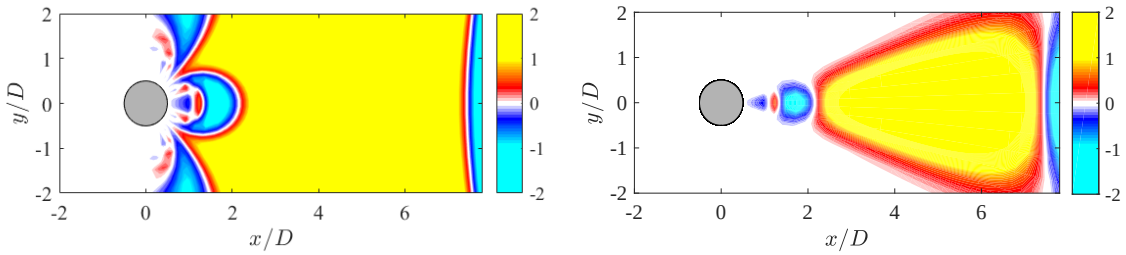

(a) Eqn. 109

(b) Eqn. 112 (*free* vortices).

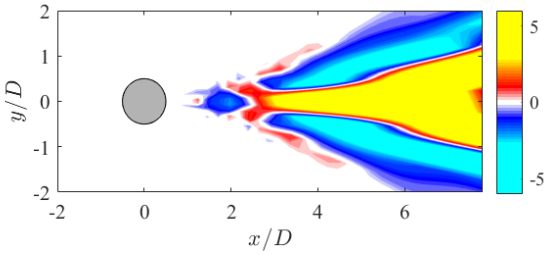

(c) Eqn. 112 with Eqn. 114 (*forced* vortices).

Figure 37: Contour of Eqns. 109 and 112 normalized by $V_\infty R$ at $Re = 140$ and $V_\infty t/R \approx 165.3$

where χ is still

$$\chi = \begin{cases} 1\ , & \theta \geq 0 \\ -1\ , & \theta < 0 \end{cases} .$$

Then $r(t)$ is modified into

$$r(t) = r\sqrt{\begin{array}{l}\left(\sin\theta(t) - \frac{V_\infty t}{r}\left(\frac{R^2}{r^2}\sin\theta(t)\cos\theta(t)\right)\right)^2 \\ +\left(\cos\theta(t) - \frac{V_\infty t}{r}\left(1 + \frac{R^2}{r^2}\left(\sin^2\theta(t) - \cos^2\theta(t)\right)\right)\right)^2\end{array}} \tag{114}$$

so that $\theta(t)$ spins the vortices about the convected vortical axes. The resulting flow

pattern of $\psi_{vortexshedding}$ is depicted in Fig. 37c. Then, using superposition, the updated viscous stream function for the cylinder flow is

$$
\begin{aligned}
&\psi_{viscous} = \psi_{NLF} + \psi_{vortex} + \psi_{sink/source} + \psi_{perifocal} + \psi_{vortexshedding} \\
&= V_\infty r \sin\theta \left(1 - \frac{R^2}{r^2}\right) \\
&-V_\infty r \sin\theta \left(1 + \frac{R^2}{r^2}\right) \mathrm{e}^{-\left(\frac{r^2}{4V_\infty^2 t^2} + \frac{qRe\sqrt{\left(1-\frac{R^2}{r^2}\right)^2 + 4\,\frac{R^2\sin^2\theta}{r^2}} + c\left(\frac{r}{R}-1\right)}{8}\right)} \ln\left(\frac{r}{R}\right) \\
&+V_\infty r \left(1 - \frac{R^2}{r^2}\right) (\theta + \sigma) (\chi \sin\theta)^{\mathrm{e}^{-\frac{V_\infty t}{r}\left(1-\frac{R}{r}\right)}} \\
&\times \left(\cos\theta - \frac{qRe}{2} \frac{\sin^2\theta\cos\theta\left(\frac{r}{R}-1\right)\frac{R^2}{r^2}}{\sqrt{\left(1-\frac{R^2}{r^2}\right)^2 + 4\,\frac{R^2\sin^2\theta}{r^2}} + c}\right) \mathrm{e}^{-\left(\frac{r^2}{4V_\infty^2 t^2} + \frac{qRe\sqrt{\left(1-\frac{R^2}{r^2}\right)^2 + 4\,\frac{R^2\sin^2\theta}{r^2}} + c\left(\frac{r}{R}-1\right)}{8}\right)} \ln\left(\frac{r}{R}\right) \\
&+ \underset{\text{new}}{\overset{\uparrow}{j}}\, V_\infty r \left(1 - \frac{R^2}{r^2}\right) \left(\cos\theta - \frac{\zeta Re}{2} \frac{\sin^2\theta\cos\theta\left(\frac{r}{R}-1\right)\frac{R^2}{r^2}}{\sqrt{\left(1-\frac{R^2}{r^2}\right)^2 + 4\,\frac{R^2\sin^2\theta}{r^2}} + c}\right) (\theta + \sigma) (\chi \sin\theta)^{\mathrm{e}^{-\frac{V_\infty t}{r}\left(1-\frac{R}{r}\right)}} \\
&\times \mathrm{e}^{-\left(\iota + \frac{r^2}{4V_\infty^2 t^2}\right) - \left(\frac{\zeta Re\sqrt{\left(1-\frac{R^2}{r^2}\right)^2 + 4\,\frac{R^2\sin^2\theta}{r^2}} + c\left(\frac{r(t)}{R}-1\right)}{8}\right)\left(\sin^2\theta + \eta^{\mathrm{e}^{-\frac{r^2}{4V_\infty^2 t^2}}}\right)} \ln\left(\frac{r}{R}\right) \\
&-\frac{\partial}{\partial\theta}\left(\phi_{perifocal}\right)
\end{aligned}
\tag{115}
$$

where the new constant, j, that represents the ratio of the vortex street velocity, V_{kvs}, relative to V_∞, is to be determined.

Figure 38 illustrates the present theoretical vortex shedding at $Re = 140$ and $V_\infty t/R \approx 165.3$ in comparison to the streaklines of an experimentally observed flow. The time stamp for the experimentally observed flow is not reported [7, Fig. 94, p. 56]. So the choice of $V_\infty t/R \approx 165.3$ for the theoretical evaluation is arbitrary. The theoretical streamlines are contours of Eqn. 115 normalized by $V_\infty R$ and plotted for two different values of j. The vortices are forced with Eqn. 113. Equation 115 is a complex function that has both real and imaginary parts. Therefore, its absolute value is plotted. However, Fig. 38a has the contour of the absolute value in white and overlaid on that of the real part of the function that is in red. Figures 38a and 38c consist of eleven linearly-spaced contour levels from 0 to 10. They are not to

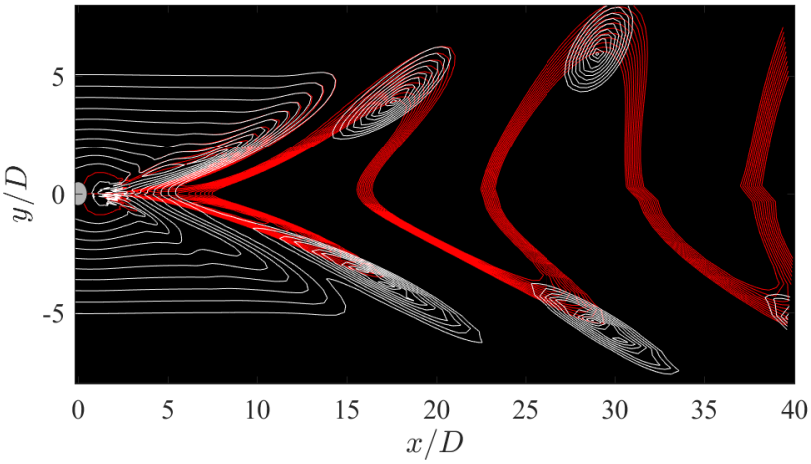

(a) Eqn. 115 with $j = 1$ (red lines for the real part and white lines for the absolute value).

(b) Experimentally observed streaklines (unknown time) [7]

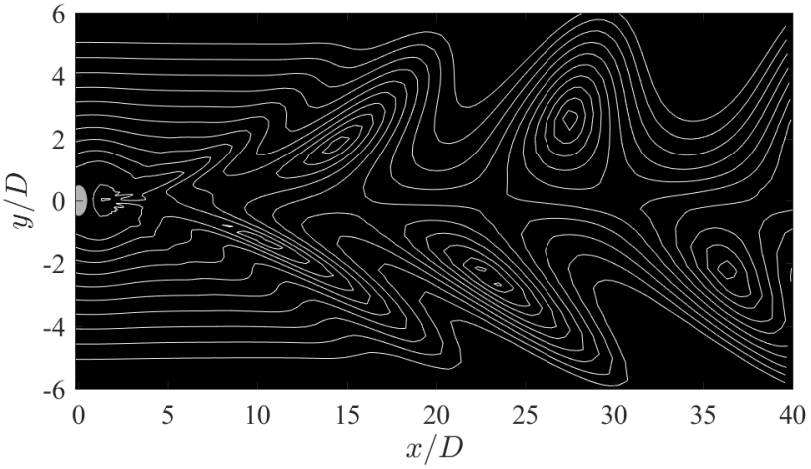

(c) Eqn. 115 with $j = 1/5$.

Figure 38: Contour of Eqn. 115 normalized by $V_\infty R$ (streamlines) showing the Kármán vortex street and the effect of j at $Re = 140$ and $V_\infty t/R \approx 165.3$ (*forced* vortices) in comparison with an experimentally observed flow.

scale with the experimentally observed flow in Fig. 38b, but they display about the same number of shedding cycles. In the vortex street, streamlines and streaklines do not coincide because of flow unsteadiness. However, the qualitative similarity of the theoretical flow oscillation to the experimentally observed one is discernible in these figures. For $j = 1$ in Fig. 38a, the oscillation amplitude about the x-axis is pronounced, and the shedding frequency is lower compared to the experimentally observed flow. Experimental observations of V_{vks}/V_∞ in the sub-critical Re regime have suggested it to be about 1/6 [72, p. 3-6]. Therefore, j is assumed to be equivalent to the proportion of $\psi_{vortexshedding}$ to $\psi_{viscous}$ in Eqn. 115, and its value is set to 1/5 in Fig. 38c. It is observable that the oscillation amplitude is damped towards the oscillation amplitude of the experimentally observed flow in Fig. 38b. However, the theoretical frequency remains the same with a variation of j.

As Re increases to very high values in an experimentally observed flow visualized with streaklines in Fig. 39a, the vortex street persists in the wake with more complexity [5, 7, 9, 15]. At a critical $Re \approx 3 \times 10^5$, the wake width shrinks [5]. However, a vortex street is not observable in Fig. 39b that illustrates the normalized absolute value of Eqn. 115 at $Re = 10,000$, $V_\infty t/R \approx 16,535$ and $j = 1/5$. An assessment of the Re-dependence of the governing equations informs the necessary modifications to $\psi_{vortexshedding}$ in the very high Re regime.

The continuity equation is unaffected by changes in Re [5,10,15,33]. The behavior of the momentum equation in very high Re regime is assessed as follow. Firstly, non-dimensional quantities and operation are defined as

$$\rho^* = \frac{\rho}{\rho_\infty} \quad V^* = \frac{V}{V_\infty} \quad p^* = \frac{p}{p_\infty} \quad \mu^* = \frac{\mu}{\mu_\infty} \quad \omega^* = \frac{2\omega R}{V_\infty} \quad t^* = \frac{V_\infty t}{R}$$
$$\nabla^* = 2R\nabla \quad ,$$

where the quantities with the ∞ subscripts have freestream reference values. For the foregoing incompressible flow analyses, $\rho^* = \rho/\rho_\infty = 1$. Then, the momentum

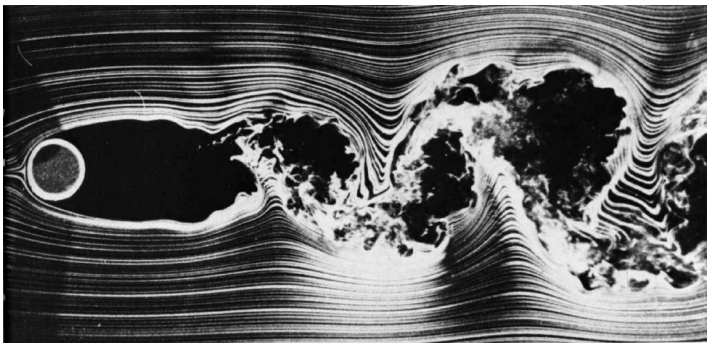

(a) Experimentally observed streaklines (unknown time) [7].

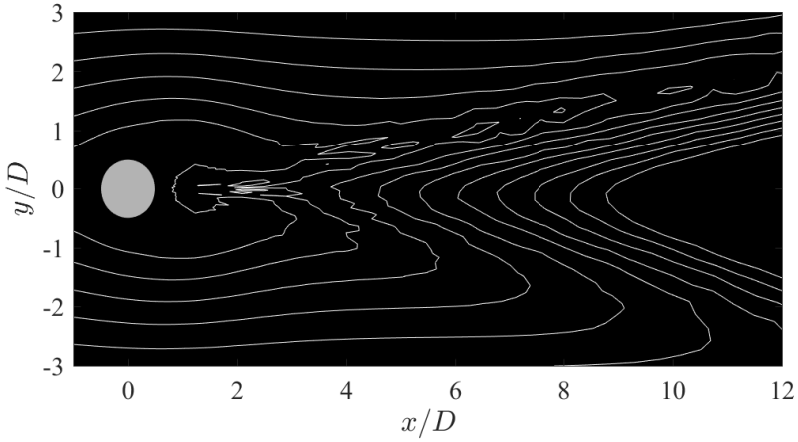

(b) Eqn. 115 at $V_\infty t/R \approx 16,535$ (*forced* vortices).

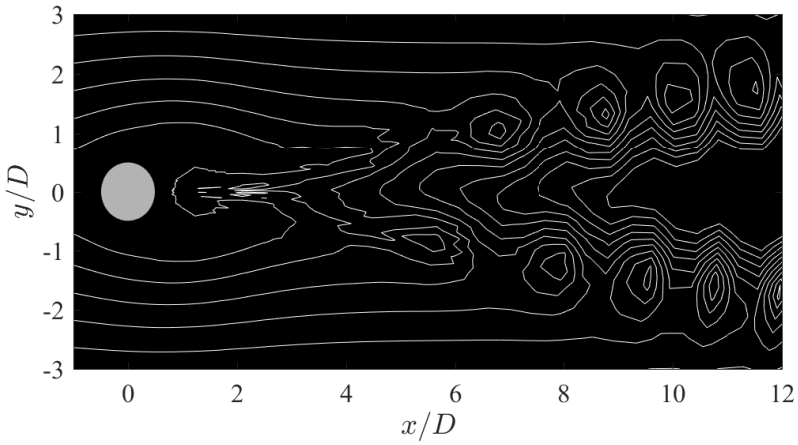

(c) Eqn. 120 at $V_\infty t/R \approx 16,535$ (*forced* vortices).

Figure 39: Experimentally observed and theoretical Kármán vortex street behind a circular cylinder at $Re = 10,000$.

equation is rewritten as

$$\frac{V_\infty^2}{R}\frac{\partial \mathbf{V}^*}{\partial t^*} + \frac{\nabla^*}{2R}\left(\frac{p_\infty}{\rho_\infty}\frac{p^*}{\rho^*} + V_\infty^2\frac{V^{*2}}{2} - 2\frac{\mu_\infty V_\infty}{\rho_\infty 2R}\frac{\mu^*}{\rho^*}\nabla^*\cdot\mathbf{V}^*\right)$$
$$= \frac{V_\infty^2}{2R}\mathbf{V}^*\times\omega^* + \frac{\mu_\infty V_\infty}{\rho_\infty 4R^2}\nabla^*\times\left(\frac{\mu^*\omega^*}{\rho^*}\right)$$

after neglecting body forces. The non-dimensional momentum equation is normalized with $V_\infty^2/2R$ as

$$2\frac{\partial \mathbf{V}^*}{\partial t^*} + \nabla^*\left(\frac{p_\infty}{\rho_\infty V_\infty^2}\frac{p^*}{\rho^*} + \frac{V^{*2}}{2} - 2\frac{\mu_\infty}{\rho_\infty V_\infty 2R}\frac{\mu^*}{\rho^*}\nabla^*\cdot\mathbf{V}^*\right) =$$
$$\mathbf{V}^*\times\omega^* + \frac{\mu_\infty}{\rho_\infty V_\infty 2R}\nabla^*\times\left(\frac{\mu^*\omega^*}{\rho^*}\right) .$$

When the substitutions

$$\frac{\mu_\infty}{\rho_\infty V_\infty 2R} = \frac{1}{Re} \qquad \frac{\mu^*}{\rho^*} = \nu^*$$

are made, the normalized non-dimensional momentum equation becomes

$$2\frac{\partial \mathbf{V}^*}{\partial t^*} + \nabla^*\left(\frac{p_\infty}{\rho_\infty V_\infty^2}\frac{p^*}{\rho^*} + \frac{V^{*2}}{2} - \frac{2}{Re}\nu^*\nabla^*\cdot\mathbf{V}^*\right) = \mathbf{V}^*\times\omega^* + \frac{1}{Re}\nabla^*\times\left(\nu^*\omega^*\right) . \tag{116}$$

Thus, it is observable that as $Re\to\infty$ in Eqn. 116, the momentum equation approaches an inviscid limit as in

$$2\frac{\partial \mathbf{V}^*}{\partial t^*} + \nabla^*\left(\frac{p_\infty}{\rho_\infty V_\infty^2}\frac{p^*}{\rho^*} + \frac{V^{*2}}{2}\right) = \mathbf{V}^*\times\omega^* . \tag{117}$$

As Re increases to high values in Eqn. 115,

$$qRe = \left(\frac{130}{Re^2}\left(\frac{3.9792Re}{130}\right)^{e^{-\frac{10}{Re}}}\right) Re\to 3.9792$$

and

$$\zeta Re = \left(\frac{130}{Re^2}\right) Re\to 0 .$$

Then, $\psi_{viscous}$ becomes less dependent on Re. This is consistent with Eqn. 117. The persistence of the vortex shedding at very high Re and the Re-independence of the momentum equation as the inviscid limit is approached both suggest that the shed

vortices in very high Re cylinder flows can be modeled on inviscid vortices. A suitable model for this is the Batchelor vortex [46, p. 260] that has its exponential term only dependent on the radial distance, r, from its core as

$$V_\theta = \frac{q}{r}\left(1 - \mathrm{e}^{-r^2}\right) \ . \tag{118}$$

Batchelor vortices are also called q-vortices [46] after the constant q in Eqn. 118. This constant is different from the q that has been introduced and used in earlier discussions in this study.

A material surface [73] that is dependent on time and viscosity is defined from the cylinder bounding surface as illustrated in Fig. 40. The radial distance, $\left(r - \sqrt{R^2 + 4\nu t}\right)$ employed in the vortex model originates from the material surface. Exponential arguments are non-dimensional, so this distance is normalized with the radius of the material surface as

$$\frac{\left(r - \sqrt{R^2 + 4\nu t}\right)}{\sqrt{R^2 + 4\nu t}} = \left(\frac{r}{\sqrt{R^2 + 4\nu t}} - 1\right) \ .$$

Then, the exponential argument of $\psi_{vortexshedding}$ is modified with $\left(\frac{r}{\sqrt{R^2+4\nu t}} - 1\right)$ to obtain

$$\begin{aligned}
&\psi_{vortexshedding} \\
&= V_\infty r\left(1 - \tfrac{R^2}{r^2}\right)\left(\cos\theta - \tfrac{\zeta Re}{2}\,\frac{\sin^2\theta\cos\theta\left(\frac{r}{R}-1\right)\frac{R^2}{r^2}}{\sqrt{\left(1-\frac{R^2}{r^2}\right)^2 + 4\,\frac{R^2\sin^2\theta}{r^2} + c}}\right)(\theta+\sigma)\left(\chi\sin\theta\right)^{\mathrm{e}^{-\frac{V_\infty t}{r}\left(1-\frac{R}{r}\right)}} \\
&\quad \times \mathrm{e}^{-\left(\iota + \frac{r^2}{4V_\infty^2 t^2}\right) - \left(\mathrm{e}^{-\zeta Re}\left(\frac{r}{\sqrt{R^2+4\nu t}} - 1\right)^2 + \frac{\zeta Re\sqrt{\left(1-\frac{R^2}{r^2}\right)^2 + 4\,\frac{R^2\sin^2\theta}{r^2}} + c\left(\frac{r(t)}{R} - 1\right)}{8}\right)\left(\sin^2\theta + \eta^{\mathrm{e}^{-\frac{r^2}{4V_\infty^2 t^2}}}\right)} \ln\left(\tfrac{r}{R}\right)
\end{aligned} \tag{119}$$

where $\mathrm{e}^{-\zeta Re}$ tends to 1 and progressively triggers the modification as Re increases.

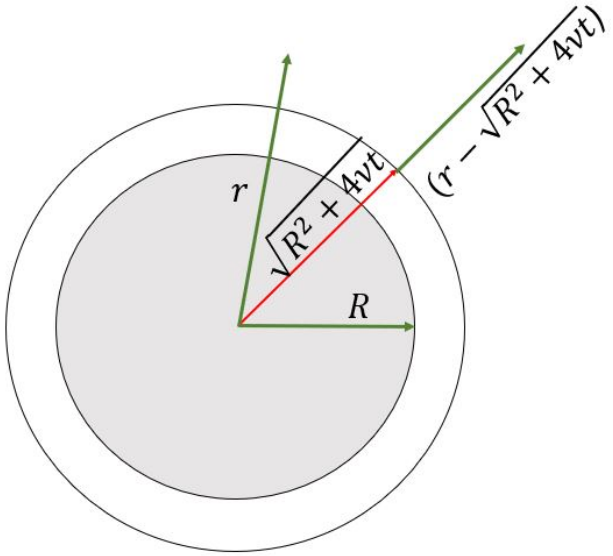

Figure 40: Vortex core model for high Re vortex shedding.

Then, the viscous stream function for the cylinder flow is

$$
\begin{aligned}
&\psi_{viscous} = \psi_{NLF} + \psi_{vortex} + \psi_{sink/source} + \psi_{perifocal} + \psi_{vortexshedding} \\
&= V_\infty r \sin\theta \left(1 - \frac{R^2}{r^2}\right) \\
&-V_\infty r \sin\theta \left(1 + \frac{R^2}{r^2}\right) \mathrm{e}^{-\left(\frac{r^2}{4V_\infty^2 t^2} + \frac{qRe\sqrt{\left(1-\frac{R^2}{r^2}\right)^2 + 4\,\frac{R^2\sin^2\theta}{r^2}} + c\left(\frac{r}{R}-1\right)}{8}\right)} \ln\left(\frac{r}{R}\right) \\
&+V_\infty r \left(1 - \frac{R^2}{r^2}\right)(\theta+\sigma)(\chi\sin\theta)^{\mathrm{e}^{-\frac{V_\infty t}{r}\left(1-\frac{R}{r}\right)}} \\
&\times \left(\cos\theta - \frac{qRe}{2}\,\frac{\sin^2\theta\cos\theta\left(\frac{r}{R}-1\right)\frac{R^2}{r^2}}{\sqrt{\left(1-\frac{R^2}{r^2}\right)^2 + 4\,\frac{R^2\sin^2\theta}{r^2}} + c}\right) \mathrm{e}^{-\left(\frac{r^2}{4V_\infty^2 t^2} + \frac{qRe\sqrt{\left(1-\frac{R^2}{r^2}\right)^2 + 4\,\frac{R^2\sin^2\theta}{r^2}} + c\left(\frac{r}{R}-1\right)}{8}\right)} \ln\left(\frac{r}{R}\right) \\
&+jV_\infty r \left(1 - \frac{R^2}{r^2}\right)\left(\cos\theta - \frac{\zeta Re}{2}\,\frac{\sin^2\theta\cos\theta\left(\frac{r}{R}-1\right)\frac{R^2}{r^2}}{\sqrt{\left(1-\frac{R^2}{r^2}\right)^2 + 4\,\frac{R^2\sin^2\theta}{r^2}} + c}\right)(\theta+\sigma)(\chi\sin\theta)^{\mathrm{e}^{-\frac{V_\infty t}{r}\left(1-\frac{R}{r}\right)}} \\
&\times \mathrm{e}^{-\left(\iota + \frac{r^2}{4V_\infty^2 t^2}\right) - \left(\mathrm{e}^{-\zeta Re}\left(\frac{r}{\sqrt{R^2+4\nu t}}-1\right)^2 + \frac{\zeta Re\sqrt{\left(1-\frac{R^2}{r^2}\right)^2 + 4\,\frac{R^2\sin^2\theta}{r^2}} + c\left(\frac{r(t)}{R}-1\right)}{8}\right)\left(\sin^2\theta + \eta^{\mathrm{e}^{-\frac{r^2}{4V_\infty^2 t^2}}}{2}\right)} \ln\left(\frac{r}{R}\right) \\
&-\frac{\partial}{\partial\theta}\left(\phi_{perifocal}\right) \ .
\end{aligned}
\tag{120}
$$

Thus, $\mathrm{e}^{-\zeta Re}(\frac{r}{\sqrt{R^2+4\nu t}} - 1)^2$ ensures that the vortex shedding continues at moderate to

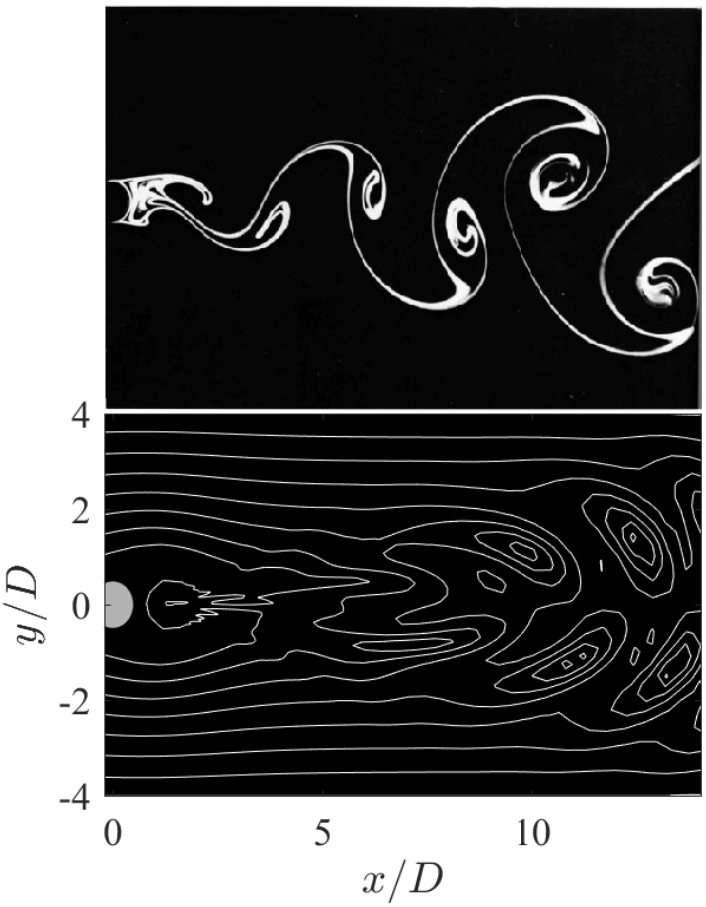

Figure 41: Experimentally observed Kármán vortex street (upper image [7]) behind a circular cylinder compared to theoretical streamlines from Eqn. 120 at $Re = 140$ (lower image, $V_\infty t/R \approx 165.3$, *forced* vortices).

high Re. This is shown in Fig. 39c that illustrates the theoretical vortex shedding at $Re = 10,000$ and $V_\infty t/R \approx 16,535$. $\mathrm{e}^{-\zeta Re}(\frac{r}{\sqrt{R^2+4\nu t}} - 1)^2$ also augments the deficient theoretical shedding frequency in Fig. 38c. This is evident in Fig. 41 which compares the experimentally observed flow to the absolute value of Eqn. 120 evaluated at the same conditions as Fig. 38c. Figure 41 illustrates about 3 shedding cycles covered over approximately the same distance for both the experimentally observed and theoretical flows.

An assessment of Fig. 42 that presents the experimentally observed vortex street streamlines from a moving cylinder in two different reference frames is suggestive that

(a) Cylinder reference frame

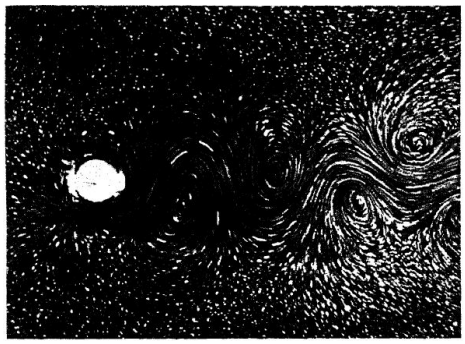

(b) Laboratory reference frame

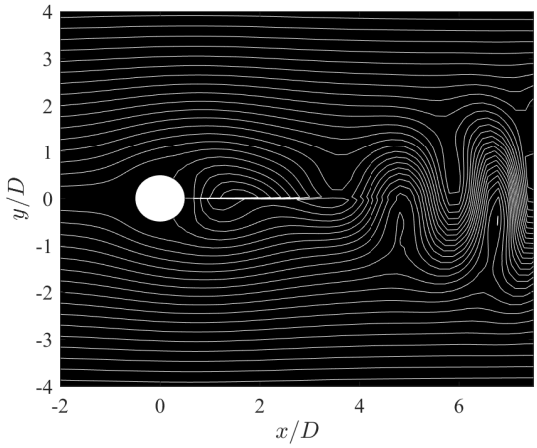

(c) Real part of Eqn. 115 with *free* vortices at $V_\infty t/R = 165.35$.

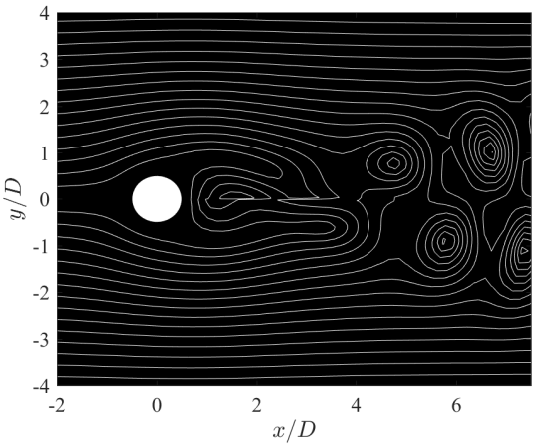

(d) Absolute value of Eqn. 115 with *free* vortices at $V_\infty t/R = 165.35$.

Figure 42: The experimentally observed vortex street streamlines behind a circular cylinder at $Re = 250$ photographed in two reference frames [10] compared with present theoretical streamlines.

the real value of Eqn. 115 corresponds to the flow in the cylinder reference frame, and its magnitude corresponds to the same flow in the Laboratory reference frame.

Using Euler's formula for complex numbers (Eqn. 110) [62], the spatio-temporal expressions for the Strouhal number, St and the vortex shedding frequency, f, are

extracted from the abridged $\psi_{vortexshedding}$ in

$$\begin{aligned}
&\psi_{vortexshedding} \\
&= \ldots \mathrm{e}^{-i\left(\mathrm{e}^{-\frac{130}{Re}}\left(\frac{r}{\sqrt{R^2+4\nu t}}-1\right)^2+\frac{130}{8Re}\sqrt{\left(1-\frac{R^2}{r^2}\right)^2+4\,\frac{R^2\sin^2\theta}{r^2}}+2\left(\frac{r(t)}{R}-1\right)\right)} \\
&= \ldots \mathrm{e}^{-i\left[\frac{10(R^2+4\nu t)\sqrt{\left(1-\frac{R^2}{r^2}\right)^2+4\,\frac{R^2\sin^2\theta}{r^2}}+2}{R^2}\frac{2R}{V_\infty}\left(\frac{\mathrm{e}^{-\frac{130}{Re}}RV_\infty\left(\frac{r}{\sqrt{R^2+4\nu t}}-1\right)^2}{20(R^2+4\nu t)\sqrt{\left(1-\frac{R^2}{r^2}\right)^2+4\,\frac{R^2\sin^2\theta}{r^2}}+2}+\frac{13\nu V_\infty t\left(r(t)-\frac{R}{V_\infty t}\right)}{32R(R^2+4\nu t)}\right)\right]}
\end{aligned} \tag{121}$$

where

$$r(t) = r\sqrt{\begin{array}{l}\left(\sin\theta(t)-\frac{V_\infty t}{r}\left(\frac{R^2}{r^2}\sin\theta(t)\cos\theta(t)\right)\right)^2 \\ +\left(\cos\theta(t)-\frac{V_\infty t}{r}\left(1+\frac{R^2}{r^2}\left(\sin^2\theta(t)-\cos^2\theta(t)\right)\right)\right)^2\end{array}}\ ,$$

and the values for the constants c and ζ have been substituted. After rearrangement, the abridged vortex-shedding stream function is

$$\psi_{vortexshedding} = \ldots \mathrm{e}^{-i\ \frac{10(R^2+4\nu t)\sqrt{\left(1-\frac{R^2}{r^2}\right)^2+4\,\frac{R^2\sin^2\theta}{r^2}}+2}{R^2}St}\ , \tag{122}$$

and the Strouhal number is

$$St = \frac{2fR}{V_\infty} = \frac{2R}{V_\infty}\left(\frac{\mathrm{e}^{-\frac{130}{Re}}RV_\infty\left(\frac{r}{\sqrt{R^2+4\nu t}}-1\right)^2}{20(R^2+4\nu t)\sqrt{\left(1-\frac{R^2}{r^2}\right)^2+4\,\frac{R^2\sin^2\theta}{r^2}}+2}+\frac{13\nu V_\infty t\left(r_0(t)-\frac{R}{V_\infty t}\right)}{32R(R^2+4\nu t)}\right) \tag{123}$$

where

$$\begin{aligned}
&r_0(t) \\
&= \sqrt{\left(\frac{r\sin\theta(t)}{V_\infty t}-\left(\frac{R^2}{r^2}\sin\theta(t)\cos\theta(t)\right)\right)^2+\left(\frac{r\cos\theta(t)}{V_\infty t}-\left(1+\frac{R^2}{r^2}\left(\sin^2\theta(t)-\cos^2\theta(t)\right)\right)\right)^2},
\end{aligned}$$

$$\theta(t) = \theta - \frac{\chi V_\infty t\sin\theta}{r}\left(1-\frac{R^2}{r^2}\right)\ ,$$

and χ and η are still as previously defined.

The comparison of Eqn. 120 to Eqn. 65 which is re-presented below as

$$\psi_{viscous}\left(r,\theta,V_\infty,\nu,t,Re\right) = V_\infty r\sin\theta\left(1-\frac{R^2}{r^2}\right)+B_0\left(r,\theta,V_\infty,\nu,t,Re\right)\ln\left(\frac{r}{R}\right)$$

reveals that B_0 is

$$
\begin{aligned}
B_0 = & -V_\infty r \sin\theta \left(1+\frac{R^2}{r^2}\right) \mathrm{e}^{-\left(\frac{r^2}{4V_\infty^2 t^2}+\frac{qRe\sqrt{\left(1-\frac{R^2}{r^2}\right)^2+4\,\frac{R^2\sin^2\theta}{r^2}}+c\left(\frac{r}{R}-1\right)}{8}\right)} \\
& + V_\infty r \left(1-\frac{R^2}{r^2}\right)(\theta+\sigma)(\chi\sin\theta)^{\mathrm{e}^{-\frac{V_\infty t}{r}\left(1-\frac{R}{r}\right)}} \\
& \times \left(\cos\theta - \frac{qRe}{2}\,\frac{\sin^2\theta\cos\theta\left(\frac{r}{R}-1\right)\frac{R^2}{r^2}}{\sqrt{\left(1-\frac{R^2}{r^2}\right)^2+4\,\frac{R^2\sin^2\theta}{r^2}+c}}\right) \mathrm{e}^{-\left(\frac{r^2}{4V_\infty^2 t^2}+\frac{qRe\sqrt{\left(1-\frac{R^2}{r^2}\right)^2+4\,\frac{R^2\sin^2\theta}{r^2}}+c\left(\frac{r}{R}-1\right)}{8}\right)} \\
& + jV_\infty r\left(1-\frac{R^2}{r^2}\right)\left(\cos\theta - \frac{\zeta Re}{2}\,\frac{\sin^2\theta\cos\theta\left(\frac{r}{R}-1\right)\frac{R^2}{r^2}}{\sqrt{\left(1-\frac{R^2}{r^2}\right)^2+4\,\frac{R^2\sin^2\theta}{r^2}+c}}\right)(\theta+\sigma)(\chi\sin\theta)^{\mathrm{e}^{-\frac{V_\infty t}{r}\left(1-\frac{R}{r}\right)}} \\
& \times \mathrm{e}^{-\left(\iota+\frac{r^2}{4V_\infty^2 t^2}\right)-\left(\mathrm{e}^{-\zeta Re\left(\frac{r}{\sqrt{R^2+4\nu t}}-1\right)^2+\frac{\zeta Re\sqrt{\left(1-\frac{R^2}{r^2}\right)^2+4\,\frac{R^2\sin^2\theta}{r^2}}+c\left(\frac{r(t)}{R}-1\right)}{8}}\right)\left(\sin^2\theta+\eta^{\mathrm{e}^{-\frac{r^2}{4V_\infty^2 t^2}}}{2}\right)}
\end{aligned}
\tag{124}
$$

since the contribution from $\psi_{perifocal}$ is negligible.

The conditions on Eqn. 120 satisfy the continuity equation as well as the boundary conditions at infinity and the surface. Verifying the algebra of these would be laborious without the use of a mathematical software like *Maple*^{TM} [74]. Using *Maple*^{TM}, it was confirmed that Eqn. 120 is divergence-free because

$$\frac{1}{r}\frac{\partial(rV_r)}{\partial r}+\frac{1}{r}\frac{\partial V_\theta}{\partial\theta}=0\,.$$

2.1.6 The Eulerian Kwasu Function

2.1.6.1 The Incompressible Kwasu Function

Equation 120 is continuously amenable to differential operations. However, it is a formidable one to analytically integrate. This is primarily due to the non-linear combinations of the natural logarithm term with the exponential terms. So, physical quantities such as the velocity, the vorticity and the shear stress that are products of differentiation of the stream function are directly obtainable. This is not so for the pressure that is an integral of non-linear expressions involving the components of the

velocity field in

$$\begin{aligned}
\frac{1}{\rho}\frac{\partial p}{\partial r} &= -\left(\frac{\partial V_r}{\partial t} + V_r\frac{\partial V_r}{\partial r} + \frac{V_\theta}{r}\frac{\partial V_r}{\partial \theta} - \frac{V_\theta^2}{r}\right) \\
&+\nu\left(\frac{1}{r}\frac{\partial}{\partial r}\left(r\frac{\partial V_r}{\partial r}\right) + \frac{1}{r^2}\frac{\partial^2 V_r}{\partial \theta^2} - \frac{2V_r}{r^2} + \frac{2}{r^2}\frac{\partial V_\theta}{\partial \theta}\right) \\
\frac{1}{\rho r}\frac{\partial p}{\partial \theta} &= -\left(\frac{\partial V_\theta}{\partial t} + V_r\frac{\partial V_\theta}{\partial r} + \frac{V_\theta}{r}\frac{\partial V_\theta}{\partial \theta} + \frac{V_r V_\theta}{r}\right) \\
&+\nu\left(\frac{1}{r}\frac{\partial}{\partial r}\left(r\frac{\partial V_\theta}{\partial r}\right) + \frac{1}{r^2}\frac{\partial^2 V_\theta}{\partial \theta^2} - \frac{V_\theta}{r^2} + \frac{2}{r^2}\frac{\partial V_r}{\partial \theta}\right)
\end{aligned} \tag{125}$$

whose complexity is complicated with the non-linearity of the cylindrical polar coordinate system. The cylindrical polar coordinate system's non-linearity is evident in the coupling of $1/r$ with operations in the θ direction as $\partial/r\partial\theta$. Differential operations in the Cartesian coordinate system are decoupled so that it offers relatively simplified pressure differentials as

$$\begin{aligned}
\frac{1}{\rho}\frac{\partial p}{\partial x} &= -\left(\frac{\partial V_x}{\partial t} + V_x\frac{\partial V_x}{\partial x} + V_y\frac{\partial V_x}{\partial y}\right) + \nu\left(\frac{\partial^2 V_x}{\partial x^2} + \frac{\partial^2 V_x}{\partial y^2}\right) \\
\frac{1}{\rho}\frac{\partial p}{\partial y} &= -\left(\frac{\partial V_y}{\partial t} + V_x\frac{\partial V_y}{\partial x} + V_y\frac{\partial V_y}{\partial y}\right) + \nu\left(\frac{\partial^2 V_y}{\partial x^2} + \frac{\partial^2 V_y}{\partial y^2}\right) .
\end{aligned} \tag{126}$$

In terms of the incompressible *Kwasu* function, $\tilde{\kappa}$, the order of differentiation can be interchanged in the right hand sides of Eqn. 126 as

$$\begin{aligned}
\frac{\partial V_x}{\partial t} &= \frac{\partial}{\partial t}\left(\frac{\partial \tilde{\kappa}}{\partial x}\right) = \frac{\partial}{\partial x}\left(\frac{\partial \tilde{\kappa}}{\partial t}\right) \\
V_x\frac{\partial V_x}{\partial x} &= \frac{1}{2}\frac{\partial (V_x^2)}{\partial x} \\
V_y\frac{\partial V_x}{\partial y} &= V_y\frac{\partial}{\partial y}\left(\frac{\partial \tilde{\kappa}}{\partial x}\right) = V_y\frac{\partial}{\partial x}\left(\frac{\partial \tilde{\kappa}}{\partial y}\right) = V_y\frac{\partial V_y}{\partial x} = \frac{1}{2}\frac{\partial (V_y^2)}{\partial x} \\
\frac{\partial^2 V_x}{\partial y^2} &= \frac{\partial^2}{\partial y^2}\left(\frac{\partial \tilde{\kappa}}{\partial x}\right) = \frac{\partial}{\partial x}\left(\frac{\partial^2 \tilde{\kappa}}{\partial^2 y}\right) \\
\frac{\partial^2 V_x}{\partial x^2} &= \frac{\partial}{\partial x}\left(\frac{\partial^2 \tilde{\kappa}}{\partial^2 x}\right)
\end{aligned}$$

because the time and space variables are decoupled. Then, the x-component of Eqn. 126 is rewritten as

$$\frac{1}{\rho}\frac{\partial p}{\partial x} = \frac{\partial}{\partial x}\left[-\left(\frac{\partial \tilde{\kappa}}{\partial t} + \frac{V_x^2}{2} + \frac{V_y^2}{2}\right) + \nu\left(\frac{\partial^2 \tilde{\kappa}}{\partial^2 x} + \frac{\partial^2 \tilde{\kappa}}{\partial^2 y}\right)\right] . \tag{127}$$

Similar manipulations of the y-component of Eqn. 126 gives

$$\frac{1}{\rho}\frac{\partial p}{\partial y} = \frac{\partial}{\partial y}\left[-\left(\frac{\partial \tilde{\kappa}}{\partial t} + \frac{V_x^2}{2} + \frac{V_y^2}{2}\right) + \nu\left(\frac{\partial^2 \tilde{\kappa}}{\partial^2 x} + \frac{\partial^2 \tilde{\kappa}}{\partial^2 y}\right)\right] . \tag{128}$$

So, the pressure field is obtained as

$$p = \rho\left[-\left(\frac{\partial \tilde{\kappa}}{\partial t} + \frac{V_x^2}{2} + \frac{V_y^2}{2}\right) + \nu\left(\frac{\partial^2 \tilde{\kappa}}{\partial^2 x} + \frac{\partial^2 \tilde{\kappa}}{\partial^2 y}\right)\right] + F(t) . \tag{129}$$

Using Eqn. 54 re-presented below as

$$\begin{aligned}
&\theta_W = \arctan\left[x_{3D}, y_{3D}\right] \\
&= \arctan\left[\cos\theta_{3D}\sqrt{x_{3D}^2 + y_{3D}^2}, \sin\theta_{3D}\sqrt{x_{3D}^2 + y_{3D}^2}\right] \\
&\theta_{3D} = \arctan\left(y_{3D} + y_m, x_{3D}\right) \\
&y_m = 7R_{3D}/20 \\
&R_{3D} = \sqrt{R_{2D}^2 + B^2\cos^2\left(\frac{z_{3D}}{\sqrt{x_{3D}^2 + y_{3D}^2 + z_{3D}^2}}\right)}
\end{aligned}$$

for a principal axis, θ_W, in $\psi_{viscous}$, the full expression for $\tilde{\kappa}$ is

$$\begin{aligned}
&\tilde{\kappa} = V_\infty r\sin\theta_W\left(1 - \tfrac{R^2}{r^2}\right) \\
&-V_\infty r\sin\theta_W\left(1 + \tfrac{R^2}{r^2}\right)\mathrm{e}^{-\left(\frac{r^2}{4V_\infty^2 t^2} + \frac{qRe\sqrt{\left(1-\frac{R^2}{r^2}\right)^2 + 4\frac{R^2\sin^2\theta_W}{r^2}} + c\left(\frac{r}{R}-1\right)}{8}\right)}\ln\left(\tfrac{r}{R}\right) \\
&+V_\infty r\left(1 - \tfrac{R^2}{r^2}\right)\theta_W\left(\chi\sin\theta_W\right)^{\mathrm{e}^{-\frac{V_\infty t}{r}\left(1-\frac{R}{r}\right)}} \\
&\times\left(\cos\theta_W - \frac{qRe}{2}\frac{\sin^2\theta_W\cos\theta_W\left(\frac{r}{R}-1\right)\frac{R^2}{r^2}}{\sqrt{\left(1-\frac{R^2}{r^2}\right)^2 + 4\frac{R^2\sin^2\theta_W}{r^2}} + c}\right)\mathrm{e}^{-\left(\frac{r^2}{4V_\infty^2 t^2} + \frac{qRe\sqrt{\left(1-\frac{R^2}{r^2}\right)^2 + 4\frac{R^2\sin^2\theta_W}{r^2}} + c\left(\frac{r}{R}-1\right)}{8}\right)}\ln\left(\tfrac{r}{R}\right) \\
&+jV_\infty r\left(1 - \tfrac{R^2}{r^2}\right)\left(\cos\theta_W - \frac{\zeta Re}{2}\frac{\sin^2\theta_W\cos\theta_W\left(\frac{r}{R}-1\right)\frac{R^2}{r^2}}{\sqrt{\left(1-\frac{R^2}{r^2}\right)^2 + 4\frac{R^2\sin^2\theta_W}{r^2}} + c}\right)\theta_W\left(\chi\sin\theta_W\right)^{\mathrm{e}^{-\frac{V_\infty t}{r}\left(1-\frac{R}{r}\right)}} \\
&\times\mathrm{e}^{-\left(\iota + \frac{r^2}{4V_\infty^2 t^2}\right) - \left(\mathrm{e}^{-\zeta Re\left(\frac{r}{\sqrt{R^2+4\nu t}}-1\right)^2} + \frac{\zeta Re\sqrt{\left(1-\frac{R^2}{r^2}\right)^2 + 4\frac{R^2\sin^2\theta_W}{r^2}} + c\left(\frac{r(t)}{R}-1\right)}{8}\right)\left(\sin^2\theta_W + \eta^{\mathrm{e}^{-\frac{r^2}{4V_\infty^2 t^2}}}\right)}\ln\left(\tfrac{r}{R}\right) \\
&-\frac{\partial}{\partial\theta}\left(\phi_{perifocal}\right),
\end{aligned} \tag{130}$$

where

$$j = 1/5,$$

$$\zeta = \frac{130}{Re^2},$$

$$\iota = \frac{125}{Re},$$

$$r(t) = r\sqrt{\begin{array}{l}\left(\sin\theta(t) - \frac{V_\infty t}{r}\left(\frac{R^2}{r^2}\sin\theta(t)\cos\theta(t)\right)\right)^2 \\ +\left(\cos\theta(t) - \frac{V_\infty t}{r}\left(1 + \frac{R^2}{r^2}\left(\sin^2\theta(t) - \cos^2\theta(t)\right)\right)\right)^2\end{array}}\ ,$$

$$\theta(t) = \theta_W - \frac{\chi V_\infty t \sin\theta_W}{r}\left(1 + \frac{R^2}{r^2}\right)\ ,$$

$$r = \sqrt{x^2 + y^2}\ ,$$

$$\eta = \begin{cases} 1\ ,\ -\frac{\pi}{2} < \arctan[X,y] < \frac{\pi}{2} \\ -1\ ,\ \frac{\pi}{2} \geq \arctan[X,y]\ \ ||\ \ \arctan[X,y] \leq -\frac{\pi}{2} \end{cases}\ ,$$

$$\chi = \begin{cases} 1\ ,\ \arctan[X,y] \geq 0 \\ -1\ ,\ \arctan[X,y] < 0 \end{cases}\ ,$$

and X is the body surface coordinate along the x-axis.

For ease of coding and cost of evaluation, χ and η are parameterized as

$$\chi = (-1)^{\exp(-\exp(N\arctan[X,y]))}\ , \tag{131}$$

and

$$\eta = (-1)^{\exp(-\exp(N\arctan[Y,x]))} \tag{132}$$

respectively where Y is the body surface coordinate along the y-axis. The surface inclination to a local flow is factored in with $\arctan[X,y]$ and $\arctan[Y,x]$. N is a very large number on the order of 10^6 such that when $\arctan[X,y]$ and $\arctan[Y,x]$ are positive,

$$\chi = (-1)^{\exp\left(-\exp(N\cancel{\arctan[X,y]}^{\infty})\right)} = (-1)^{\exp(-\infty)} = 1\ ,$$

and

$$\eta = (-1)^{\exp\left(-\exp\left(N \operatorname{arctan}[Y,x]\right)^{\infty}\right)} = (-1)^{\exp(-\infty)} = 1$$

respectively. When they are negative,

$$\chi = (-1)^{\exp\left(-\exp\left(N \operatorname{arctan}[X,y]\right)^{0}\right)} = (-1)^{\exp(-0)} = -1 \,,$$

and

$$\eta = (-1)^{\exp\left(-\exp\left(N \operatorname{arctan}[Y,x]\right)^{0}\right)} = (-1)^{\exp(-0)} = -1$$

respectively.

From Eqn. 54 and subsequently, R refers to R_{3D}. However, the freestream Reynolds number, Re_∞, is based on the cylinder center plane radius, R_{2D}. Therefore, the local Reynolds number, Re, in Eqn. 130 is substituted with

$$Re = \frac{V_\infty 2R}{\nu_\infty} \,.$$

The wind circumferential coordinate, $\tilde{\theta}$, is defined as

$$\tilde{\theta} = \begin{cases} |\arctan(x_{3D}, y_{3D} + y_n)| \,, \text{for} \quad |\arctan(x_{3D}, y_{3D})| < \theta_s & \text{(Cylinder)} \\ -|\arctan(x_{3D}, y_{3D} + y_n)| \,, \text{for} \quad |\arctan(x_{3D}, y_{3D})| < \theta_s & \text{(Sphere)} \\ \tilde{\theta}_n \,, \quad |\arctan(x_{3D}, y_{3D})| \geq \theta_s \,, & \end{cases} \tag{133}$$

where θ_s is the circumferential coordinate of the flow separation point measured in radians from the front stagnation point. $\tilde{\theta}$ is illustrated in Fig. 43. It is used in

$$\theta_W = \arctan\left[\cos\tilde{\theta}\sqrt{x_{3D}^2 + y_{3D}^2}, \sin\tilde{\theta}\sqrt{x_{3D}^2 + y_{3D}^2}\right]$$

to compute the pressure. In Eqn. 133, y_n and $\tilde{\theta}_n$ are geometrical constants that primarily control the pressure variation in the wake. From investigations of experimentally observed cylinder crossflow pressure distributions, they were determined to be $3R/4$ and $54\pi/180$ $(rads)$ respectively.

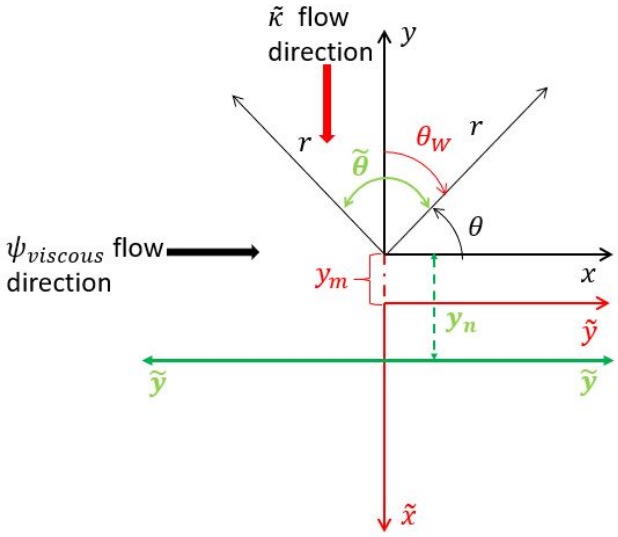

Figure 43: Pictorial representation of y_m, y_n, θ_W and $\tilde{\theta}$ in the $z = 0$ plane.

In Fig. 43, the positive directions of the geometric variables are denoted with the arrowheads. All the angular coordinates are in radians. θ_W is observed to vary from the windward direction. Therefore, the constant σ that appropriately places the counter-rotating vortices at the cylinder rear in $\psi_{viscous}$ (Fig. 21) is not necessary in Eqn. 130. This is evident in Fig. 44 that illustrates the real part of Eqn. 130 normalized by $V_\infty R$ at $Re_\infty = 26$, $V_\infty t/R = 7$ and $z = 0$. The theoretical time is arbitrary. Ten linearly-spaced contour levels from -4 to $+4$ are plotted and compared to an experimentally observed flow. The theoretical stationary vortex is revealed, and the flow pattern is qualitatively similar to the experimentally observed flow which is visualized with aluminum powder in water [5, 7].

Figure 45a compares the real part of the normalized *Kwasu* function to an experimentally observed flow photographed at $Re_\infty = 100$ by Wu et al. [6]. They visualized the streamlines with $50\mu m$ polyamide tracer particles in a mixture of glycerol and water [6]. The theoretical streamlines were evaluated in the $z = 0$ plane and at an arbitrary $V_\infty t/R = 57.86$. They were plotted with eighty-six linearly-spaced contour levels from -10 to $+10$. The shed vortices are *free*. Figure 45b also compares an experimentally observed vortex street at $Re_\infty = 105$ to the normalized absolute value

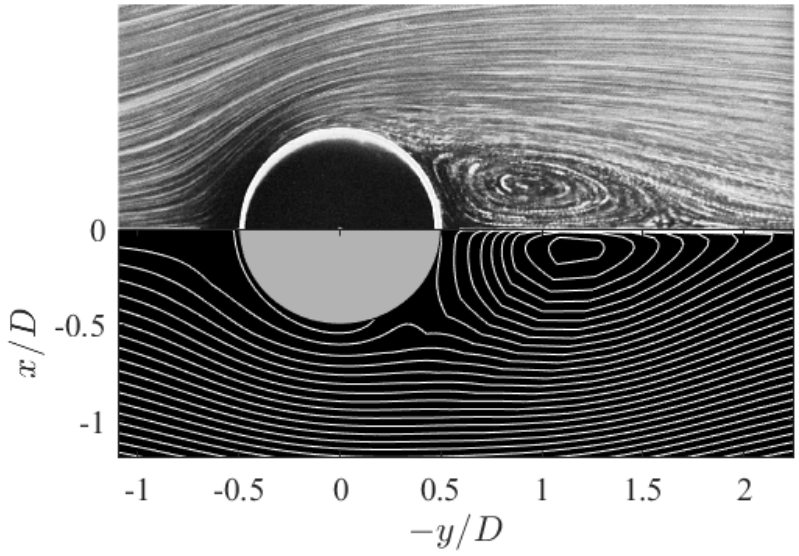

Figure 44: Comparison of an experimentally observed flow (upper image [7]) and present theoretical streamline (Eqn. 130 (lower image)) at $Re_\infty = 26$ (and $V_\infty t/R = 7$ in Eqn. 130).

of Eqn. 130 at the same Re, $V_\infty t/R = 165.3$ and $z = 0$. The experimentally observed flow streaklines are shown by electrolytic precipitation in water [7]. The theoretical time is also arbitrary, and twenty-one linearly-spaced contour levels from 0 to 4 are shown to illustrate the *forced* vortices. The observable qualitative similarity between refined potential theory and experiment in these figures is agreeable.

Figure 46a presents a schematic of a vortex street behind a finite cylinder showing streamwise vortex pairs that are characteristic of the three-dimensional nature of the flow. These streamwise vortices have been observed in actual experiments and DNS [75]. Figure 46b presents an experimental streakline visualization of the streamwise vortices in a plane parallel to the cylinder axis and perpendicular to the flow direction as illustrated with section AA in Fig. 46a [75]. The freestream Reynolds number is 300. The streamwise distance of section AA from the cylinder and the time stamp of the visualization were not reported [75]. So, arbitrary $y/D \approx 6.2$ and $V_\infty t/R \approx 495.9$ were used for the present theoretical evaluation with Eqn. 130 at the same Re_∞

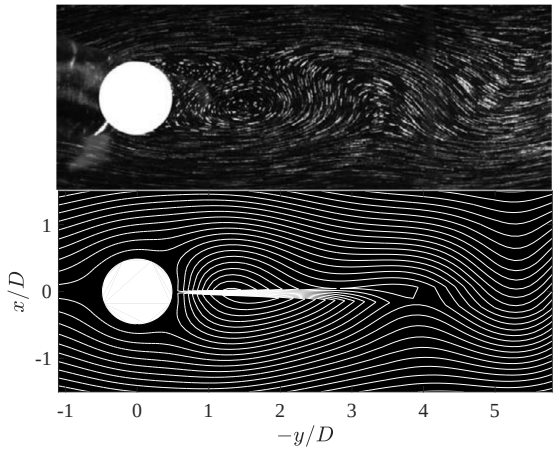

(a) An experimentally observed flow (upper image[6]) and Eqn. 130 (lower image) at $Re_\infty = 100$ ($V_\infty t/R = 57.86$, *free* vortices).

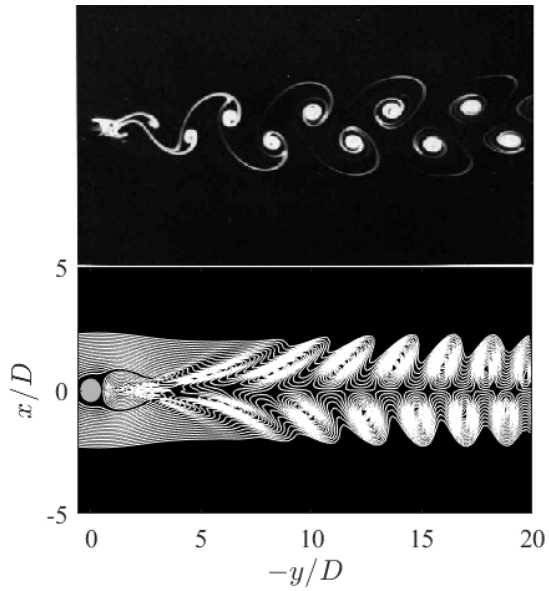

(b) An experimentally observed flow (upper image [7]) and absolute value of Eqn. 130 (lower image) at $Re_\infty = 105$ ($V_\infty t/R = 165.3$, *forced* vortices).

Figure 45: Comparison of an experimentally observed flows with present theoretical streamlines (the real and absolute values of Eqn. 130).

shown in Fig. 46c. Nine linearly-spaced contour levels from 0 to 3 of the absolute value of Eqn. 130 normalized with $V_\infty R$ are shown. The span of the theoretical cylinder is $2\pi R$. This is also arbitrary. The vortices are *forced*. The figure captures the streamwise vortices. The conditions in Fig. 46c are the same for the theoretical evaluation in Fig. 47b that is obtained in an inclined plane to the cylinder axis and flow direction as depicted in Fig. 47a. The planar angle of inclination is approximately 21°, and thirty-one linearly-spaced contour levels from 0 to 3 are plotted. It can also be observed that Fig. 47b is in agreement with an actual visualization of the plan view of the three-dimensional vortex shedding in Fig. 47c.

2.1.6.2 The Compressible Kwasu Function

For larger Re_∞, the vortex street metamorphoses into a distinct wake [5, 9, 15] as presented in Figs. 48 and 49a. The wake enlarges with progressive Re_∞ from Fig. 44 and develops into a turbulent wake at very high Re_∞ [5, 7, 15]. Figure 48 compares an experimentally observed vortex street at $Re_\infty = 10,000$ to the normalized real part of Eqn. 130 at same Re_∞, $V_\infty t/R = 16,535$ and $z = 0$. The theoretical time is arbitrary, and eighty-six linearly-spaced contour levels from -6 to 6 are shown. The theoretical flow pattern is qualitatively similar to the experimentally observed flow visualization. The shed vortices are *forced*. Figure 49a illustrates the normalized real part of Eqn. 130 at $Re_\infty = 4.0 \times 10^5$, $V_\infty t/R \approx 8.3 \times 10^5$ and $z = 0$. Eighty-seven linearly-spaced contour levels from -6 to 6 are displayed to include the level at zero. At such a high Re_∞ and very large time, the theoretical vortical axes spin so fast that the velocity towards the vortices' cores approach values that are orders of magnitude higher than the freestream velocity. The vortex shedding pattern is observable when the local speed is normalized with the maximum speed in the wake ($real(V/V_{max})$) in Fig. 49b. One hundred and one linearly-spaced contour levels from 0 to 0.066 are shown in the figure. The evaluation was made on a body-fitted grid with one hundred

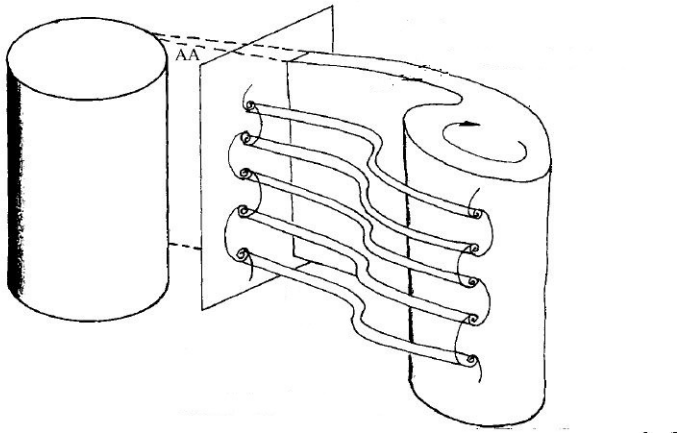

(a) Schematic of three-dimensional vortex shedding [75] in (b) and (c).

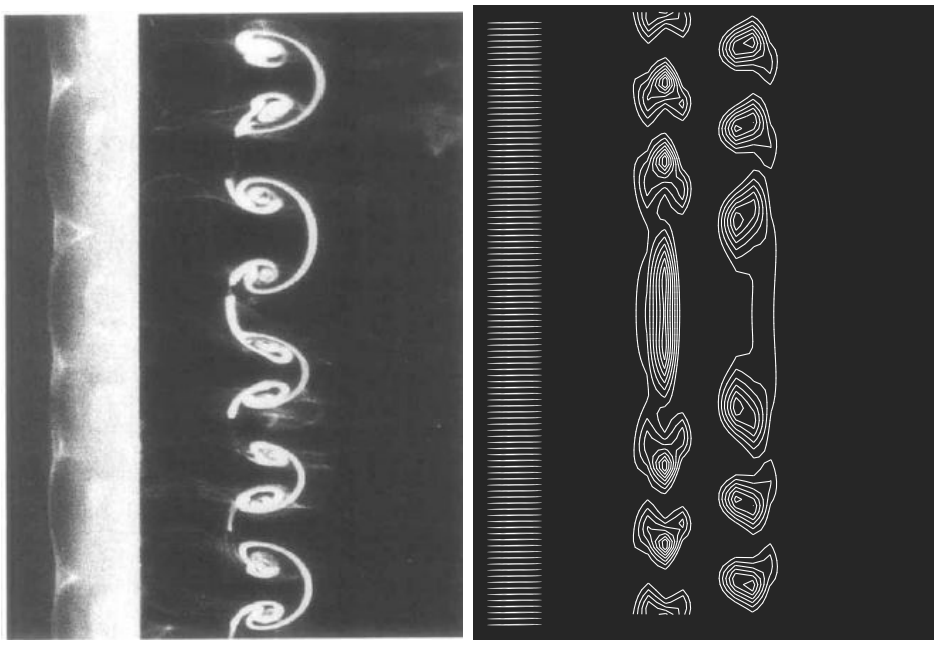

(b) An experimentally observed flow [75].(c) Eqn. 130 at $V_\infty t/R \approx 495.9$ $y/D \approx 6.2$, *forced* vortices).

Figure 46: Comparison of an experimentally observed flow with present theoretical streamlines (absolute values of Eqn. 130) showing three-dimensional vortex shedding at $Re_\infty = 300$.

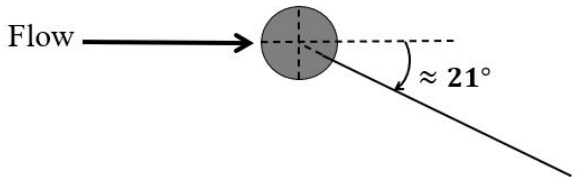

(a) Plane of theoretical flow in (b).

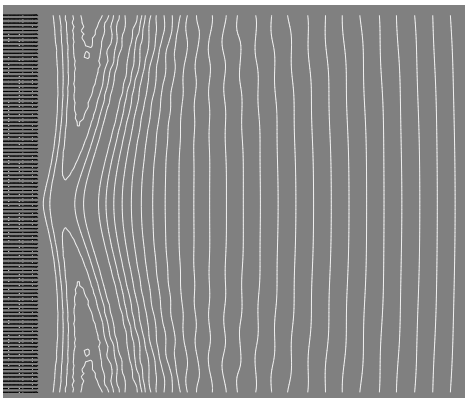

(b) Eqn. 130 at $Re_\infty = 300$, $V_\infty t/R = 495.9$, (*forced* vortices).

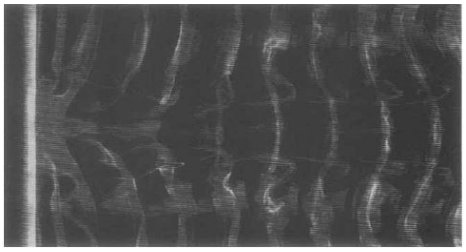

(c) An experimentally observed flow [75].

Figure 47: Comparison of an experimentally observed flow with present theoretical streamlines (absolute value of Eqn. 130) showing three-dimensional vortex shedding.

linearly-spaced gridpoints from R to $24R$ in the radial direction, and the same number of points from $-\pi$ to π in the circumferential direction.

The conservation of mass requires that the mass flow rate ($\dot{m} = \rho V A$) is constant in any arbitrary differential control volume in Fig. 49a. Then, the differential of the mass flow rate,

$$d(\rho V A) = 0$$

where A is a variable cross-sectional area with unit depth into the page. This gives a relation between the changes in V, A and ρ [76] as

$$\frac{dV}{V} + \frac{dA}{A} + \frac{d\rho}{\rho} = 0 \, . \tag{134}$$

For a flow that is assumed to be incompressible as the foregoing, $d\rho/\rho$ is small and negligible [5]. The differential change in velocity, dV/V, between the freestream and any part of the flow is modest. This is accompanied with corresponding change in area, dA/A between the streamlines. This explains the clustering of $\tilde{\kappa}$ contour lines towards the cylinder crests from the freestream in Fig. 49a. However, dV/V is very high towards the core of the shed vortices as Fig. 49b illustrates. This suggests that there are also corresponding changes in density that are not negligible.

The approach used to derive the full classical velocity potential equations [5, pp. 714 -716] is employed to include compressibility effects. The square of the adiabatic speed of sound

$$a^2 = a_0^2 - \frac{\gamma - 1}{2} V^2 \quad , \tag{135}$$

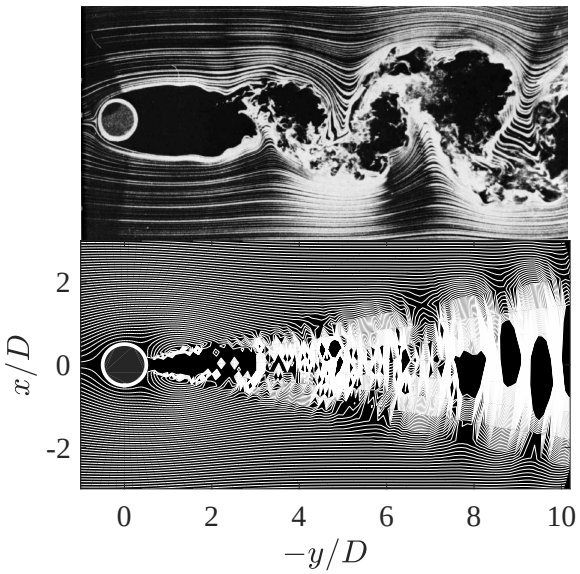

Figure 48: An experimentally observed flow (upper image [7]) and the theoretical streamlines obtained with real part of Eqn. 130 (lower image) at $Re_\infty = 10,000$ ($V_\infty t/R = 16,535$, *forced* vortices).

along with an isentropic relation between pressure and density

$$\begin{aligned} dp &= a^2 d\rho \\ dp &= -\rho V dV = -\frac{\rho d(V^2)}{2} \\ \frac{d\rho}{\rho} &= -\frac{d(V^2)}{2a^2} \\ &= -\frac{1}{2\left(a_0^2 - \frac{\gamma-1}{2}V^2\right)} d(V^2)\,. \end{aligned} \tag{136}$$

are used to model the propagation of disturbances in the flow field. In Eqn. 136, V is obtained from $\tilde{\kappa}$, and γ is the ratio of the specific heats of the fluid [5]. Therefore, the density field

$$\frac{\rho}{\rho_\infty} = \left(\frac{1 - \frac{\gamma-1}{2}M_\infty^2}{1 - \frac{\gamma-1}{2}M^2}\right)^{\frac{1}{\gamma-1}} \tag{137}$$

is derived from the integration of the differential equation in ρ and V. It is assumed

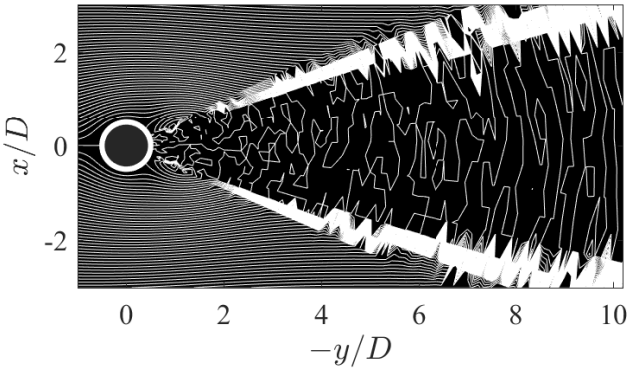

(a) $real(\tilde{\kappa}/V_\infty R)$ (streamlines)

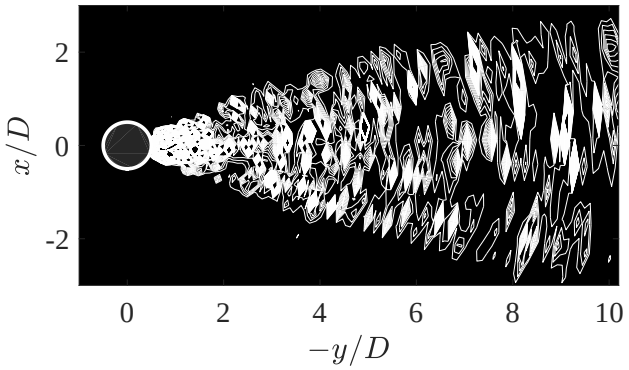

(b) $real(V/V_{max})$

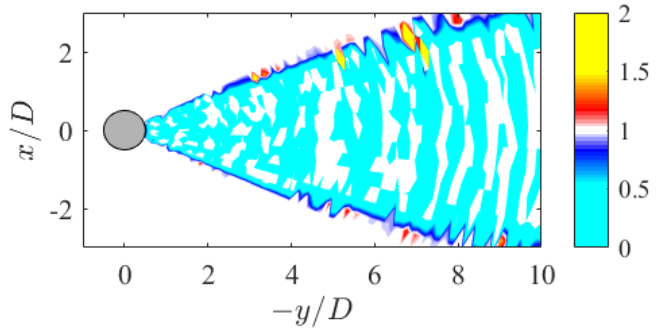

(c) $real(\rho/\rho_\infty)$

Figure 49: The present theoretical flow in a cylinder wake at $Re_\infty = 4.0 \times 10^5$ for $V_\infty t/R \approx 8.3 \times 10^5$, $\gamma = 1.4$ and $a_\infty = 343 m/s$.

that the stagnation speed of sound, a_0, is equal to the freestream value, a_∞. Thus, the freestream Mach number, M_∞ is equal to V_∞/a_∞, and the local Mach number, M is equal to V/a_∞ in Eqn. 137. Figure 49c presents a contour of Eqn. 137 corresponding to Figs. 49a and 49b. It is observable that the density in the shed wake vortices is generally lower than the freestream.

With Eqn. 137, the compressible *Kwasu* function, κ is defined as

$$\kappa = \rho\tilde{\kappa} \, . \tag{138}$$

The velocity components in the cylindrical coordinate system are derived as

$$\left\{ \begin{array}{c} V_r \\ \\ V_\theta \\ \\ V_{\tilde{z}} \end{array} \right\} = \frac{\nabla \times \kappa}{\rho} = \left\{ \begin{array}{c} \dfrac{1}{\rho r}\dfrac{\partial \kappa}{\partial \theta} \\ \\ -\dfrac{1}{\rho}\dfrac{\partial \kappa}{\partial r} \\ \\ 0 \end{array} \right\} , \tag{139}$$

and in the Cartesian coordinate system as

$$\left\{ \begin{array}{c} V_{\tilde{x}} \\ \\ V_{\tilde{y}} \\ \\ V_{\tilde{z}} \end{array} \right\} = \frac{\nabla \kappa}{\rho} = \left\{ \begin{array}{c} \dfrac{1}{\rho}\dfrac{\partial \kappa}{\partial x} \\ \\ \dfrac{1}{\rho}\dfrac{\partial \kappa}{\partial y} \\ \\ \dfrac{1}{\rho}\dfrac{\partial \kappa}{\partial z} \end{array} \right\} . \tag{140}$$

The compressible *Kwasu* function satisfies the conservation of mass in

$$
\begin{aligned}
&\oint_{\mathcal{V}} \left[\frac{\partial \rho}{\partial t} + \nabla \cdot (\rho \mathbf{V})\right] d\mathcal{V} \\
&= \oint_{\mathcal{V}} \left[\frac{\partial \rho}{\partial t} + \frac{1}{r}\frac{\partial (r\rho V_r)}{\partial r} + \frac{1}{r}\frac{\partial (\rho V_\theta)}{\partial \theta} + \underbrace{\frac{\partial (\rho V_{\tilde{z}})}{\partial z}}_{=0}\right] d\mathcal{V} \\
&= \oint_{\mathcal{V}} \left[\frac{\partial \rho}{\partial t} + \frac{\rho V_r}{r} + \frac{\partial (\rho V_r)}{\partial r} + \frac{1}{r}\frac{\partial (\rho V_\theta)}{\partial \theta}\right] d\mathcal{V} \\
&= \oint_{\mathcal{V}} \left[\frac{\partial \rho}{\partial t} + \frac{1}{r^2}\frac{\partial \kappa}{\partial \theta} - \frac{1}{r^2}\frac{\partial \kappa}{\partial \theta} + \frac{1}{r}\frac{\partial^2 \kappa}{\partial r \partial \theta} - \frac{1}{r}\frac{\partial^2 \kappa}{\partial \theta \partial r}\right] d\mathcal{V} \\
&= \oint_{\mathcal{V}} \frac{\partial \rho}{\partial t} d\mathcal{V} \\
&= \frac{\partial}{\partial t}\left[\oint_{\mathcal{V}} \rho d\mathcal{V}\right] \\
&= 0 \quad (t \geq 0),
\end{aligned}
\tag{141}
$$

because the volume integral of the transient variation of the density is zero in the domain. It also conserves the momentum in

$$
\begin{aligned}
&\oint_{\mathcal{V}} \left[\frac{\partial (\rho \mathbf{V})}{\partial t} + \nabla \cdot (\mathbf{V}(\rho \mathbf{V})) - \nabla (2\mu \nabla \cdot \mathbf{V}) - \nabla \times (\mu \omega) + \nabla p\right] d\mathcal{V} \\
&= \oint_{\mathcal{V}} \left[\frac{\partial \left(\rho \dfrac{\nabla \kappa}{\rho}\right)}{\partial t} + \nabla \cdot (\mathbf{V}(\rho \mathbf{V})) - \nabla (2\mu \nabla \cdot \mathbf{V}) - \nabla \times (\mu \omega) + \nabla p\right] d\mathcal{V} \\
&= \oint_{\mathcal{V}} \left[\nabla \frac{\partial \kappa}{\partial t} + \mathbf{V} \underbrace{\nabla \cdot (\rho \mathbf{V})}_{=0} + \underbrace{(\rho \mathbf{V}) \cdot \nabla \mathbf{V}}_{=\nabla \rho \frac{V^2}{2} - \rho \mathbf{V} \times \omega} - \nabla (2\mu \nabla \cdot \mathbf{V}) - \nabla \times (\mu \omega) + \nabla p\right] d\mathcal{V} \\
&= \oint_{\mathcal{V}} \left[\nabla \left(p + \frac{\partial \kappa}{\partial t} - 2\mu \underbrace{\nabla \cdot \mathbf{V}}_{\nabla \cdot \left(\frac{\nabla \kappa}{\rho}\right)}\right) + \underbrace{\nabla \rho \frac{V^2}{2}}_{\nabla \frac{\rho}{2}\left(\frac{\nabla \kappa}{\rho}\right)^2} - \underbrace{\rho \mathbf{V} \times \omega - \nabla \times (\mu \omega)}_{=0}\right] d\mathcal{V} \\
&= \oint_{\mathcal{V}} \left[\nabla \left(p + \frac{\partial \kappa}{\partial t} + \frac{\rho}{2}\left(\frac{\nabla \kappa}{\rho}\right)^2 - 2\mu \nabla \cdot \left(\frac{\nabla \kappa}{\rho}\right)\right)\right] d\mathcal{V} \\
&= 0 \, .
\end{aligned}
\tag{142}
$$

Then, the compressible thermodynamic pressure field is obtained as

$$p = -\frac{\partial \kappa}{\partial t} - \frac{\rho}{2}\left(\frac{\nabla \kappa}{\rho}\right)^2 + 2\mu \nabla \cdot \left(\frac{\nabla \kappa}{\rho}\right) + F(t) \tag{143}$$

where $F(t)$ is a function of time. $F(t)$ is taken to be the freestream thermodynamic pressure, p_∞. Because the *Kwasu* function is defined on a principal axis of the flow, the second coefficient of viscosity, λ, and the viscous normal stresses cannot be neglected in Eqns. 2 and 4. Therefore, the mechanical pressure field is given as

$$\tilde{p} = -\frac{\partial \kappa}{\partial t} - \frac{\rho}{2}\left(\frac{\nabla \kappa}{\rho}\right)^2 + \left(\lambda + \frac{2}{3}\mu\right) \nabla \cdot \left(\frac{\nabla \kappa}{\rho}\right) + p_\infty \, . \tag{144}$$

This is used to express the pressure coefficient subsequently.

The *Kwasu* function models the three-dimensional unsteady compressible cylinder flow field in an Eulerian frame. It simultaneously satisfies the continuity equation and NSE. It exhibits a singularity at the absolute spatio-temporal origin where $x = y = z = t = 0$. However, it is continuous in time and space away from the origin except at $\theta = 0$. Therefore, ϵ is incorporated to remove singularities at $r = \theta = 0$ as

$$\epsilon = \begin{cases} +O(10^{-3}) \, , & r = 0; \theta \geq 0 \\ -O(10^{-3}), & \theta < 0 \end{cases} \, . \tag{145}$$

Other parameters employed in the *Kwasu* function are summarized in Table 4.

The condition of the wall velocity components are

$$\begin{aligned}
V_{r,w} &= \mu_g \left[\frac{1}{\rho r}\frac{\partial \rho}{\partial \theta}\frac{1}{r}\frac{\partial \mathcal{T}}{\partial \theta} + \frac{1}{r^2}\frac{\partial^2 \mathcal{T}}{\partial \theta^2}\right]_w \\
V_{\theta,w} &= -2V_\infty \sin\theta \left(1 - \mathrm{e}^{-\frac{R^2}{V_\infty^2 t^2}}\right) - \mu_g \left[\frac{1}{\rho}\frac{\partial \rho}{\partial r}\frac{\partial \mathcal{T}}{r\partial \theta} + \frac{1}{r}\frac{\partial^2 \mathcal{T}}{\partial r \partial \theta} - \frac{1}{r^2}\frac{\partial \mathcal{T}}{\partial \theta}\right]_w \\
V_{z,w} &= 2V_\infty \sin\theta \left(1 - \mathrm{e}^{-\frac{R^2}{V_\infty^2 t^2}}\right) \cos\varphi + \mu_g \left[\frac{1}{\rho}\frac{\partial \rho}{\partial r}\frac{\partial \mathcal{T}}{r\partial \theta} + \frac{1}{r}\frac{\partial^2 \mathcal{T}}{\partial r \partial \theta} - \frac{1}{r^2}\frac{\partial \mathcal{T}}{\partial \theta}\right]_w \cos\varphi \, .
\end{aligned} \tag{146}$$

Lauga et al. [77] identify factors such as the surface roughness, shear rate, and pressure that affect the slip velocity. It is observed that these factors are present in

Eqn. 146 through R, t and V_∞ respectively. For a constant R and V_∞, when $t = 0$, $\mathrm{e}^{-R^2/V_\infty^2 t^2} = 0$. Then, the wall velocity components are

$$\begin{aligned} V_{r,w} &= \mu_g \left[\frac{1}{\rho r} \frac{\partial \rho}{\partial \theta} \frac{1}{r} \frac{\partial \mathcal{T}}{\partial \theta} + \frac{1}{r^2} \frac{\partial^2 \mathcal{T}}{\partial \theta^2} \right]_{w,t=0} \\ V_{\theta,w} &= -2V_\infty \sin\theta - \mu_g \left[\frac{1}{\rho} \frac{\partial \rho}{\partial r} \frac{\partial \mathcal{T}}{r \partial \theta} + \frac{1}{r} \frac{\partial^2 \mathcal{T}}{\partial r \partial \theta} - \frac{1}{r^2} \frac{\partial \mathcal{T}}{\partial \theta} \right]_{w,t=0} \\ V_{z,w} &= 2V_\infty \sin\theta \cos\varphi + \mu_g \left[\frac{1}{\rho} \frac{\partial \rho}{\partial r} \frac{\partial \mathcal{T}}{r \partial \theta} + \frac{1}{r} \frac{\partial^2 \mathcal{T}}{\partial r \partial \theta} - \frac{1}{r^2} \frac{\partial \mathcal{T}}{\partial \theta} \right]_{w,t=0} \cos\varphi \,. \end{aligned} \tag{147}$$

As t tends to infinity, $\mathrm{e}^{-R^2/V_\infty^2 t^2} \to 1$, and the wall velocity components approach

$$\begin{aligned} V_{r,w} &= \mu_g \left[\frac{1}{\rho r} \frac{\partial \rho}{\partial \theta} \frac{1}{r} \frac{\partial \mathcal{T}}{\partial \theta} + \frac{1}{r^2} \frac{\partial^2 \mathcal{T}}{\partial \theta^2} \right]_{w,t\to\infty} \\ V_{\theta,w} &= -\mu_g \left[\frac{1}{\rho} \frac{\partial \rho}{\partial r} \frac{\partial \mathcal{T}}{r \partial \theta} + \frac{1}{r} \frac{\partial^2 \mathcal{T}}{\partial r \partial \theta} - \frac{1}{r^2} \frac{\partial \mathcal{T}}{\partial \theta} \right]_{w,t\to\infty} \\ V_{z,w} &= \mu_g \left[\frac{1}{\rho} \frac{\partial \rho}{\partial r} \frac{\partial \mathcal{T}}{r \partial \theta} + \frac{1}{r} \frac{\partial^2 \mathcal{T}}{\partial r \partial \theta} - \frac{1}{r^2} \frac{\partial \mathcal{T}}{\partial \theta} \right]_{w,t\to\infty} \cos\varphi \,. \end{aligned} \tag{148}$$

Equation 148 is in agreement with Brenner's experimental observations that the fluid compressibility affects the no-slip condition. Brenner proposes

$$V_w = -\alpha \frac{1}{\rho} \frac{\partial \rho}{\partial s}|_w \tag{149}$$

for the streamwise slip velocity along a relatively flat wall where α is the fluid's thermometric diffusivity, and δs is the distance measured along the wall [34].

2.2 The Lagragian Kwasu Function

Experimentally observed flows are usually dynamically unsteady as they become turbulent with localized fluctuations [15, 78]. A Lagrangian description is used to model these dynamic and localized fluctuations in RPT. The overlay of the real part of Eqn. 115 on its absolute value in Fig. 38a bears some resemblance to the simultaneous visualization of experimental streamlines and streaklines in Fig. 34c. This suggests that the normalized stream function theorizes the streaklines as follow.

The *Kwasu* function is a stream function that has different constant values c_1, c_2 and so on for each streamline as depicted in Fig. 50 for a two-dimensional uniform

Table 4: A summary of the semi-empirical parameters in the RPT.

Parameter	Value	Purpose
c	2	removes discontinuity
q	$\frac{130}{Re^2}\left(0.03061Re\right)^{\mathrm{e}^{-10/Re}}$	wake dimension
χ	$(-1)^{\exp\left(-\exp\left(N\arctan\left[X,y\right]\right)\right)}$	symmetry about wind $\tilde{x}$-axis
j	$1/5$	coefficient of vortex shedding function
ζ	$130/Re^2$	extends vortex shedding to very high Re
ι	$125/Re$	triggers vortex shedding at $Re \approx 50$
η	$(-1)^{\exp\left(-\exp\left(N\arctan\left[Y,x\right]\right)\right)}$	vortex shedding in the wake
N	1.8×10^6	controls χ and η
σ	$\begin{cases} -\pi, & \theta \geq 0 \\ \pi, & \theta < 0 \end{cases}$	wake positioning in $\psi_{sink/source}$
ϵ	$\begin{cases} +O(10^{-3}) \ , & r = 0; \theta \geq 0 \\ -O(10^{-3}), & \theta < 0 \end{cases}$	removes discontinuities at $r = \theta = 0$
y_m	$7R/20$	controls the flow axis
y_n	$3R/4$	controls the flow axis
$\tilde{\theta}_n$	$54\pi/180 \ (rads)$	controls wake pressure variation

flow. The flow is moving with a velocity, V. ΔA is a rectangular cross-sectional area of the depicted control volume with a unit depth into the page. ΔA is chosen such that V is constant across it. Because κ is a compressible stream function, its change, $\Delta\kappa$ along ΔA between the depicted streamlines ab and cd is equal to the mass flow rate through the control volume between these streamlines. That is

$$\Delta\kappa = c_2 - c_1 \equiv \rho V \Delta x(1),$$

and

$$\frac{\Delta\kappa}{\Delta x} = \rho V \ . \tag{150}$$

The limit as $\Delta x \to 0$ gives

$$\rho V = \lim_{\Delta x \to 0} \frac{\Delta\kappa}{\Delta x} \equiv \frac{\partial \kappa}{\partial x} \ . \tag{151}$$

That is

$$\frac{\partial \kappa}{\partial x} = \rho V \ .$$

The frestream values of ρ and V are constant. So,

$$\frac{\partial \kappa}{\partial x} = \rho_\infty V_\infty \ , \tag{152}$$

and the *Kwasu* function for the uniform flow is integrated as

$$\kappa = \rho_\infty V_\infty x + c \ , \tag{153}$$

where c is an arbitrary constant that can be set to zero for $x = 0$. This means for any specific x location, κ describes the mass flow rate tracing the particles that have passed through that location. Therefore, the x locus of these particles as they flow along the y-axis, that is the streakline, is obtained by normalizing Eqn. 153 as

$$x = \frac{\kappa}{\rho_\infty V_\infty} \ .$$

It is observable in Fig. 50 that this results in lines of constant x-coordinate for the uniform flow. The geometric x-axis is equivalent to the wind $\tilde{y}$-axis in the present

theory. Thus, for the cylinder flow described with Eqn. 138, the wind $\tilde{y}$-axis is

$$\tilde{y} = \frac{\kappa}{\rho_\infty V_\infty} \, . \tag{154}$$

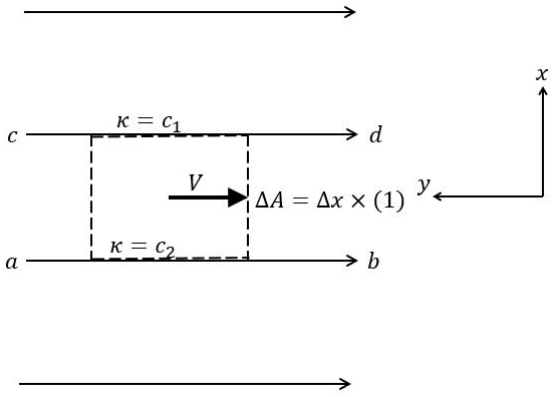

Figure 50: A uniform freestream flow.

Figure 51 compares an experimentally observed flow to the present theoretical streamlines and streaklines in the and $z = 0$ plane, and at $Re_\infty = 2,000$ and $V_\infty t/R = 165.35$. The flow was evaluated on a static meshgrid with one hundred linearly-spaced points for $-1.5 \leq x/D \leq 1.5$, the same number of points for $-4 \leq y/D \leq 2$, and eleven points for $-\pi \leq z/D \leq \pi$. The thoeretical streamlines in Fig. 51a are contours of the normalized absolute value of Eqn. 130. The theoretical time is arbitrary, and forty-four linearly-spaced contour levels from 0 to 1.3 are shown. The theoretical streamline pattern is qualitatively similar to the experimentally observed flow visualized in Fig. 51b. The quiescent recirculation flow in the near-wake between the shedding vortices from the cylinder crests is noticeable. However, the separation points are further downstream in the theory than in the experiment. This is likely because of other experimental conditions that are not modeled. It may also be because flow separation is unsteady. Figure 51c is a plot of the streakline cross-flow coordinate, $\tilde{y}/D$ (wind y-axis) corresponding to the flow conditions in Fig. 51a. The flow was evaluated on the same grid as in Fig. 52. Twenty-one streaklines with

starting coordinates $(x_0/D, y_0/D) = (-0.9242 \geq x/D \geq -0.3182, 2)$ and the same number with starting coordinates $(x_0/D, y_0/D) = (0.2879 \leq x/D \leq 0.8939, 2)$ are plotted in red and blue lines respectively. Figure 51d provides a close-up view of the freestream of Fig. 51c.

The fluid element pathline coordinates are obtained from the Eulerian velocity field as

$$\begin{aligned}
\tilde{X} &= \int \frac{\partial \tilde{X}}{\partial t} dt = \frac{1}{\rho_\infty} \int \rho V_{\tilde{x}} dt = \frac{1}{\rho_\infty} \rho V_{\tilde{x}} t - \frac{1}{\rho_\infty} \int \underset{\uparrow}{t} \underset{u}{} d(\rho V_{\tilde{x}}) \\
\tilde{Y} &= \int \frac{\partial \tilde{Y}}{\partial t} dt = \frac{1}{\rho_\infty} \int \rho V_{\tilde{y}} dt = \frac{1}{\rho_\infty} \rho V_{\tilde{y}} t - \frac{1}{\rho_\infty} \int \underset{\uparrow}{t} \underset{v}{} d(\rho V_{\tilde{y}}) \\
\tilde{Z} &= \int \frac{\partial \tilde{Z}}{\partial t} dt = \frac{1}{\rho_\infty} \int \rho V_{\tilde{z}} dt = \frac{1}{\rho_\infty} \rho V_{\tilde{z}} t - \frac{1}{\rho_\infty} \int \underset{\uparrow}{t} \underset{w}{} d(\rho V_{\tilde{z}})
\end{aligned} \tag{155}$$

using integration by parts. To obtain the underset integrals in Eqn. 155, the displacements of each fluid element along its path in three-dimensional space (u, v and w corresponding to x, y and z directions respectively) are assumed to be independently governed by one-dimensional wave equations in each of the coordinate directions. Then, the wave equations [62, p. 700] for these displacements are specified as

$$\begin{aligned}
&\frac{\partial^2 u}{\partial t^2} = V_\infty^2 \frac{\partial^2 u}{\partial x^2}, \quad u(t_0, x, y, z) = x_0, \quad \frac{\partial u}{\partial t} \equiv \frac{1}{\rho_\infty V_\infty} \frac{\partial \kappa}{\partial t}, \; t > 0 \\
&\frac{\partial^2 v}{\partial t^2} = V_\infty^2 \frac{\partial^2 v}{\partial y^2}, \quad v(t_0, x, y, z) = y_0, \quad \frac{\partial v}{\partial t} \equiv \frac{1}{\rho_\infty V_\infty} \frac{\partial \kappa}{\partial t}, \; t > 0 \\
&\frac{\partial^2 w}{\partial t^2} = V_\infty^2 \frac{\partial^2 w}{\partial z^2}, \quad w(t_0, x, y, z) = z_0, \quad \frac{\partial w}{\partial t} \equiv \frac{1}{\rho_\infty V_\infty} \frac{\partial \kappa}{\partial t}, \; t > 0 \; .
\end{aligned} \tag{156}$$

The solutions to these equations are obtained with the d'Alembert's solution for one-dimensional transverse wave equations [62, p. 705] and the Eulerian *Kwasu* function

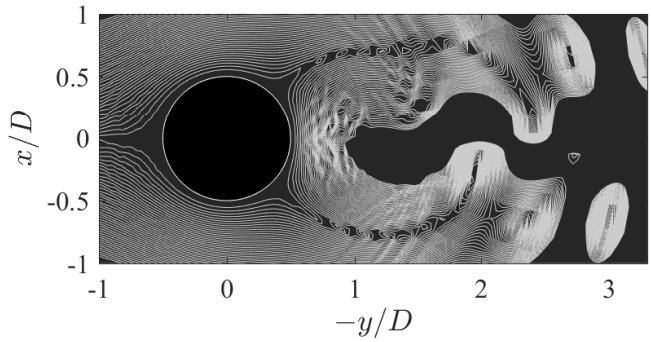

(a) Present theoretical streamlines (*forced* vortices)

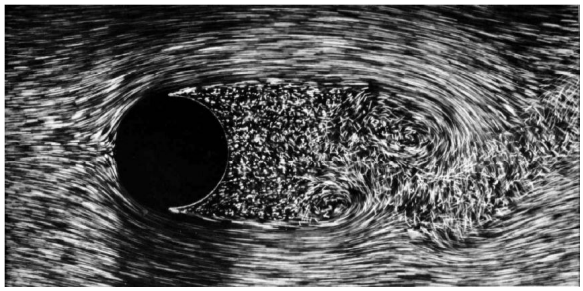

(b) An experimental flow [7]

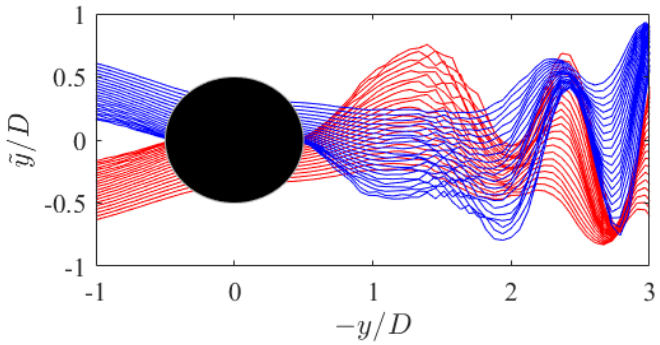

(c) Present theoretical streaklines (*forced* vortices)

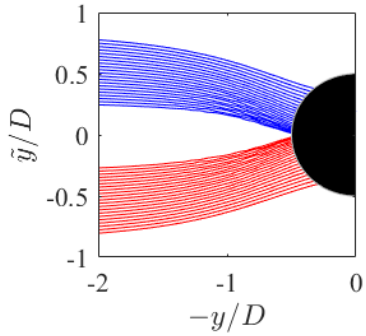

(d) Theoretical streaklines in the frestream of (c).

Figure 51: The present theoretical cylinder crossflow compared with a photograph of an experimentally observed flow at $Re_\infty = 2,000$.

as

$$
\begin{aligned}
u(t,x,y,z) &= \frac{1}{2\rho_\infty V_\infty}\int_{x-V_\infty t}^{x+V_\infty t}\rho V_{\tilde{x}}dx = \frac{\kappa(t,x+V_\infty t,y,z)-\kappa(t,x-V_\infty t,y,z)}{2\rho_\infty V_\infty} \\
v(t,x,y,z) &= \frac{1}{2\rho_\infty V_\infty}\int_{y-V_\infty t}^{y+V_\infty t}\rho V_{\tilde{y}}dy = \frac{\kappa(t,x,y+V_\infty t,z)-\kappa(t,x,y-V_\infty t,z)}{2\rho_\infty V_\infty} \\
w(t,x,y,z) &= \frac{1}{2\rho_\infty V_\infty}\int_{z-V_\infty t}^{z+V_\infty t}\rho V_z dz = \frac{\kappa(t,x,y,z+V_\infty t)-\kappa(t,x,y,z-V_\infty t)}{2\rho_\infty V_\infty}
\end{aligned}
\quad . \tag{157}
$$

That is, for $u(t,x,y,z)$, the substitutions

$$
r = \sqrt{(x+V_\infty t)^2+y^2+z^2} \qquad \theta = \arctan\left[y,(x+V_\infty t)\right]
$$

and

$$
r = \sqrt{(x-V_\infty t)^2+y^2+z^2} \qquad \theta = \arctan\left[y,(x-V_\infty t)\right]
$$

are made in $\kappa(t,x+V_\infty t,y,z)$ and $\kappa(t,x-V_\infty t,y,z)$ in Eqn. 157 respectively. Similar substitutions are used in the expressions for v and w.

These equations are not functions of the individual particle label characteristic of an original Lagrangian description. However, they are in consistence with Andrews' and McIntyre's Eulerian description of Lagrangian-mean flows [79]. Thus, the Eulerian *Kwasu* function is interpreted as a time-dependent mean flow because it was derived from a time-invariant theory. The time-dependent pathline coordinates are subsequently used to define the time-dependent body axis as

$$
\begin{aligned}
x(t) &= x_{(t=0)} - \tilde{Y} \\
y(t) &= y_{(t=0)} + \tilde{X} \\
z(t) &= z_{(t=0)} - \tilde{Z}
\end{aligned}
\tag{158}
$$

in which the negative sign of the $\tilde{Y}$ displacement is because the flow is from left to right. The signs of the other displacements are set to be consistent with this flow direction. $x_{(t=0)}$, $y_{(t=0)}$ and $z_{(t=0)}$ are the coordinates of the static three-dimensional domain in Eqn. 56. They are the constants of integration in Eqn. 155. The pairing of $y_{(t=0)}$ with $\tilde{X}$ (and $x_{(t=0)}$ with $\tilde{Y}$) is because the freestream is aligned with the

geometric y-axis in the *Kwasu* function. Equation 158 is illustrated in Fig. 52 for a cylinder crossflow at the same conditions as Fig. 51a

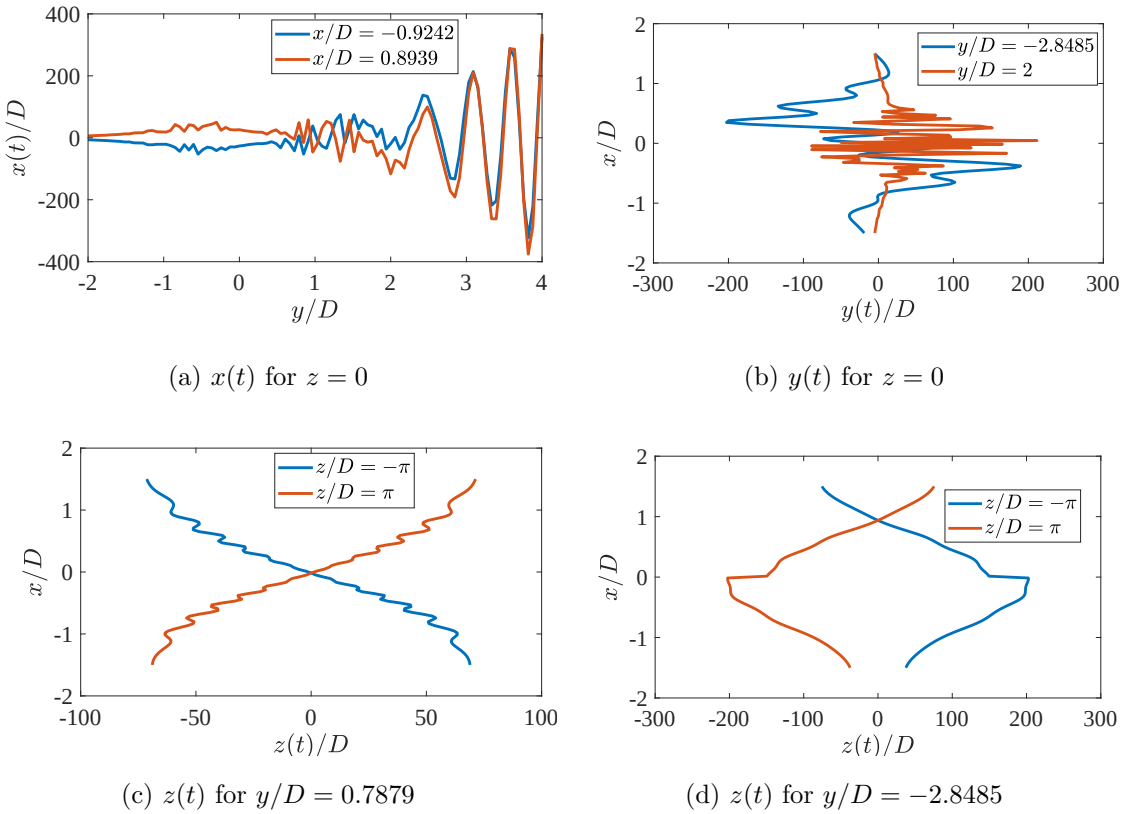

(a) $x(t)$ for $z = 0$

(b) $y(t)$ for $z = 0$

(c) $z(t)$ for $y/D = 0.7879$

(d) $z(t)$ for $y/D = -2.8485$

Figure 52: The present theoretical cylinder crossflow pathlines at $Re_\infty = 2,000$ and $V_\infty t/R = 165.35$ (*forced* vortices).

Equation 158 is referred to as a dynamic grid. When it is used in place of the static grid in Eqn. 56, it introduces dynamic unsteadiness into the flow field. Thus, the interaction of the local oscillatory motions with the statically unsteady mean flow is described in consistence with the generalized Lagrangian-mean (GLM) theory [79]. The freestream velocity can be unsteady depending on the prescribed motions of the body. In a steady freestream as the present case, the three means by which unsteady fluctuations have been introduced into the refined potential theory are:

1. the transient variation in the exponential terms of Eulerian κ;

2. the oscillatory displacements of the fluid element paths; and

3. the dynamic grid.

The dynamic grid introduces large-amplitude local variations into the foregoing solution. This results in a field equivalent to a Lagrangian disturbance field in GLM [79, 80].

The instantaneous Lagrangian-mean *Kwasu* function, κ^L is defined as

$$\kappa^L = \kappa^E + \kappa^S \tag{159}$$

where κ^E represents the Eulerian-mean *Kwasu* function and κ^S denotes the Stokes' correction to account for differences in the frame of reference for the averages [79,80]. Both of these are evaluated on a static grid. The definition in Eqn. 159 is used for all other field quantities including the velocity as

$$V^L = V^E + \underset{\substack{\uparrow \\ \text{drift velocity}}}{V^S} \quad . \tag{160}$$

The drift velocity is the Stokes' correction for the velocity [79,80]. The Stokes' correction is a wave property that can be evaluated from a mean flow and linearized wave solutions as in Eqn. 157 [79,80]. The Lagrangian velocity components are time derivatives of the dynamic grid coordinates. The Lagrangian-mean velocity components are subsequent time-averaged integrals of Lagrangian velocity components. Thus, these

components are obtained as

$$
\begin{aligned}
V_x^L &= \frac{\rho_\infty}{t\rho}\int_0^t \rho V_x dt \\
&= \frac{\rho_\infty}{t\rho}\int_0^t \frac{\partial x(t)}{\partial t} dt \\
&= \frac{\rho_\infty (x(t) - x(0))}{t\rho} \\
&= -\frac{\rho_\infty \tilde{Y}}{t\rho} \\
&= -V_{\tilde{y}} + \frac{\rho_\infty v}{t\rho} \\
V_y^L &= \frac{\rho_\infty}{t\rho}\int_0^t \rho V_y dt \\
&= \frac{\rho_\infty}{t\rho}\int_0^t \frac{\partial y(t)}{\partial t} dt \\
&= \frac{\rho_\infty (y(t) - y(0))}{t\rho} \\
&= \frac{\rho_\infty \tilde{X}}{t\rho} \\
&= V_{\tilde{x}} - \frac{\rho_\infty u}{t\rho} \\
V_z^L &= \frac{\rho_\infty}{t\rho}\int_0^t \rho V_z dt \\
&= \frac{\rho_\infty}{t\rho}\int_0^t \frac{\partial z(t)}{\partial t} dt \\
&= \frac{\rho_\infty (z(t) - z(0))}{t\rho} \\
&= -\frac{\rho_\infty \tilde{Z}}{t\rho} \\
&= V_{\tilde{z}} - \frac{\rho_\infty w}{t\rho}\,.
\end{aligned}
\tag{161}
$$

The radial and tangential Lagrangian-mean velocity components are

$$
\begin{aligned}
V_r^L &= V_x^L \cos\theta + V_y^L \sin\theta \\
&= -\frac{\rho_\infty \tilde{Y}}{t\rho}\cos\theta + \frac{\rho_\infty \tilde{X}}{t\rho}\sin\theta \\
&= -(-V_{\tilde{y}} + \frac{\rho_\infty v}{t\rho})\cos\theta + (V_{\tilde{x}} - \frac{\rho_\infty u}{t\rho})\sin\theta \\
&= \underbrace{(V_{\tilde{y}}\cos\theta + V_{\tilde{x}}\sin\theta)}_{V_r^E} - \underbrace{(\frac{\rho_\infty v}{t\rho}\cos\theta + \frac{\rho_\infty u}{t\rho}\sin\theta)}_{V_r^S} \\
V_\theta^L &= -V_x^L \sin\theta + V_y^L \cos\theta \\
&= \frac{\rho_\infty \tilde{Y}}{t\rho}\sin\theta + \frac{\rho_\infty \tilde{X}}{t\rho}\cos\theta \\
&= (-V_{\tilde{y}} + \frac{\rho_\infty v}{t\rho})\sin\theta + (V_{\tilde{x}} - \frac{\rho_\infty u}{t\rho})\cos\theta \\
&= \underbrace{(-V_{\tilde{y}}\sin\theta + V_{\tilde{x}}\cos\theta)}_{V_\theta^E} + \underbrace{(\frac{\rho_\infty v}{t\rho}\sin\theta - \frac{\rho_\infty u}{t\rho}\cos\theta)}_{V_\theta^S} .
\end{aligned}
\tag{162}
$$

Other Lagrangian-mean quantities like the vorticity are expressed based on these Lagrangian-mean velocity components accordingly. For instance, the magnitude of the Lagrangian-mean specific angular momentum of a fluid particle is

$$h^L = rV_\theta^L . \tag{163}$$

In the perifocal frame, h is equivalent to the negative of the stream function (see page 72). Thus, the Lagrangian-mean *Kwasu* function is

$$\kappa^L = -h^L = -rV_\theta^L . \tag{164}$$

2.3 The Bulk Viscosity Coefficient

The determination of the coefficient of bulk viscosity, $\left(\lambda + \frac{2}{3}\mu\right)$ is integral to the applicability of refined potential theory. This can be observed from the pressure

coefficient, C_p, in

$$\begin{aligned} C_p &= \frac{2\left(p - p_\infty\right)}{\rho_\infty V_\infty^2} \\ &= -\frac{2}{\rho_\infty V_\infty^2}\left(\frac{\partial \kappa}{\partial t} + \frac{\rho}{2}\left(\frac{\nabla \kappa}{\rho}\right)^2 - \left(\lambda + \tfrac{2}{3}\mu\right)\nabla \cdot \left(\frac{\nabla \kappa}{\rho}\right)\right) . \end{aligned} \tag{165}$$

However, the coefficient of bulk viscosity has been the subject of debate in the literature [15, 30, 33, 38, 39, 81].

Stokes hypothesized that the second coefficient of viscosity is given as [15,33,38,39]

$$\lambda = -\frac{2}{3}\mu \, . \tag{166}$$

This hypothesis assumes that the dilatation of a fluid element does not constitute any viscous stress [15, 38]. It is consistent with the thermodynamics requirement that

$$\lambda + \frac{2}{3}\mu \geq 0$$

for a positive definite dissipation function in the energy equation [15, 39]. Conflicting viewpoints about the hypothesis based on the kinectic theory of gases exist [38, 39]. Although difficult to obtain, indirect experimental measurements of λ show that it is positive for polyatomic gases [38] and most liquids [15, 39]. It can also be orders-of-magnitude-greater than the dynamic viscosity, μ [15, 38]. Therefore, the second part of the thermodynamics required inequality is the one in agreement with observations. Thus, a further assumption of an incompressible flow ($\nabla \cdot \mathbf{V} = 0$) is necessary [15,39]. This is also not supported by actual measurements of sound absorption in liquids that is affected by λ even though the nearly incompressible nature of liquids suggests otherwise [15]. λ is possibly frequency-dependent which suggests that it may not be a solely thermodynamic property [15, 39].

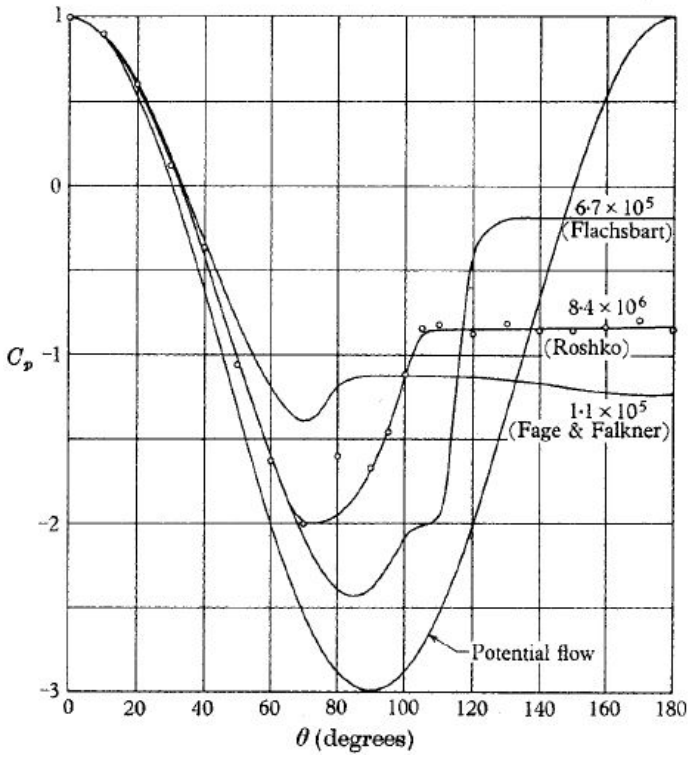

Figure 53: Comparison of the classical theoretical pressure distribution over a circular cylinder with experimental data for subcritical and supercritical Re_∞ [11].

The bulk viscosity is related to the dissipation of mechanical energy in the dispersion of sound waves in a fluid [33, 39, 82]. The presence of an obstacle in a flow is communicated through the fluid by sound waves some of which originate from the incident stagnation point [5]. Figure 53 presents a comparison of theoretical and experimental pressure distributions which shows the $C_p = 1$ at the stagnation point. Therefore, the stagnation point C_p yields an expression for the second coefficient of viscosity as

$$\lambda = \frac{\rho_\infty \left(\frac{V_\infty^2}{2} + \frac{1}{\rho_\infty} \frac{\partial \kappa}{\partial t} + \frac{\rho}{2\rho_\infty} \left(\frac{\nabla \kappa}{\rho} \right)^2 \right)}{\nabla \cdot \left(\frac{\nabla \kappa}{\rho} \right)} - \frac{2}{3} \mu \, . \tag{167}$$

in which κ is an Eulerian-mean quantity. The stagnation point is situated at $\tilde{\theta} = 0$. However, the singularity in the present solution at $\theta = 0$ precludes the evaluation of

Eqn. 167 at this point. Thus, λ is evaluated at $\tilde{\theta} = \pi$ for a cylinder (and at $\tilde{\theta} = -\pi$ for a sphere) using

$$\lambda = \frac{\rho_\infty \left(\frac{V_\infty^2}{2} - \frac{1}{\rho_\infty}\frac{\partial \kappa}{\partial t} + \frac{\rho}{2\rho_\infty}\left(\frac{-\nabla\kappa}{\rho}\right)^2 \right)}{\nabla \cdot \left(\frac{-\nabla\kappa}{\rho}\right)} - \frac{2}{3}\mu \, . \tag{168}$$

2.4 The Prediction of the Points of Separation and Transition, and the Boundary Layer Thickness

The shear stress vanishes at the onset of flow separation and/or reattachment at the wall because the velocity gradient goes through a change of sign [15, 33]. With reference to Fig. 32, the shear stress in the body axis is

$$\tau_{r\theta} = \mu \left(\frac{\partial V_\theta}{\partial r} - \frac{V_\theta}{r} + \frac{1}{r}\frac{\partial V_r}{\partial \theta} \right) \, . \tag{169}$$

This is illustrated in Fig. 54a ($c_f = 2\tau_{r\theta}/\rho_\infty V_\infty^2$) for varying values of $V_\infty t/R$ in a cylinder crossflow at $Re_\infty = 3,900$ and $z = 0$. The unsteady flow separation and/or attachment points are observable in this figure where the c_f distributions go through changes of sign. An analytical determination of these points cannot be made from solving Eqn. 169. This is because of the difficulty in isolating θ from the equation. However, this can be resolved in the perifocal frame as follow. With a further reference to Fig. 32, the shear stress in the perifocal frame is

$$\begin{aligned}
\tau_{\varrho\Theta} &= \mu \left(\frac{\partial V_\Theta}{\partial \varrho} - \frac{V_\Theta}{\varrho} + \frac{1}{\varrho}\frac{\partial V_\varrho}{\partial \Theta} \right) \\
&= \mu \left(\frac{\partial V_\Theta}{\partial \varrho} - \frac{V_\Theta}{\varrho} + \frac{1}{\varrho}\frac{\partial}{\partial \Theta}\left(\frac{\mu_g}{h}\varepsilon \sin\Theta \right) \right) \\
&= \mu \left(\frac{\partial V_\Theta}{\partial \varrho} - \frac{V_\Theta}{\varrho} + \frac{1}{\varrho h}\mu_g \varepsilon \cos\Theta \right) \\
&= \mu \left(\frac{\partial V_\Theta}{\partial \varrho} - \frac{V_\Theta}{\varrho} + \frac{1}{\varrho^2 V_\Theta}\mu_g \varepsilon \cos\Theta \right)
\end{aligned} \tag{170}$$

where all the variables are as previously defined in Sec. 2.1.4.2 and repeated below as

$$h = \varrho V_\Theta,$$

$$V_\Theta = \frac{h}{\varrho} = \frac{\mu_g}{h}\left(1 + \varepsilon\cos\Theta\right),$$
$$V_\varrho = \frac{\mu_g}{h}\varepsilon\sin\Theta,$$

and

$$\varepsilon = \sqrt{1 + \frac{h^2}{\mu_g^2}(V^2 - \frac{2\mu_g}{\varrho})}\,.$$

For a specific orbit, h and ε are constants [67]. The perifocal frame circumferential coordinate or true anomaly at $\tau_{\varrho\Theta} = 0$, $\Theta_{\tau_{\varrho\Theta}=0}$, is

$$\Theta_{\tau_{\varrho\Theta}=0} = \cos^{-1}\left[\left(\frac{\varrho V_\Theta^2 - \varrho^2 V_\Theta \dfrac{\partial V_\Theta}{\partial \varrho}}{\mu_g \varepsilon}\right)\right]. \tag{171}$$

Then, the right hand side of Eqn. 171 is expressed in the body axis to give

$$\Theta_{\tau_{\varrho\Theta}=0} = \cos^{-1}\left[\left(\frac{rV_\theta^2 - r^2 V_\theta \dfrac{\partial V_\theta}{\partial r}}{\mu_g \underbrace{\sqrt{1 + \dfrac{h^2}{\mu_g^2}\left(V^2 - \dfrac{2\mu_g}{r}\right)}}_{\varepsilon}}\right)_{r=R}\right] \tag{172}$$

in which the expression for the eccentricity, ε, has been substituted, and all the flow variables are Lagrangian-mean quantities.

A similar procedure is followed for determining the flow transition point. A divergence in the rate of change of the wall shear stress distribution in the local flow direction occurs in a natural transition to turbulent flow in the boundary layer [15,33].

The derivative of $\tau_{\varrho\Theta}$ in Θ-direction is

$$\begin{aligned}
\frac{1}{\varrho}\frac{\partial \tau_{\varrho\Theta}}{\partial \Theta} &= \mu \frac{1}{\varrho}\frac{\partial}{\partial \Theta}\left(\overset{h/\varrho}{\overset{\uparrow}{\frac{\partial V_\Theta}{\partial \varrho}}} - \frac{V_\Theta}{\varrho} + \frac{1}{\varrho}\frac{\partial V_\varrho}{\partial \Theta}\right) \\
&= \mu \frac{1}{\varrho}\frac{\partial}{\partial \Theta}\left(-\frac{V_\Theta}{\varrho} - \frac{V_\Theta}{\varrho} + \frac{1}{\varrho}\frac{\partial}{\partial \Theta}\left(\frac{\mu_g}{h}\varepsilon \sin\Theta\right)\right) \\
&= \mu \frac{1}{\varrho}\frac{\partial}{\partial \Theta}\left(-\frac{2V_\Theta}{\varrho} + \frac{1}{\varrho h}\mu_g \varepsilon \cos\Theta\right) \\
&= \mu \frac{1}{\varrho}\frac{\partial}{\partial \Theta}\left(-\frac{2\mu_g\left(1+\varepsilon\cos\Theta\right)/h}{h^2/\left(\mu_g\left(1+\varepsilon\cos\Theta\right)\right)} + \frac{1}{\varrho h}\mu_g \varepsilon \cos\Theta\right) \\
&= \mu \frac{1}{\varrho}\frac{\partial}{\partial \Theta}\left(-\frac{2\mu_g^2\left(1+\varepsilon\cos\Theta\right)^2}{h^3} + \frac{1}{\varrho h}\mu_g \varepsilon \cos\Theta\right) \\
&= \mu \frac{1}{\varrho}\frac{\partial}{\partial \Theta}\left(-\frac{2\mu_g^2\left(1+\varepsilon\cos\Theta\right)^2}{h^3} + \frac{1}{\varrho h}\mu_g \varepsilon \cos\Theta\right) .
\end{aligned} \tag{173}$$

At transition, Eqn. 173 diverges towards infinity. Examination of this equation indicates transition occurs when the specific angular momentum, h tends to zero. From $\varrho = h^2/\mu_g(1+\varepsilon\cos\Theta)$, an expression for h in terms of Θ is

$$h = \sqrt{\varrho\mu_g(1+\varepsilon\cos\Theta)}\,.$$

At the cylinder surface, $\varrho \neq 0$. μ_g is a very small number that is also not equal to zero. This implies $h \to 0$ when $(1+\varepsilon\cos\Theta) \to 0$. Therefore,

$$\Theta_{h=0} = \cos^{-1}\left[\left(-\frac{1}{\varepsilon}\right)_{\varrho=r=R}\right]$$

in the perifocal frame, and it is

$$\Theta_{h=0} = \cos^{-1}\left[\left(-\frac{1}{\sqrt{1+\frac{h^2}{\mu_g^2}\left(V^2 - \frac{2\mu_g}{r}\right)}}\right)_{r=R}\right] \tag{174}$$

in the body axis. All the flow variables in this equation are Lagrangian-mean quantities.

Equations 172 and 174 can result in complex numbers. For example, when their denominators are equal to zero, the inverse cosine gives $0 + i\infty$. Therefore, their real values are the physical quantities. When both the numerator and denominator in Eqn. 172 are zero, the inverse cosine is indeterminate. Then, $\Theta_{\tau_{\varrho\Theta}=0}$ is defaulted to zero.

To reference quantities in the perifocal frame to the body axis, the following fluid orbital elements are obtained as

$$\varphi_i = \cos^{-1}\left(\frac{h_z}{h}\right), \tag{175}$$

$$V_\varrho = \frac{(xV_{\tilde{x}} + yV_{\tilde{y}} + zV_z)}{r}, \tag{176}$$

$$\Omega = \cos^{-1}\left[\frac{h_y}{\sqrt{h_x^2 + h_y^2}}\right], \tag{177}$$

$$\Upsilon = \cos^{-1}\left[\frac{\frac{h_y}{\mu_g}\left[\left(V^2 - \frac{\mu_g}{r}\right)x - rV_\varrho V_{\tilde{x}}\right] - \frac{h_x}{\mu_g}\left[\left(V^2 - \frac{\mu_g}{r}\right)y - rV_\varrho V_{\tilde{y}}\right]}{\sqrt{\left(h_x^2 + h_y^2\right)\left(1 + \frac{h^2}{\mu_g^2}\left(V^2 - \frac{2\mu_g}{r}\right)\right)}}\right], \tag{178}$$

and

$$\{\mathbf{r}\}_{\tilde{x}} = \varrho \begin{Bmatrix} \cos\Theta \\ \sin\Theta \\ 0 \end{Bmatrix} \tag{179}$$

where φ_i is the orbital inclination, V_ϱ is the orbital radial velocity, Ω is the right ascension, Υ is the argument of the perigee, and $\mathbf{r}$ is radial position vector [67]. These equations are brought over from orbital mechanics, and all the flow variables are Lagrangian-mean quantities.

The Euler angle matrix for the transformation between the fluid element perifocal

frame and the body axis is then given as [67]

$$[\mathbf{Q}]_{\tilde{x}x} = \begin{bmatrix} -\sin\Omega\cos\varphi_i\sin\Upsilon + \cos\Omega\cos\Upsilon & -\sin\Omega\cos\varphi_i\cos\Upsilon - \cos\Omega\sin\Upsilon & \sin\Omega\sin\varphi_i \\ \cos\Omega\cos\varphi_i\sin\Upsilon + \sin\Omega\cos\Upsilon & \cos\Omega\cos\varphi_i\cos\Upsilon - \sin\Omega\sin\Upsilon & -\cos\Omega\sin\varphi_i \\ \sin\varphi_i\sin\Upsilon & \sin\varphi_i\cos\Upsilon & \cos\varphi_i \end{bmatrix}, \tag{180}$$

so that the position vector with respect to the body axis is obtained as

$$\{\mathbf{r}\}_x = [\mathbf{Q}]_{\tilde{x}x}\{\mathbf{r}\}_{\tilde{x}} \,. \tag{181}$$

Hence, $\Theta_{\tau_{\varrho\Theta}=0}$ and $\Theta_{h=0}$ are located in the body axis as

$$\theta_{\tau_{\varrho\Theta}=0} = \tan^{-1}\left[\frac{\sin\Omega\cos\left(\Upsilon+\Theta_{\tau_{\varrho\Theta}=0}\right)+\cos\Omega\sin\left(\Upsilon+\Theta_{\tau_{\varrho\Theta}=0}\right)\cos\varphi_i}{\cos\Omega\cos\left(\Upsilon+\Theta_{\tau_{\varrho\Theta}=0}\right)-\sin\Omega\sin\left(\Upsilon+\Theta_{\tau_{\varrho\Theta}=0}\right)\cos\varphi_i}\right], \tag{182}$$

and

$$\theta_{h=0} = \tan^{-1}\left[\frac{\sin\Omega\cos\left(\Upsilon+\Theta_{h=0}\right)+\cos\Omega\sin\left(\Upsilon+\Theta_{h=0}\right)\cos\varphi_i}{\cos\Omega\cos\left(\Upsilon+\Theta_{h=0}\right)-\sin\Omega\sin\left(\Upsilon+\Theta_{h=0}\right)\cos\varphi_i}\right] \tag{183}$$

respectively. These are also illustrated in Figs. 54b and 54c respectively for the same unsteady flow conditions in Fig. 54a.

Figure 55a illustrates the theoretical Lagrangian-mean c_f distribution along with the predictions of perifocal angular locations of vanishing velocity gradients, $\theta_{\tau_{\varrho\Theta}=0}$ (Eqn. 182) for a particular $V_\infty t/R \approx 515.77$ of the flow in Fig. 54. The step changes in the $\theta_{\tau_{\varrho\Theta}=0}$ variation coincide with points where $c_f = 0$. These are the case at other times (Fig. 54b) and are indicators of flow separation/reattachment at the wall. In Fig. 55a, the flow first separates at about 90° from the stagnation point. Then, it reattaches around 140° at the rear of the cylinder and stays attached before a final separation 20° further away. Flow reattachment and separation in the rear of the cylinder is in agreement with the raw experimental data of Dimopoulos and Hanratty [83] and Son and Hanratty [13]. They observed multiple points where $c_f = 0$ including at the rear of the cylinder in the Re_∞ range $60 - 360$ [83] and $5 \times 10^3 - 10^5$ [13]. The

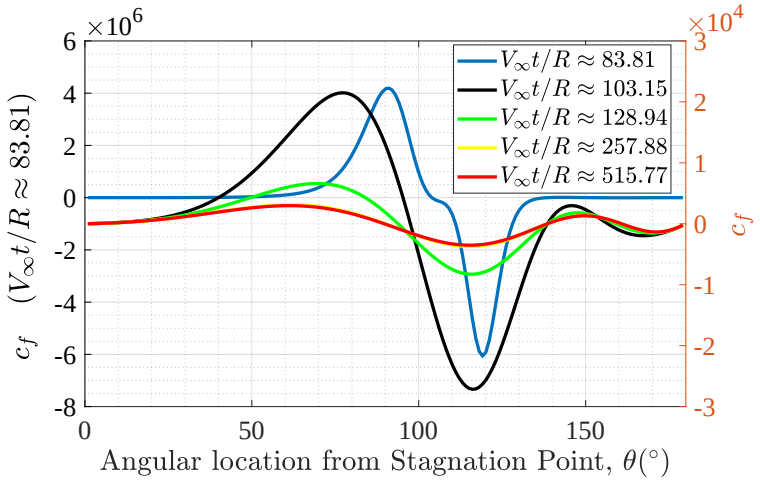

(a) Lagrangian-mean c_f distributions.

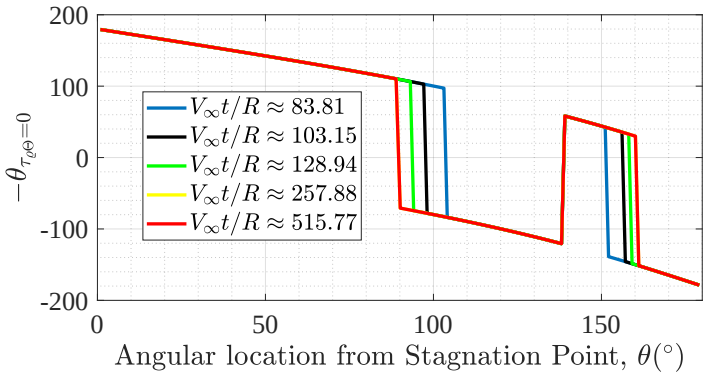

(b) $\theta_{\tau_{\varrho\Theta}=0}$ distributions.

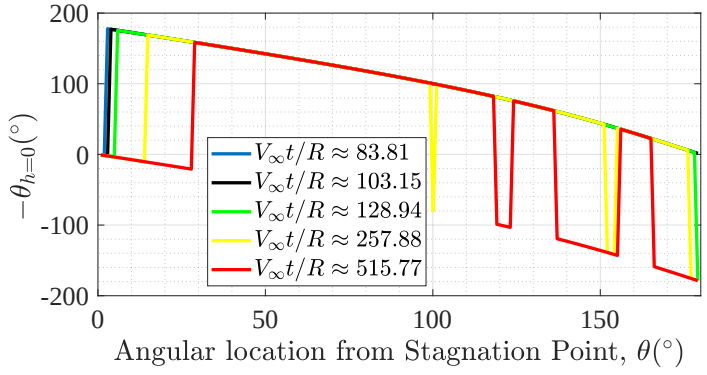

(c) $\theta_{h=0}$ distributions.

Figure 54: Present theoretical surface distributions of c_f, $\theta_{\tau_{\varrho\Theta}=0}$ and $\theta_{h=0}$ in a cylinder crossflow as functions of $V_\infty t/R$ ($Re_\infty = 3,900$, $z = 0$).

linear portions of the $\theta_{\tau_{\varrho\Theta}=0}$ distribution in Fig. 55a signify other locations than at wall flow separation/attachment where the velocity gradient vanishes.

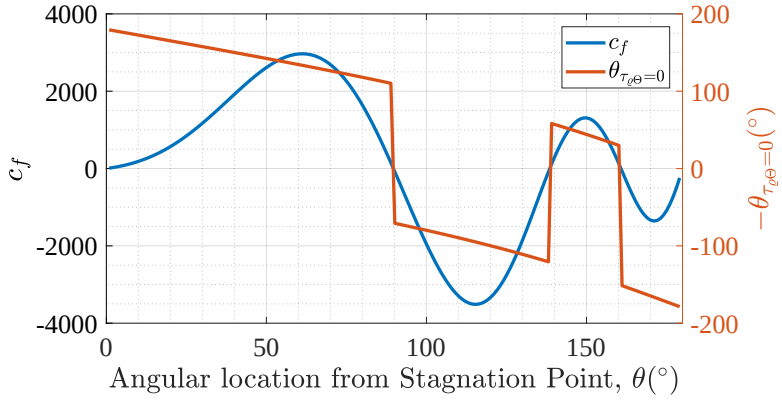

(a) c_f and $\theta_{\tau_{\varrho\Theta}=0}$ distributions.

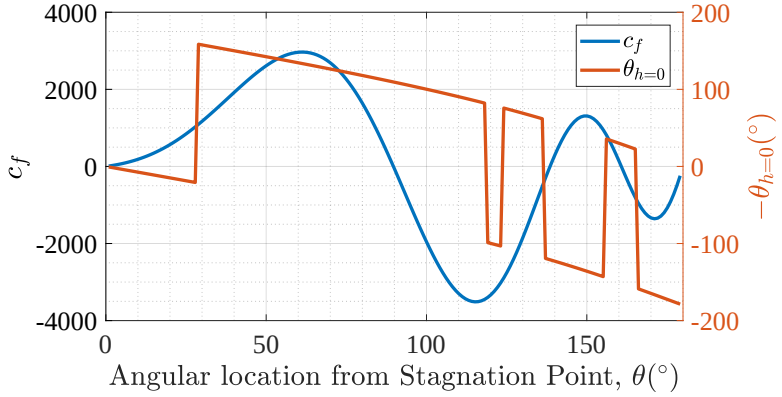

(b) c_f and $\theta_{h=0}$ distributions.

Figure 55: Present theoretical surface distributions of c_f, $\theta_{\tau_{\varrho\Theta}=0}$ and $\theta_{h=0}$ in a cylinder crossflow ($Re_\infty = 3,900$, $z = 0$ and $V_\infty t/R \approx 515.77$).

Similarly, Fig. 55b presents the variation of RPT natural transition point perifocal angle, $\theta_{h=0}$ (Eqn. 183) against the Lagrangian-mean c_f distribution at the same flow conditions in Fig. 55a. A natural transition process occurs over a smooth surface in a quiet flow [15]. A quiet flow is one with very little or no freestream disturbance. The trough starting from the stagnation point and extending to $\theta \approx 27^\circ$ in the linear variation from the stagnation point signify an unsteady transition region that includes

turbulence spots. These are the case at other times as Fig. 54c shows. Figure 54c also shows that the extent of the present theoretical transition region grows with time. Boundary layer flow transition occurs over a finite region in which turbulence spots precede the onset of a fully turbulent flow [7, 15]. There is a favorable pressure gradient in the windward region from the stagnation point in Fig. 55b ($\tilde{\theta} < 90°$). The maximum favorable pressure gradient in this figure is achieved at $\theta \approx 60°$ where c_f also attains its maximum value [9]. A favorable pressure gradient extends the span of the transition region and relaminarizes turbulent outbursts [7, 15]. Thus, the flow relaminarizes, and another post-separation transition region occurs at $\theta \approx 119° - 124°$. This is in agreement with the pressure gradient effect and appropriately places the present flow of $Re_\infty = 3.9 \times 10^3$ into Zdravkovich's classification of $(1 \times 10^3 - 2 \times 10^3) < Re_\infty < (20 \times 10^3 - 40 \times 10^3)$ as a free-shear layer transition regime [9]. It is also consistent with observations that flow separation below $Re_\infty \approx 3 \times 10^5$ is of the laminar type [5, 9]. The surface flow eventually becomes turbulent at $\theta \approx 136°$. A turbulent separated flow region is energetic and can work against an adverse pressure gradient to force a flow reattachment [5, 9, 15]. Due to this mechanism in the adverse pressure gradient region in the rear of the cylinder, the flow reattaches at $\theta \approx 140°$ and forms a turbulent boundary layer in which the pressure gradient is favorable. Favorable pressure gradients stretch and relaminarize turbulent boundary layers [7]. Thus, the reattached turbulent boundary layer relaminarizes at $\theta \approx 155°$. However, it finally separates at $\theta \approx 160°$ under a restored adverse pressure gradient and becomes turbulent again at $\theta \approx 165°$.

The shear stress also tends towards zero at inflexion points in adverse pressure gradient boundary layers and generally at the edge of the boundary layer [15,33]. The definition of the boundary layer edge is arbitrary [9, 84]. In numerical solutions of boundary layer equations, it is usually taken to be the distance above a wall at which

the wall-retarded flow attains 99% of the local freestream velocity for practical purposes [9, 15, 84]. However, the mathematical boundary condition for these equations is that the velocity gradient vanishes at the boundary layer edge [5, 15, 33]. Thus, this is the assumption for the present theoretical approach. Therefore, the substitution of Eqn. 172 into Eqn. 170 results in a quadratic equation for ϱ that is solved to locate the boundary layer extent from the surface as

$$\delta_e = \left[\frac{V_\Theta^2 \pm \sqrt{V_\Theta^4 - 4V_\Theta \dfrac{\partial V_\Theta}{\partial \varrho} \mu_g \varepsilon \cos\left(\theta_{\tau_{\varrho\Theta=0}}\right)}}{2V_\Theta \dfrac{\partial V_\Theta}{\partial \varrho}} \right]_{\varrho=r=R}$$

in the perifocal frame. In the body axis, this is

$$\delta_e = \left[\frac{V_\theta^2 \pm \sqrt{V_\theta^4 - 4V_\theta \dfrac{\partial V_\theta}{\partial r} \mu_g \varepsilon \cos\left(\theta_{\tau_{\varrho\Theta=0}}\right)}}{2V_\theta \dfrac{\partial V_\theta}{\partial r}} \right]_{r=R} . \tag{184}$$

To differentiate the boundary layer edge from other inflexion points in the shear stress distribution, all variables except $\theta_{\tau_{\varrho\Theta=0}}$ in Eqn. 184 are calculated using the Eulerian-mean of the inviscid term in Eqn. 130.

Figure 56 presents the Eulerian-mean velocity profiles obtained in the boundary layer at various consecutive angular locations with the *Kwasu* function in comparison with Falkner-Skan profiles [15]. The angle is measured from the front stagnation point. The boundary layer thickness is predicted with the absolute value of Eqn. 184. This result is for a steady freestream flow on the cylinder in a static grid. Unlike the Blasius flat plate boundary layer profiles, the profiles on the cylinder are not self-similar [9, 15, 33]. This is observable in the figure. The boundary layer flow is driven by the pressure gradient in the flow direction [15, 33]. Thus, it is a function of the curvature of the body. For $\theta = 60.1^\circ - 84.1^\circ$, there is a favorable pressure gradient. The flow is attached and accelerating. The convex profiles thus resemble those of the Falkner-Skan profiles [15] in Fig. 56b for $\beta \geq 0$. In this figure, f' is the non-dimensional velocity, η is the non-dimensional distance above the wall,

and β is a non-dimensional pressure gradient parameter. The Falkner-Skan profiles are in agreement with Fage's experiment traversing the cylinder boundary layer [9]. Downstream of $\theta = 60.1° - 84.1°$, an adverse pressure gradient signified by $\beta < 0$ retards the flow.

In the separated flow region, the Falkner-Skan solutions become inaccurate [15]. This is because they are products of boundary layer theory that assumes thin attached boundary layer [15, 33]. However, the separated region is bounded by the wall and the free shear layer of the wake which is large in its extent. Thus, the profiles for $\theta = 107.9°$ and $115.9°$ have the characteristic shape of the profiles of free-shear flows between two fluids where one is stationary, and the other is moving [15].

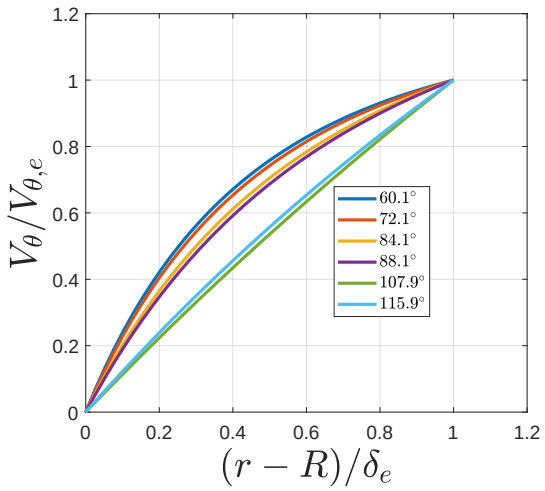

(a) RPT Eulerian-mean boundary layer velocity profiles ($Re_\infty = 3,900$, $z = 0$, $t = 3,610.6s$).

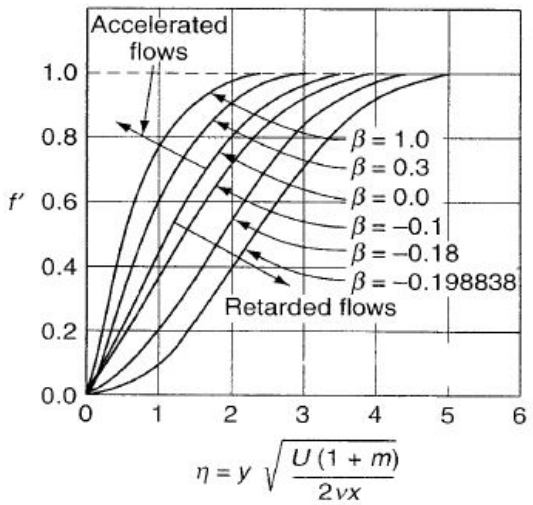

(b) Falkner-Skan boundary layer velocity profiles [15].

Figure 56: Profiles of RPT Eulerian-mean circumferential velocity at different stations in the boundary layer over a cylinder in a crossflow compared with the Falkner-Skan boundary layer profiles.

2.5 Viscous Flows over Arbitrary Geometries

The refined potential theory is extensible to the general solution of the Laplace equation

$$\psi(r,\theta) = \sum_{m>0} A_m r^m \sin\left[m\left(\theta - \theta_m\right)\right]\left(1 - \left(\frac{R^2}{r^2}\right)^m\right)$$

for which $m \geq 1$. Therefore, complete closed-form analytical solutions to the flow field around arbitrary geometries can be obtained. However, it may not be known what m corresponds to what geometry. Also, some m may give nonphysical solutions.

Therefore, it was proposed in Ref. 50 (current author's own publication) to use the analytical conformal map [63]

$$\begin{aligned}
l &= \frac{(a^2-b^2)^{\frac{1}{2}}}{2} \\
r &= \sqrt{[lexp(\cosh^{-1}\mathcal{P})]^2 + z^2} \\
\theta &= \tan^{-1}\left(\frac{y}{x}\frac{\mathcal{P}}{[\mathcal{P}^2-1]^{\frac{1}{2}}}\right) \\
R &= \sqrt{(a^2\cos^2\theta + b^2\sin^2\theta + z^2)} \\
\mathcal{P} &= \left[\frac{\frac{x^2}{l^2}+\frac{y^2}{l^2}+4+\left(\left[\frac{x^2}{l^2}+\frac{y^2}{l^2}+4\right]^2 - \frac{16x^2}{l^2}\right)^{\frac{1}{2}}}{8}\right]^{\frac{1}{2}}.
\end{aligned} \tag{185}$$

(and/or numerical ones) to map the cylinder flow to other geometries. However, this mapping would introduce further complexity into the present solution, and there is also a singularity when $a = b$. So, the cylinder flow would not be recoverable.

However, the present solution is a smooth and well-behaved function in the spherical polar coordinate system. The variation of R as a function of θ and φ for an arbitrary geometry is adequate to obtain the flow about it. Thus, a conformal mapping is redundant. Essentially, every point in the flow corresponds to an equivalent flow over a sphere with a spherically symmetric mass distribution and with a radius

equal to the local R at that $[\theta, \varphi]$ location as illustrated in Fig. 57.

Therefore, the surface coordinates

$$(X_n, Y_n, Z_n) \tag{186}$$

are used to define R. For a finite cylinder, $X_n = R_C \cos\theta$, $Y_n = R_C \sin\theta$, and $Z_n = (B\cos\varphi)/2$ where R_C is the cylinder radius in the x-y plane, and B is the span in the z-axis (Fig. 57a). For a sphere, $X_n = R_S \cos\theta \sin\varphi$, $Y_n = R_S \sin\theta \sin\varphi$, and $Z_n = R_S \cos\varphi$ where R_S is the sphere radius (Fig. 57b). For a spheroid, $X_n = b\cos\theta\sin\varphi$, $Y_n = b\sin\theta\sin\varphi$, and $Z_n = acos\varphi$ where a is the semi-major axis aligned along the body z-axis and b is semi-minor axis aligned along the body y-axis (Fig. 57c).

The rolling, yawing and pitching of the body depicted in Fig. 57 are factored in with Euler angles

$$\begin{bmatrix} X \\ Y \\ Z \end{bmatrix} = \begin{bmatrix} \cos\beta\cos\alpha & \sin\beta\cos\alpha & -\sin\alpha \\ \cos\beta\sin\alpha\sin\varsigma - \sin\beta\cos\varsigma & \sin\beta\sin\alpha\sin\varsigma + \cos\beta\cos\varsigma & \cos\alpha\sin\varsigma \\ \cos\beta\sin\alpha\cos\varsigma + \sin\beta\sin\varsigma & \sin\beta\sin\alpha\cos\varsigma - \cos\beta\sin\varsigma & \cos\alpha\cos\varsigma \end{bmatrix} \begin{bmatrix} X_n \\ Y_n \\ Z_n \end{bmatrix}. \tag{187}$$

Alternatively, quaternions are more practical for instances when α approaches $\pi/2$ at which there is a singularity [67]. These can all be functions of time depending on the prescribed motion. Similarly, corresponding transformed geometric axes (x, y and z) based on the prescribed motion are obtained with the quarternions. Finally, the local radius,

$$R = \sqrt{X^2 + Y^2 + Z^2} \tag{188}$$

which completes the theoretical formulation.

Figure 58 compares the normalized absolute value of the *Kwasu* function for a sphere to experimentally observed flow photographs obtained by Ozgoren et al. at

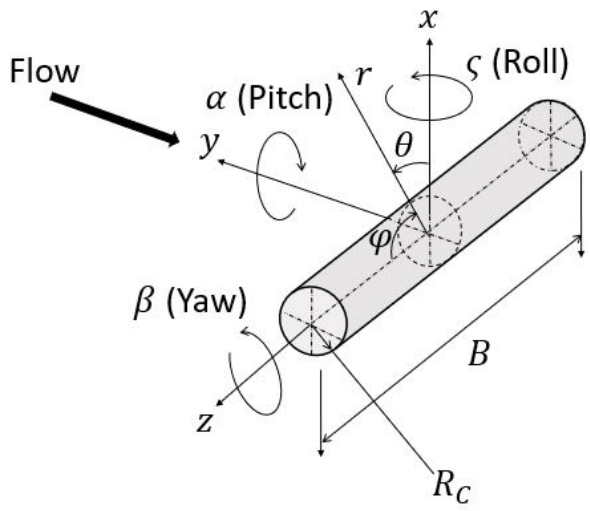

(a) Cylinder flow

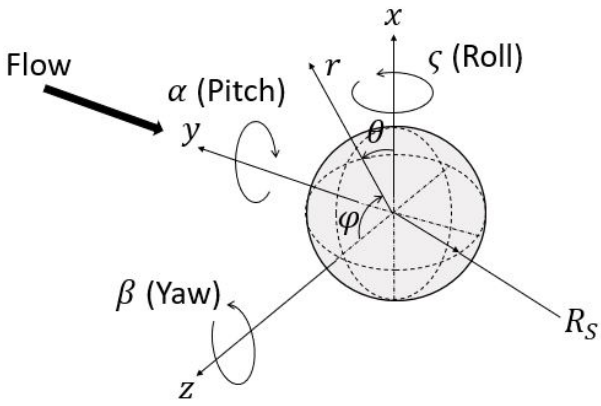

(b) Sphere flow

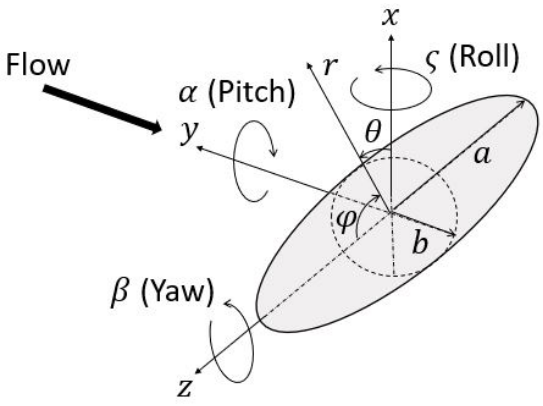

(c) Spheroid flow

Figure 57: Pictorial representation of the flow axes and geometric variables for the cylinder, sphere and spheroid flows.

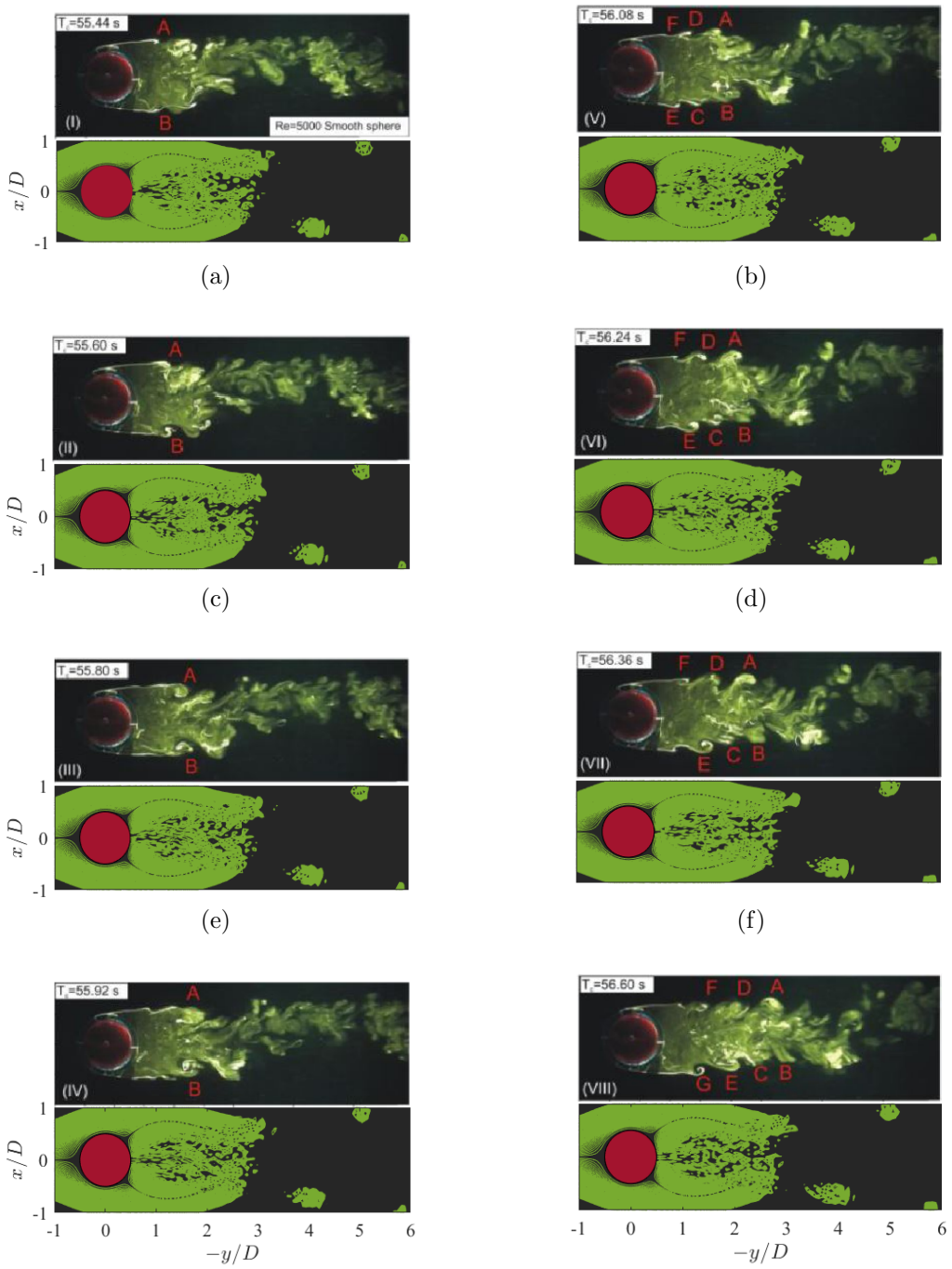

Figure 58: Comparison between experimental flows [3] and present theoretical streamlines for a sphere flow at $Re_\infty = 5,000$ ($R = 0.02125m$).

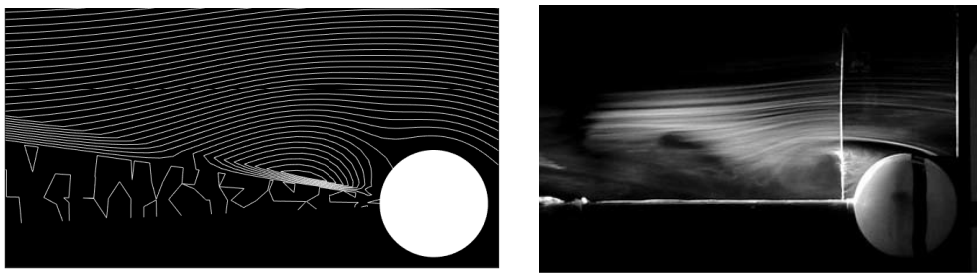

(a) Present theory (b) Experiment by Jeon et al. [2]

Figure 59: Comparison between the present theoretical sphere flow streamlines and an experimentally observed flow [2] at $Re_\infty = 10^5$.

$Re_\infty = 5,000$ [3]. The photographs are presented in the upper images of the figure. The distilled water flow was visualized with $10\mu m$ silver metallic coated hollow plastic spheres [3]. The time stamps for the flow visualization are provided, and the flow is from left to right. These provide an assessment of the time-accuracy of the present theory in the lower images that were obtained with the same time from start-up as the experimentally observed flow and in the $z = 0$ plane. The vortices are *forced*. Fifty-one linearly-spaced contour levels from 0 to 1 are shown in all the theoretical plots. Ozgoren et al. [3] used the labeling on the small scale vortices in the deforming shear layers in Fig. 58 to track them across the snapshots. These labelled vortices are not replicable due to other experimental conditions that are not modeled. Additionally, the theoretical evaluation was obtained on a static grid. However, the general agreement of the present theory with an experimentally observed flow pattern is discernible in Fig. 58.

Figure 59 also illustrates the normalized real part of Eqn. 130 at $Re_\infty = 10^5$, $t = 3,610.6$ and $z = 0$ for a sphere. The flow is from right to left. Eighty-seven linearly-spaced contour levels from -6 to 6 are displayed to include the level at zero. This figure was also evaluated on a static grid. Figure 59b presents the smoke visualization of an experimentally observed flow photographed by Jeon et al. [2] at $Re_\infty = 10^5$. The experimental sphere has a supporter at the rear end. This was

not modeled. However, the qualitative agreement between the present theory and experiment is noticeable.

The interaction of shear layers with a cylinder have some effects on the integrated quantities (forces) especially when the flow is parallel to its axis (axial flow) [9,72,85]. Some of these effects are affected by the cylinder aspect ratio and Re_∞ as presented in Fig. 60 that illustrates the present theoretical axial flow on a circular cylinder (i.e. the cylinder is rolled through $\varsigma = \pi/2$) with varying values of these parameters. These figures are contours of normalized *Kwasu* function for $z = 0$ on static grids. The flow is from left to right in these figures. Twenty-one linearly-spaced contour levels from 0 to 0.01 are shown in all of the figures. For an aspect ratio $L/D \approx 0$ (where L is length of cylinder in the streamwise direction, and D is the diameter of the cylinder normal to the flow), the flow separates at the edge of the disk into a large wake as depicted in Fig. 60a. With $L/D = 1$ while keeping Re_∞ constant in Fig. 60b, the shear layers impact parts of the cylinder downstream of the leading edge separation. However, the cylinder streamwise dimension is not long enough to experience some flow reattachment. A further increment of L/D to 2 at the same Re_∞ encourages flow reattachment, and some of the separated shear layer are observed to deflect towards the cylinder surface at the rear in Fig. 60c. This behavior is replicated at a higher Re_∞ but same L/D and time in Fig. 60d. Since wake flow evolution is unsteady, all the figures in Fig. 60 were obtained with the same time for the comparison.

Figure 61a illustrates the absolute value of Eqn. 130 normalized with $2V_\infty a$ at $Re_\infty = 4,000$, $t = 345.760 \times 2b/V_\infty$ and $z = 0$ for a $6:1$ $(a:b)$ prolate spheroid. The Reynolds number is based on $2b$. The spheroid is inclined at 45° to the freestream crossflow that is from right to left. Fourteen linearly-spaced contour levels from 0 to 1.5 are displayed. This figure was also evaluated on a static grid. Figure 61b presents a perspective view of the streaklines from direct numerical simulation (DNS) of the flow by Strandenes et al. [12] at the same conditions. The qualitative similarity of

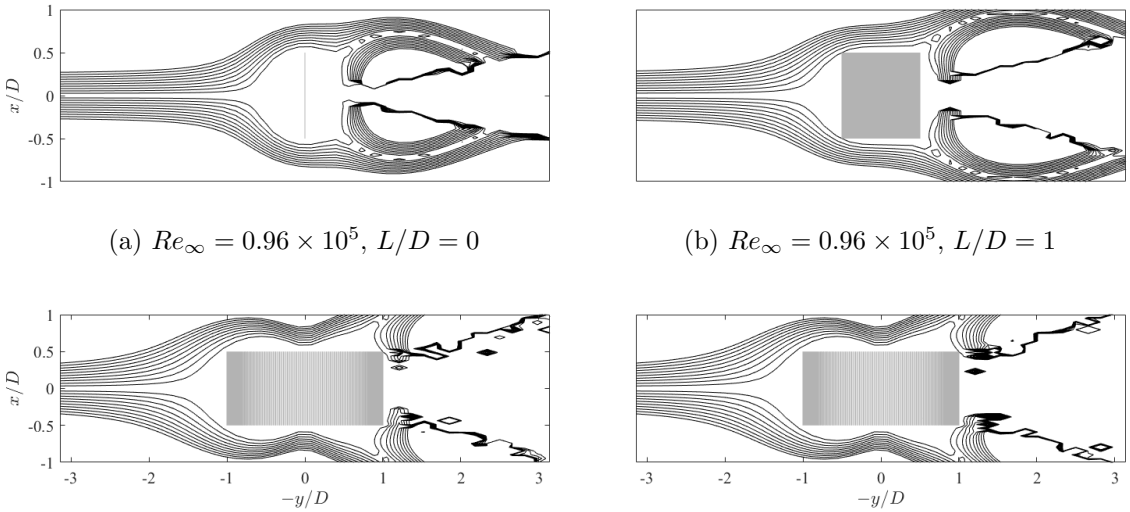

(a) $Re_\infty = 0.96 \times 10^5$, $L/D = 0$

(b) $Re_\infty = 0.96 \times 10^5$, $L/D = 1$

(c) $Re_\infty = 0.96 \times 10^5$, $L/D = 2$

(d) $Re_\infty = 1.56 \times 10^5$, $L/D = 2$

Figure 60: The present theoretical streamline contours ($|\tilde{\kappa}|/(V_\infty R)$) for cylinder axial flows with varying Reynolds number and aspect ratios at $t = 3610.6s$.

the RPT flow pattern to the DNS pattern is observable.

2.6 The Resolution of D'Alembert's Paradox

The surface pressure coefficient

$$\begin{aligned} C_p &= \frac{2\left(p - p_\infty\right)}{\rho_\infty V_\infty^2} \\ &= -\frac{2}{\rho_\infty V_\infty^2}\left(\frac{\partial \kappa}{\partial t} + \frac{\rho}{2}\left(\frac{\nabla \kappa}{\rho}\right)^2 - \left(\lambda + \tfrac{2}{3}\mu\right)\nabla \cdot \left(\frac{\nabla \kappa}{\rho}\right)\right) \end{aligned} \tag{189}$$

and the shear stress coefficient

$$\begin{aligned} c_f &= \frac{\tau_{r\theta}}{\rho_\infty V_\infty^2} \\ &= \frac{2\nu}{V_\infty^2}\left(\frac{\partial V_\theta}{\partial r} - \frac{V_\theta}{r} + \frac{1}{r}\frac{\partial V_r}{\partial \theta}\right) \end{aligned} \tag{190}$$

are integrated to obtain the axial, normal and side force coefficients acting on the cylinder as

$$C_A = \frac{1}{S}\left[\int_{-z/2}^{z/2}\int_{LE}^{TE}\left(C_{p,u} - C_{p,l}\right)dydz + \int_{-z/2}^{z/2}\int_{LE}^{TE}\left(c_{f,u} + c_{f,l}\right)dxdz\right], \tag{191}$$

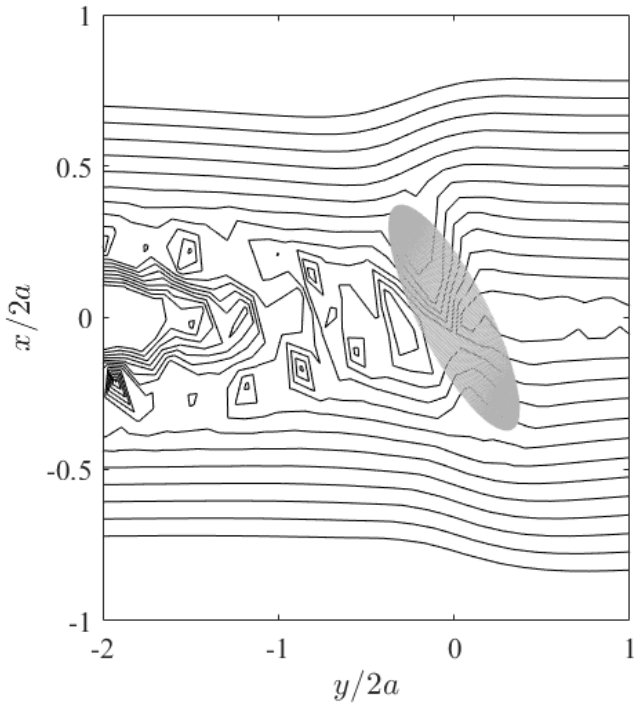

(a) Streamlines from present theory ($z/2b \approx 0.13$ plane; *forced* vortices)

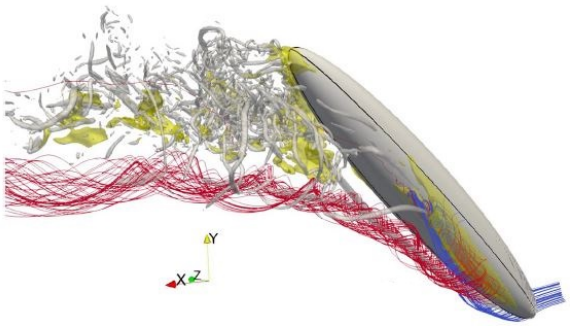

(b) Streaklines from DNS [12]

Figure 61: Comparison between the present theoretical spheroid flow and direct numerical simulation (DNS) [12] at $Re_\infty = 4,000$ and $t = 345.760 \times 2b/V_\infty$.

$$C_N = \frac{1}{S}\left[\int_{-z/2}^{z/2}\int_{LE}^{TE}\left(C_{p,l} - C_{p,u}\right)dxdz + \int_{-z/2}^{z/2}\int_{LE}^{TE}\left(c_{f,u} + c_{f,l}\right)dydz\right] , \qquad (192)$$

and

$$C_S = \frac{1}{S}\left[\int_{LE}^{TE}\int_{LE}^{TE}\left(C_{p,l} - C_{p,u}\right) + \left(c_{f,u} + c_{f,l}\right)dxdy\right] \qquad (193)$$

respectively where S is the force area [5, 71, 76, 86]. Equations 189 and 190 are illustrated in Fig. 62 for a cylinder crossflow at $Re_\infty = 3,900$. The limits of integration in the flow direction are from the windward leading edge (LE) to the leeward trailing edge (TE) as shown in Fig. 63. In the cylindrical polar coordinate,

$$\begin{aligned} y &= R\sin\theta \qquad & dy &= R\cos\theta d\theta \\ x &= R\cos\theta \qquad & dx &= -R\sin\theta d\theta \ . \end{aligned} \qquad (194)$$

Equation 194 is substituted in Eqns. 191, 192 and 193 to give

$$C_A = \frac{1}{S}\left[\int_{-z/2}^{z/2}\int_{LE}^{TE}\left(C_{p,u} - C_{p,l}\right)R\cos\theta d\theta dz - \int_{-z/2}^{z/2}\int_{LE}^{TE}\left(c_{f,u} + c_{f,l}\right)R\sin\theta d\theta dz\right] , \qquad (195)$$

$$C_N = \frac{1}{S}\left[-\int_{-z/2}^{z/2}\int_{LE}^{TE}\left(C_{p,l} - C_{p,u}\right)R\sin\theta d\theta dz + \int_{-z/2}^{z/2}\int_{LE}^{TE}\left(c_{f,u} + c_{f,l}\right)R\cos\theta d\theta dz\right] , \qquad (196)$$

and

$$C_S = -\frac{1}{S}\int_{LE}^{TE}\int_{LE}^{TE}\left[\left(C_{p,l} - C_{p,u}\right) + \left(c_{f,u} + c_{f,l}\right)\right]R^2\sin\theta\cos\theta d\theta d\theta \ . \qquad (197)$$

The subscripts u and l in the pressure and shear stress coefficients denote the upper and lower surfaces of the cylinder respectively. Equations 189 and 190 are expressions that cover both surfaces although the sign of Eqn. 190 flips between the surfaces as shown in Fig. 62. When these surfaces are accounted for, and the corresponding limit of integration in the θ coordinate, $0 - 2\pi$ employed [5, pp. 271-272], Eqns. 195 to 197 yield

$$C_A = \frac{1}{S}\left[-\int_{-z/2}^{z/2}\int_{0}^{2\pi}C_p R\cos\theta d\theta dz + \int_{-z/2}^{z/2}\int_{0}^{2\pi}c_f R\sin\theta d\theta dz\right] , \qquad (198)$$

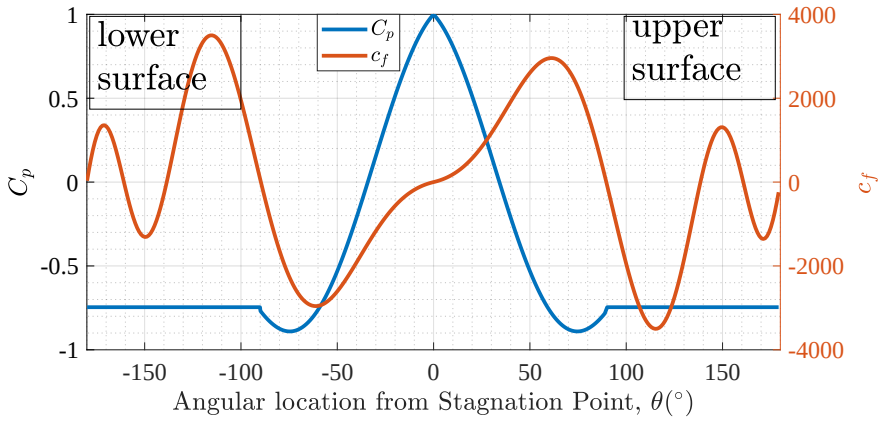

Figure 62: RPT Eulerian-mean cylinder C_p and c_f distributions at $Re_\infty = 3,900$ ($z = 0$, $t = 3,610.6s$).

$$C_N = \frac{1}{S}\left[\int_{-z/2}^{z/2}\int_0^{2\pi} C_p R\sin\theta d\theta dz - \int_{-z/2}^{z/2}\int_0^{2\pi} c_f R\cos\theta d\theta dz\right], \tag{199}$$

and

$$C_S = \frac{1}{S}\int_0^{2\pi}\int_0^{\theta}\left[C_p + c_f\right] R^2\sin\theta\cos\theta d\theta d\theta \tag{200}$$

respectively. However, these integration are analytically difficult in the body axis because the C_p and c_f are very complicated expressions of θ. Therefore, the perifocal frame which is coincident with planes of constant $\tilde{\varphi}$ (wind azimuthal coordinate) as illustrated in Fig. 63 is used to obtain these integrals as follow.

From Sec. 2.2, the Lagrangian-mean *Kwasu* function, κ^L is equal to the negative Lagrangian-mean specific angular momentum, h^L as

$$\kappa^L = -h^L = -rV_\theta^L\,. \tag{201}$$

The corresponding eccentricity is

$$\varepsilon = \sqrt{1 + \frac{h^{L^2}}{\mu_g^2}(V^{L^2} - \frac{2\mu_g}{r})}\,. \tag{202}$$

These are calculated with Eqns. 163 and 160. Equations 163 and 160 are obtained from the Eulerian-mean *Kwasu* function (Eqn. 138). h^L and ε are constants for a particular orbit [67]. The circumferential velocity in the perifocal frame is

$$V_\Theta = \frac{\mu_g}{h^L}\left(1 + \varepsilon\cos\Theta\right), \tag{203}$$

and the radial velocity is

$$V_\varrho = \frac{\mu_g}{h^L}\varepsilon \sin\Theta \, . \tag{204}$$

It is observable that these are only variant with the perifocal circumferential variable (or true anomaly), Θ for a particular orbit.

Then, the coefficient of wall shear stress is

$$\begin{aligned} c_f &= \frac{\tau_{\varrho\Theta}}{\rho_\infty V_\infty^2} \\ &= \frac{2\nu}{V_\infty^2}\left(\frac{\partial V_\Theta}{\partial \varrho} - \frac{V_\Theta}{\varrho} + \frac{1}{\varrho}\frac{\partial V_\varrho}{\partial \Theta}\right) \\ &= \frac{2\nu}{V_\infty^2}\left(-\frac{2V_\Theta}{\varrho} + \frac{1}{\varrho}\frac{\partial}{\partial\Theta}\left(\frac{\mu_g}{h^L}\varepsilon\sin\Theta\right)\right) \\ &= \frac{2\nu}{V_\infty^2}\left(-\frac{2\mu_g}{\varrho h^L}\left(1+\varepsilon\cos\Theta\right) + \frac{\mu_g}{\varrho h^L}\varepsilon\cos\Theta\right) \\ &= -\frac{2\nu\mu_g}{V_\infty^2}\left(\frac{2+\varepsilon\cos\Theta}{\varrho h^L}\right) \, . \end{aligned} \tag{205}$$

For c_f, Eqns. 201 to 204 are obtained from the Eulerian-mean *Kwasu* function (Eqn. 138) with the rotated polar coordinate equal to

$$\theta_W = \arctan\left[\cos\theta_{3D}\sqrt{x_{3D}^2+y_{3D}^2}, \sin\theta_{3D}\sqrt{x_{3D}^2+y_{3D}^2}\right] \tag{206}$$

where

$$\theta_{3D} = \arctan\left(y_{3D}+y_m, x_{3D}\right),$$

$$y_m = 7R/20,$$

R is defined in Eqn. 188,

$$x_{3D} = r\cos\theta\sin\varphi,$$

and

$$y_{3D} = r\sin\theta\sin\varphi$$

as previously defined in Sec. 2.1.2.

Similarly, the wall pressure coefficient is

$$
\begin{aligned}
C_p &= \frac{2\left(p-p_\infty\right)}{\rho_\infty V_\infty^2} \\
&= -\frac{2}{\rho_\infty V_\infty^2}\left(-\rho_\infty \frac{\partial h^L}{\partial t} + \frac{\rho_\infty}{2}\left(V_\varrho^2 + V_\Theta^2\right) + \left(\lambda + \frac{2}{3}\mu\right)\left(\frac{\partial V_\Theta}{\partial \varrho} + \frac{V_\Theta}{\varrho} - \frac{1}{\varrho}\frac{\partial V_\varrho}{\partial \Theta}\right)\right) \\
&= -\frac{2}{\rho_\infty V_\infty^2}\left(\begin{array}{l} \left[-\rho_\infty \dfrac{\partial h^L}{\partial t} + \dfrac{\rho_\infty \mu_g^2}{2{h^L}^2}\left(\varepsilon^2 \sin^2\Theta + \left(1+\varepsilon\cos\Theta\right)^2\right)\right] \\ -\left(\lambda + \dfrac{2}{3}\mu\right)\left(\dfrac{\mu_g \varepsilon \cos\Theta}{\varrho h^L}\right) \end{array}\right) .
\end{aligned}
\tag{207}
$$

For C_p, Eqns. 201 to 204 are obtained from the Eulerian-mean *Kwasu* function (Eqn. 138) with the rotated polar coordinate equal to

$$
\theta_W = \arctan\left[\cos\tilde{\theta}\sqrt{x_{3D}^2 + y_{3D}^2}, \sin\tilde{\theta}\sqrt{x_{3D}^2 + y_{3D}^2}\right] \tag{208}
$$

where $\tilde{\theta}$ is (as previously defined in Sec. 2.1.6.1)

$$
\tilde{\theta} = \begin{cases} \left|\arctan\left(x_{3D}, y_{3D} + y_n\right)\right| \text{ , for } \left|\arctan\left(x_{3D}, y_{3D}\right)\right| < \theta_s & \text{(Cylinder)} \\ -\left|\arctan\left(x_{3D}, y_{3D} + y_n\right)\right| \text{ , for } \left|\arctan\left(x_{3D}, y_{3D}\right)\right| < \theta_s & \text{(Sphere)} \\ \tilde{\theta}_n \text{ , } \left|\arctan\left(x_{3D}, y_{3D}\right)\right| \geq \theta_s \text{ ,} & \end{cases}
$$

and θ_s is the point(s) of separation.

Then, the axial and normal force coefficients, C_A and C_N are obtained as

$$
\begin{aligned}
C_A &= \frac{2}{\rho_\infty V_\infty^2 S} \\
&\times \int_{LE}^{TE}\int_{-z/2}^{z/2} \left[\begin{array}{l} \left[-\rho_\infty \dfrac{\partial h^L}{\partial t} + \dfrac{\rho_\infty \mu_g^2}{2{h^L}^2} \left(\varepsilon^2 \sin^2\Theta + (1+\varepsilon\cos\Theta)^2 \right) \right] \\ -\left(\lambda + \dfrac{2}{3}\mu \right) \dfrac{\mu_g \varepsilon \cos\Theta}{\varrho h^L} \end{array} \right] \varrho \cos\Theta d\Theta dz \\
&-\frac{2\nu\mu_g}{V_\infty^2 S} \int_{LE}^{TE}\int_{-z/2}^{z/2} \frac{2+\varepsilon\cos\Theta}{\varrho h^L} \varrho \sin\Theta d\Theta dz \\
&= \frac{2z}{\rho_\infty V_\infty^2 S} \left(\begin{array}{l} -\rho_\infty \varrho \dfrac{\partial h^L}{\partial t} \sin\Theta \\ +\dfrac{\rho_\infty \varrho \mu_g^2}{2{h^L}^2} \left(\begin{array}{l} \sin\Theta + \varepsilon(\Theta + \sin\Theta\cos\Theta) \\ +\dfrac{\varepsilon^2}{3}\left(\cos^2\Theta\sin\Theta + 2\sin\Theta + \sin^3\Theta \right) \end{array} \right) \\ -\left(\lambda + \dfrac{2}{3}\mu \right) \left(\dfrac{\mu_g \varepsilon \left(\Theta + \cos\Theta\sin\Theta \right)}{2h^L} \right) \end{array} \right)_{LE}^{TE} \\
&+\frac{2\nu\mu_g z}{V_\infty^2 S} \left(\frac{\cos\Theta(4+\varepsilon\cos\Theta)}{2h^L} \right)_{LE}^{TE},
\end{aligned}
\tag{209}
$$

and

$$
\begin{aligned}
C_N &= -\frac{2}{\rho_\infty V_\infty^2 S} \\
&\times \int_{LE}^{TE} \int_{-z/2}^{z/2} \left[\begin{array}{l} \left[-\rho_\infty \dfrac{\partial h^L}{\partial t} + \dfrac{\rho_\infty \mu_g^2}{2{h^L}^2} \left(\varepsilon^2 \sin^2\Theta + (1+\varepsilon\cos\Theta)^2 \right) \right] \\ -\left(\lambda + \dfrac{2}{3}\mu \right) \dfrac{\mu_g \varepsilon \cos\Theta}{\varrho h^L} \end{array} \right] \varrho \sin\Theta d\Theta dz \\
&+ \frac{2\nu\mu_g}{V_\infty^2 S} \int_{LE}^{TE} \int_{-z/2}^{z/2} \frac{2+\varepsilon\cos\Theta}{\varrho h^L} \varrho \cos\Theta d\Theta dz \\
&= -\frac{2z}{\rho_\infty V_\infty^2 S} \left(\begin{array}{l} \rho_\infty \varrho \dfrac{\partial h^L}{\partial t} \cos\Theta \\ -\dfrac{\rho_\infty \varrho \mu_g^2}{2{h^L}^2} \left(\begin{array}{l} \cos\Theta + \varepsilon\cos^2\Theta \\ +\dfrac{\varepsilon^2}{3} \left(\cos^3\Theta + \sin^2\Theta\cos\Theta + 2\cos\Theta \right) \end{array} \right) \\ +\left(\lambda + \dfrac{2}{3}\mu \right) \left(\dfrac{\mu_g \varepsilon \cos^2\Theta}{2h^L} \right) \end{array} \right)_{LE}^{TE} \\
&+ \frac{2\nu\mu_g z}{V_\infty^2 S} \left(\frac{(4\sin\Theta + \varepsilon(\Theta + \sin\Theta\cos\Theta))}{2h^L} \right)_{LE}^{TE}
\end{aligned}
\tag{210}
$$

respectively. The side force coefficient, C_S is also obtained as

$$C_S = -\frac{2}{\rho_\infty V_\infty^2 S}$$
$$\times \int_{LE}^{TE}\int_0^\Theta \left[\begin{array}{l} \rho_\infty\left[-\dfrac{\partial h^L}{\partial t}+\dfrac{\mu_g^2\left(\varepsilon^2\sin^2\Theta+(1+\varepsilon\cos\Theta)^2\right)}{2h^{L^2}}\right] \\ -\left(\lambda+\dfrac{2}{3}\mu\right)\left(\dfrac{\mu_g\varepsilon\cos\Theta}{\varrho h^L}\right)\end{array}\right]\varrho^2\cos\Theta\sin\Theta d^2\Theta$$

$$-\frac{2\nu\mu_g}{V_\infty^2 S}\int_{LE}^{TE}\int_0^\Theta \frac{2+\varepsilon\cos\Theta}{\varrho h^L}\varrho^2\sin\Theta\cos\Theta d^2\Theta$$

$$= -\frac{2}{\rho_\infty V_\infty^2 S}\left(\begin{array}{l} \rho_\infty\dfrac{\partial h^L}{\partial t}\dfrac{\varrho^2}{4}\left(\cos\Theta\sin\Theta+\Theta\right) \\ -\dfrac{\rho_\infty\varrho^2\mu_g^2}{2h^{L^2}}\left(\dfrac{\cos\Theta\sin\Theta+\Theta}{4}+\dfrac{\left(4+2\cos^2\Theta\right)\varepsilon\sin\Theta}{9}+\dfrac{\varepsilon^2\sin\Theta\cos\Theta}{4}\right) \\ -\left(\lambda+\dfrac{2}{3}\mu\right)\dfrac{\mu_g\varepsilon\varrho\cos^3\Theta}{3h^L}\end{array}\right)_{LE}^{TE}$$

$$+\frac{2\nu\mu_g\varrho}{V_\infty^2 S}\left(\frac{\left(3\cos^2\Theta+\varepsilon\cos^3\Theta\right)}{3h^L}\right)_{LE}^{TE}. \tag{211}$$

The integrals were obtained with *Maple*^{TM} [74]. Then, Θ is obtained with

$$\Theta = \cos^{-1}\left[\frac{1}{\varepsilon}\left(\frac{h^{L^2}}{\mu_g r}-1\right)\right], \tag{212}$$

and Eqns. 209 to 211 are all evaluated at the cylinder surface where $\varrho = r = R$.

The limits of integration are employed in Eqns. 206 and 208. For both C_A and C_N, the limits from LE to TE correspond to $(\theta,\phi) = (\epsilon, \pi/2)$ to $(\theta,\phi) = (2\pi+\epsilon, \pi/2)$ respectively for a crossflow as illustrated in Fig. 63. For C_S, the limits are from $(\theta,\phi) = (\epsilon, 0)$ to $(\theta,\phi) = (2\pi+\epsilon, \pi)$. ϵ is defined in Sec. 2.1.6.1. For the cylinder crossflow in Fig. 63a, $\tilde{\varphi}$ is parallel to the flow and is constant at $\pi/2$ along the cylinder span. Thus, z is a unit depth in Eqns. 209 and 210. However, $\tilde{\varphi}$ is perpendicular to the flow direction for the sphere flow depicted in Fig. 63b. Therefore, the limits

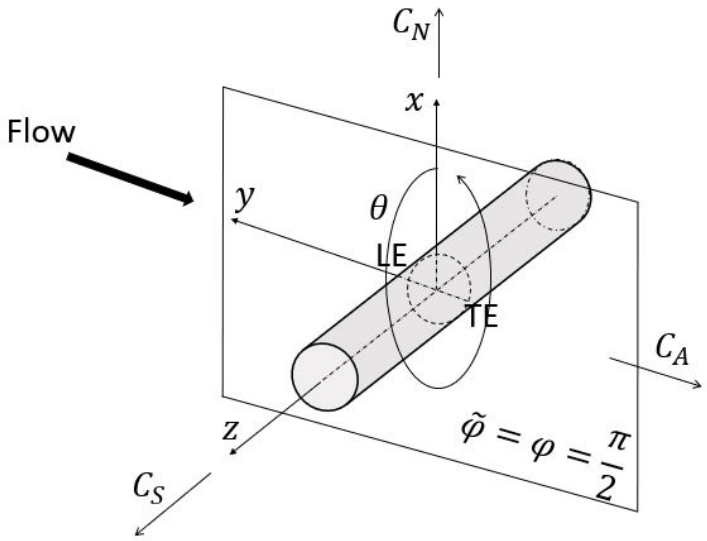

(a) Cylinder crossflow

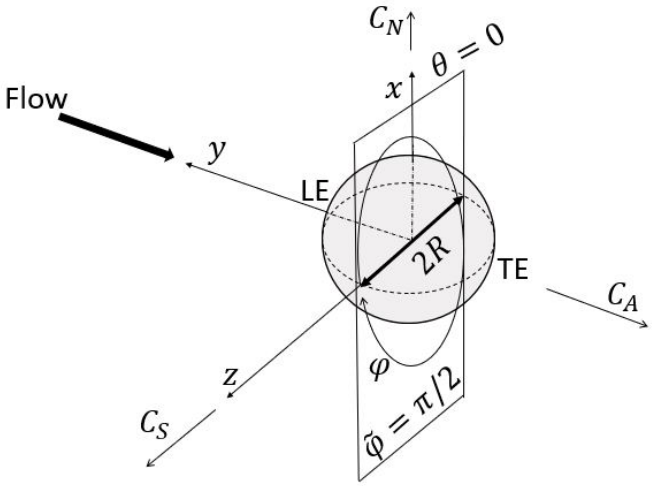

(b) Sphere axial flow

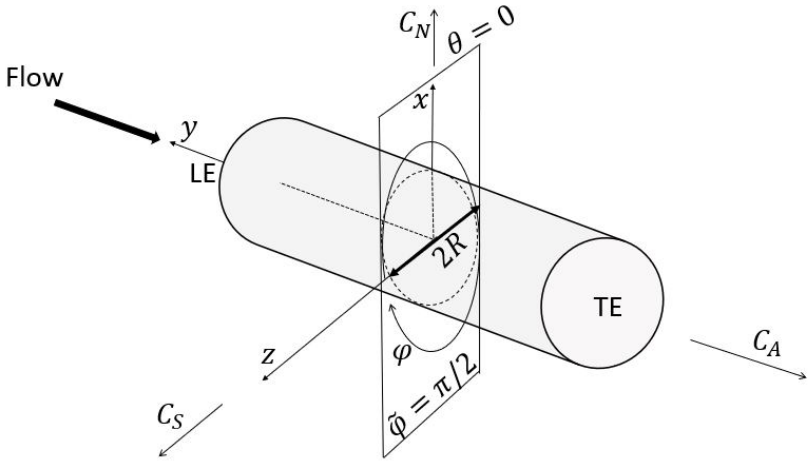

(c) Cylinder axial flow

Figure 63: The forces resolved in the perifocal frame.

from LE to TE for both C_A and C_N correspond to $(\theta, \phi) = (\epsilon, 2\pi)$ to $(\theta, \phi) = (\epsilon, 0)$ respectively, and $z = 2R$ for the sphere in Eqns. 209 and 210. For C_S, the limits are from $(\theta, \phi) = (\pi + \epsilon, 2\pi)$ to $(\theta, \phi) = (\epsilon, 0)$. This is the same for an axial flow on a cylinder (illustrated in Fig. 63c) and a spheroid when z equals their windward spans.

The force integration can sometimes result in a negative axial force in the perifocal frame because Θ is dependent on the flow condition. It can also give a complex-valued result. However, the axial force is real and always positive along the wind axis in an experimentally observed flow as illustrated in Fig. 63. Therefore, the magnitude of the real part of the axial force integral is used. When there are disparities in the sign of the force coefficients, directions that are consistent with a positive axial force are used for the normal and side forces.

Usually, the force integration in Eqns. 209 to 211 correspond to net signed areas [87, p. 5.2.7] under the perifocal c_f and C_p curves. However, variations in flow conditions can result in Θ (Eqn. 212) having the same values for the LE and TE, and the net signed area becomes zero. When this happens, the physical force integration in the body axis correspond to the total area [87, p. 5.2.7] under the perifocal c_f and C_p curves.

Each term introduced in the refinement of CPT cannot be verified and validated individually. However, the predicted velocity distributions and the shear stress, the integrated quantities like the pressure distribution and the forces offer avenues to assess the foregoing refinement. This is the subject of the following chapter.

CHAPTER III

VERIFICATION AND VALIDATION

The verification and validation of refined potential theory (RPT) is carried out on a cylinder in cross and axial flows for varying Re_∞. In the crossflow configuration, the comparison is carried out in the plane $z = 0$ for planar quantities. The conditions presented in Table 5 are used unless otherwise stated. The choice of the cylinder radius is arbitrary and is also true for the mass of the cylinder. To make these assessments, the quantities of interest for comparison are the

- boundary layer thicknesses and velocity profiles;
- surface shear stress and pressure distributions;
- points of separation on the cylinder;
- coefficients of drag and lift; and
- Strouhal number, wake velocity profiles and energy spectra.

3.1 A Cylinder in Crossflow with Varying Reynolds Numbers

Figure 64 compares the theoretical boundary layer Eulerian-mean velocity profiles with the experiments of Fage and Falkner [1]. In conjunction with this, Table 6

Table 5: Cylinder radius and flow conditions.

Radius, R (m)	ρ_∞ (kgm^{-3})	a_∞ (ms^{-1})	ν_∞ (m^2s^{-1})
0.047	1.225	343	1.46069×10^{-5}
λ_∞ $(kgm^{-1}s^{-1})$	G $(m^3kg^{-1}s^{-2})$	$\mathcal{M}_B$ (kg)	t (s)
-1.19236×10^{-5}	6.67408×10^{-11}	1	3610.6
p_∞ (Nm^{-2})	Span, B (m)	S (m^2)	z-plane
101325	$2\pi R$	$4\pi R^2$	0

presents a comparison of the corresponding boundary layer thicknesses and the flow conditions. The angular location is measured from the front stagnation point. Fage and Falkner only surveyed the outer portion of the boundary layer with surface tubes of the Stanton type [1]. The uncertainties in these measurements were not reported [1], however, the effect of increasing Re_∞ on the convex profile of the boundary layer is noticeable for both refined potential theory and experiment with good comparative agreement. This effect is essentially a velocity effect since other flow conditions were kept constant [1]. Boundary layer profiles are more convex in turbulent flows [5,15,33]. Therefore, it is most likely that the difference in the RPT and measured profiles is due to experimental freestream turbulence.

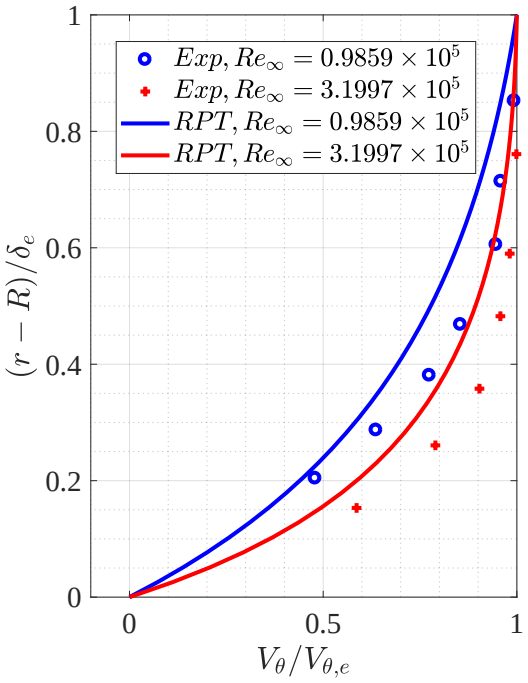

Figure 64: Present theoretical and experimental boundary layer velocity profiles for the circular cylinder in a crossflow [1].

A freestream turbulence effect thickens the boundary layer [5, 15, 33], and it is expected that the measured thicknesses be larger than RPT thicknesses with zero freestream turbulence. However, this is not the case in Table 6 in which it is observable

Table 6: Comparison of present theoretical and experimental (by Fage and Falkner[1]) boundary layer thicknesses.

$R = 0.113m$	δ_e (m)	
Re_∞	Exp. $(AR = 0.1854, BR = 0.1854)$	RPT $(AR = 3.142, BR = 0)$
0.9859×10^5	0.000881 $(\theta = 49.4°)$	0.0593 $(\theta = -49.1°)$
3.1997×10^5	0.001105 $(\theta = 49.8°)$	0.1004 $(\theta = 49.9°)$

that the RPT thicknesses are about two orders of magnitude larger than experimental ones. Other factors such as the viscosity, the blockage ratio (BR), the aspect ratio and the nature of the boundary layer flow also affect its extent [9]. The theoretical flow does not differ in viscosity with Fage's and Falkner's experiment, but it occurs in an unconstrained domain unlike a wind tunnel. Wind tunnel walls constrict an incident stream and squeeze it so that a body in a test section only sees a fraction of its actual extent [9]. Thus, boundary layers can become thinner with blockage ratios. Observations of extensive blockage effects on a cylinder flow have not been noticed at high Re_∞ as much as at low Re_∞ [9, 88]. However, West and Apelt [88] report a distinct change in the character of the flow once BR becomes greater than 6% for all aspect ratios and $10^4 < Re_\infty < 6 \times 10^4$ they compared. With 18% experimental blockage ratio of Fage's and Falkner's [1] in contrast to 0% in the present theory, it is likely there are some blockage effects in the boundary layer thickness disparity. The aspect ratio has a correlation with the three-dimensionality of the flow mid-span [9]. Due to three-dimensional relieving effects [5, p. 495], the mid-span plane flow accelerates less over lower aspect ratio cylinders than higher aspect ratio ones. Higher boundary layer flow accelerations result in larger adverse pressure gradients in the flow direction [15, 33, 84]. An adverse pressure gradient thickens a boundary layer [84, p. 497]. Therefore, with an order of magnitude difference in aspect ratios, it is possible that three-dimensional relieving effects also contribute to the disparity in the compared boundary layer thicknesses.

Fage and Falkner also report some c_f distributions. These were not directly measured but estimated with velocity measurements above the surface [1,9]. They also do not feature the entire rear of the cylinder [1,9]. They compared their c_f distributions with Boundary Layer Theory (BLT) calculations and concluded that some of these distributions were unreliable because of a surface-tube-to-boundary-layer-thickness sizing mismatch [1,13]. Therefore, the experiments of Son and Hanratty [13] in which electrochemical techniques were used to measure the velocity gradients are resorted to for the quantitative verification of the RPT Lagrangian-mean c_f distributions. Figure 65 illustrates this. The electrochemical technique is also an indirect method that indicates only the magnitude of these wall gradients and involves some simplifying assumptions [13, 83]. The corrections for the experimental errors in this technique were found to be significant only for low Reynolds numbers and in the vicinity of flow separation [83]. Son and Hanratty included methods with which they determined the direction of the gradients and detected reversals of signs in the rear of the cylinder [13]. The directional variation of RPT results is presented in Fig. 66, but their magnitudes are used in Fig. 65 to facilitate a comparison with the experimental data. The RPT gradients are greater. Boundary Layer Theory predicts that measurements of the non-dimensional velocity gradient obtained at varying Re_∞ fall on a single curve when normalized by $\sqrt{Re_\infty}$ [13]. Whereas Son's and Hanratty's [13] data do not show significant Re_∞ dependence, the RPT results do. Dimopoulos and Hanratty also made observations that the normalized gradients still show some Re_∞ variations for $60 < Re_\infty < 105$ [83]. However, there is agreement between refined potential theory and experiment on the laminar separation point in the front of the cylinder.

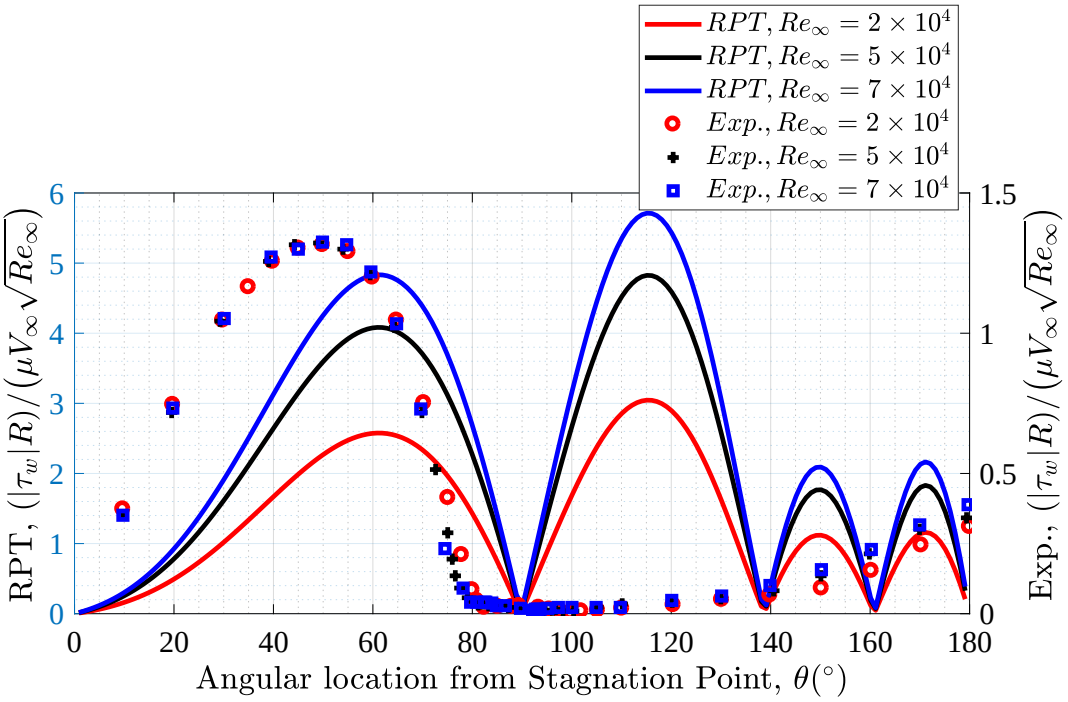

Figure 65: Comparison of normalized magnitude of RPT wall Lagrangian-mean velocity gradient in a cylinder crossflow against experimental result from Son and Hanratty [13] ($R = 0.0254m$).

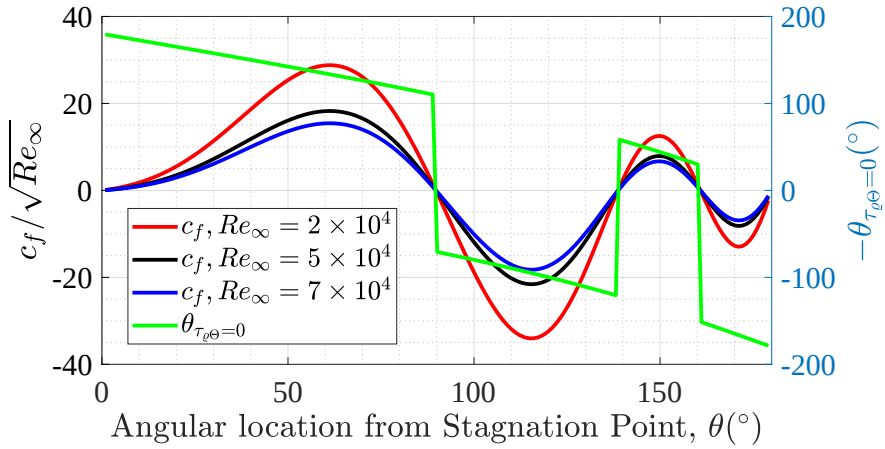

Figure 66: Present theoretical Lagrangian-mean c_f distributions at three Reynolds numbers.

Figure 67 compares the RPT Eulerian-mean cylinder pressure distribution to

classical potential theory and experimental data [14, 18] for $Re_\infty = 3,900$. The $Re_\infty = 3,900$ cylinder flow is a classic test case which is the subject of a coupled experimental/Large Eddy Simulation (LES) work of Ong and Wallace [89] and Kravchenko and Moin [14]. This is because of the regions of the massively separated boundary layer flow. The pressure distribution, separation point, near wake velocity profiles and velocity power spectra analyses at specific locations as well as the St were reported [14, 89]. The experimental data presented in Fig. 67 was obtained from Kravchenko and Moin [14] who cited private communications with C. Norberg for it. The experimental error was not reported. However, Norberg's experiments at some different Re_∞ reviewing the the effects of pressure tap dimensions on measurements puts the uncertainty at $\pm 1\%$ [90]. This is after corrections for tunnel blockage ratio effects [90]. Norberg's [90] error band was used for the error bars in Fig. 67. In conjunction with this figure, Table 7 presents time-averaged experimental data, nemerical results and RPT predictions. The quantities compared include $\bar{C}_D$, C_{p_b} (base pressure coefficient), θ_s, Strouhal number, St, and $\bar{V}_{x_{min}}/V_\infty$. The experimental C_{p_b} and θ_s are at $Re_\infty = 4,020$ and $Re_\infty = 5,000$ respectively [14]. All the other experimental quantities, the numerical results and the present theoretical evaluations are at $Re_\infty = 3,900$. The RPT C_D and θ_s are Lagrangian-mean quantities while the C_{p_b}, St and $\bar{V}_{x_{min}}/V_\infty$ are Eulerian-mean quantities.

The $Re_\infty = 3,900$ case has also been used by Lynch [91] and Hodara [18] in the verification of their numerical simulations. Large eddy simulations of NSE try to resolve the large scales of a flow and model the small scales for turbulence closure [15, 92]. Lynch employed a hybrid Reynolds-averaged Navier-Stokes / LES (HRLES) turbulence model [91]. Hodara developed a transitional hybrid Reynolds-averaged Navier-Stokes-LES turbulence model (tHRLES) and explored its performance against HRLES, Shear Stress Transport (SST) model, and Langtry-Menter (LM) model [18].

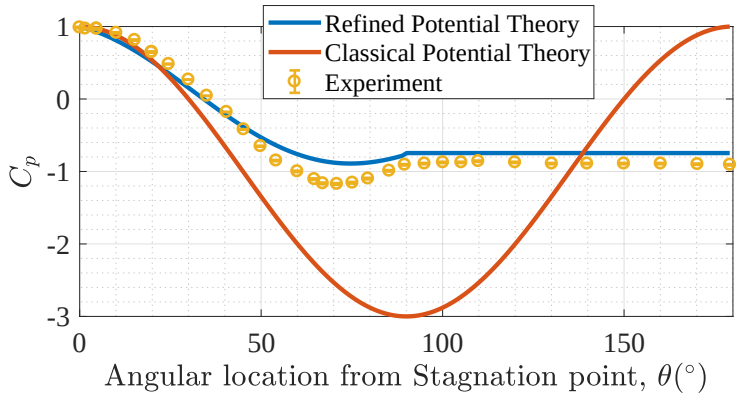

Figure 67: Comparison of RPT cylinder pressure distribution to classical potential theory and experimental data [14] for $Re_\infty = 3,900$.

He concludes that tHRLES produced significantly better results than the other mentioned turbulence models [18]. Therefore, comparative discussions are focused on refined potential theory, tHRLES and experiment in Table 7. The experiments of Ong and Wallace were carried out in a wind tunnel at the Turbulence Research Laboratory, University of Maryland, and X-array hot wire sensors were used to take measurements of the wake velocity field [89].

The agreement between refined potential theory and experimental data is observable in Fig. 67. The point at which $C_p = 0$ for refined potential theory comes less than 5° closer to the stagnation point than the experimental data. The predicted base suction, $-C_{pb}$, of 0.75 is within 10% of error bound of the experimental result. However, the experimental $-C_{pb}$ in Table 7 is at a higher Re_∞. Refined potential theory successfully predicts the wake suction. It resolves d'Alembert's Paradox with a prediction of C_D that is within the error bound of measured data and tHRLES prediction. It gives values of St and $\bar{V}_{x_{min}}/V_\infty$ that agree with measurements. Its prediction of the separation point is 2° away from the upper error bound of the experimental data. Therefore, these close the gap that is observable between classical potential theory and experiment in Fig. 67 and Table 7. It is emphasized that the discussed RPT

Table 7: Measured and predicted circular cylinder characteristics at $Re_\infty = 3,900$ for the verification and validation of the refined potential theory.

Data from	$\bar{C}_D$	$-C_{p_b}$	St	$\theta_s(^\circ)$	$\bar{V}_{x_{min}}/V_\infty$
CPT	0	-1	–	–	–
Expt (Refs. 14, 91)	0.99 ± 0.05	0.88 ± 0.05	0.215 ± 0.005	86.0 ± 2	-0.24 ± 0.1
LES (Ref. 14)	1.04	0.94	0.210	88.0	-0.37
HRLES (Ref. 91)	0.971	–	0.216	85.8	–
HRLES (Ref. 18)	1.05	–	0.210	86.7	–
LM (Ref. 18)	1.35	–	0.230	96.5	–
tHRLES (Ref. 18)	1.03	–	0.209	88.0	–
SST (Ref. 18)	1.58	–	0.238	98.4	–
Present theory	0.989	0.75	0.197	90	-0.20

results are instantaneous Lagrangian-mean and Eulerian-mean quantities as opposed to the time-averaged experimental and CFD results. Thus, they have some transient variations but with very small amplitudes [79]. It was observed that accurate results were not obtained by integrating only the Eulerian-mean surface pressure and shear stress distributions until the Stoke's corrections were included. This observation is in agreement with Andrew's and McIntyre's analyses that identify these corrections as necessary for effective transport of wave momentum in the flow field [79].

The variation of $\bar{C}_D$ with Re_∞ on the cylinder is presented in Fig. 213 to validate refined potential theory. It is the subject of numerous experimental investigations [5, 9, 15, 16, 72]. An empirical model of this relationship (Eqn. 3-228 in Ref. 15) is given as

$$C_{D_{cylinder}} \approx 1 + \frac{10.0}{Re_\infty^{2/3}} \, . \tag{213}$$

This is valid for very low Re_∞ till $Re_\infty \approx 250,000$ [15]. It is labeled as 'Exp. Curve fit' in the figure. The RPT points were obtained at the same Re_∞ as the experimental points. All flow conditions were kept constant at their values employed for $Re_\infty = 3,900$ except the second coefficient of viscosity. This was calculated based on keeping $C_p = 1$ at the stagnation point for all the Re_∞. Tritton estimated the overall experimental error in his data to be about 6% [16, p. 553]. This was used to plot

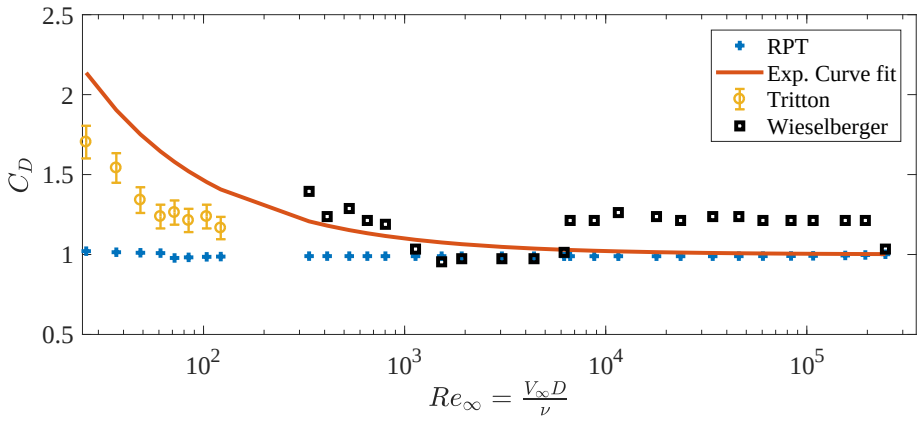

Figure 68: Comparison of refined potential theory in crossflow with experimental data by Tritton [15, 16], Wieselberger [15], and experimental data curve fit by White [15].

the error bars in the figure. Wieselberger did not discuss the systematic error in his data [16, p. 554]. However, the agreement of refined potential theory with experiment in capturing the magnitude of the C_D over the range $300 \leq Re_\infty < 300,000$ is noticeable.

This agreement of trend is also observable in this Re_∞ range in Fig. 69 which illustrates the theoretical sectional lift (lift per unit span) variation with Re_∞ against a set of empirical curve fits. The time-averaged lift on a stationary circular cylinder in crossflow is equal to zero [5]. However, the instantaneous lift is not always zero due to periodic and alternate shedding of vortices from around its crests [9, 17]. Thus, refined potential theory predicts finite instantaneous Lagrangian-mean values. Norberg [17] reviewed published experimental and numerical results on the root mean square

(r.m.s) of fluctuating sectional lift coefficient and suggests

$$\hat{C}_{L'} = \begin{cases} \sqrt{\left(Re_\infty - 47\right)/1410 + \left(Re_\infty - 47\right)^2/198810} & 47 \le Re_\infty \le 190 \\ 0.43 \times \left(Re_\infty/300\right) & 165 < Re_\infty \le 230 \\ 0.78 \times \left(Re_\infty/260\right) - 0.26 & 230 < Re_\infty \le 260 \\ 0.045 + 1.05 \times \left(1 - Re_\infty/1600\right)^{4.5} & 260 \le Re_\infty \le 1.6 \times 10^3 \\ 0.045 + 3.0 \times \left[\log\left(Re_\infty/1600\right)\right]^{4.6} & 1.6 \le Re_\infty/10^3 \le 5.4 \\ 0.52 - 0.06 \times \left[\log\left(Re_\infty/1600\right)\right]^{-2.6} & 5.4 \le Re_\infty/10^3 \le 220\,, \end{cases} \tag{214}$$

for its variation with Re_∞ . These curve fits are plotted in Fig. 69 in comparison with refined potential theory. The RPT $\hat{C}_{L'}$ data points were obtained with the same conditions used in Fig. 68. The magnitudes are plotted because the directions change across the Re_∞ range. Factors including the aspect ratio, blockage ratio, surface roughness and freestream turbulence all affect the integrated quantities of an experimental cylinder flow and its fluctuating lift in particular [9, 17]. Zdravkovich [9] linked the disparities in the measured $\hat{C}_{L'}$ by different researchers to the effects of these parameters. Norberg [17] also identifies the spatio-temporal domain resolution, the boundary conditions employed, and the three-dimensionality of the simulated flow as factors that affect the reviewed numerical experiments. However, the general agreement of the theoretical range of the $\hat{C}_{L'}$ magnitude with these results is still noticeable in Fig. 69.

It appears the refined potential theory predictions of the surface quantities are viable. Therefore, its performance in the wake is also assessed. Figure 70 presents a theoretical instantaneous Eulerian-mean streamwise velocity profile on the center line in the wake of a circular cylinder against time-averaged experimental data. The uncertainty in Lourenco's and Shih's data was not reported [14]. Ong and Wallace systematically analyzed the error in their measurements. They determined a maximum uncertainty of about 26% for some orientations of their X-array of probes

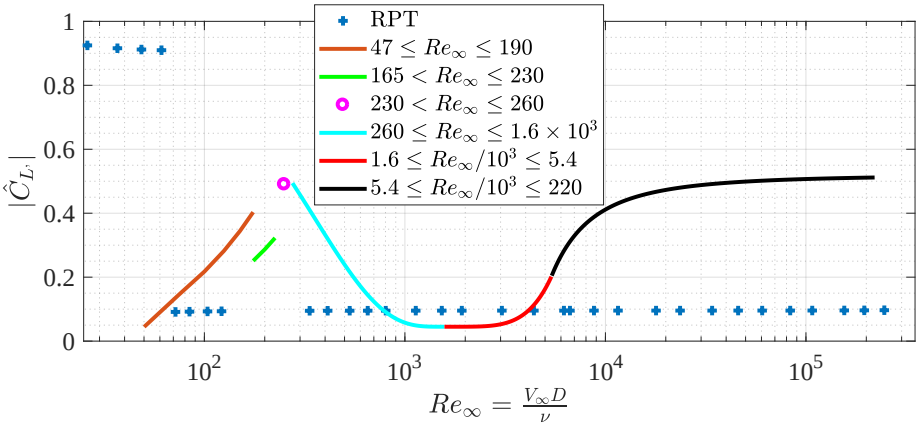

Figure 69: Comparison of refined potential theory in crossflow with data curve fits (experimental and numerical) by Norberg [17].

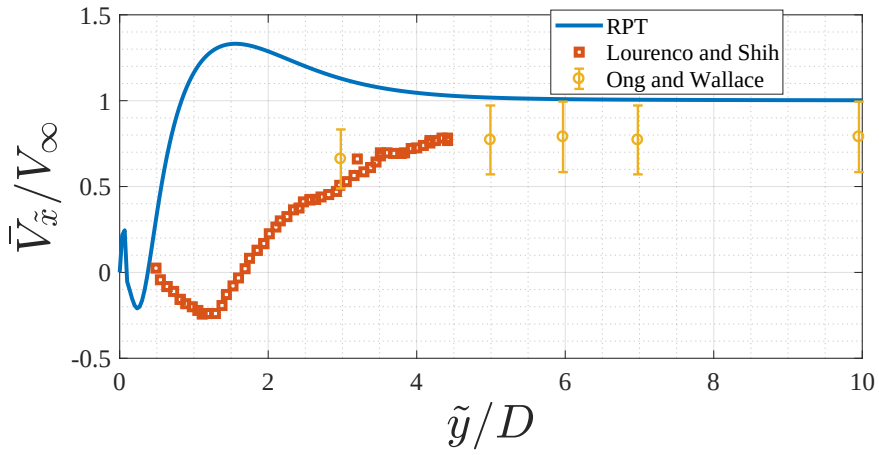

Figure 70: Comparison of the RPT instantaneous Eulerian-mean streamwise velocity on the center line in the wake of a circular cylinder with time-averaged experimental data by Lourenco and Shih [14], and Ong and Wallace [14] at $Re_\infty = 3,900$.

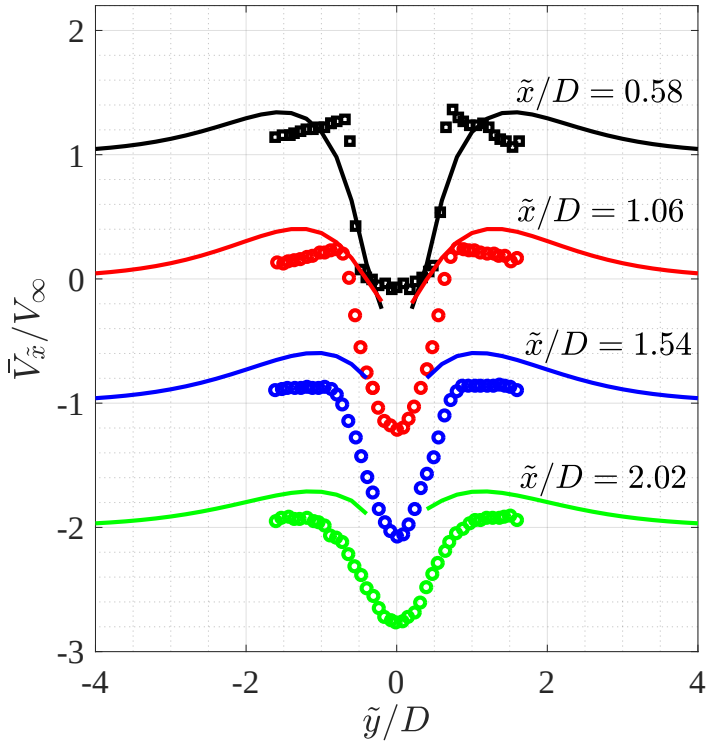

Figure 71: Comparison of RPT instantaneous Eulerian-mean streamwise velocity profiles (lines) at several downstream locations behind a circular cylinder with time-averaged experimental data (□ [18] and ∘ [14]) at $Re_\infty = 3,900$.

[89, p. 444]. This is used to create the error bars in Fig. 70. The general outline of the experimental profile is captured but with an overshoot at $\tilde{y}/D \approx 1.5$ compared to Lourenco's and Shih's data [14]. Whereas Ong's and Wallace's [89] profile indicates the freestream velocity is not recovered at $\tilde{y}/D \approx 5$, the theoretical profile shows this to be the case. This agrees with the upper bound of the experimental error but, it also implies that the experimentally observed wake width may be larger than predicted. The extent of the theoretical recirculation region is also smaller. However, the prediction of $\bar{V}_{x_{min}}/V_\infty$ in Table 7 falls within 13% of the lower experimental error bound.

Figure 71 compares the theoretical instantaneous Eulerian-mean streamwise velocity profiles at four downstream locations behind a circular cylinder against time-averaged experimental data [14, 18] at $Re_\infty = 3,900$. In tandem, Fig. 72 presents

the corresponding theoretical instantaneous Eulerian-mean crossflow velocity against time-averaged experimental data [14]. The uncertainty in these measurements were not reported. Starting with $\tilde{x}/D = 1.06$, each successive profile in these figures is shifted in the vertical axis by -1. For both figures, 41 linearly spaced points were sampled for $-4 \leq \tilde{y}/D \leq 4$. The magnitudes of some theoretical velocities at some of these points directly in the wake and close to $\tilde{y}/D = 0$ tend to infinity. Therefore, these points were not plotted in the figures. These velocities also have changing directions. There are two reasons for the behavior at these points. The Lamb-Oseen vortex model, upon which the present refinement of classical potential theory relies, describes a time-dependent viscous diffusion of a line vortex [9, 15, 46]. It is an exact solution of NSE [9, 15, 46]. However, it has a singularity at the vortex core origin where the velocity tends to infinity. In the vicinity of this core, the velocity also gets unrealistically high [9]. In addition, the theoretical vortices are *forced*. Thus, when the Reynolds number and time are considerably large, the convected local vortical axes spin so fast that the local velocity tends towards very high values at their cores (see Sec. 2.1.6.2). The changes in direction of the velocity is because of the instantaneity of the theoretical profiles. An assessment of the general profiles in the figures is possible when the singularities are excluded. At $\tilde{x}/D = 0.58$ in Fig. 71, the wake advanced about a cylinder radius out. There is reasonable agreement at the neck of the profile trough. However, the theoretical profile veers off from the experimental U-profile fanning out into a V-profile. V-shaped wake velocity profiles close to the cylinder are characteristic of early separating shear layer transitions which shorten the vortex formation region [14]. This suggests that a time mismatch is most likely responsible for the disparity in the magnitude and shape of the theoretical and experimental profiles except at the trough base. The theoretical profiles also capture the profiles' symmetry around the center line in Fig. 71. A general similarity of the theoretical profiles to the experimental ones is discernible in Fig. 72 at $\tilde{x}/D = 1.54$

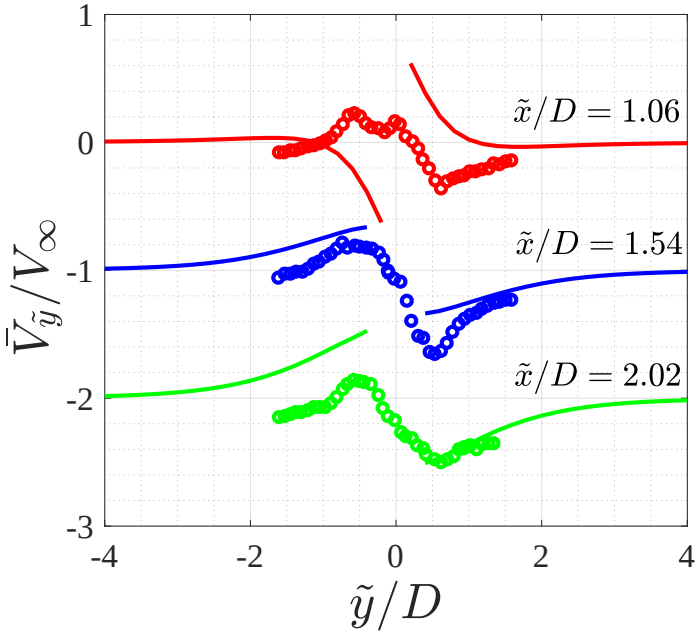

Figure 72: Comparison of RPT instantaneous Eulerian-mean crossflow velocity (lines) at three locations in the wake of a circular cylinder with time-averaged experimental data ($\circ$) [14] at $Re_\infty = 3,900$.

and $\tilde{x}/D = 2.02$.

Figure 73a illustrates the one-dimensional energy spectrum of the instantaneous streamwise Stoke's drift velocity in the wake of a cylinder. The energy spectrum is presented with Kolmogorov scaling [78]. It was computed using the Fast-Fourier Transform (FFT). It is a Taylor's-hypothesis-converted frequency spectrum with the freestream velocity as the convection velocity [78, 89]. It was obtained with a static grid. An initial time, $t_0 = 3606.25s$ was assumed and $13,000$ samples were computed at $\Delta t = 336.54\mu s$ to $t = 3,610.6s$ to identify the nature of the unsteadiness in the solution. The choice of the sampling rate and number of samples are based on those used by Kravchenko and Moin [14]. A plot of the time variation of the shedding frequency was made. t_0 is ten shedding cycles later from the quasi-steady state, and the time variation over seven additional shedding cycles from t_0 was obtained for the analyses.

In a homogeneous isotropic turbulence field, the viscous dissipation of the mean flow based on the mean strain rate is [78]

$$\varepsilon = 15\nu\overline{\left(\frac{\partial V_{\tilde{x}}}{\partial x}\right)^2} \tag{215}$$

and the Kolmogorov length scale [78],

$$\eta \equiv \left(\nu^3/\varepsilon\right)^{1/4} \ . \tag{216}$$

The dissipation rate is actually based on three-dimensional velocity gradients [33, 78, 92]. However, homogeneity and isotropy of the turbulence field are assumptions usually invoked to simplify its estimates from experimental data [78]. Assuming this is true for the present theoretical solution, the computed values are listed in the figure label. The strain rate in Eqn. 215 was calculated as an instantaneous Lagrangian-mean quantity. ε and η are used for the viscous dissipation and Kolmogorov length scale to be consistent with Fig. 73b. The dissipation rate is proportional to the local mean strain rate and is nearly equal to the production term that signifies the transfer of energy from the large scales in the turbulence kinetic energy budget [78]. Thus, it varies spatially, and it is usually positive as presented in Table 8. However, there can be local backscatter characterized by regions of negative dissipation rates [78]. Therefore, Table 8 is consistent with this observation. Even though the mean strain rates are squared to obtain the dissipation rates, the negative values arise because the strain rates are complex-valued. In the inertial sub-range ($k_1\eta > 0.1$), in Fig. 73a, the present theoretical scaled energy spectrum continues to be proportional to $(k_1\eta)^{-5/3}$ where k_1 is the magnitude of the wavenumber vector in the $\tilde{x}$-direction [78]. It is assumed to be equivalent to $k = 2\pi/(\Delta t V_\infty)$ because the freestream flow does not have components in the other directions. Figure 73a is consistent with Kolmogorov's Five-Thirds law of turbulence [78]. It is also in agreement with verified and validated experimental and theoretical analyses in Fig.73b [78, 93].

Table 8: Spatial variation of viscous dissipation, ε (m^2s^{-3}) in a cylinder wake at $Re_\infty = 3,900$.

$\tilde{y}/D$ \ $\tilde{x}/D$	3	5	7	10
0.7500	$6.6146e^{-05}$	$2.1182e^{05}$	$-2.6353e^{07}$	$-1.3306e^{08}$
0.7511	$5.7915e^{-05}$	$-1.6185e^{05}$	$1.3199e^{07}$	$2.2822e^{08}$
1.7500	$5.6158e^{-04}$	$1.1194e^{-04}$	$3.8127e^{-05}$	-0.7273
1.7511	$5.6176e^{-04}$	$1.1202e^{-04}$	$3.8188e^{-05}$	-0.5497

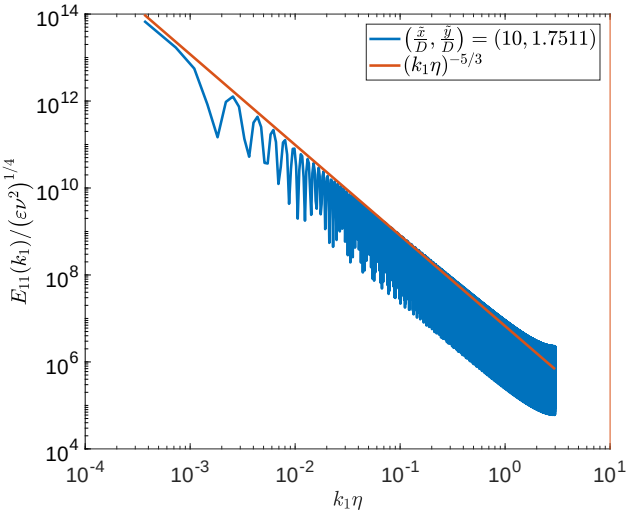

(a) One-dimensional energy spectrum of $V_{\tilde{x}}^S$ in a cylinder wake predicted with present theory ($\varepsilon = -0.5497m^2s^{-3}$, $\eta = 1.9403e^{-04}m$).

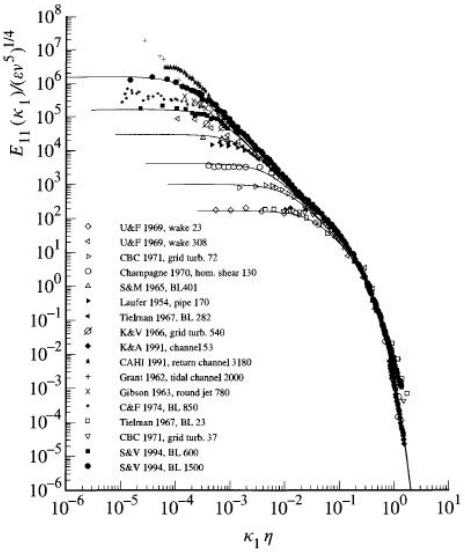

(b) Measurements of one-dimensional longitudinal velocity spectra (symbols) and model spectra (lines) for different Taylor scale Reynolds numbers (Data from many sources) [78].

Figure 73: The RPT one-dimensional energy spectrum of the streamwise Stoke's drift velocity fluctuations in a cylinder wake at $Re_\infty = 3,900$, $t_0 = 3,606.3s$, and $\Delta t = 3.3654e^{-04}s$ juxtaposed with several experimental measurements of velocity spectra.

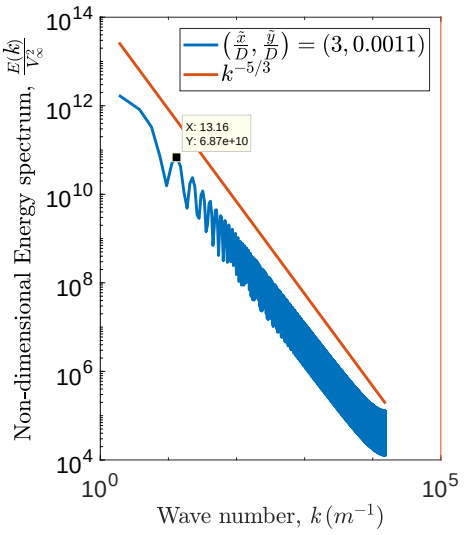

(a) Power spectrum of $\frac{V^E}{V_\infty}$ at $\left(\frac{\tilde{x}}{D}, \frac{\tilde{y}}{D}, \frac{z}{D}\right) = (3, 0.0011, 0)$.

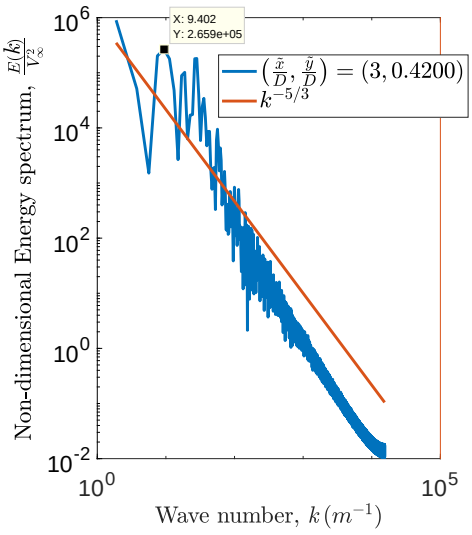

(b) Power spectrum of $\frac{V^E}{V_\infty}$ at $\left(\frac{\tilde{x}}{D}, \frac{\tilde{y}}{D}, \frac{z}{D}\right) = (3, 0.4200, 0)$.

Figure 74: The one-dimensional energy spectrum analyses in a cylinder wake at $Re_\infty = 3,900$.

Figures 74 to 77 present non-dimensionalized one-dimensional energy spectra of the Eulerian-mean velocity magnitude fluctuations in a cylinder wake at four downstream and two crossflow locations using similar conditions as in Fig. 73a. The freestream velocity is used as the convection velocity for the wave number. The dominant wave number identified on six of these figures is $13.16m^{-1}$ corresponding to a Strouhal number, $St = kR/\pi \approx 0.197$. This is comparable in value to experimental and large eddy simulation (LES) results presented in Table 7. It is about 6% short of the lower error bound of the experimental result. At half-wake locations in Figs. 74a and 76b, the captured dominant frequencies give $St \approx 0.141$ and $St \approx 0.113$ respectively. Both of these points give evidence suggestive of a spatial variation of St that is consistent with Ong's and Wallace's [89] experimental observations of peak frequencies in the cylinder wake.

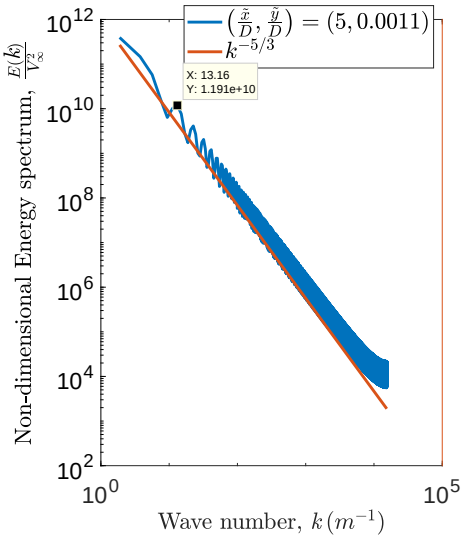

(a) Power spectrum of $\frac{V^E}{V_\infty}$ at $\left(\frac{\tilde{x}}{D}, \frac{\tilde{y}}{D}, \frac{z}{D}\right) = (5, 0.0011, 0)$.

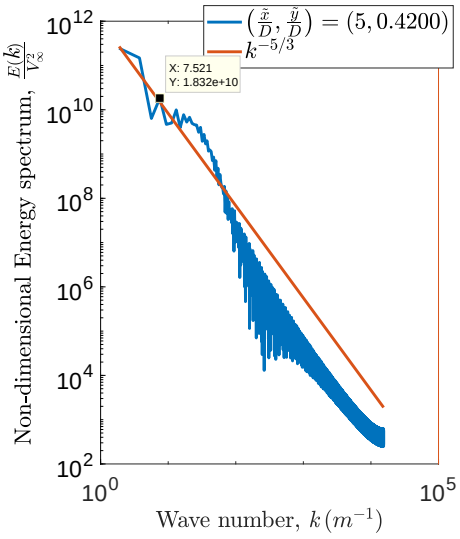

(b) Power spectrum of $\frac{V^E}{V_\infty}$ at $\left(\frac{\tilde{x}}{D}, \frac{\tilde{y}}{D}, \frac{z}{D}\right) = (5, 0.4200, 0)$.

Figure 75: The one-dimensional energy spectrum analyses in a cylinder wake at $Re_\infty = 3,900$.

Table 9 presents calculated time-averaged St at several locations in the cylinder wake over the same period as in Fig. 73 to 77. It highlights some of these slight variations spatial variations of the St. The values of St presented in this table were computed using Eqn. 123. A general agreement between these values and those obtained from the energy spectra plots is observable.

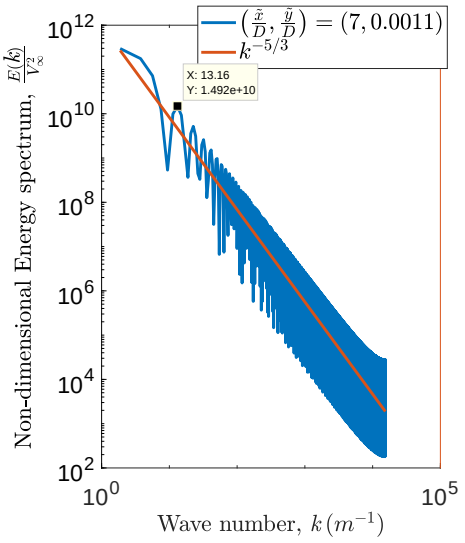

(a) Power spectrum of $\frac{V^E}{V_\infty}$ at $\left(\frac{\tilde{x}}{D}, \frac{\tilde{y}}{D}, \frac{z}{D}\right) = (7, 0.0011, 0)$.

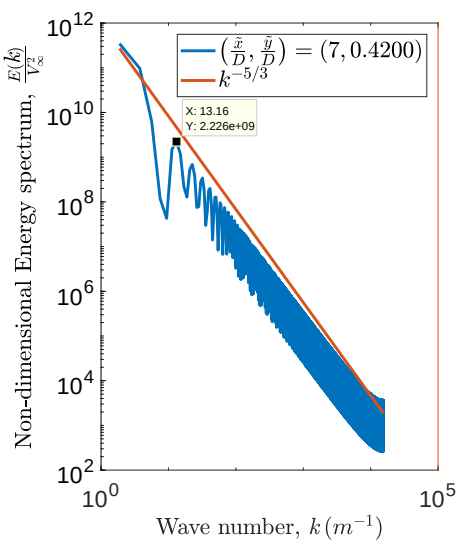

(b) Power spectrum of $\frac{V^E}{V_\infty}$ at $\left(\frac{\tilde{x}}{D}, \frac{\tilde{y}}{D}, \frac{z}{D}\right) = (7, 0.4200, 0)$.

Figure 76: The one-dimensional energy spectrum analyses in a cylinder wake at $Re_\infty = 3,900$.

Table 9: Spatial variation of Strouhal number in a cylinder wake at $Re_\infty = 3,900$.

$\tilde{y}/D$ \ $\tilde{x}/D$	3	5	7	10
0.0011	0.2013	0.1999	0.2004	0.2013
0.4200	0.2050	0.2005	0.2021	0.2019
0.5600	0.2001	0.2030	0.2016	0.2021
0.7000	0.1968	0.1990	0.2014	0.2019
0.7500	0.1963	0.1994	0.2015	0.2012
1.7500	0.1993	0.2018	0.2006	0.2015

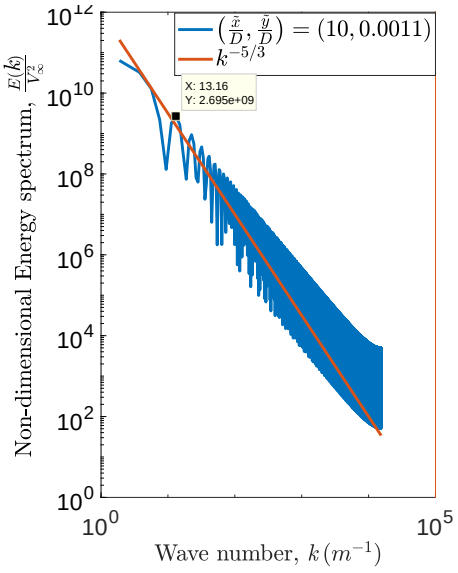

(a) Power spectrum of $\frac{V^E}{V_\infty}$ at $\left(\frac{\tilde{x}}{D}, \frac{\tilde{y}}{D}, \frac{z}{D}\right) = (10, 0.0011, 0)$.

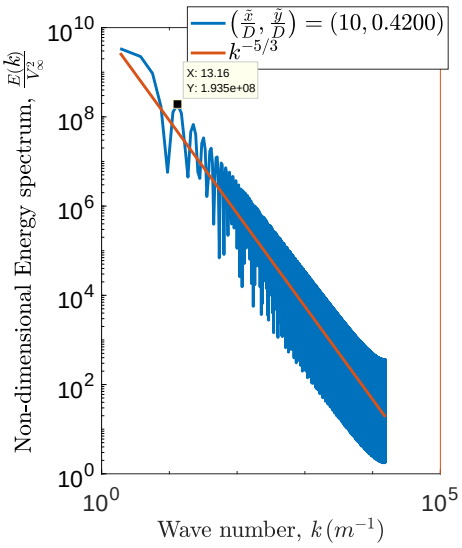

(b) Power spectrum of $\frac{V^E}{V_\infty}$ at $\left(\frac{\tilde{x}}{D}, \frac{\tilde{y}}{D}, \frac{z}{D}\right) = (10, 0.4200, 0)$.

Figure 77: The one-dimensional energy spectrum analyses in a cylinder wake at $Re_\infty = 3,900$.

3.2 A Cylinder in Axial Flow with Varying Reynolds Numbers and Aspect Ratios

Prosser and Smith [85] conducted high-fidelity LES of the flow over a non-rotating finite circular cylinder in axial flow with varying aspect ratios at $Re_\infty = 0.96 \times 10^5 -$

Table 10: Comparison of C_D on the circular cylinder in an axial flow with varying aspect ratios (L: Length, D: Diameter).

Data from	Re_D	L/D	C_D
Hoerner [72]	$10^3 - 10^7$	≈ 0	1.17
Tian et al. [94]	$10^3 - 6.04 \times 10^4$	≈ 0	$1.1 - 1.3$
Present theory	0.96×10^5	0	0.73
Prosser and Smith [85]	0.96×10^5	1	1.17
Present theory	0.96×10^5	1	1.03
Prosser and Smith [85]	0.96×10^5	2	0.84
Present theory	0.96×10^5	2	0.85
Prosser and Smith [85]	1.56×10^5	2	0.83
Present theory	1.56×10^5	2	0.78

Table 11: Cylinder axial flow conditions.

Re_D	L/D	λ_∞ $(kgm^{-1}s^{-1})$	$S(m^2)$
0.96×10^5	0	-1.19241×10^{-5}	πR^2
0.96×10^5	1	-1.19232×10^{-5}	πR^2
0.96×10^5	2	-1.19217×10^{-5}	πR^2
1.56×10^5	2	-1.19229×10^{-5}	πR^2

1.56×10^6. They report time-averaged C_D that are in good agreement with experimental results [85]. The refined potential theory results are presented in comparison with Prosser's and Smith's computation in Table 10. To obtain the theoretical axial flow, the cylinder in Fig. 57a is rolled through $\varsigma = \pi/2$. Table 11 presents the specific flow conditions used for the axial flow. Table 10 also compares the present theoretical result on a disk in axial flow with experimental results from numerous sources reported by Hoerner [72]. The disk C_D displays a near constant variation across a huge Re_∞ range from 10^3 to 10^7 [72]. However, Tian et al. [94] discuss some experimental result that displayed a variation in the time-averaged C_D between $1.1 - 1.3$ for $10^3 < Re_\infty \leq 6.04 \times 10^4$ [94]. In this experiment, the disk was towed in a channel of glycerine/water mixture [94]. The disk C_D is also affected by blockage ratio and freestream turbulence [72]. Hoerner [72] writes that it increases with freestream turbulence by as much as 5%. Compared to data discussed by Hoerner [72], the refined

potential theory underpredicts the disk drag coefficient by about 38%. A freestream turbulence effect should result in a lower theoretical prediction because the theoretical freestream has zero turbulence. However, the percentage theoretical underprediction is larger than the reported percentage change due to freestream turbulence effects in experiments. This suggests that the disparity is likely enhanced by other factors that may include blockage effect and instantaneity of the theoretical result.

Although there are slight discrepancies between the present theory and validated computations of Prosser's and Smith's [85], the general agreement is noticeable in Table 10. At the same Re_∞ and aspect ratio of one, refined potential theory underpredicts the C_D by about 12%. A 100% increase in the aspect ratio at a constant Re_∞ produced about 17.5% decrease in theoretical drag in contrast to 40% decrease in the computational result. A 63% increase in Re_∞ at a constant aspect ratio results in about 8.2% decrease in theoretical drag against around 1.2% decrease in the LES result. Thus, the disparity is more pronounced with increasing Re_∞ and aspect ratios. However, there is agreement in the relative insensitivity and sensitivity of an axial flow over a circular cylinder to Reynolds number and aspect ratios respectively. The qualitative results and discussion on these are presented in Fig. 60 in Sec. 2.5. The further agreement is displayed at $Re_\infty = 0.96 \times 10^5$ and $L/D = 2$ when the RPT result is within 1.2% of the computational result.

3.3 Cost of Evaluation

The symbolic mathematics and calculus in the evaluation of RPT were carried out in *Maple*^{TM} [74], and *Matlab*^{TM} [95] scripts were generated using the *with(CodeGeneration)* and *Matlab(Variable,optimize)* commands. Table 12 presents the computational time of refined potential theory in comparison with classical potential theory at a specific evaluation point in time, space coordinates and flow conditions. The CPT variables were also evaluated in a similar way to the RPT. These were evaluated on a computer

Table 12: Computational cost of RPT

Variable	Lines code generated with *Maple*^{TM} [74]	Time (s)
ψ (CPT)	4	0.0334
$\tilde{\kappa}$ (RPT)	$1,960$	0.6845
$V_r = \frac{1}{r}\frac{\partial \psi}{\partial \theta}$ (CPT)	4	0.0133
$V_r = \frac{1}{r}\frac{\partial \tilde{\kappa}}{\partial \theta}$(RPT)	$7,889$	2.4486
$V_\theta = -\frac{\partial \psi}{\partial r}$ (CPT)	5	0.0715
$V_\theta = -\frac{\partial \tilde{\kappa}}{\partial r}$(RPT)	$9,321$	2.6697
V_z (CPT)	–	–
$V_z = \frac{\partial \tilde{\kappa}}{\partial r}\cos\varphi$(RPT)	$6,957$	2.0238
Force coefficients (RPT)	$O(10^4)$	297.1543

with a Intel(R) Core(TM) i5-4200U CPU @ $1.60GHz$ $2.30GHz$ processor, a 16GB (15.8GB usable) random access memory (RAM) size and a Microsoft Windows 10 operating system. For the variables compared in this table, RPT generally required about three orders of magnitude of more lines of *Maple*^{TM}-generated codes than CPT. It also requires about two orders-of-magnitude more run time than CPT. Obtaining the first differentials of $\tilde{\kappa}$ required about four times more lines of *Maple*^{TM}-generated code and one order-of-magnitude more time than evaluating $\tilde{\kappa}$. The second differentials and secondary quantities require more than these. The force coefficients were obtained in about $300s$. The computational cost grows when multiple evaluation points are required. For instance, evaluating $\tilde{\kappa}$ on a grid of $100 \times 100 \times 10$ with the use of a *for* loop would require about twenty (20) hours. This is cut down significantly into minutes by vectorization of the code.

CHAPTER IV

APPLICATION

The flow over a sphere with varying Reynolds numbers and that over a prolate spheroid at two Reynolds numbers are explored to demonstrate the application of refined potential theory. These geometries have similar axial cross-sections to the circular cylinder (Fig. 57), and they offer further avenues to explore three-dimensional flow features. Aside from these, spherical objects are encountered a lot in practice especially in sports. They have a wind range of engineering applications [15]. Similarly, a prolate spheroid is a suitable canonical model for numerous vehicular applications in the aerospace and nautical fields [12]. The spheroid wake flow has also been of particular interest in DNS due to the inherent complexity of its physics [12].

For the following comparisons, all flow conditions except the second coefficient of viscosity are kept constant at values used for the verification and validation unless they are stated otherwise.

4.1 A Sphere in a Flow with Varying Reynolds Numbers

Figure 78 compares the present theoretical instantaneous Eulerian-mean pressure distribution over a sphere against the classical potential theory and the experiment of Jeon et al. [2]. A qualitative comparison is presented in Fig. 59 (page 138). Table 13 presents the specific flow conditions used for the present sphere flow. The experimental data are time-averaged and were obtained using 23 pressure taps with a

Table 13: Sphere flow conditions.

Re_∞	$S(m^2)$	$\lambda_\infty\ (kgm^{-1}s^{-1})$
1×10^5	πR^2	-1.19236×10^{-5}

Table 14: Measured and predicted sphere flow characteristics at $Re_\infty = 10^5$ (Ref. 2 and present theory) and $Re_\infty = 5,000$ (Ref. 3).

Data from	Re_∞	$\bar{C}_D$	$-C_{p_b}$	$\theta_s(^\circ)$
CPT	–	0	−1	–
Expt (Ref. 2)	1×10^5	$0.51 \pm 2.5\%$	–	$80 - 90$
Expt (Ref. 3)	5×10^3	–	–	85 ± 5
Present theory	1×10^5	0.64	0.25	90

scannivalve and a pressure transducer. The resolution of the MKS220DD transducer is 0.001% at full scale of 10 Torr [2]. Its accuracy of ±0.15% of reading [96] was used to create the error bars in Fig. 78. The present theoretical curve falls within reasonable variation of instantaneous measurements. The laminar separation angle is fairly constant with Re_∞ in the post-bifurcation sub-critical Re_∞ regime. This is evident in the experimental results presented in Table 14 that shows the agreement of the present theoretical separation point with the actual measurements.

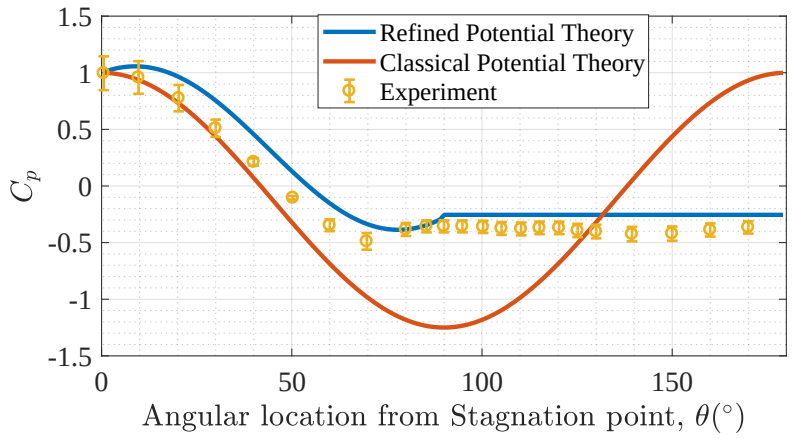

Figure 78: Comparison of RPT pressure distribution over a sphere to CPT and time-averaged experimental data obtained by Jeon et al. [2] at $Re_\infty = 10^5$.

The variations of the time-averaged total drag coefficient with Re_∞ on the sphere has been the subject of numerous experimental investigations. An empirical model

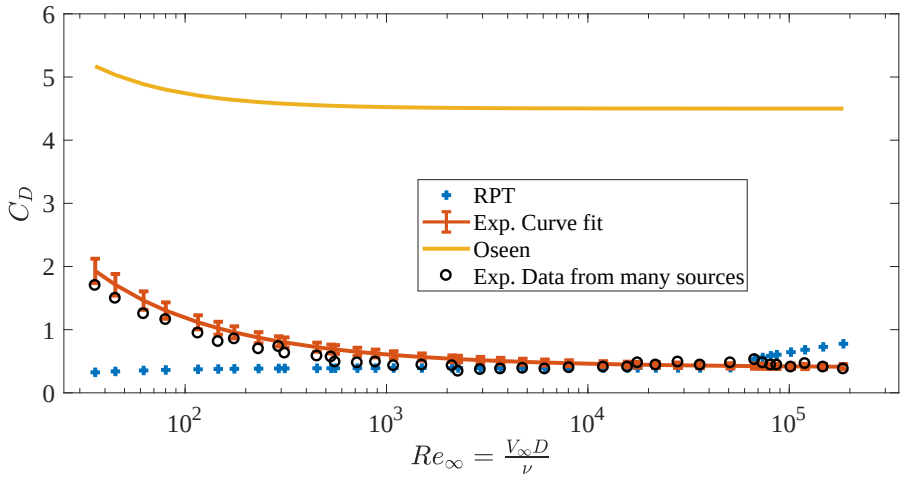

Figure 79: Comparison of theoretical instantaneous Eulerian-mean C_D against time-averaged experimental C_D over a sphere [15].

of this relationship for the sphere (Eqn. 3-225 in Ref. 15) is given [15] as

$$C_{D_{sphere}} \approx \frac{24}{Re_\infty} + \frac{6}{1+\sqrt{Re_\infty}} + 0.4 \qquad 0 \leq Re_\infty \leq 2 \times 10^5 \,. \tag{217}$$

It is reported to be accurate to $\pm 10\%$ of experimental data up to the drag crisis [15, p. 175]. It is plotted in Fig. 79 (with $\pm 10\%$ error band) against time-averaged experimental data from many sources, the Oseen approximation [15, p. 175] and the present theoretical instantaneous Lagrangian-mean result for $25 \leq Re_\infty < 350,000$. The Oseen approximation features an ad hoc linearized convective acceleration in the momentum equation as an improvement on the Stoke's paradox [15]. It results in

$$C_{D_{sphere}} = \frac{24}{Re_\infty}\left(1 + \frac{3}{16}Re_\infty + \cdots\right) \tag{218}$$

for the sphere [15, p. 175]. A generally good agreement is observed in the prediction of the experimental trend for $Re_\infty \geq 2,000$. Jeon et al. [2] report an experimental C_D of $0.51 \pm 2.5\%$ in contrast to the present theoretical value of 0.64 at $Re_\infty = 10^5$ as presented in Table 14. The percentage uncertainties in the experimental data in Fig. 79 were not discussed [15, p. 176], however, the figure illustrates that the Re_∞-dependent flow over a sphere can also be resolved with the refined potential theory, and that the refined theory improves upon the Oseen approximation.

4.2 The Flow over a Prolate Spheroid at an Angle of Attack

Jiang et al. [97] and Strandenes et al. [12] directly simulated the flow over an inclined $6:1$ prolate spheroid at $Re_\infty = 3,000$ and $4,000$ respectively. The Reynolds number is based on the semi-minor axis diameter ($2b$) of the spheroid. At these Reynolds numbers, the flow is incompressible and transitional [12, 97]. They used a parallel code that was developed for efficient DNS and LES of complex geometries [12,97,98]. Figure 80 presents the computational domain employed by Strandenes et al. [12].

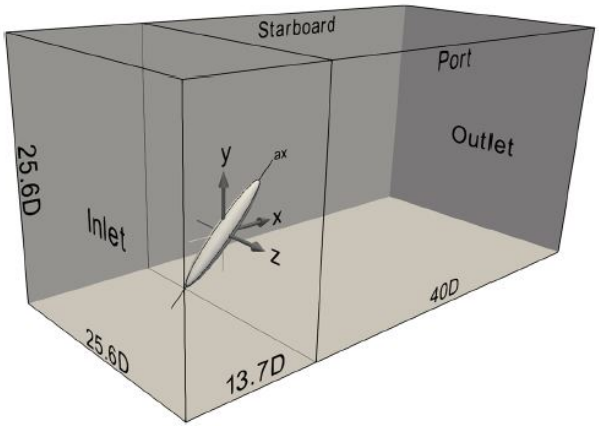

Figure 80: Computational domain used by Strandenes et al. [12].

Table 15 presents some of the flow conditions used for the present theoretical spheroid flow. Figure 61 (page 141) presents the corresponding qualitative comparison between RPT and DNS for the spheroid flow. The reference area for the force coefficients, the angle of attack and the time are all in consistence with the DNS conditions. The second coefficient of viscosity is evaluated at the stagnation point in the windward face of the meridian plane $A - A$ at $y/2a = 0.0$ in Fig. 81a. This is point c in the figure. The radial distance used for this calculation is equal to 1.817 times the radius of an equivalent sphere with the same volume as the spheroid [12]. This is the same radius Strandenes et al. [12] used for the force area, S, in Table 15. The time-averaged simulated C_p distribution on this meridian plane is presented in

Table 15: Spheroid flow conditions.

$b\ (m)$	$a\ (m)$	$S(m^2)$	$\beta(^\circ)$	$t(s)$
0.2	1.2	$\pi(2 \times 1.817b)^2/4$	45	$345.760 \times 2b/V_\infty$

Re_∞	$\lambda_\infty\ (kgm^{-1}s^{-1})$
$3,000$	-1.19091×10^{-5}
$4,000$	-1.19053×10^{-5}

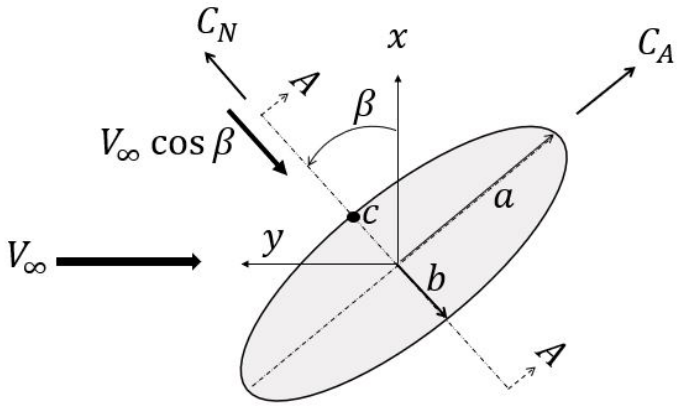

(a) Schematic of the spheroid flow (not to scale).

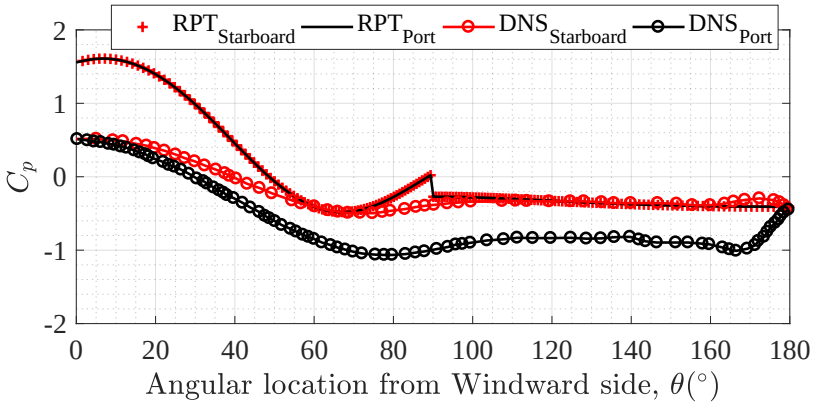

(b) Present theoretical and DNS [12] Eulerian-mean C_p distributions in a plane perpendicular to the major spheroid axis at $y/2a = 0.0$ ($\beta = 45°$, $Re_\infty = 4,000$).

Figure 81: The asymmetric spheroid flow.

Fig. 81b in comparison with the present theoretical instantaneous Eulerian-mean C_p at $Re_\infty = 4,000$. Equation 133 for the sphere was used for the local wind axis in the theoretical pressure evaluation and the incident freestream was $V_\infty \cos\beta$ as illustrated in Fig. 81a. To obtain the equivalent orientation to the DNS results, the spheroid semi-major axis a in Fig. 57c is first rolled through $\varsigma = \pi/2$ into an axial flow. Then, it is yawed through $\beta = \pi/4$. However, the theoretical flow was evaluated as a cross-flow over the spheroid as shown in Fig. 81a. Thus, the limits of integration from LE to TE for both C_A and C_N correspond to $(\theta, \phi) = (\epsilon, -\varsigma)$ to $(\theta, \phi) = (2\pi + \epsilon, \pi - \varsigma)$ respectively for the spheroid crossflow illustrated in Fig. 81a. For C_S, the limits are from $(\theta, \phi) = (\epsilon, -\varsigma)$ to $(\theta, \phi) = (2\pi + \epsilon, \pi - \varsigma)$ in the body axis.

The RPT C_p curve for both the starboard and port sides are almost coincident in Fig. 81b. This means the theoretical flow is nearly symmetric around this plane. It does not differentiate between the two sides, however it captures the separation location in this plane. The slight asymmetry that is not observable in the figure is responsible for the small side force to the port that is presented in Table 16. Table 16 compares the present theoretical force coefficients with corresponding DNS results.

Both of the DNS results show that substantially greater side forces are experienced by the spheroid than the present theory captures. These are due to the asymmetric wake flow that is illustrated in the dissimilarity of the port and starboard DNS pressure distributions in Fig. 81b. Refined potential theory captures the direction of the side force at $Re_\infty = 4,000$ but not at $Re_\infty = 3,000$. However, the DNS results show that each of the directions are equally likely [12].

At the rear of the spheroid, the present theoretical result is consistent with only the starboard pressure distribution. There is more disparity between the present theory and DNS in the windward face. The pressure difference between these faces give rise to the normal force on the spheroid. The directions of the RPT normal forces (C_N) are not consistent with the DNS results because of the disparities in the

Table 16: Comparison of predicted spheroid force coefficient at $Re_\infty = 3,000$ and $Re_\infty = 4,000$.

Data from	C_A	C_N	C_S
		$Re_\infty = 3,000$	
DNS (Mean) (Ref. 12, 97)	0.879	−0.796	−0.645
RPT	0.167	0.092	0.006
		$Re_\infty = 4,000$	
DNS (Mean) (Ref. 12)	0.852	−0.807	0.637
RPT	0.166	0.098	0.006

theoretical and DNS pressure distributions. The DNS results are about an order of magnitude greater. The RPT axial force coefficients (C_A) are also about five times less than the DNS results.

An increase in Re_∞ from 3,000 to 4,000 gives about 3% reduction in the axial force, about 1% increase in the normal force and about 2% reduction in the magnitude of the side force for the DNS results. There are about 50% reduction in the mean torque coefficients and 50% increase in the rms value of their fluctuations (not presented in Table 15) [12]. Strandenes et al. attribute these changes and a distinct change in the wake flow structure to the transitional nature of the flow at these Reynolds numbers [12]. For the refined potential theory, the same change in Re_∞ gives about 0.6% reduction in the axial force, about 6.1% increase in the normal force and approximately no change in the side force. The direction of the changes in the normal and axial force coefficients captured are consistent with the DNS results.

These disparities with the DNS suggest that the refined potential theory requires further research to adequate resolve and explore spheroid flows. Also, further analyses of the other flow separation locations will be required. These analyses are subjects of further studies.

CHAPTER V

CONCLUSION

The three main approaches to exploring fluid dynamics are actual experiments, numerical simulations, and theoretical solutions. In classical potential theory, the steady inviscid incompressible flow over a body can be obtained by the superposition of elementary flows with known analytical solutions. Analytical solutions can offer huge advantages over numerical and experimental solutions in the understanding of fluid flows and design. These advantages are in terms of cost and time consumption. However, the classical potential theory falls short of reconciling the actions of viscosity in an experimentally observed flow with the theoretical analysis of such a flow. As such, it is unable to resolve the boundary layer and predict the especially important flow separation phenomenon that results in the pressure drag experienced by a body in the flow. This has relegated the use of potential theory to idealized cases of little practical importance.

Therefore, an attempt is made in this thesis to refine the classical potential theory of the flow over a circular cylinder to bridge the gap between the theory and experimentally observed flows. This is to enhance the ability to predict and/or control the flows' aerodynamic quantities and the evolution of the wake for design purposes. The refinement is achieved by introducing a viscous sink-source-vortex sheet on the surface of the cylinder to model the boundary layer. These vortices, sources and sinks introduced at the cylinder surface are modeled as concentric at every location. The vortices are modeled as Burgers' vortices, and analytic expressions for their strengths and those of the sinks/sources are obtained from the classical theory. These are employed to obtain a viscous and time-dependent stream function that captures critical

qualitative features of the flow including flow separation, reattachment, wake formation, and vortex shedding.

After that, a viscous potential function, the *Kwasu* function, with which the pressure field is obtained from the Navier-Stokes equation, is derived from the stream function. It is obtained by defining the viscous stream function on a principal axis of the flow about which the vorticity vector is identically zero. Strategies have also been developed to account for the finite extent of the cylinder and dynamic unsteadiness of the flow, and to predict the points of separation/reattachment/transition and the boundary layer thickness. Additionally, the strategies are used to obtain forces and apply the solution to arbitrary geometries focusing on spheres and spheroids. These strategies include the gravity analogy that considers a fluid element-cylinder scenario to be like a two-body problem in orbital mechanics. This analogy introduces the perifocal frame of fluid motion and exploits it to resolve the d'Alembert's Paradox. The perifocal frame is also used to predict flow separation/reattachment/transition and explain the observation of sign changes in the shear stress distribution at the rear of a circular cylinder in a crossflow.

The refined potential theory is verified against experimental and numerical data on the cylinder in an incompressible crossflow at $Re_\infty = 3,900$. Its drag prediction is within the error bound of measured data and tHRLES prediction. The predictions of the pressure distribution, separation point and Strouhal number are also within acceptable ranges. Its prediction of the force coefficients over the range $25 \leq Re_\infty < 300,000$ is validated against experimental and theoretical data on the cylinder in crossflow. There is a good agreement in the magnitude and trend for $Re_\infty > 100$. For $Re_\infty < 100$, there is a disparity in magnitude that is unsafe for design purposes. Similarly, it under-predicts the coefficient of drag in some of the explored axial flow configurations. However, at $Re_\infty = 96,000$ and an aspect ratio of 2, the RPT drag prediction falls within 1.2% of validated computational result. The energy spectra of

Table 17: Summary of the comparison between the classical potential theory (CPT), refined potential theory (RPT) and experimentally observed flows.

	CPT	Experimentally observed flows	RPT
Satisfies Continuity Eqn., $\nabla \cdot \mathbf{V} = 0$	✓	✓	✓
Bounded at infinity	✓	✓	✓
Smooth and Continuous	✓	✓	✓
Satisfies NSE	✓	✓	✓
$d\mathbf{s} \times \mathbf{V} = 0$	✓	✓	✓
Three-dimensions	mostly ×	✓	✓
No-slip condition	×	×, ✓	×, ✓
Vorticity, $\omega \neq 0$	×	✓	✓
Boundary layer	×	✓	✓
Re_∞ dependence	×	✓	✓
Wake	×	✓	✓
Vortex shedding	×	✓	✓
Unsteadiness, Turbulence	×	✓	✓
Compressible	✓	✓	✓
Drag	×	✓	✓

the wake velocity display the Kolmogorov's Five-Thirds law of homogeneous isotropic turbulence. This verifies and validates the unsteadiness in refined potential theory as turbulent in nature.

The drag coefficient of a sphere for $25 \leq Re_\infty < 300,000$ is explored to demonstrate the application of refined potential theory. Additionally, the flow over a sphere at $Re_\infty = 100,000$ is explored in detail. A generally good agreement is observed in the prediction of the experimental trend for $Re_\infty \geq 2,000$. The transitional incompressible flows over a $6:1$ prolate spheroid at an angle of attack $\beta = 45^\circ$ for $Re_\infty = 3,000$ and $Re_\infty = 4,000$ are also explored. The present theoretical pressure distribution has a close agreement with the DNS result in the starboard rear of the spheroid. However, the magnitude of the predicted force coefficients are generally less than five times the corresponding DNS results. The asymmetry of the DNS pressure distribution in the meridian plane is not captured. Therefore, further analyses of the spheroid flow including the separation locations are recommended for further studies.

Table 17 presents a summary of the extent of refinement of classical potential which has been achieved with refined potential theory in comparison with experimentally observed flows. It is concluded that the refined potential theory can be used to resolve, explore and/or control the aerodynamic quantities of the flows around canonical bluff bodies as well as the evolution of their wakes.

CHAPTER VI

RECOMMENDATIONS AND FUTURE WORK

Due to time constraint for the present study and the practical need for a limited scope, a number of research extensions were identified but not explored. Some of these are highlighted in the following discussion.

It was observed that for given values of all other variables, the predicted flow topology and quantities (of the cylinder in crossflow) vary not just with the Reynolds number but also with the specific values for its constituent variables. Holding all other variables constant while varying only the flow velocity does not give rise to significant Re-dependent changes in the profile of pressure and shear stress distributions in a specific Re regime. However, noticeable changes occur in their magnitudes and across regimes [9]. This possibly explains the discrepancies between refined potential theory and experimental values in the creeping flow regime presented in Figs. 82 and 83. The flow velocity is about three orders of magnitude smaller than at $Re_\infty = 3,900$. Thus, the quantities non-dimensionalized by the flow velocity are over-predicted. This is supported by prior analyses of researchers who observed that $C_D \to \infty$ as $Re_\infty \to 0$ because of of the dependence of the drag on V_∞^2 [9]. Zdravkovich writes about a resistance coefficient, C_R, that is better suited for analyzing the creeping flow since $C_R \to 0$ as $Re_\infty \to 0$ [9]. He reports disparities in the measured C_R and the theoretical result of Lamb . These were linked to factors including finite cylinders and BR effects [9]. Additionally, Figs. 82 and 83 were obtained with a value of the second coefficient of viscosity calibrated with $C_p = 1$. However, the stagnation point C_p is greater than one for creeping flows due to Barker's effect [9]. Therefore, these factors are suggested to be partly responsible for the disparity between refined potential theory

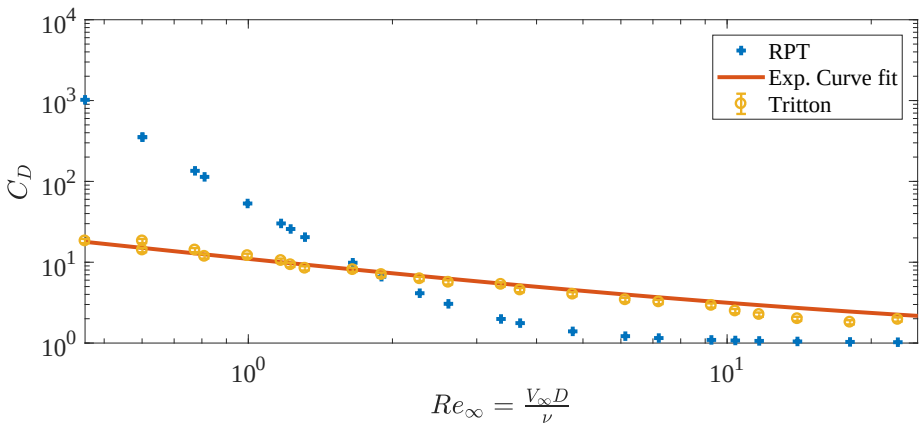

Figure 82: Comparison of refined potential theory in crossflow with experimental data by Tritton [15, 16] and experimental data curve fit by White [15] for very low Re_∞.

and measurements in the creeping flow regime. However, these need to be investigated further.

The analyses presented on the spheroid flow suggest that further investigation including the exploration of the spheroid separation locations are required. These are recommended for further investigations.

The aeroelastic response of a body was not considered in the present theory. However, this can be very important in some design applications. Thus, extending the refined potential theory to such avenues is recommended.

The interaction of the internal flow within an object with the external flow over it e.g. flow over toroids and through pipes, can be explored by defining the radial coordinate in Eqn.130 with an extra term as

$$r = |\sqrt{x^2 + y^2} - R_d| \tag{219}$$

where R_d defines the internal body radial coordinate. Theoretical explorations of these flows are identified for further studies.

The attention of the present studies was focused on incompressible flows. However, refined potential theory can also be used to explore compressible flows. The verification and validation of the compressible refined potential theory is therefore,

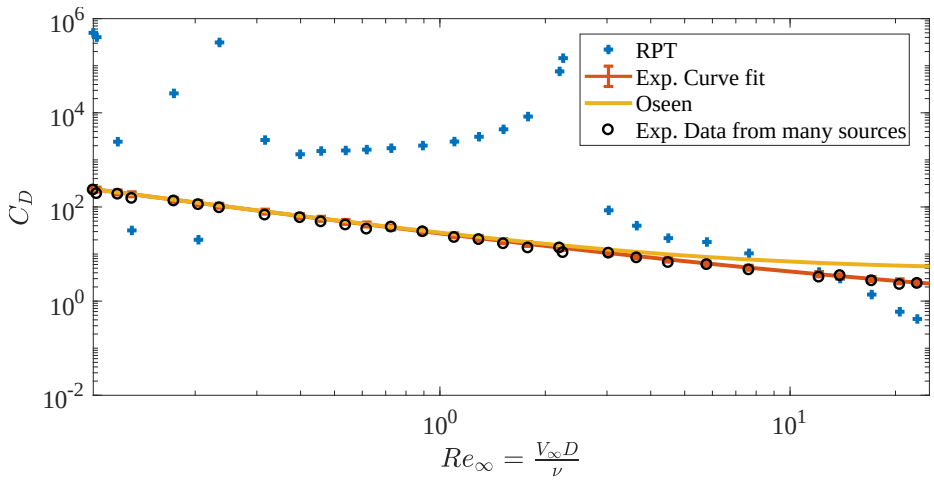

Figure 83: Comparison of present theoretical instantaneous Lagrangian-mean C_D against time-averaged experimental C_D over a sphere [15] for very low Re_∞.

identified for future work.

Finally, it was demonstrated that the present theory captures the three-dimensional vortices of the cylinder wake. This is an interesting result that can be used to explore the problem of trailing vortices in aviation. Therefore, further research can be made into extending the potential theory to more complex geometries like aircraft relying on the guage-invariance of the equations of fluid motion.

REFERENCES

[1] Fage, A. and Falkner, V. M., "Further Experiments on the Flow around a Circular Cylinder," Tech. Rep. Aeronautical Research Committee Reports and Memoranda No. 1369, Air Ministry, London, 1931. Available at http://naca.central.cranfield.ac.uk/reports/arc/rm/1369.pdf - Last accessed: August 26, 2020.

[2] Jeon, S., Choi, J., Jeon, W.-P., Choi, H., and Park, J., "Active Control of Flow Over a Sphere for Drag Reduction at a Subcritical Reynolds Number," *Journal of Fluid Mechanics*, vol. 517, pp. 113–129, 2004. Available at https://doi.org/10.1017/S0022112004000850 - Last accessed: August 26, 2020.

[3] Ozgoren, M., Okbaz, A., Kahraman, A., Hassanzadeh, R., Sahim, B., Akilli, H., and Dogan, S., "Experimental Investigation of the Flow Structure Around a Sphere and Its Control with Jet Flow via PIV," *6th International Advanced Technologies Symposium*, pp. 272–277, 2011. Available at http://web.firat.edu.tr/iats/cd/subjects/Energy/ETE-50.pdf - Last accessed: August 26, 2020.

[4] Sato, M. and Kobayashi, T., "A Fundamental Study of the Flow Past a Circular Cylinder using Abaqua/CFD," *SIMULIA Community Conference*, 2012. Available at https://imechanica.org/files/Sato_MDAC_final_2232012.pdf - Last accessed: August 26, 2020.

[5] Anderson, J. D., *Fundamentals of Aerodynamics*. New York: McGraw-Hill, 5th ed., 2011.

[6] Wu, M.-H., Wen, C.-Y., Yen, R.-H., Weng, M.-C., and Wang, A.-B., "Experimental and Numerical Study of The Separation Angle for Flow Around a Circular Cylinder at Low Reynolds Number," *Journal of Fluid Mechanics*, vol. 515, pp. 223–260, 2004. Available at https://doi.org/10.1017/S0022112004000436 - Last accessed: August 25, 2020.

[7] Van Dyke, M., *An Album of Fluid Motion*. Stanford, California 94305-0030: The Parabolic Press, 4th ed., 1988. Available at http://courses.washington.edu/me431/handouts/Album-Fluid-Motion-Van-Dyke.pdf - Last accessed: August 26, 2020.

[8] Dennis, S. and Shimshoni, M., "The Steady Flow of a Viscous Fluid Past a Circular Cylinder," Tech. Rep. C. P. No. 797, Aeronautical Research Council, Ministry of Aviation, London, 1965. Available at http://naca.central.cranfield.ac.uk/reports/arc/cp/0797.pdf - Last accessed: August 25, 2020.

[9] Zdravkovich, M. M., *Flow Around Circular Cylinders Volume 1: Fundamentals*. Oxford: Oxford Science Publications, 1997.

[10] Prandtl, L. and Tietjens, O. G., *Applied Hydro- and Aeromechanics*. United States of America: United Engineering Trustees, Inc., 1st ed., 1934.

[11] Roshko, A., "Experiments on the Flow Past a Circular Cylinder at Very High Reynolds Number," *Journal of Fluid Mechanics*, vol. 10, no. 3, pp. 345–356, 1961. Available at http://dx.doi.org/10.1017/S0022112061000950 - Last accessed: August 26, 2020.

[12] Strandenes, H., Jiang, F., Pettersen, B., and Andersson, H. I., "Near-Wake of an Inclined 6 : 1 Spheroid at Reynolds Number 4000," *AIAA Journals*, vol. 57, no. 4, pp. 1364–1372, 2019. Available at https://doi.org/10.2514/1.J057615 - Last accessed: August 26, 2020.

[13] Son, J. and Hanratty, T. J., "Velocity Gradients at the Wall For Flow Around a Cylinder at Reynolds Numbers 5×10^3 to 10^5," *Journal of Fluid Mechanics*, vol. 35, no. 2, pp. 353–368, 1969. Available at https://doi.org/10.1017/S0022112069001157 - Last accessed: August 26, 2020.

[14] Kravchenko, A. G. and Moin, P., "Numerical Studies of Flow Over a Circular Cylinder at $Re_D = 3900$," *Physics of Fluids*, vol. 12, no. 2, pp. 403–417, 2000. Available at https://doi.org/10.1063/1.870318 - Last accessed: August 26, 2020.

[15] White, F. M., *Viscous Fluid Flow*. New York: McGraw-Hill, 3rd ed., 2006.

[16] Tritton, D. J., "Experiments on the Flow Past a Circular Cylinder at Low Reynolds Numbers," *Journal of Fluid Mechanics*, vol. 6, no. 4, pp. 547–567, 1959. Available at https://www.cambridge.org/core/services/aop-cambridge-core/content/view/0386A4A3A98750248AEB772532863BB6/S0022112059000829a.pdf/experiments_on_the_flow_past_a_circular_cylinder_at_low_reynolds_numbers.pdf - Last accessed: October 06, 2020.

[17] Norberg, C., "Fluctuating Lift on a Circular Cylinder: Review and New Measurements," *Journal of Fluids and Structures*, vol. 17, pp. 57–96, 2003. Available at https://doi.org/10.1016/S0889-9746(02)00099-3 - Last accessed: August 26, 2020.

[18] Hodara, J., *Hybrid RANS-LES Closure For Separated Flows in the Transitional Regime*. PhD thesis, Georgia Institute of Technology, 2016. Available at http://hdl.handle.net/1853/54995 - Last accessed: August 26, 2020.

[19] Hafez, M. and Wahba, E., "Inviscid Flows Over a Cylinder," *Comput. Methods Appl. Mech. Engrg.*, vol. 193, pp. 1981–1995, 2004. Available at https://doi.org/10.1016/j.cma.2003.12.048 - Last accessed: August 25, 2020.

[20] Eldredge, J. D., *Mathematical Modelling of Unsteady Inviscid Flows*. Switzerland: Springer, 2019. Available at https://doi.org/10.1007/978-3-030-18319-6 - Last accessed: August 28, 2020.

[21] Day, M. A., "The No-Slip Condition of Fluid Dynamics," *Erkenntnis*, vol. 33, pp. 285–296, 1990. Available at https://doi.org/10.1007/BF00717588 - Last accessed: August 24, 2020.

[22] Feffermann, C. L., *The Millennium Prize Problems: Existence and Smoothness of the Navier-Stokes*. Providence, RI: American Mathematical Society, 2006. Available at https://www.ams.org/publications/authors/books/postpub/mprize - Last accessed: August 25, 2020.

[23] Institute, C. M., "NavierStokes Equation," 2018. Available at http://www.claymath.org/millennium-problems/navierstokes-equation - Last accessed: November 16, 2020.

[24] Muriel, A., "An Exact Solution of The 3-D Navier-Stokes Equation," *Results in Physics*, vol. 1, pp. 2–8, 2011. Available at https://doi.org/10.1016/j.rinp.2011.04.002 - Last accessed: August 25, 2020.

[25] Muriel, A., "Exact Solutions of the Navier-Stokes Equation as Subsets of Time Evolution Equations," tech. rep., Program in Mathematics, Graduate Center, City University of New York, 2015. Available at http://dx.doi.org/10.13140/RG.2.1.1126.7046 - Last accessed: August 25, 2020.

[26] Scholle, M., Haas, A., and Gaskell, P. H., "A First Integral of Navier-Stokes Equations and Its Applications," *Proceedings of the Royal Society*, vol. 467, pp. 127–143, 2010. Available at https://doi.org/10.1098/rspa.2010.0157 - Last accessed: August 25, 2020.

[27] Hoffman, J., Jansson, J., and Johnson, C., "New Theory of Flight," *Journal of Mathematical Fluid Mechanics*, vol. 18, pp. 219–241, 2015. Available at https://link.springer.com/article/10.1007%2Fs00021-015-0220-y - Last accessed: August 25, 2020.

[28] Buckmaster, T. and Vicol, V., "Nonuniqueness of Weak Solutions to the Navier-Stokes Equation," *Annals of Mathematics*, vol. 189, no. 1, 2017. Available at https://arxiv.org/abs/1709.10033 - Last accessed: August 26, 2020.

[29] Scholle, M., Gaskell, P. H., and Marner, F., "Exact Integration of the Unsteady Incompressible Navier-Stokes Equations, Gauge Criteria, and Applications," *Journal of Mathematical Physics*, vol. 59, no. 043101, pp. 522–548, 2018. Available at https://doi.org/10.1063/1.5031119 - Last accessed: August 25, 2020.

[30] Sheng, W., "A Revisit of Navier-Stokes Equation," *European Journal of Mechanics/B Fluids*, vol. 80, pp. 60–71, 2020. Available at https://doi.org/10.1016/j.euromechflu.2019.12.005 - Last accessed: August 26, 2020.

[31] Talaei, A. and Garrett, T., "An Analytical Solution to the Navier-Stokes Equation for Incompressible Flow Around a Solid Sphere," 2020. Preprint on webpage at https://www.researchgate.net/publication/343738295_An_analytical_solution_to_the_Navier-Stokes_equation_for_incompressible_flow_around_a_solid_sphere - Last accessed: August 21, 2020.

[32] Walsh, D., "Existence and smoothness of solutions to the 3D Driving Force Free NavierStokes Equation," 2020. Preprint on webpage at https://www.researchgate.net/publication/339973166_EXISTENCE_AND_SMOOTHNESS_OF_SOLUTIONS_TO_THE_3D_DRIVING-FORCE_FREE_NAVIER-STOKES_EQUATION - Last accessed: August 30, 2020.

[33] Schlichting, H., *Boundary-Layer Theory*. New York: McGraw-Hill Book Company, 7th ed., 1979.

[34] Brenner, H., "Beyond the No-Slip Boundary Condition," *Physical Review E*, vol. 84, 2011. Available at https://doi.org/10.1103/PhysRevE.84.046309 - Last accessed: August 24, 2020.

[35] Zhu, Y. and Granick, S., "Limits of the Hydrodynamic No-Slip Boundary Condition," *Physical Review Letters*, vol. 88, pp. 1061021–1061024, 2002. Available at https://doi.org/10.1103/PhysRevLett.88.106102 - Last accessed: August 25, 2020.

[36] Hoffman, J. and Johnson, C., "Resolution of D'Alembert's Paradox," *Journal of Mathematical Fluid Mechanics*, vol. 12, pp. 321–334, 2008. Available at https://doi.org/10.1007/s00021-008-0290-1 - Last accessed: August 25, 2020.

[37] Deane, A. E., Kevrekidis, I. G., Karniadakis, G. E., and Orszag, S. A., "Low-Dimensional Models for Complex Geometry Flows: Application to Grooved Channels and Circular Cylinders," *Physics of Fluids A: Fluid Dynamics*, vol. 3, no. 2337, 1991. Available at https://doi.org/10.1063/1.857881 - Last accessed: August 24, 2020.

[38] Buresti, G., "A Note on Stokes' Hypothesis," *Acta Mech*, vol. 226, pp. 3555–3559, 2015. Available at https://link.springer.com/article/10.1007/s00707-015-1380-9 - Last accessed: August 26, 2020.

[39] Gad-el Hak, M., "Questions in Fluid Mechanics: Stokes' Hypothesis for a Newtonian, Isotropic Fluid," *Journal of Fluids Engineering*, vol. 117, no. 1, pp. 3–5, 1995. Available at https://doi.org/10.1115/1.2816816 - Last accessed: August 26, 2020.

[40] Lamb, H., *Hydrodynamics*. London: Cambridge University Press, 4th ed., 1916.

[41] Joseph, D. D., "Potential Flow of Viscous Fluids: Historical Notes," *International Journal of Multiphase Flow*, vol. 32, pp. 285–310, 2006. Available at https://doi.org/10.1016/j.ijmultiphaseflow.2005.09.004 - Last accessed: August 26, 2020.

[42] Saffman, P. G., "Dynamics of Vorticity," *Journal of Fluid Mechanics*, vol. 106, pp. 49–58, 1981. Available at https://doi.org/10.1017/S0022112081001511 - Last accessed: August 25, 2020.

[43] Förnberg, B., "Steady Viscous Flow Past a Circular Cylinder up to Reynolds Number 600," *Journal of Computational Physics*, vol. 61, pp. 297–320, 1985. Available at https://doi.org/10.1016/0021-9991(85)90089-0 - Last accessed: August 24, 2020.

[44] Nieuwstadt, F. and Keller, H. B., "Viscous Flow Past Circular Cylinders," *Computers and Fluids*, vol. 1, pp. 59–71, 1973. Available at https://doi.org/10.1016/0045-7930(73)90026-1 - Last accessed: August 25, 2020.

[45] D'Alessio, S. J. D. and Dennis, S. C. R., "A Vorticity Model for Viscous Flow Past a Cylinder," *Computers Fluids*, vol. 23, no. 2, pp. 279–293, 1994. Available at https://doi.org/10.1016/0045-7930(94)90041-8 - Last accessed: August 24, 2020.

[46] Wu, J. Z., Ma, H. Y., and Zhou, M. D., *Vorticity and Vortex Dynamics*. Verlag Berlin Heidelberg: Springer, 2006.

[47] Tuann, S.-Y. and Olson, M. D., "Numerical Studies of the Flow Around a Circular Cylinder by a Finite Element Method," *Computers and Fluids*, vol. 6, pp. 219–240, 1978. Available at https://doi.org/10.1016/0045-7930(78)90015-4 - Last accessed: August 25, 2020.

[48] Tazzioli, R., "D'Alembert's Paradox, 1900 – 1914: Levi-Civita and His Italian and French Followers," *Comptes Rendus Mecanique*, vol. 345, pp. 488–497, 2017. Available at https://doi.org/10.1016/j.crme.2017.05.006 - Last accessed: August 25, 2020.

[49] Chen, G.-Q. and Kratka, M., "Global Solutions to the Navier-Stokes Equations for Compressible Heat-Conducting Flow with Symmetry and Free Boundary," *Communications in Partial Differential Equations*, vol. 27 (5 and 6), pp. 907–943, 2007. Available at https://doi.org/10.1081/PDE-120004889 - Last accessed: August 25, 2020.

[50] Amoloye, T. O., "Kwasu Function: A Closed-Form Analytical Solution to the Complete Three-Dimensional Unsteady Compressible Navier-Stokes Equation," *2018 AIAA Aerospace Sciences Meeting, AIAA SciTech Forum*, no. AIAA 2018-1288, 2018. Available at https://doi.org/10.2514/6.2018-1288 - Last accessed: August 25, 2020.

[51] Yaremchuk, A. I., "Clebsch Transformation of Hydrodynamic Equations," *Theoretical and Mathematical Physics*, vol. 115, pp. 434–440, 1998. Available at https://link.springer.com/article/10.1007/BF02575501 - Last accessed: August 26, 2020.

[52] Gu, X.-J., Barber, R. W., John, B., and Emerson, D. R., "Non-Equilibrium Effects on Flow Past a Circular Cylinder in the Slip and Early Transition Regime," *Journal of Fluid Mechanics*, vol. 860, pp. 654–681, 2019. Available at https://doi.org/10.1017/jfm.2018.869 - Last accessed: August 26, 2020.

[53] Lucia, D. J., Beran, P. S., and Silva, W. A., "Reduced-Order Modelling: New Approaches for Computational Physics," *Progress in Aerospace Sciences*, pp. 51–117, 2004. Available at https://doi.org/10.1016/j.paerosci.2003.12.001 - Last accessed: August 24, 2020.

[54] Sirovich, L., "Turbulence and The Dynamics of Coherent Structures Part I: Coherent Structures," *Quarterly of Applied mathematics*, vol. XLV, no. 3, pp. 561–571, 1987. Available at https://doi.org/10.1090/S0033-569X-1987-0910462-6 - Last accessed: August 24, 2020.

[55] Podvin, B. and Fraigneau, Y., "A Few Thoughts on Proper Orthogonal Decomposition in Turbulence," *Physics of Fluids*, vol. 29, no. 020709, 2017. Available at http://dx.doi.org/10.1063/1.4974330 - Last accessed: August 24, 2020.

[56] Hemati, M. S., Williams, M. O., and Rowley, C. W., "Dynamic Mode Decomposition for Large and Streaming Datasets," *Physics of Fluids*, vol. 26, 2014. Available at https://doi.org/10.1063/1.4901016 - Last accessed: August 24, 2020.

[57] Noack, B. R., Afanasiev, K., Morzynski, M., Tadmor, G., and Thiele, F., "A Hierarchy of Low-Dimensional Models for the Transient and Post-Transient Cylinder Wake," *Journal of Fluid Mechanics*, vol. 497, pp. 335–363, 2003. Available at https://doi.org/10.1017/S0022112003006694 - Last accessed: August 26, 2020.

[58] Raissi, M., Yazdani, A., and Karniadakis, G. E., "Hidden Fluid Mechanics: A Navier-Stokes Informed Deep Learning Framework for Assimilating Flow Visualization Data," *Preprint submitted to Journal Name*, 2018. Available at https://arxiv.org/abs/1808.04327 - Last accessed: August 26, 2020.

[59] Taneda, S., "Flow Field Visualization. In: Niordson F.I., Olhoff N. (eds.)," *Theoretical and Applied Mechanics*, pp. 399–410, 1985. Available at https://doi.org/10.1016/B978-0-444-87707-9.50031-2 - Last accessed: September 16, 2020.

[60] Merzkirch, W., *Springer Handbook of Experimental Fluid Mechanics: Flow Visualization*. Berlin Heidelberg: Springer- Verlag, 2007.

[61] White, F. M., *Fluid Mechanics*. New York: McGraw-Hill, 7th ed., 2011.

[62] Zill, D. G. and Wright, W. S., *Advanced Engineering Mathematics*. Burlington, MA 01803: Jones & Barlett Learning, LLC, an Ascend Learning Company, 5th ed., 2014.

[63] Fitzpatrick, R., *Theoretical Fluid Mechanics*. Bristol: IOP Publishing, 2017. Available at `https://iopscience.iop.org/book/978-0-7503-1554-8` - Last accessed: August 25, 2020.

[64] Patel, V. A., "Karman Vortex Street Behind a Circular Cylinder by the Series Truncation Method," *Journal of Computational Physics*, vol. 28, pp. 14–42, 1978. Available at `https://doi.org/10.1016/0021-9991(78)90044-X` - Last accessed: August 25, 2020.

[65] Sen, S., Mittal, S., and Biswas, G., "Steady Separated Flow Past a Circular Cylinder at Low Reynolds Numbers," *Journal of Fluid Mechanics*, vol. 620, pp. 89–119, 2009. Available at `https://doi.org/10.1017/S0022112008004904` - Last accessed: August 25, 2020.

[66] Patel, V. A., "Symmetry of the Flow Around a Circular Cylinder," *Journal of Computational Physics*, vol. 71, pp. 65–99, 1987. Available at `https://doi.org/10.1016/0021-9991(87)90020-9` - Last accessed: August 25, 2020.

[67] Curtis, H. D., *Orbital Mechanics for Engineering Students*. Oxford: Elsevier Aerospace Engineering Series, 3rd ed., 2014. Available at `https://www.elsevier.com/books/orbital-mechanics-for-engineering-students/curtis/978-0-08-097747-8` - Last accessed: August 25, 2020.

[68] Fitzpatrick, R., *An Introduction to Celestial Mechanics*. Cambridge: Cambridge University Press, 2012. Available at `https://doi.org/10.1017/CBO9781139152310` - Last accessed: August 25, 2020.

[69] Pines, S., "Uniform Representation of the Gravitational Potential and Its Derivatives," *AIAA Journal*, vol. 11, no. 11, pp. 1508–1511, 1973. Available at `https://doi.org/10.2514/3.50619` - Last accessed: August 25, 2020.

[70] Mohr, P. J., Newell, D. B., and Taylor, B. N., "CODATA Recommended Values of The Fundamental Physical Constants: 2014," *Reviews of Modern Physics*, vol. 88, no. 035009, 2016. Available at `https://journals.aps.org/rmp/abstract/10.1103/RevModPhys.88.035009` - Last accessed: August 26, 2020.

[71] Anderson, J. D., *Hypersonics and High-Temperature Gas Dynamics*. Reston, Virginia: American Institute of Aeronautics and Astronautics, Inc., 2nd ed., 2006.

[72] Hoerner, S. F., *Fluid-Dynamic Drag*. Bakersfield, California: Hoerner Fluid Dynamics, 1965.

[73] Dusan, E. B., "On the Difference between a Bounding Surface and a Material Surface," *Journal of Fluid Mechanics*, vol. 75, no. 4, pp. 609–623, 1976. Available at https://doi.org/10.1017/S0022112076000414 - Last accessed: September 9, 2020.

[74] Maple, "Maple," *2018 Student Edition. Maplesoft, A Division of Waterloo Maple Inc., Waterloo, Ontario.*, 2018.

[75] Williamson, C. H. K., "Three-Dimensional Wake Transition," *Journal of Fluid Mechanics*, vol. 328, pp. 345–407, 1996. Available at https://doi.org/10.1017/S0022112096008750 - Last accessed: September 20, 2020.

[76] Anderson, J. D., *Mordern Compressible Flows with Historical Perspectives*. New York: McGraw-Hill, 3rd ed., 2003.

[77] Lauga, E., Brenner, M. P., and Stone, H. A., *Springer Handbook of Experimental Fluid Mechanics - Microfluidics: The No-Slip Boundary Condition*. Berlin Heidelberg: Springer- Verlag, 2007.

[78] Pope, S. B., *Turbulent Flows*. Cambridge; New York: Cambridge University Press, 2000. Available at https://doi.org/10.1017/CBO9780511840531 - Last accessed: August 25, 2020.

[79] Andrews, D. G. and McIntyre, M. E., "An Exact Theory of Nonlinear Waves on a Lagrangian-Mean Flow," *Journal of Fluid Mechanics*, vol. 89, no. 4, pp. 609–646, 1978. Available at https://doi.org/10.1017/S0022112078002773 - Last accessed: August 26, 2020.

[80] van den Bremer, T. S. and Breivik, O., "Stokes Drift," *Philosophical Transactions of the Royal Society A*, vol. 376, pp. 1–23, 2017. Available at http://dx.doi.org/10.1098/rsta.2017.0104 - Last accessed: August 26, 2020.

[81] Kozachok, A., "Justification of Stokes' Hypothesis and Navier-Stokes First Exact Transformation for Viscous Compressible Fluid," *European Journal of Mechanics/B Fluids*, vol. 72, pp. 701–705, 2018. Available at https://doi.org/10.1016/j.euromechflu.2018.08.006 - Last accessed: August 26, 2020.

[82] Karim, S. M. and Rosenhead, L., "The Second Coefficient of Viscosity of Liquids and Gases," *Reviews of Modern Physics*, vol. 24, no. 2, pp. 108–116, 1952. Available at https://doi.org/10.1103/RevModPhys.24.108 - Last accessed: August 26, 2020.

[83] Dimopoulos, H. G. and Hanratty, T. J., "Velocity Gradients at the Wall For Flow Around a Cylinder For Reynolds Numbers Between 60 and 360,"

Journal of Fluid Mechanics, vol. 33, no. 2, pp. 303–319, 1968. Available at https://doi.org/10.1017/S0022112068001321 - Last accessed: August 26, 2020.

[84] Kundun, P. K., Cohen, I. M., and Rowling, D. R., *Fluid Mechanics*. Amsterdam: Elsevier, 6th ed., 2016. Available at https://doi.org/10.1016/B978-0-12-405935-1.01001-7 - Last accessed: August 26, 2020.

[85] Prosser, D. T. and Smith, M. J., "Numerical Characterization of Three-Dimensional Bluff Body Shear Layer Behaviour," *Journal of Fluid Mechanics*, vol. 799, pp. 1–26, 2016. Available at https://doi.org/10.1017/jfm.2016.344 - Last accessed: August 26, 2020.

[86] Anderson, J. D., *Introduction to Flight*. New York, NY 10121: McGraw-Hill, 8th edition ed., 2016.

[87] Libretexts, *MTH 210 Calculus I*. 1000 East Henrietta Road Rochester, NY 14623 585.292.2000: Monroe Community College, 2020. Available at https://math.libretexts.org/Courses/Monroe_Community_College/MTH_210_Calculus_I - Last accessed: October 24, 2020.

[88] West, G. S. and Apelt, C. J., "The Effects of Tunnel Blockage and Aspect Ratio on the Mean Flow Past a Circular Cylinder with Reynolds Numbers between 104 and 105," *Journal of Fluid Mechanics*, vol. 114, pp. 361–377, 1982. Available at https://doi.org/10.1017/S0022112082000202 - Last accessed: August 26, 2020.

[89] Ong, L. and Wallace, J., "The Velocity Field of the Turbulent Very Near Wake of a Circular Cylinder," *Experimental Fluids*, vol. 20, no. 6, pp. 441–453, 1996. Available at https://link.springer.com/article/10.1007/BF00189383 - Last accessed: August 26, 2020.

[90] Norberg, C., "Pressure Distributions around a Circular Cylinder in Cross-Flow," *Symposium on Bluff Body Wakes and Vortex-Induced Vibrations (BBVIV3)*, 2002. Available at https://pdfs.semanticscholar.org/8524/8eed0eb5354adf3358105cbe6725de116e86.pdf - Last accessed: August 26, 2020.

[91] Lynch, C. E., *Advanced CFD Methods For Wind Turbine Analysis*. PhD thesis, Georgia Institute of Technology, 2011. Available at http://hdl.handle.net/1853/39491 - Last accessed: August 26, 2020.

[92] Pollard, A., Castillo, L., Danaila, L., and Glauser, M., eds., *Whither Turbulence and Big Data in The 21st Century?* Switzerland: Springer International Publishing, 2017. Available at https://link.springer.com/book/10.1007/978-3-319-41217-7 - Last accessed: August 24, 2020.

[93] Tennekes, H. and Lumley, J. L., *A First Course in Turbulence*. Cambridge, Massachusetts: The MIT Press, 1972.

[94] Tian, X., Ong, M. C., Yang, J., and Myrhaug, D., "Large-Eddy Simulations of Flow Normal to A Circular Disk at $Re = 1.5 \times 10^5$," *Computers and Fluids*, vol. 140, pp. 422–434, 2016. Available at `https://doi.org/10.1016/j.compfluid.2016.10.023` - Last accessed: August 26, 2020.

[95] Matlab, "Matlab," *MATLAB R2017a - Academic Use, The MathWorks, Inc., Natick, Massachusetts, United States.*, 2017.

[96] MKS Instruments, "220DD 1-25000 Torr Heated (45°C) Baratron® Differential Capacitance Manometer." Available at `https://www.mksinst.com/f/220dd-heated-differential-capacitance-manometers`-Last accessed: October 14, 2020.

[97] Jiang, F., Gallardo, J. P., Andersson, H. I., and Zhang, Z., "The Transitional Wake behind an Inclined Prolate Spheroid," *Physics of Fluids*, vol. 27, no. 9, pp. 1–17, 2015. Available at `https://doi.org/10.1063/1.4929764` - Last accessed: August 26, 2020.

[98] Manhart, M., Tremblay, R., and Friedrich, R., "MGLET: A Parallel Code for Efficient DNS and LES of Complex Geometries," *Parallel Computational Fluid DynamicsTrends and Applications*, pp. 449–456, 2001. Available at `https://doi.org/10.1016/B978-044450673-3/50123-8` - Last accessed: August 26, 2020.

VITA

Mr. Taofiq Omoniyi Amoloye is from Igboho, Oyo state, Nigeria. He was born to Dr. Mrs. Bilqis Ajoke Amoloye and late Dr. Abdul-Jelil Adebayo Amoloye on the 3rd of February, 1988 in Ilorin, Nigeria. He attended the demonstration schools of Kwara State College of Education (KWCOED), Ilorin for both of his primary and secondary schools education. He graduated from KWCOED Model secondary school in 2004.

Right from his primary school days, he had been fascinated about space and planets. He went on to study B.Sc. Aerospace Engineering at Kwame Nkrumah University of Science and Technology in Kumasi, Ghana from August, 2005 to June, 2009. Afterwards, he went for about 7 months internship at the aerodynamics research and development group of Volvo Car Corporation in Sweden starting from August 2009. He went back to Nigeria for his yearlong National Youth Service Corps program at the National Space Research and Development Agency in Abuja. Then, he proceeded for an M.Sc. in Aerospace Dynamics at Cranfield University, United Kingdom in October, 2011. He went back to a department of aeronautics and astronautics in its infancy at Kwara State University (KWASU), Malete where he found suitable and gainful employment in Nigeria in March, 2013. He assisted in the teaching of undergraduate classes in aerodynamics, applied aerodynamics, thermofluid dynamics, astrodynamics and space vehicle design. In January 2015, he started a Ph.D. in Aerospace Engineering at Georgia Institute of Technology on a staff development scholarship award from KWASU. He was awarded M.Sc. Aerospace Engineering degree in May 2017, and he successfully defended his doctoral dissertation on May 5, 2020.

He is literate in Yoruba, English, Arabic and French languages.